Production
of
Al - Mg - Transition Element
Alloys

By

Efklidis K. Ioannidis

A thesis submitted for the degree of
Doctor of Philosophy of the
University of London

Section of Mechanical Working
John Percy Research Group
Department of Materials
Imperial College of Science and Technology
London SW7 2BP
U.K.

April 1987

Abstract

A comparative investigation has been performed on three Al-Mg rapidly solidified alloys containing single additions of the transition elements Cr, Fe and Mn. The objectives of the project were firstly to establish the principles governing the behaviour during mechanical processing of rapidly solidified aluminium alloy powders which have metastable structures, and secondly to investigate the resultant mechanical properties. The research programme has been conducted in three stages: (a) powder characterisation, (b) consolidation of the fine air atomized powders by cold compaction and hot extrusion and (c) property assessment of the extrudates and examination of the structure at relevant stages.

Powder characterisation involved study of the powder size and shape, microstructural examination, phase identification and study of the decomposition behaviour during heating of the metastable powder microstructure. A large variety of microstructural morphologies have been observed in the powder particles, such as dendritic, microcellular and partitionless. The heterogeneity of the microstructure was attributed to solidification mechanisms and has been related to the size of the individual powder particles.

Extrusions were conducted within the temperature range of 350°C to 550°C. Round- and rectangular-bar extrudates were produced to study the anisotropy of the properties of the final product with respect to the extrusion direction. Limit diagrams have been constructed for each alloy composition. The Cr bearing alloy exhibited the best hot working characteristics, while the Al-Mg-Fe alloy the worst. The powder compacts conformed to the extrusion behaviour of cast alloys and relationships between extrusion pressure, extrusion ratio and temperature compensated strain rate have been established. The examination of partial extrusions has allowed the consolidation route from the powders to be assimilated.

The mechanical properties of the powder alloys have been determined in terms of tensile tests at room and elevated temperatures, hardness and notch tensile tests, and have been related to the microstructure and processing parameters. Cr and Fe containing alloys display the best combination of strength and ductility. Mg reduces the density of the alloy, while Mn improves the elastic modulus. Poor fracture toughness has been observed attributed to high volume fraction of dispersoids. Coarser structures have been produced at higher processing temperatures for all three alloys, resulting in deterioration of the tensile strength and hardness.

Acknowledgements

Firstly, I would like to express my sincere gratitude to my supervisor Professor Terry Sheppard for the initiation of the project, his helpful guidance, patience and constructive criticisms on my work throughout the entire period, and to Dr. Graeme J. Marshall for his encouragement, help, and critical review at various stages of my research.

I would also like to acknowledge Dr. Henry McShane for the essential second proof reading and his valuable suggestions; "Bodossakis Foundation" for their financial support; the technical staff: Mr. A. Neve and his colleagues for the press maintenance and help; Mr. R. Sweeney for his assistance in the X-Ray work; Mr. G. Briers for his assistance in electron microscopy; Mr. J. Rossdale for the photographic reproduction; Dr. B. J. Briscoe and his group (Particle Technology, Department of Chemical Engineering), especially Mr. D. Liatsis, for the laser-printer facilities and finally all of my colleagues.

Above all, my profound thanks go to my parents, Mr. Kosmas and Mrs Fotini Ioannidou, for none of this could have been done without their unending indulgence, support, enthusiasm and love. Finally I would like to thank my friend Mr. A. Papaspyridis, whose encouragement and moral support have greatly helped me, during my stay in London.

Contents

List of Figures

Chapter 5

Chapter 6

List of Tables

Chapter 2

Chapter 3

Chapter 4

Chapter 5

Chapter 6

Introduction

Chapter 1. Introduction

Materials offering the possibility of achieving improved mechanical properties are under intense development internationally. The requirements for materials with superior properties such as higher strength, higher resistance to corrosion, higher modulus, fatigue and thermal stability stimulated the development of Powder Metallurgy processes using rapidly solidified particulate feedstock.

Rapid solidification techniques can offer considerable advantages over current ingot metallurgy practices with the potential to produce materials with unique properties. The advantages are attributed to microstructural refinement, the absence of macrosegregation, the extension of solid solubility limits and the creation of non-equilibrium phases.

During the last decade aluminium alloys have received increased attention due to their potential for excellent property improvements. Research being focused on the production and processing of aluminium alloy powders is highly likely to result in a novel family of aluminium alloys. The driving force for such development is generally based on weight savings (aerospace engines, weapons) and energy savings (aerospace, automotive, transport). In particular, the aim of current research falls into two basic categories {Mac Cormack (1986)}:

- components with special properties for high technology applications, such as airframe industry, where cost is of secondary importance and

- high production, low cost components to compete with other materials, such as steel and plastic for uses in vehicles and various domestic appliances.

The growing awareness of aluminium alloys as potential powder metallurgy base metals has received added impetus as a result of the significant increase in strength that can be achieved by the incorporation of a dispersion of fine intermetallic or non-metallic particles. Strengthening of aluminium powder alloys is of course achieved by various mechanisms, e.g. solid solution, age and dispersion hardening; among these the most effective is particle hardening. Hence, a particularly interesting problem concerns the selection and design of novel particle hardened alloy compositions.

Research currently taking place at Imperial College concerns the study of powder metallurgy Al-Mg alloys. In general, Al-Mg alloys exhibit medium to high strength, high ductility and high corrosion resistance. These can be used as cast and as wrought up to approximately 10wt%Mg and 5wt%Mg respectively. By using the '*rapid solidification - powder metallurgy*' approach, the level of Mg can be increased up to 37wt% with enhanced workability and mechanical properties. Several aluminium-magnesium binary alloys have been produced {Tan (1984)} as potentially light-weight structural materials. The major strengthening mechanism of the binary Al-Mg alloys, which are not heat treatable, is that due to solid solution effects. However, solid solution strengthening by Mg in the aluminium matrix does not improve high temperature strength over conventional Al-alloys, e.g. 2618 (Al-2.3Cu-1.6Mg-1Ni) and 2219 (Al-6.3Cu-0.3Mn). To increase the elevated temperature strength a fine dispersion of stable precipitates would be essential. As the strength of Al-Mg binary alloys is relatively high, the addition of a suitable element such as the transition elements Cr, Mn and Fe need not require excessive quantities.

Transition elements have been considered to fulfill the requirements for microstructural stability, high strength at elevated temperatures and high modulus. The selection of transition elements is attributed to their inherent properties of (a) high solubility in molten aluminium, (b) low solid solubility in aluminium, (c) low diffusion rate in aluminium and (d) tendency to form stable precipitates at elevated temperatures. These qualities serve one of the requirements for high temperature strength which is to retain the microstructural stability by the introduction of a fine dispersion of thermodynamically stable precipitates.

The present work is part of a research programme concerning the study of Al-Mg alloys containing single additions of the transition elements Cr, Mn and Fe. Moreover, the powder metallurgy route appears more attractive for the production of Al-Mg-Transition element alloys because by using rapid solidification the solid solubility of Cr, Mn and Fe in aluminium can be considerably increased, i.e. from 0.72wt%, 1.4wt% and 0.05wt% to 9-11wt%, 11.5-16.7wt% and 7.9-11.7wt% respectively, {Jones (1978)}. This research is building upon existing knowledge of Al-Mg alloys. Since the binary Al-7%Mg alloy has been shown by Tan (1984) to have as-extruded strengths and ductility superior to most of the commercial aluminium alloys available, the addition of the transition metals would be expected to result in alloys with high strength at elevated temperature and high modulus.

Chromium improves the corrosion resistance and the stress corrosion resistance, while in ternary Al-Mg-Cr alloys the high temperature strength and creep resistance have been reported by Mondolpho (1976) to improve proportionally with the percentage of the $Al_{18}Mg_3Cr_2$ compound. The manganese is well known to improve the stiffness significantly {Starke (1982)}, while additions of iron are also beneficial in increasing the high temperature strength. In general, the presence of iron in cast aluminium alloys has a deleterious effect on properties as a result of the relatively coarse intermetallic particles formed. However, it has been shown by Thursfield and Stowell (1974) that rapid solidification of Al-Fe alloys results in very fine dispersions of stable Fe_4Al_{13} or metastable $FeAl_6$ particles and therefore in better high temperature properties than the existing commercial high temperature aluminium alloys.

The present work has endeavoured to characterise three alloy compositions:

i) Al-6%Mg-3%Cr
ii) Al-6%Mg-7%Mn
iii) Al-6%Mg-5%Fe

The study involves:

(a) a detailed assessment of the powder characteristics, including powder size shape, microstructure and phase identification,

(b) consolidation of the powders, incorporating a study of the evolution of the powder microstructure to the microstructure of the final engineering product and

(c) the relation of the microstructural features to the mechanical properties of the as-extruded engineering material.

The Origins, Development
and
Potential
of
Powder Metallurgy

Chapter 2. The Origins, Development and Potential of Powder Metallurgy

2.1. Introduction

The major industrialized nations have long recognized the enormous potential for technological development offered by materials and so have led in the research of this field. Materials have played, and will continue to play, a predominant role in the technological revolution. The requirements for superior properties, as well as the necessity to save energy and to preserve the environment are constantly the driving force for the development of advanced materials. Such development is also stimulated by the continuously increasing technical requirements and the constantly sought new uses. These provide a strong impetus to the materials engineer towards research in more sophisticated and complex structures, as well as in the application of novel techniques.

Modern techniques include powder metallurgical processing routes using rapidly solidified powder feedstock. The advent and extensive research in this field have enabled the creation and fabrication of several new engineering materials. This implies the design, implementation, development and use of new alloys as well as the upgrading of more conventional materials to a higher level of sophistication. Novel alloys have been produced, with superior properties, based on aluminium, copper, iron, titanium, nickel and magnesium.The importance of rapidly solidified alloys derives mainly from the ability to produce materials from new combinations of the elements of the periodic table, as a consequence of the extension in solid solubility limits, being previously unobtainable due to limitations imposed by thermodynamics.

In the last decade, substantial progress has been achieved by expanding the applications envelope of aluminium alloys. The use of aluminium provides benefits in every sphere of its use ranging from the simple cooking utensils to sophisticated aerospace assemblies. This is attributed to the correct appreciation of its own inherent properties: low density, resistance to corrosion, high conductivity and ease of fabrication. On the other hand, the requirements for high calibre properties such as high strength at room and elevated temperatures, high modulus, fatigue and thermal stability can be met by the development of *powder* aluminium alloys due to their potential for excellent property improvements. It is therefore highly likely that Powder Metallurgy route will result in a novel family of aluminium alloys with unique microstructures and improved mechanical properties.

The present work is part of research focused on the production of aluminium alloys by using rapidly solidified powders. In this chapter a brief review will be presented on both the properties and the applications of aluminium alloys that can be achieved by the P/M route, and the powder metallurgy process with particular emphasis on the parameters affecting the formation and development of the microstructure. This is necessary since the use of materials depends on the ability to produce a suitable microstructure in the final fabricated product in order to obtain desirable mechanical properties. Towards this end, an understanding of the parameters affecting the rapidly solidified microstructures (solidification mechanisms), formed in complex alloys, and the evolution of the microstructure during the thermomechanical process (extrusion), has been considered to be essential in determining the optimum fabrication practice.

2.2. Powder Metallurgy

Powder Metallurgy (P/M) is an old technique dating back to about 3000 BC in ancient Egupt, where iron tools and weapons were fabricated by hammering iron-rich particles at temperatures below their melting point; this technique is a typical example of hot pressing and sintering. Since the obtainable temperatures were not high enough to melt iron or other metals, P/M processes were used exclusively for the production of weapons and agricultural implements. However, the evolution of furnace technology set Powder Metallurgy aside, until the 1800's when components from platinum and tungsten, owing to their high melting point, could only be manufactured by Powder Metallurgy process. A commercial application of Powder Metallurgy is the production of tungsten filaments for the electric bulbs which started in the early 1900's and has been in use until today.

At the end of the Second World War, sintered aluminium products (SAP) were accidentally discovered during experiments involving the preparation of Al-C extruded wires. After this discovery research was initiated on the creep resistance and high temperature properties of extruded aluminium powders. More rapid growth has since occurred and it has been proven that the powder metallurgy route offers distinct advantages in terms of material utilization, ease of component manufacture and cost energy saving. Table 2.1 {Lawley (1986)} illustrates, chronologically, the achievements in powder metallurgy processes.

Nowadays, it is generally recognized that Powder Metallurgy processing routes can be exploited for the manufacture of many complex industrial components and offer the potential for the production of materials with improved mechanical properties. The main advantages of the Powder Metallurgy route over the Ingot Metallurgy result from the intimate coupling between Powder Metallurgy and Rapid Solidification (R/S). This is because the superior properties of the metal powders are attributed to their microstructural characteristics that, due to high cooling rates, fall within the R/S regime; control of the rapidly solidified materials microstructure can be exercised through the solidification mechanisms that govern the process. Clearly, the advent and development of rapid solidification processes have enabled the production of very fine structure materials with extended solid solubility and greater homogeneity. Generally all the advantages of the P/M approach can be exploited in the development of new or extended alloy families with enhanced mechanical properties.

Table 2.1. Examples of Powder Metallurgy

Early Examples		
Iron Base Implements	Egypt	3000 BC
Iron Pillar	Delhi-India	400 AD
High Quality Swords	Arabia	1000 AD
Precious metals Objects	Incas/Peru	1500 AD
Copper Coins	Osann/Germany	1840 AD
Platinum Ingots	Wollaston/U.K.	1826 AD
	Sobolenvskiy/Russia	1834 AD
Modern Era		
Tungsten Filaments via P/M - Collidge		1910
Friction Materials		1920-1930's
Self-Lubricating Bearings		1920's
Copper-Graphite Brushes		
Cemented Carbides		
Electrical Contact Materials		
P/M parts via Press+Sinter - Modern Cements		1930's
High Density Structural Materials via Forging		1960's-Onwards
Specialty Alloys Rapid Solidification HIP, Spray Forming		1970's-Onwards

In order to appreciate the advantages of powder metallurgy route over conventional ingot metallurgy, when using rapidly solidified particulates, the description of the rapid solidification process will be presented, as well as the mechanisms that govern it.

2.3. Rapid Solidification

Rapid solidification was developed during the last two decades, being stimulated by Pol Duwez and his co-workers {Duwez et al (1960) and (1965)}, who reported the production of "unusual" structures by rapid quench rates from the melt. The features of the "unusual" (metastable) structures motivated the metallurgical world towards investigation of the potential for structure-property control via rapid solidification. Since then, a plethora of methods have been developed to achieve high cooling rates; the most typical of them are documented by Jones (1982) and Savage and Froes (1984). These can be mainly classified in three main categories: (a) spray methods (including atomization) in which the melt is fragmented into droplets prior to quenching, (b) chill methods in which the continuity of the melt is preserved up to and during quenching and finally (c) weld methods in which rapid solidification occurs in a limited depth melt at the surface of a substantial thickness material, which serves as a heat sink.

Powder particulates are bestowed with several benefits of rapid solidification, of which microstructural refinement, absence of macrosegregation, greater homogeneity, elimination of undesirable intermetallic compounds, extension of solid solubility and formation of intermetallic phases are the most important. The various structural manifestations afforded by rapid solidification techniques are the consequence of the large nucleation undercoolings, high solidification interface velocities and high rate of heat extraction during both liquid and solid state cooling. An example of the relationship between the cooling rate and a microstructural feature (the dendrite arm spacing) for several alloy systems and powder processing modes is illustrated in Figure 2.1 {German (1984)}.

In order to achieve rapid solidification and the consistent improvements in microstructure, three solidification mechanisms have been listed by Jones (1982), which can in fact be inter-related: (a) a sufficiently large undercooling of the liquid will alleviate the problems of recalescence; (b) imposing a high advance velocity across a steep temperature gradient creates a plane solidification front and finally (c) a high heat extraction rate will result in a high solidification front velocity governed directly by the rate of heat loss to the surroundings.

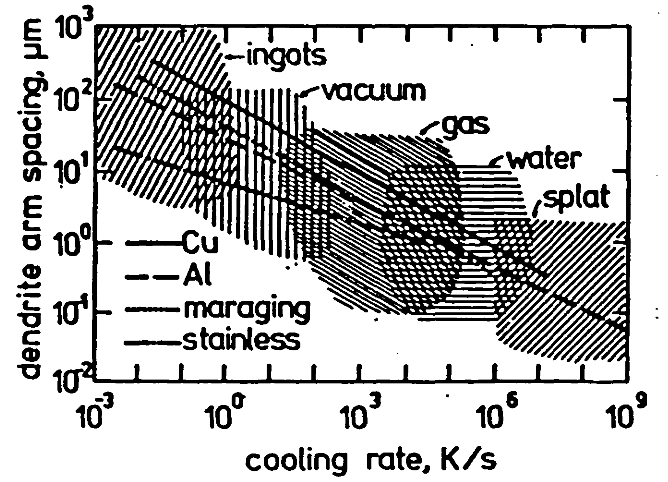

Figure 2.1. Dependence of secondary dendrite arm spacing on cooling rate {German (1984)}.

2.3.1. Atomization

The requirements for higher tonnages of powders have encouraged a multitude of rapid solidification techniques. These include atomization techniques which offer real promise for production of high quality powders at costs that can be competitive to similar alloys produced by ingot technology. The most widely used atomization technique is twin fluid atomization, in which solidification is achieved by sub-dividing the melt into small liquid droplets followed by rapid heat extraction by the cooling fluid. The mechanism of disintegration is a three stage process involving formation of sheets, ligaments and finally liquid droplets, {Adam (1985)}. Since interactions with moulds substrates or other particles are absent, the active nucleation catalysts will be isolated in a small fraction of the total volume, consequently resulting in high undercoolings prior to nucleation. The rapid heat extraction by the cooling fluid also provides rapid post-solidification cooling, thus inhibiting solid state decomposition. Typical obtainable cooling rates in gas atomization range from 10^3 K/s to 10^6 K/s.

The characteristics of the as-atomized droplets, such as *size, shape* and *microstructure* are dependent upon the parameter governing the atomization process and are very important in terms of the metal powder usage. For example catalysts and powder fuels require high specific surface area, thus fine, spherical powders are used. This is not the case for powders destined for use in structural aerospace applications, {Adam (1985)}. Since the size of the powder particulates plays an essential role in the P/M processing route, a brief description of the atomizing parameters, which determine it, as well as its significance are presented below in Section §2.3.2.

Finally, the microstructure of the powder particles can be explained in terms of the solidification mechanisms. It is now established that the cooling rate is important only in subjecting the liquid droplet to a large nucleation undercooling, and in fact nucleation, growth rates and stability of the moving solid/liquid interface will determine the thermal history of the solidifying droplets. Theories governing the rapid solidification of liquid droplets during atomization have been documented {Levi and Mehrabian (1982,a) and Jones (1982)}. These will be presented briefly, in Section §2.3.3, in order to support the discussion on formation of the powder microstructure during atomization (presented in Chapter 4).

2.3.2. Powder particle size

The particle size can be related to the atomization parameters, but even though the atomization technique came into the aluminium field as early as the 1920's few investigations of the process exist and an understanding of the factors which influence the particle size is lacking. Briefly the process parameters affecting the particle size are listed below; however, it is not within the aims of the present work to investigate the interrelation between the atomization parameters and particle size.

1. The melt temperature,
2. The type of gas used,
3. The gas flow to metal flow ratio,
4. The velocity of gas at impact,
5. The properties of the melt, such as surface tension, viscosity and density,
6. The properties of the gas, such as viscosity, density and heat transfer coefficient, and
7. Nozzle design.

The actual solidification rate is largely related to the powder particle size, since it is the single most important variable that governs the heat transfer, {Grant (1982)}, while another important variable is the velocity of the liquid droplet in its atmosphere. The solidification rate also varies with the type of gas used, e.g. helium offers up to an order of magnitude increase in solidification rate over argon and nitrogen. The conductivities of the gas and metal or alloy are secondary factors. Finally, the degree of superheat of the liquid metal has several effects. Enough superheat is required to permit pouring of a small diameter stream, since the viscosity of the melt decreases at higher temperatures, while excessive superheat will of course decrease the solidification rate.

The size of powder particles is a very important parameter in Powder Metallurgy, because it exerts an influence not only on every processing step during powder consolidation (cold-compaction – hot-extrusion), but also affects the powder microstructure and the properties of the final engineering product.

The compaction qualities are largely dependent on the size of the powder particles (see Sections §2.3.2 and §5.1). The green strength has been observed to increase with decreasing particle size for bidirectionally die pressed compacts {In-Hyung Moon (1984)}, which is attributed to the increase in the number of contact points. The green density of the compacts has also been reported {Paramanand (1984)} to be greater with coarser powders. The extrusion pressure requirements are also dependent on powder particle size. Sheppard and Chare (1972) showed that the maximum pressure required to extrude powder aluminium alloys increases with decreasing particle size, which is expected since a greater amount of energy is required to consolidate finer powders. In that work, they also showed that the tensile properties of the final fabricated product depend on the initial powder particle size; especially, when the mean particle diameter decreases the proof stress increases and the elongation decreases. Moreover, Chare and Sheppard (1973) and more recently Sheppard et al (1983,b), working on Al-Fe and Al-Mn-Al_2O_3 powder alloys respectively, reported that a Hall-Petch relationship can be applied to the final product strength and the powder particle size as the grain-size analogue.

Another parameter affected by the powder particle size is the oxide content, which increases with decreasing particle size. The finer the powder, the larger the total surface area exposed to oxidization and the higher the oxide content. The presence of oxide particles affects the properties of the final product.

Finally, it must be noted that the microstructure of the as-solidified powder is closely related to the particle size. Adam and Bourdeau (1980) have reported that since cooling rate and nucleation undercooling vary with the size of the liquid droplet during atomization, microstructural variety maybe expected from particle to particle and even within individual particles; this inhomogeneity can be generally alleviated with decreasing particle size. Marshall (1986) reported that in a R/S Al-Cu alloy (2014) the phases present in the "as-atomized" powder and the precipitation kinetics during post atomization heat treatment were determined by the powder particle size. Moreover, the finer starting particles provide enhanced strength and improve other properties. This is because the size of grains/subgrains and the second phase particles, as well as their dispersion are largely affected by the size of the powder particles.

2.3.3. Solidification Mechanisms-Heat Transfer Analysis

Early solidification models concentrated predominantly on the external heat transfer to the cooling gas, suggesting that the internal solidification process was largely controlled by the rate of heat removal from the droplet surface. However, considering the main interrelating factors determining the thermal history of the powder solidification, such as particle size, nucleation undercooling, cooling rate, recalescence (release of latent heat) and solid-liquid interface velocity, Gill et al (1981) showed that the solidification process consisted of two regimes. The first could be termed the *recalescence or rapid solidification stage*, in which the latent heat, released by the advancing solid-liquid interface, is absorbed by the undercooled liquid. During this regime the cooling rate or the rate of heat extraction to the surroundings played a minor role, while the amount of material solidified depended upon the size of the droplet and the degree of undercooling. The second regime, which could be also termed *pseudo-isothermal*, develops after the termination of "rapid solidification" where the droplet undercooling has been largely relieved and the remaining liquid solidifies under conditions dictated by external heat transfer.

Levi and Mehrabian (1982,b) presented an analysis for solidification of spherical droplets with a discrete melting temperature by using an enthalpy model. In their model, the thermal history of powder solidification was presented mathematically by using dimensionless enthalpy-temperature plots, see Figure 2.2. The enthalpy (H) of a system is given as a function of temperature (T) and fraction solidified (g).

$$(H-H_{SM}) = \left[\Delta H_M + C_L(T-T_M)\right](1-g) + C_S(T-T_M)g \quad \ldots\ldots\ldots\ldots(2.1)$$

where H_{SM}: the enthalpy of the solid at the melting temperature,
C_L,C_S: specific heat of the liquid and solid respectively and
ΔT_M: heat of fusion.

The equation '2.1' can be written in terms of dimensionless enthalpy and temperature:

$$\psi = (1+\theta)(1-g) + \left(\frac{C_S}{C_L}\right) g\,\theta \quad \ldots\ldots\ldots\ldots\ldots\ldots\ldots\ldots \quad (2.2)$$

$$\text{where } \psi = \frac{(H - H_{SM})}{\Delta H_M} \quad \text{dimensionless enthalpy}$$

$$\theta = \frac{C_L\,(T - T_M)}{\Delta H_M} \quad \text{dimensionless temperature}$$

The dimensionless enthalpy is negative or zero ($\psi \leq 0$) when the droplet is solid ($g=1$) because $\theta \leq 0$; but greater than unity ($\psi \geq 1$) for a volume of superheated liquid ($\theta > 0$, $g=0$). The system can follow any path of decreasing enthalpy in the supercooled region ($\psi < 1$) starting at the nucleation temperature ($\theta_N < 0$) on the liquid line and ending at some point on the solid line.

A vertical path, shown in Figure 2.2, represents isothermal solidification, whilst an horizontal one represents adiabatic (isenthalpic) solidification. Limiting cases are path 1 corresponding to the no-undercooling situation; and path 2, where the system can undergo complete solidification without further heat extraction requirements, since nucleation has been suppressed until an amount of enthalpy equivalent to the heat of fusion has been withdrawn *(hypercooling)*. A more general case is described by path 3, in which the droplet is undercooled ($-1 < \theta_N < 0$) and concurrently heat extraction occurs. Two different stages can be identified, which are in agreement with the analysis presented by Gill et al (1981): (a) "rapid solidification" where solidification is always rapid and the liberated heat of fusion is partially absorbed by the undercooled liquid droplet accompanied by increase in its own temperature and (b) "isothermal solidification", characterised by slower growth, since solidification takes place under conditions dictated by the rate of external heat transfer. It is therefore evident that increasing undercooling prior to nucleation increases the rapid solidification rate and thus reduces the relative contribution of the external heat flow.

Finally, the thermal history of the powder particles reflecting the competition between the external heat flow and the recalescence rate (≈dg/dt) can also be represented by the slope of the dimensionless enthalpy-temperature curve ($d\psi/d\theta$). Predominance of the recalescence rate translates into a shallow negative slope for the ψ–θ curve in the "rapid solidification stage, which becomes steeper (more negative) and eventually positive as the external heat flow becomes dominant.

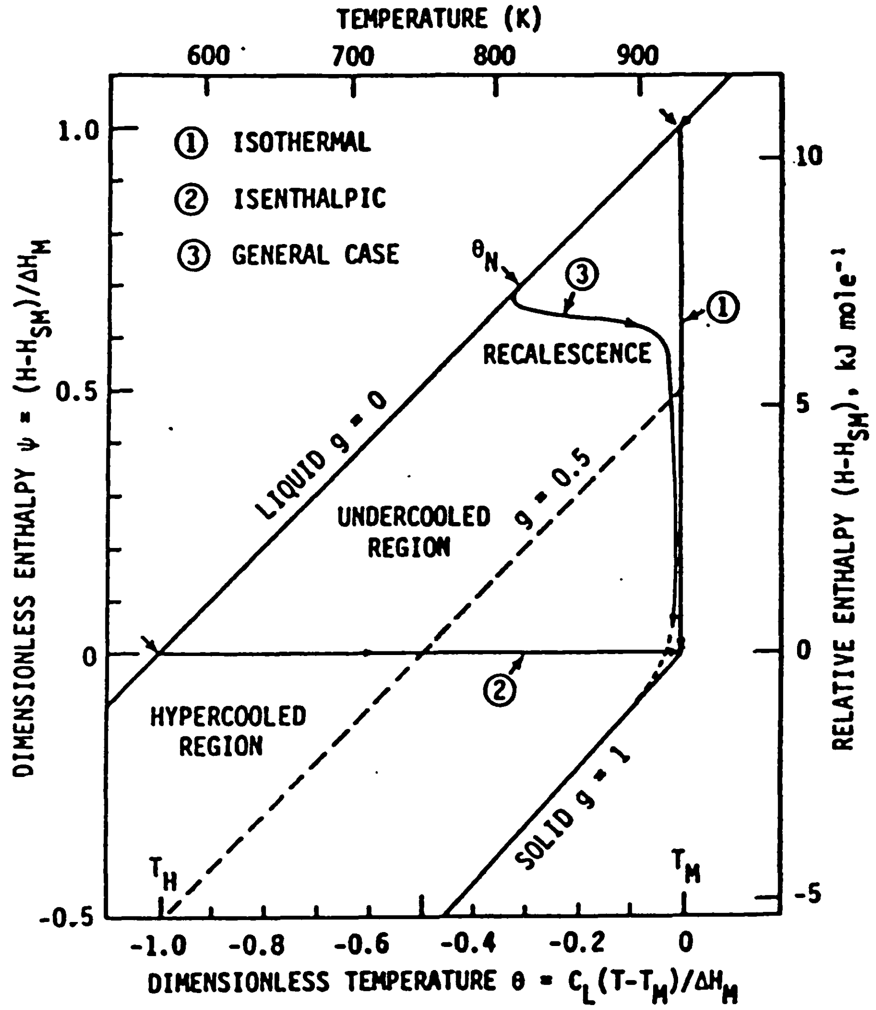

Figure 2.2. Dimensionless Enthalpy - Temperature diagram showing possible solididification 'paths', {after Levi & Mehrabian (1982)}.

The solidification models discussed previously have described the mechanisms that determine the way the heat is extracted from the liquid droplet to produce solid powder particles. In addition, another important issue in dealing with the microstructures of undercooled liquid droplets concerns the growth characteristics of the moving solid-liquid interface, such as the velocity and stability, which, nevertheless, can be inter-related. The attainable solid-liquid interface velocities are a complex function of the initial undercooling, the heat transfer coefficient at the droplet/environment interface and the growth kinetics of the interface. Since this is a particularly interesting and important subject, it will be discussed, in more detail, below.

2.3.4. Solid-liquid interface stability

The classical theory of constitutional supercooling developed by Tiller et al (1953) has been widely used as an adequate guideline in determining the growth conditions that result in unstable interfaces at low interface velocities. This principle is an application of thermodynamics to determine if the liquid ahead of a moving interface is undercooled with respect to its composition. The stability parameter that emerges from this theory is the ratio of the temperature gradient in the liquid ahead of the moving interface to its velocity (G_L/R). Figure 2.3 illustrates the influence of the G_L/R ratio on the interface morphology. Greater stability is promoted by increasing the G_L/R ratio. The line between the planar and cellular areas is the constitutional supercooling criterion for a binary alloy:

$$G_L \geq m_L G_c = \frac{[m_L R C_\infty (k - 1)]}{D_L k} \qquad \text{.......................} \quad (2.3)$$

where G_c : unperturbed temperature gradient
c_∞: is the bulk solute concentration,
D_L: the liquid diffusion constant,
m_L: the slope of the liquidus line
k: the equilibrium distribution coefficient

To the left and above this line plane growth is morphologically stable with compositional homogeneity, whilst to the right and below this line the solute gradient effect dominates, where, due to rejection of solute by the the growing interface, the undercooled liquid layer makes the shape of the interface unstable resulting in the formation of cells or dendrites that could protrude into the liquid. However, the assumptions and simplifications listed below cast doubts on the validity of the constitutional supercooling theory:

- surface tension and latent heat evolution are neglected, even though these could have a stabilizing effect,

- kinetic equations for the thermal and diffusion fields, showing how interface fluctuations can lead to instability, are not taken into account, and

- the assumption of local equilibrium at the interface, with the distribution coefficient (partition coefficient) describing the amount of solute rejected by the growing solid, is not valid. Complete solute trapping could occur if the interface velocity significantly exceeds the diffusion velocity.

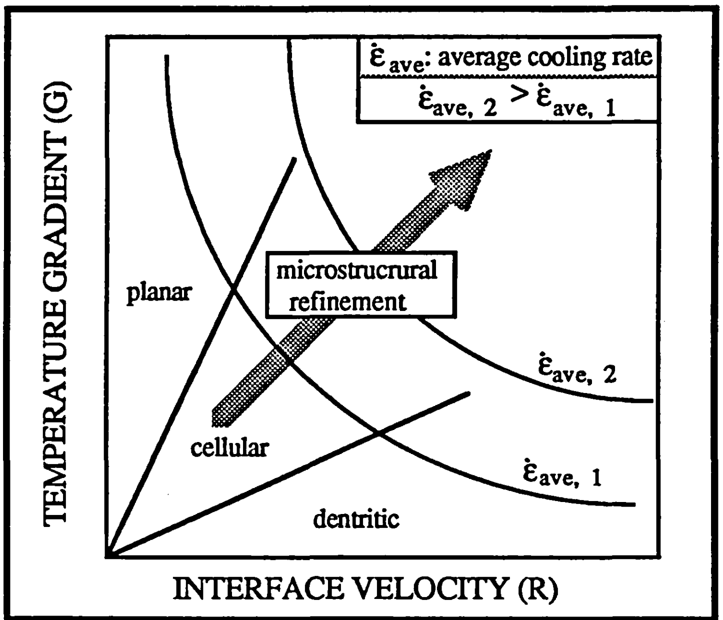

Figure 2.3. Dependence of solidification morphology on temperature gradient and solidification velocity {after R. Mehrabian (1982)}.

The theory of morphological stability, developed by Mullins and Sekerka (1964) and Sekerka (1965), approaches the problem from a kinetic point of view, in order to establish more accurately the growth characteristics of the advancing solid-liquid interface. This considered the time dependence of a general sinusoidal perturbation of the interface with respect to solute and heat-diffusion fields and surface tension. The resulting criterion for stability-instability demarcation identifies three factors contributing to the overall stability of the interface: the solute field, the capillarity forces, and the thermal field. The interface is stable when the sum of the three terms in equation (2.4) is negative. The first term of this equation represents the influence of the solute field, the second of the capillarity forces and the last one of the thermal field.

$$m_L G_C \frac{(\omega^* - R/D_L)}{\left[\omega^* - (1 - \mathfrak{k})R/D_L\right]} - \frac{T_M \gamma \omega^2}{\Delta H_M \rho_S} - \frac{k_S G_S + k_L G_L}{2\bar{k}} \gtrless 0 \text{ .... } (2.4)$$

solute field **capillarity force** **thermal field**
always > 0 **always < 0** $\gtrless 0$

where $\mathfrak{k}$: equilibrium partition coefficient

G_S, G_L: temperature gradient in solid, liquid respectively, at solid/liquid interface

G_C: unperturbed solute gradient, $RC_\infty(\mathfrak{k}-1)/D_L\mathfrak{k}$

$\bar{k} = (k_S + k_L)/2$

ρ_S: the solid density

γ: the solid/liquid interface energy and

$\omega^* = R/2D_L + \left[(R/2D_L)^2 + \omega^2\right]^{1/2}$

D_L: liquid diffusion coefficient of solute

Hence, the solute field is always destabilizing, while the capillarity forces oppose the growth of a perturbation. The thermal field will be stabilizing if the numerator is positive and destabilizing if it is negative.

Extensive reviews available in the literature {Delves (1974), Langer (1974), Sekerka (1973), and Wollkind (1979)} have demonstrated that the constitutional supercooling and morphological stability theory lead to similar results. The simplicity of the first one makes it more popular. However, since both surface tension and evolution of latent heat have a stabilizing effect, the morphological stability theory predicts far greater stability during rapid solidification, especially at high interface velocities where stability is independent of temperature gradient. Moreover, recent studies concluded that two other effects are also important in rapid solidification phenomena. The first one, known as absolute stability, suggests that the interface remains stable at high velocities and the second one suggests that most departures from local equilibrium enhance the interface stability especially when the partition coefficient tends towards unity. Cohen et al (1980) have shown that increasing the cooling rate and decreasing the solute content promotes planar interfaces.

2.4. Consolidation process

2.4.1. Introduction

Powder Metallurgy has now evolved to the point that fully dense wrought structural alloys with improved mechanical properties are commercially available. Rapid Solidification constitutes the primary step of the production of P/M alloys, whilst the consolidation of the atomized powder is the other key process in wrought P/M technology. A variety of methods and processes have been utilized for achieving the fabrication of the powders, {Tietz and Palmer (1981) and Pickens (1981)}. Amongst them, the most prevalent are hot isostatic pressing, vacuum hot pressing and Alcoa's two methods a) cold press - degas - hot press and b) cold press - extrusion.

Generally, the consolidation processes are classified in two categories. Those which occur without or with little material deformation i.e. hot isostatic pressing {Arzt et al (1983) and Fischmeister (1978)}, and those in which consolidation is only achieved by deformation i.e. forging, extrusion and rolling. When extrusion is employed, Sheppard et al (1983,b) have shown that consolidation occurs during the high temperature deformation, in which the material attains its full strength. Hence, it would be possible to extrude powders by feeding them directly into the extrusion press; however in that case the extrusion process would become awkward and impractical. Thus, it is imperative to produce firstly billets/compacts having enough strength to withstand handling for transport to the extrusion chamber.

2.4.2. Compaction

As previously explained, the compaction of the powder particles constitutes an indispensable step in the manufacture of parts by the powder metallurgy route. The aim of cold compaction is to bring the powder particles together, so that interparticle bonding will be developed and billets will be produced with adequate strength and density. Due to its significance, the powder compaction process has been the focus of attention for many researchers, and has been extensively studied, {Hewitt et al (1973); Kunin and Yurschenco (1963); Paramanand (1984); and Penrice (1958)}. It is now well established that there are three stages involved during compaction of loose powder:

1st: Packing of the undeformed particles,
2nd: Elastic and plastic deformation and
3rd: Cold working of the compact as a whole.

During the 1st stage the particles are rearranged into a smaller volume which is dictated by the nature (shape and size) of the particles themselves. During the second stage, the powder particles slide over each other, while the attractive junctions, which are formed between adjacent particles, flatten them elastically. Densification of the compact is then promoted by deformation, while the oxide skin, formed during atomization, ruptures, thus resulting in metal/metal contact and interparticle bonding. During this stage, the interparticle bonds break and reform continuously, as the compact approaches full density, while the total interparticle area increases leading to enhanced compact strength. The driving force that keeps the particles pressed together arises from the reduction of surface energy.

The green strength of a cold-pressed billet is an important property because most industrial processes necessitate a certain amount of handling before the thermomechanical process. Consequently, the billets are required to have sufficient green strength and density. The strength of the powder compacts has been shown {Easterling and Thölen (1973); Strömgen et al (1973)} to depend mainly on the hardness of the powder particles, the strain hardening, the nature of the powder particle surface, the elastic properties of the metal and finally on the number of the metal/metal interfaces formed and their adhesive strength.

In addition, the shape and the size distribution of the powder particles as well as the compaction pressure play a very significant role in the compaction process, since both the green strength and green density of the compacts depend largely on them. Irregularly shaped particles and a wide size distribution are more preferable, because the small particles fill interstices created by larger particles, thus producing greater density and forming a larger number of interfaces. Furthermore, irregularly shaped particles can cause asymmetrical loading between particles, thus creating shear stresses, interparticle sliding and frictional welding of freshly exposed surfaces, {Hewitt (1974)}.

The influence of the compaction pressure on the density of the compact has been extensively studied and the most widely known relationship has been suggested by Shapiro and Kolthoff (1974), which has the form:

$$p = l + c \ln \frac{1}{1-D} \quad \ldots\ldots\ldots\ldots\ldots\ldots\ldots \quad (2.5)$$

where p: compaction pressure (MN/m^2), D: density (kg/m^3) and l,c: constants depending upon the compaction behaviour of the powder.

The validity of this equation has been proven for many powder alloys. Relatively recently, Sheppard and McShane (1980) working with an Al-Mg-Si alloy have shown the validity of the equation, and that the strength of the cold compact can be expressed as a function of the compacting pressure:

$$S = f\left[\left(\exp\frac{p}{\gamma} - \exp\frac{\lambda}{\gamma}\right)^{-2/3}\right] \quad \ldots\ldots\ldots\ldots\ldots\ldots\ldots \quad (2.6)$$

where S: compact strength
p: compaction pressure
λ,γ: constants

Finally, the powder compactability is also affected by the oxide film formed during atomization. It has different effects on the compaction properties. On the one hand it reduces the surface tension of the molten droplets, which produces a greater proportion of irregularly shaped particles and on the other hand it affects the bond strength of the interfaces that keep the particles pressed together. If metal/metal contact is not obtained the strength of the billets is very low. The oxide skin should then be avoided if good strength and induction heating properties are required.

2.4.3. Hot Extrusion

The extrusion process is a convenient route by which metal powder compacts are forced through a die orifice of a particular shape and size and consequently are converted into a 100% dense product. The powders are extruded at elevated temperatures for two main reasons. Firstly, to give a convenient flow stress, as high temperature prevents work hardening, which increases the pressure and energy requirements, and secondly to avoid the brittleness of a cold worked structure.

The extrusion process has been extensively studied for cast metals and powder compacts, {McShane (1978); Parkinson (1983); Vierod (1983)}. In the case of metal powders, extrusion combines both consolidation and hot working in a single operation. At the beginning of extrusion the approximately 80% dense billet breaks and fills the container; this is the stage in which the extrusion load increases non-linearly with displacement, as illustrated in an ideal load-displacement curve, see Figure 2.4 stage -'a'. During this stage the air trapped among the particles emerges apparently through the cracks formed and the interconnecting porosity of the compact until the billet attains the theoretical 100% density. Subsequently, the load increases linearly up to a maximum (stage -'b'). A deformation zone has not been established yet, however extrusion has started at some intermediate location as indicated on the load displacement curve (Figure 2.4). The peak load increment has been proven by Castle and Sheppard (1976) to be associated with the excess energy required to establish a quasi-static deformation zone. During this stage, the billet is further compressed while dislocations play a dominant role in the creation of the deformation zone by their generation, migration and annihilation. After the peak load a deformation zone has been established while the load decreases to a minimum value, see Figure 2.4, stage -'c'. The minimum load remains constant throughout the remainder of the extrusion (Figure 2.4, stage -'d'), this stage is called steady-state. During steady state, the material passes through the quasi-static deformation zone in which consolidation occurs; the deformation zone remains constant and the rates of dislocation generation and annihilation are equal. In an ideal process the load required to maintain extrusion consists of the load required to work the material in the deformation zone plus the load required to overcome friction between billet surface and the container.

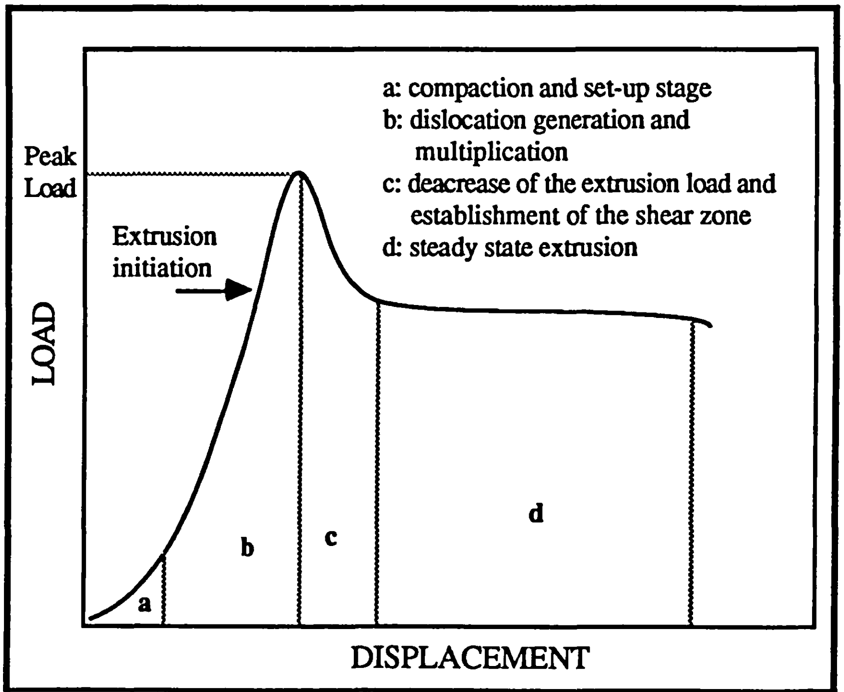

Figure 2.4. Typical Load Displacement Curve

The theoretical parameters that affect the extrusion of metal powders are: initial billet temperature, extrusion ratio, shape of the die, ram speed, billet length, lubrication and powder characteristics. The powder variables include chemical composition, particle size distribution and oxide content. The quality of the extrudates varies with the processing parameters. Acceptable extrudates can be produced within a range determined by the processing parameters and properties of the material. The requirements for an acceptable extrudate are complex depending on surface conditions, the attainment of a suitable structure and the related mechanical properties. Requirements imposed by the material usage must also be taken into consideration. For example Al-Mg-Si powder alloys for domestic uses are required to have excellent surface finishes, while high strength P/M alloys used for airframe applications are machined down to the required shape and thus any undesirable bad surface finish or recrystallized surface layer is removed.

The extrusion range can be depicted by a diagramatic representation considering the interaction of structure, strain rate and temperature. Hirst and Ursell (1958) were the first to present such diagrams. A typical limit diagram consisting of two lines is shown in Figure 2.5. The line on the right represents the incipient melting limit. The incipient melting limit line lies between two extreme conditions, the *isothermal* and the *adiabatic*. When the deformation is occurring at extremely low strain rates the heat is dissipated without raising the billet temperature (isothermal condition); however, at very high strain rates all the heat of deformation goes into the billet raising its temperature, (adiabatic condition) resulting in a narrower range. The limiting line on the left represents the press capacity; insufficient press capacity determines the low temperature limit for extrusion. With increasing press capacity the extrusion range increases. The operating region for satisfactory extrusion lies beneath these two lines, as shown in Figure 2.5.

Limit diagrams can also be constructed from theoretical data. The pressure line can be specified by using the modified Johnson's equation {Johnson (1955)} and the incipient melting line by a correct knowledge of the flow stress and temperature rise during extrusion. However, the derivation of such limit diagrams does not take into account parameters of primary importance. For example, the onset of recrystallization, which causes susceptibility to stress corrosion, must become paramount to that of hot shortness or incipient melting. Generally the microstructure of the extrudate is the controlling parameter since it determines the as-extruded mechanical properties and their response to further heat treatment. Sheppard and Raybould (1973) made further improvements, in which the temperature rise and the dependence of both limit curves on the strain rate are combined into modified equations. Moreover, by plotting constant strain rate curves instead of ram speed the diagram can include lines for various effects such as surface checking, surface recrystallization and subgrain size.

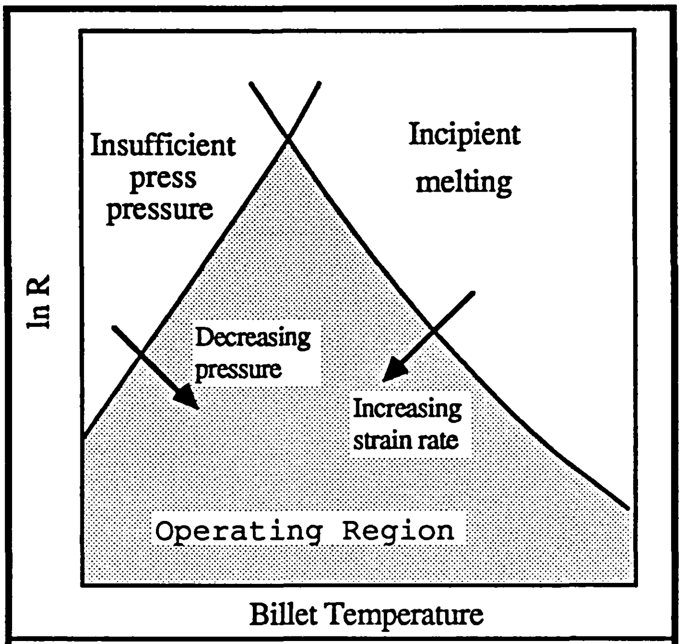

Figure 2.5. Limit Diagrams

Finally, it is important to realize that extrusion is a complex thermomechanical process that involves interaction between the processing variables and the material high temperature properties.

2.4.4. Hot Working

A deformation process can be considered analogous to a chemical reaction in which the composition remains constant but the bond structure of the atoms is changed. During deformation of metals and alloys, atomic planes slip over each other assisted by dislocations, whilst individual atomic bonds are broken and new bonds are formed. Hence deformation actually occurs by a bond breaking/reforming process

There is an analogue between a chemically reacting system and plastic deformation of crystalline materials. In a reacting system, Arrhenious has established that there is an equilibrium between the number of 'ordinary' and 'active' atoms and that only the latter are able to react. In crystalline materials the bond breaking process occurs in regions with 'active atoms' which are lattice imperfections, i.e. dislocations. The energy barrier is low at the dislocation core and is lowered further by the application of a shear stress such that there is a high probability that bond breaking will be possible under the effect of a small temperature increase. Hence bond breaking occurs preferentially at high energy configurations and the imperfect structure provides the space necessary for mass transfer.

The chemical reaction rate (x) is given by the Arrhenious equation:

$$x = A_0 e^{\frac{-\Delta H}{kT}} \quad \ldots\ldots\ldots\ldots\ldots\ldots\ldots\ldots\ldots\ldots \quad (2.7)$$

where T: absolute temperature and k, A_0: constants.

During plastic deformation the rate equation, has been shown by Sellars and Tegart (1966), to have the form:

$$\dot{\varepsilon} = A\left[\mathrm{Sinh}(\alpha\bar{\sigma})\right]^{\eta} \exp\left(-\frac{\Delta H}{\Re T}\right) = Z \exp\left(-\frac{\Delta H}{\Re T}\right) \quad \ldots\ldots\ldots\ldots \quad (2.8)$$

where $\dot{\varepsilon}$: mean strain rate, ΔH: activation energy

α, η: constants, $\bar{\sigma}$: mean flow stress

$\Re$ =8.314 kJ/mol °K, the universal gas constant and

Z: the temperature compensated strain rate

The similarity of these two equations, '2.7' and '2.8', is apparent. The rate of plastic deformation depends on the various mechanisms by which dislocations can move, e.g. cross-slip, climb, glide e.t.c. and more than one may be operative at any one time. Among the operative mechanisms the slowest one requires the highest activation energy and is the rate controlling.

The parameter Z in equation '2.8' is very important and obviously can be expressed in terms of the temperature of deformation and the strain rate. During deformation Z plays a dominant role, and it would be more precise to consider Z as a strain rate compensated temperature.

Obviously, plastic deformation is promoted at high temperatures (greater than 0.6 of the melting point), at which a constant flow stress can be attained for large strains. This is attributed to dislocation dynamics, since the strain hardening is counterbalanced by the concurrent softening mechanisms of dynamic recovery and/or dynamic recrystallization. The difference between these two processes is that in dynamic recovery, mechanisms such as cross slip, climb, and node unpinning permit the dislocations to unravel from hardening networks and annihilate each other, while in dynamic recrystallization, new grains nucleate, grow and deform as they grow and recrystallization takes place again and again. The stacking fault energy of the material as well as the size and the distribution of the dispersoids determine whether recovery or recrystallization will occur.

The capacity of the materials to dynamically recover diminishes with decrease in stacking fault energy (SFE). This is attributed to two main factors. Firstly the number of partial dislocations is greater, since less energy is associated with the formation of each one. Secondly, since the width (d) {see equation '2.9'} of the partial dislocations is greater, constrictions, permitting cross slip, form less readily.

$$d = \frac{G(b_2 \cdot b_3)}{2\pi\gamma} \quad \ldots\ldots\ldots\ldots\ldots\ldots\ldots\ldots\ldots\ldots \quad (2.9)$$

where G: shear modulus; b_2, b_3 : Burgers vectors and γ: stacking fault energy

Materials that dynamically recover are characterised by the formation of well defined subgrains in the hot worked structure. Higher deformation temperatures result in more perfect subgrains or grains during dynamic recovery or rectrystallization respectively.

Pure aluminium is a metal with high stacking fault energy, so that the dominant softening process is dynamic recovery. During the initial stages of hot working the flow stress increases, which is attributed to dislocation accumulation, since at the beginning of deformation the rate of dislocation generation is greater than that of annihilation. With increasing dislocation density, the dislocations form tangles and rearrange themselves into a cellular structure. By the time the steady state regime is reached the flow stress remains constant, while the dislocations have arranged themselves into subgrains whose perfection, dimension and misorientation are dependent on the metal, strain rate and deformation temperature. The strain required for subgrain formation increases with decreasing temperature of deformation.

During the steady-state deformation (stage -'d', Figure 2.4) the flow stress depends on the strain rate. The rate of dislocation generation is equal to the rate of annihilation and the dislocation density remains constant within the subgrains as well as the dislocation content of the sub-boundaries. Thus, the misorientation does not increase. Dynamic recovery results in an equiaxed subgrain structure even at larger strains. One possible interpretation is that the subboundaries are constantly migrating in such a way to keep the substructure equiaxed. The driving force for migration is the stress acting on the boundary dislocations, possibly assisted by the pressure built up inside the subgrains by the concentrations of like edge dislocations "piled-up" behind the sub-boundaries awaiting climb. The larger the subgrains the higher the internal pressure. Thus, they constantly consume the smaller subgrains. An equilibrium subgrain size ensues, because the rate of generation of new subgrains inside the large is equal to the rate of annihilation. Extensive availability of vacancies permits the sub-boundary migration. At sufficiently high strains sub-boundary migration cannot take place, thus another contributing feature is repolygonization. This involves the repeated unraveling of the sub-boundaries and the subsequent reformation of new sub-boundaries at locations which keep their dislocation density and the average spacing constant.

Alloying additions in aluminium affect the stacking fault energy due to changes in the electronic structure. When the alloying additions decrease the SFE, the susceptibility to recrystallization increases. Sheppard and Tutcher (1980) reported evidence of a duplex deformation substructure incorporating dynamically recovered subgrains modified by the presence of outcrops of small dynamically recrystallized grains in a commercial Al-5%Mg alloy. Moreover, Sheppard et al (1983,d) presented overwhelming evidence that dynamic recrystallization is the dominant mode during extrusions of cast Al-7%Mg. More recently, Tan (1984) working on P/M Al-Mg alloys reported that his alloys exhibited dynamic recrystallization. However, additions of transition elements have been shown to serve as recrystallization refiners, Conserva and Leoni (1975) have also reported their refining action in an Al-7%Mg alloy.

2.5. Powder Metallurgy of Aluminium Alloys, Properties and Applications

In recent years there has been an explosion of interest in aluminium as a potential P/M base metal. The incentives in the aluminium industry were to develop alloys having one or more of the following characteristics:

- high room temperature strength,
- high strength at elevated temperatures,
- high strength allied to corrosion resistance and
- low density, high modulus.

Towards this end, aluminium alloys, which are the most extensively investigated R/S alloys, have been developed via the P/M route, and it has been shown that they have the potential for excellent property modification, thus increasing the range of their applications.

In the 1940s and 1950s aluminium powders were investigated for use in wrought components. Sintered aluminium products utilized dispersions of Al_2O_3, in order to improve the high temperature strength of parts consolidated from milled aluminium powder. Since then, experimental work on atomized aluminium powders produced encouraging results prompting the metallurgists to pursue the issue further-the genesis of research on current P/M aluminium alloys.

Initially, it is valuable to look at the benefits of the microstructural refinement due to rapid solidification, and to highlight the structural parameters of importance that determine the mechanical properties.

Refined grain size. Rapid solidification produces alloys with grain sizes often down to about 1 μm and routinely down to 1-20 μm, which are significantly finer than those developed in conventional casting. Moreover, fine grain sizes are usually obtained in the consolidated material as a result of the significant refinement of the dispersoid particle size. Microstructure refinement has been shown to be a method of strengthening, but it also improves ductility , fracture toughness and stress corrosion resistance.

Increased solid solubility. This is an area of extreme interest, because, although most metals alloy with aluminium, comparatively few have sufficient solid solubility to serve as major alloying additions. For example, only zinc, magnesium, copper and silicon have significant solubilities, see Table 2.2, {Jones (1978)}. However, several other elements with solubilities below 1at% confer important improvements to alloy properties. Amongst them stand the transition elements, e.g. chromium, manganese and zirconium. Rapid solidification techniques overcome the limitations imposed by thermodynamics, allowing a significant extension of solid solubility limits and thus resulting in a great deal of benefits such as in the use of transition elements for high strength and high temperature improvements. The degree of solid solubility extension reported for various alloying elements has been compiled by Jones (1978); some data are shown in Table 2.2.

Solute	Maximum Solubility	Temperature (°K)	Extended solubility
Ge	2.8	697	40
Co	0.01	930	5
Cr	0.44	934	5 - 6
Cu	2.5	821	17 - 18
Fe	0.025	928	4 - 6
Mg	18.9	723	34 - 40
Mn	0.7	923	6 - 9
Ni	0.023	913	1.2 - 7.7
Ti	0.15	938	2
V	0.20	933	6
Zn	66.5	936	
Si	1.59	850	10 - 16
Zr	0.083	936	1.5
Mo	0.07	933	> 1.0
Ce	0.01	911	1.9

Table 2.2. Solid Solubility limits of some elements in aluminium in at%.

Refinement of the intermetallic phases. The most important factor affecting the mechanical properties of aluminium alloys is the type and distribution of intermetallic phases. Rapid solidification can both eliminate the complex constituent particles and reduce the size of the second phase particles, thus producing a fine dispersion of sub-micron sized intermetallics with an improvement in mechanical properties. The refinement occurs in two ways: either as a result of the decrease in time available for nucleation and growth of the second phase particles during solidification, or as a result of the formation of supersaturated solid solutions from which precipitation occurs on a finer scale during subsequent exposure to heat treatment.

In order to appreciate the properties of R/S alloys it is essential to review the strengthening mechanisms that are employed in P/M alloys. Starke and Wert (1985) have reported that the strengthening mechanisms are similar to those in any metallic material irrespective of the production route. At low and intermediate temperatures, deformation occurs primarily by glide, while at elevated temperatures climb, bulk diffusion and grain boundary sliding operate simultaneously. At low temperatures the traditional subgrain refinement is modified by solid solution strengthening and particle hardening. Effective solid solution strengthening requires a high solid solubility of an element having a different modulus and a significant atomic size difference from the aluminium, however, although rapid solidification increases the solid solubility limits, most current methods used for consolidation negate any advantages obtained in this manner. Effective precipitation and dispersion strengthening depends on a fine distribution of second phase particles. The degree of strengthening resulting from the second phase particles depends on their size and distribution in the ductile matrix. Precipitates are usually produced by low temperature aging of a supersaturated solid solution, while dispersoids are usually termed second phase particles that have incoherent interfaces often produced by eutectoid decomposition, internal oxidation or mechanical mixing of particulates following by powder consolidation. A major problem associated with dispersion strengthening is the difficulty of producing a dispersion of small and hard particles. Transition elements, due to their limited solubility and low diffusion rates in aluminium, form stable intermetallic particles that hinder dislocation movement and boundary sliding. Strengthening at elevated temperatures can be achieved by having a fine dispersion and fine sub-structure material. The presence of a large volume fraction of dispersoids can also lead to a significant increase in modulus.

Three main categories of aluminium alloys, manufactured via P/M route, attract interest for structural applications. In the first category a large number of R/S aluminium alloys have been evolved along the lines of the traditional heat treatable 2xxx and 7xxx ingot metallurgy series. Such development has been stimulated to a large degree by the aircraft industry's need to develop aircraft that meet higher performance requirements with increased reliability and lower life-cycle costs. The rapid solidification approach is used to obtain a fine grain size and a fine dispersion of second phase particles. Small amounts of transition elements were added in order to obtain the fine dispersoids. Such development led to alloys that combine superior strength, fracture toughness and corrosion resistance properties. For example the 7075 alloy, designed by Alcoa to Boeing specifications, exhibits improved corrosion resistance and high strength. Alcoa's researchers updated the development status of their second generation 7xxx series with goals of improving fracture toughness and fatigue properties proportional to tensile strength improvements. These alloys contain small amounts of insoluble elements, i.e. Zr and Ni to form dispersoids to control recrystallization.

The second category includes the dispersion strengthened P/M aluminium alloys, containing fine dispersions of relatively insoluble intermetallic phases of transition elements. These alloys were initially destined for a wide range of aerospace applications {Drive (1985)}, such as in gas-turbine engines and in missile applications. The aim was to compete with titanium alloys on a specific strength basis over the temperature range of 200°C to 350°C. They exhibit a good high temperature strength, thermal stability and a high modulus of elasticity. Typical examples are the Al-8%Fe-2%Mo or Al-8%Fe-4Ce of Pratt and Whitney and Alcoa respectively, or the Al-Cr-Zr system of Alcan. Considerable development work is necessary, however, before consolidated product will be available in commercial quantities.

Finally, the third category based on Al-Li alloys has been developed in an effort to utilize the high elastic modulus and low density, which are inherent properties of these alloys. Since 1% Li addition increases the modulus by 6% and reduces the alloy density by 3%, the potential uses in stiffness-critical aircraft components are clear, {Froes and Pickens (1984)}. It must also be emphasized that Al-Li is capable of offering comparable weight savings to fibre reinforced materials whilst avoiding a radical departure from well established technology and manufacturing practices.

The use of aluminium based alloys prepared from rapidly solidified materials has been already demonstrated, e.g. in the space shuttle, and their future looks very promising. The diversity of application will ensure that components prepared from R/S powders will capture some part of the potential market.

Future research will be focused not only on the creation of new alloy compositions, but also on the selection of the appropriate processing parameters that will lead to a final product with the desired microstructure and properties, in order to meet the technical requirements.

Experimental

Procedure

Chapter 3. Experimental procedure

3.1. Introduction

The present investigation has been focused on the production of three rapidly solidified aluminium alloys and assessment of their mechanical properties. For that reason a detailed study must be performed on the processing of these alloys, as well as on the relationships among processing parameters, alloy microstructure and finally developed mechanical properties. The study can be classified in three main areas:

(i) characterization of the starting material (powder characterization),
(ii) consolidation of the powders to a fully dense product (fabrication processing) and
(iii) study of the mechanical properties of the final engineering product.

This chapter describes the techniques and the methods used to implement the present investigation. The experimental procedure will be presented briefly and greater emphasis will be placed on the newly developed techniques rather than the conventional ones.

3.2. The Material

The material was supplied by the Aluminum Company of America (Alcoa) in the form of fine powders produced by an up-draught air-atomization technique using an air blast.

The chemical composition is given in Table 3.1. There are two common characteristics of these powders; firstly the Mg concentration is about 6wt% and secondly the next major alloying element is a transition one. The transition elements are Cr, Mn and Fe for the alloys #1, #2 and #3 respectively. The Mg concentration was aimed to be 7%, however, since much higher temperatures than conventional are required to prevent phase separation of the transition elements and magnesium, an amount of Mg is burnt-of, thus depleting the final composition of the powders.

Table 3.1. Chemical Composition

Elements wt% Alloy	Si	Fe	Mn	Mg	Cr	Ni	Zn	Cu	O_2	Al
Al-Mg-Cr	0.24	0.10	0.80	5.97	3.32	0.01	0.01	0.01	0.400	89.27
Al-Mg-Mn	0.09	0.05	7.00	6.13	0.12	0.00	0.01	0.00	0.475	86.13
Al-Mg-Fe	0.12	5.14	1.52	5.87	0.10	0.01	0.01	0.00	0.516	86.73

3.3. Powder Characterisation

3.3.1. Powder Particle Size

The size distribution of the three powder alloys, given by Alcoa and presented in Table 3.2, shows that the powders are very fine with the bulk volume fraction of the powder particles to be smaller than 45μm. However, in order to obtain a more detailed size distribution, triplicate experiments for each alloy have been conducted using a Malvern Laser particle sizer. The working principles of a laser particle sizer are based on the scattering and diffraction of a laser beam which strikes an assembly of particles in suspension. The angle of the diffraction beam is then used to determine the particle size, the smaller the particle the greater the angle. The data are recorded by a Commodore PET computer and analysed as follows. The computer programme generates a size distribution, then calculates the light diffraction pattern and compares it to the signal. An error minimization procedure is then repeated until the best fit is obtained, giving thus an output with the size distribution.

The advantages of this method are: It is independent of the concentration over a wide range, it is not too sensitive to particle shape and it is quick and reproducible. On the other hand the main disadvantage is that the sample under analysis is critical since measurements are carried out on such a small quantity, less than 1g.

Size Distribution of powder particles Table3.2.

	Screen Fractions - μm (%wt)			Average Particle
	-150+75	-75+45	-45	diameter by Fisher Sizer-Microns
1.	0.6	3.0	96.4	12.8
2.	0.2	0.8	99.0	11.7
3.	1.6	4.8	93.6	12.3

3.3.2. Powder Shape

The shape of the powder has been studied using a Jeol T-200 Scanning Electron Microscope (SEM). Specimens were examined at magnifications varying from 50 to 3,500 times and because of its great depth of focus the SEM gives three dimensional details and thus considerable information about the shape of the particles and therefore their surface morphology. A frequently described method of preparing specimens is to distribute a small amount of powder on the top of an aluminium stub and to deposit a 10 Å gold film as an electron conductive material.

3.3.3. Microstructural study

The powder microstructure has been examined by optical and transmission Electron Microscopy.

3.3.3.1. Optical Microscopy

A small amount of each alloy composition was mounted in Metset and subsequently the specimens were ground, polished and etched using Kellers reagent (2ml HF, 3ml HCl, 5ml HNO_3 and 190ml distilled water). A Reichert optical microscope was then used to examine the structures up to 1,000 magnifications.

3.3.3.2. Transmission Electron Microscopy

Although the very finest powder particles (2 µm) may be electron transparent, the bulk of the particles are too thick and therefore require thinning prior to examination. To allow production of thin powder sections, the powders must firstly be embedded in a suitable matrix.

Thin nickel foils impregnated with powder particles were prepared by electrolytic deposition of nickel. The chemical composition of the electrolytic solution and the conditions of electrolysis are given in Table 3.3 (solution A). The sacrificial anode was of pure nickel and the cathode of stainless steel. The latter one was highly polished in order to prevent nickel adhering. A few grams of powder were added to the electrolytic bath; the powder particles were maintained in suspension by a stiring action and while they were falling onto the horizontal cathode they were firmly incorporated within the nickel foil which was being built up during electrolysis. The process was carried out in about 3 hours resulting in a foil of approximate thickness 250 µm that could be easily removed.

Disks of 3 mm diameter were punched from the foil and then mechanically ground to 50 μm thickness. Subsequently the discs were either electropolished (Table 3.3 solution B), especially the Al-Mg-Mn and Al-Mg-Fe alloys, or thinned in a Gatan ion beam thinner, mainly the Al-Mg-Cr alloy.

The study was performed using a 1,000 kV HVEM (High Voltage Electron Microscope) and a Jeol 120CX transmission electron microscope with an accompanying STEM attachment and Links Energy Dispersive X-ray analysis unit.

Chemical solutions used for the preparation samples for TEM.		Table 3.3.
Solution A		
Nickel sulphamate	$Ni(Ni_4SO_3)_2.4H_2O$	600.0 g/l
Nickel chloride	$NiCl_2.6H_20$	4.4 g/l
Boric acid	HBO_3	40.0 g/l
Hydrogen Peroxide	H_2O_2	2-3 droplets
Distilled water		ballance
Temperature: 50°C, potential: 2.5 V and current density: 50 mA/cm2		
Solution B		
ethanol	CH_3CH_2OH	80%
perchloric acid	$HCLO_4$	10%
2-butoxyethanol		10%
Temperature: -30°C, potential: 20V		

3.3.4. X-ray diffraction study

Phase identification was performed by using primarily a Philips X-ray diffractometer with filtered Cu K_a radiation on samples from both as-atomized and heat treated powder. The powder samples for heat treatment were encapsulated in silicon tubes in an argon atmosphere and then heated at 50°C intervals in the temperature range from 100°C to 500°C. The silicon tubes were water quenched to ensure rapid cooling of the powder.

The d-spacings of the phases were calculated from the diffraction patterns using the Bragg Law:

$$n\lambda=2d\sin\theta \quad \ldots\ldots\ldots\ldots\ldots\ldots\ldots\ldots \quad (2.1)$$

The process to accurately calculate the lattice parameter of aluminium (**a**) was very complex. The relationship between the lattice parameter and d-spacings for a face center cubic metal such as aluminium is given by the equation:

$$\frac{1}{d^2} = \frac{h^2 + k^2 + l^2}{a^2} \quad \dots\dots\dots\dots\dots\dots\dots\dots\dots\dots\dots \quad (2.2)$$

It is therefore obvious that a value of **a** can be experimentally determined from the position of the (hkl) 'peaks' of the X-ray diffraction patterns, specified by the diffraction angle (θ), by using the relationship:

$$a = \frac{n\lambda}{2\sin\theta} \sqrt{h^2 + k^2 + l^2} \quad \dots\dots\dots\dots\dots\dots\dots \quad (2.3)$$

The varying lattice parameter values, calculated for each 'peak' were then plotted against the Nelson-Riley function $\{\cos^2\theta/\sin\theta\}$ and an $\mathbf{a}_0$ value obtained by extrapolation, as illustrated in Figure 3.1.

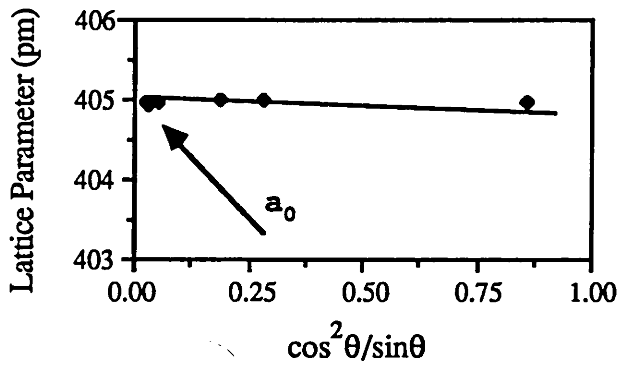

Figure 3.1. Extrapolation of measured lattice parameters against $\cos^2\theta/\sin\theta$

3.4. Consolidation

Consolidation of the loose powder has been achieved by extrusion. The process can be classified into two stages:

- pre-extrusion handling
- hot extrusion

3.4.1. Pre-extrusion handling

The first stage of the consolidation process concerns the preparation of billets which can be subsequently heated and extruded. This production of billets can be separated into two steps.

- cold compaction and
- lubrication

3.4.1.1. Cold Compaction

In the manufacture of parts through the powder metallurgy route, compaction is a very important step and for this a closed die system is most commonly used. In the present investigation, single action piston compaction was employed by using a compaction press (TANGYE) with maximum capacity of 210 tonnes and a 71 mm diameter cylindrical die and ram set made by boronised heat treated steel KEA 145. A solution of zinc stearate in chloroform was used as lubricant to coat the die and ram surfaces in order to prevent pick up of aluminium particles on the tooling. The die was filled with 600 g of loose powder and compaction was carried out to pressures up to 330.4 MPa. However, production of good billets of all the three powder compositions was not achieved even when the pressure was increased up to 508.3 MPa. For that reason, it was decided to line the lubricated die with aluminium foil and produce billets wrapped with Al-foil; this technique was proven effective in the case of a fine Al-15Mg atomized powder studied by Tan (1984), but did not work in the case of these alloys. Generally, despite the large number of experiments performed, it was not feasible to compact the powders using the single action technique, since the majority of the billets were broken into two or more pieces. Attempts to compact the powder in the extrusion chamber, in which pressures up to 1,250 MPa were applied, were also meaningful.

Eventually, compaction was achieved by using a tapered die of 71 mm small diameter and 1° angle, in combination with a double action technique. The pressure pad, used at the bottom of the die, was wrapped with masking tape to enable a tight fit along the die length. The compaction was carried out in two stages:

a) single action compaction up to 101.7 MPa and
b) double action up to 508.3 MPa.

The density of the billets of the three powder compositions Al-Mg-Cr, Al-Mg-Fe and Al-Mg-Mn was 81%, 76% and 78% respectively.

Finally, in order to prepare specimens for study during in-situ heating at the HVEM, cold compacted pads were subsequently hot compacted in the extrusion chamber, after heating in an air-circulating furnace at 300°C and 375°C for half an hour. The produced compacts were approximately 100% dense and coherent.

3.4.1.2. Billet Lubrication

In order to prevent pick up of powder particles on the extrusion tooling, the compact surfaces were coated with an acetone based graphite lubricant, DAG 580. The more volatile hydrocarbons burn off during heating leaving a graphite layer on the billet surfaces acting as lubricant.

3.4.2. Hot Extrusion

The extrusion process was carried out in two steps:

- billet preheat and
- extrusion

3.4.2.1. Billet preheat

The billets were heated prior to extrusion at 50°C temperature intervals within a range from 300°C to 600°C. The heating was performed in a medium frequency Banyard Metalheat induction furnace, which gave rapid heating times between 4 to 8 mins depending upon the alloy composition and the desired temperature.

In order to control the temperature four thermocouples were attached to each billet, as shown in Figure 3.2. Thermocouples a and d (Figure 3.2) were used to measure the temperature and the other two to control the differential.

Heat losses during the transfer from the induction heater to the extrusion chamber were negligible because of the short time delay between the heater being turned off and the pressure pad contacting the top of the billet.

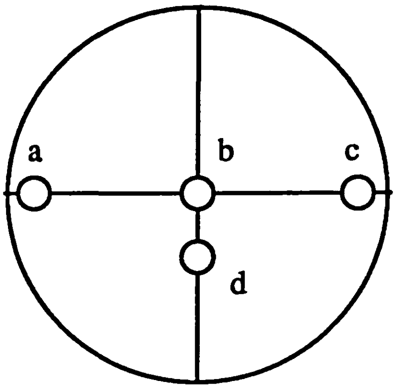

Figure 3.2. Locations of the attached thermocouples

3.4.2.2. Extrusion

Extrusions were carried out in an ENEFCO 5MN hydraulic vertical press acting in the direct mode. A 75 mm diameter liner was fitted in the container which was maintained at 50°C below the billet temperature to allow for temperature rise during extrusion. The extrusion ratios were changed by altering the dies of the extrusion press. Round shaped dies were used of diameter 23.71, 16.77, 13.69, 12.13 and 10.60 mm to achieve reduction ratios 10, 20, 30, 40 and 50:1 respectively. A rectangular die 8x37 mm, giving approximately a reduction ratio of 15:1, was also used in order to produce rectangular-bar extrudates and therefore study the mechanical properties along the transverse direction. The ram speed was maintained constant at approximately 8 mm/s. The extrudes were water quenched upon emerging from the die to retain a structure representative of that due to the hot working.

In addition, a number of partial extrusions have been performed in order to study the properties of the materials and the development of the microstructure from the powder to a fully dense product. The partial extrusions were terminated at three different positions of the pressure displacement curve; 1-before the peak pressure, 2-at the peak and 3-during the steady state, (see Section §2.4.3). The partial extruded billets were removed from the press and water quenched within approximately 2 mins.

The extrusion data, that is ram displacement, the load and the hydraulic pressure of the press, were recorded by both a Datalab DL2800 multichannel transient recorder and an IBM personal computer. Subsequently, a print-out was obtained using a Servoscribe chart recorder and an IBM Graphics printer linked respectively.

3.5. Extrudate Characterisation

3.5.1. Structural analysis

To investigate the microstructure of the extrudates TEM study has been performed on specimens extracted from longitudinal and transverse sections of the extrudates. Furthermore, thin slices were extracted from various positions of the partially extruded billets. The samples were mechanical ground to 250 μm thickness and then 3 mm diameter disks were punched and thinned electrolytically using a jet technique (in a Struers unit), a methanol solution of 5% perchloric acid and 1.5% nitric acid, at -40°C, 20 V and 75 mA. The specimens were then studied on a JEOL CX120 transmission electron microscope.

In order to study the flow patterns and the consolidation mode the partially extruded billets were cross sectioned along the longitudinal axis. Subsequently, one quarter of the billet was ground, polished and etched in a mixed acids reagent of 160 ml HCl, 14 ml HNO_3, 20ml HF and 80ml distilled water to allow macroscopic examination.

3.5.2. X-Ray Analysis

X-ray study has been conducted on the as-extruded and heat treated material using a Philips diffractometer, as already described in Section §3.3.4. The solid specimens were placed on a rotating plate (spinner) to avoid increased intensity reflections due to preferred orientations attributed to the extrusion process.

3.6. Mechanical properties

3.6.1. Hardness

Hardness tests have been carried out on the as-extruded and heat treated material using transverse sections of the extrudates. The specimens were ground flat and a Vickers Hardness machine with a diamond pyramid identor was used with 10 kg load. Tests were performed on the centre of the specimen, mid-radious and on three different circumferential locations and the average value of the five identations was calculated.

3.6.2. Density

The density of the extrudes were measured by using an archimedean fluid displacement method. Machined cylindrical specimens were weighted suspended from an accurate balance twice, firstly in air and secondly immersed in methanol of specified density ($d_{methanol}$ =0.791 g/ml at 20°). The density of the specimen was then calculated by the measured dry weight (B) of the specimen and its weight in methanol (B-A: dry weight minus the buoyancy force), using the relationship below and the resultsare given in Table 3.4.

$$d_{Al\text{-}alloy} = d_{methanol} \cdot B/A$$

Alloy Composition	Density gr/cm^3	Statistical Error
Al-Mg-Cr	2.705	0.005
Al-Mg-Mn	2.770	0.001
Al-Mg-Fe	2.764	0.002

Table 3.4. Density of the consolidated product

3.6.3. Tensile tests

3.6.3.1. At room temperature

Standard Hounsfield No.13 were machined from longitudinal sections of the roundbar extrudates and No. 11 from both longitudinal and transverse sections of the rectangular-bar extrudates, as illustrated in Figure 3.3.

The tests were performed by using an INSTRON machine at room temperature and constant crosshead speed. The calculated strain rates were 5.19×10^{-4} and 7.34×10^{-4} for the no. 13 and 11 respectively.

3.6.3.2. At elevated temperatures

Longitudinal sections from the roundbar extrudates were heated at 150°C, 250°C and 350°C for 99h and then rapidly quenched. From these sections Hounsfield No. 13 specimens were machined and tested in situ, after heating at the corresponding temperatures for 1h; using a split electrical furnace with the controlling thermocouple attached to the specimen collar.

3.6.3.3. Modulus

The modulus of elasticity was determined by testing B.S. 970:1950 specimens machined from 10:1 roundbar extrudates. An extensometer was attached at gauge length 50 mm. The tests were performed using a Denison hydraulic machine.

3.6.3.4. Notched tensile tests

Hounsfield specimens No. 14 and 12 were machined from roundbar and rectangular-bar extrudates. A notch was machined in the middle of the gauge length according to ASTM E 602-81 dimensions.

The tests were also performed at room temperature using an INSTRON machine at strain rates 3.67×10^{-4} and 5.19×10^{-4} respectively.

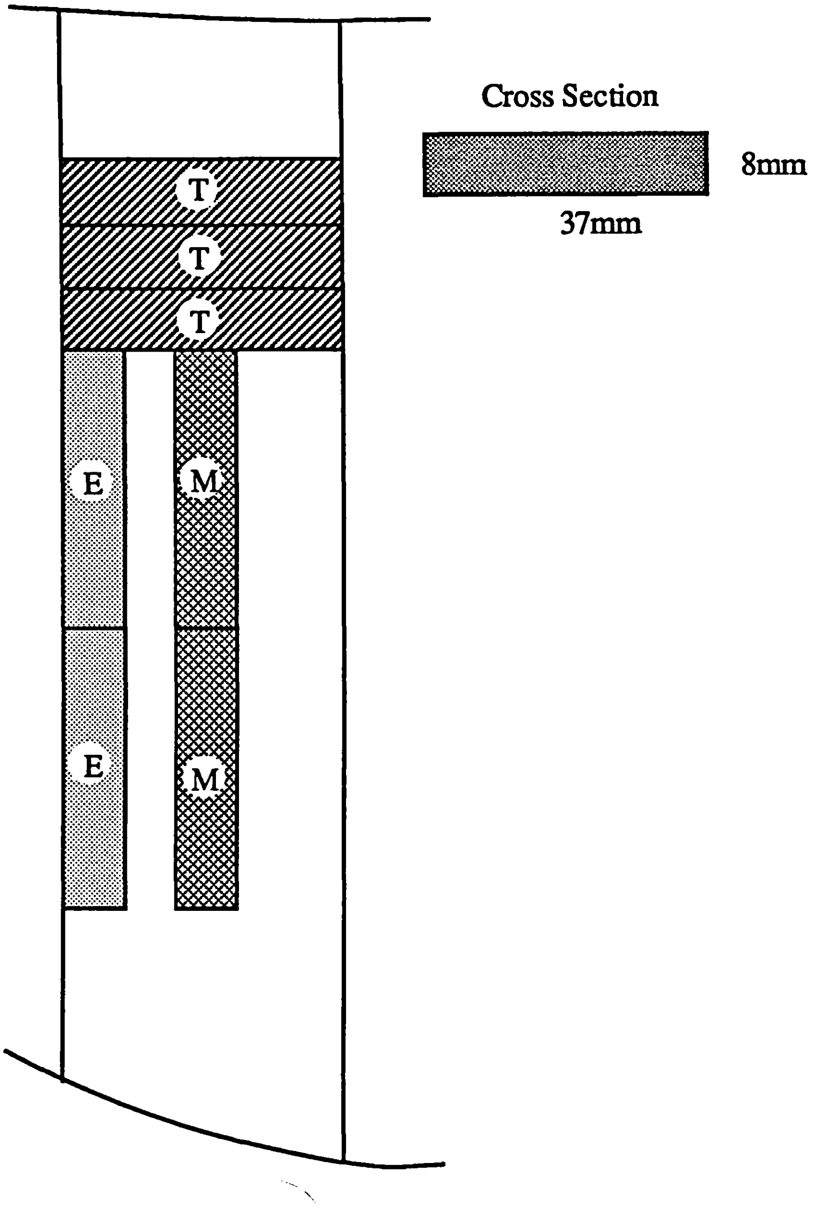

Figure 3.3. Locations from which tensile specimens were prepared in the rectangular-bar extrudates.

Powder

Characterisation

Chapter 4. Powder Characterisation

4.1. Introduction

It has been already reported that the advantages of the 'Rapid Solidification - Powder Metallurgy' route are attributed mainly to the enhanced microstructural refinement of the powder particles. It also is well established that the behaviour of the material during consolidation, i.e. compaction and extrusion, as well as the mechanical properties of the consolidated material depend to a certain degree on the nature of the starting material. Consequently, one of the most important parts of the present investigation is the characterisation of the as-atomized powders.

Powder characterisation involves firstly the study of the general characteristics of the powders, such as their shape morphology and size distribution, and secondly microstructural analysis, phase identification and decomposition behaviour during thermal exposure.

The study of the powder microstructure is an indispensable step in the present investigation, because the mechanical properties of the final fabricated engineering product are determined by the quality of its microstructure. It is therefore important to study the evolution of the microstructure at each stage, from the liquid droplet to the engineering material. An understanding and explanation of the mechanisms involved in firstly the solidification and secondly the consolidation processes are essential in order to control the parameters affecting the final structure and thus improve the mechanical properties. For that reason, in this chapter, a detailed account of the rapidly solidified microstructure of the three alloys will be presented, while the consolidation behaviour will be dealt with in the next chapter.

In order to understand the formation of the powder microstructures during atomization, it is essential to discuss the microstructural features with due consideration to the factors influencing rapid solidification. Indeed, the main parameters that determine the thermal history of the powder particles are liquid droplet size, nucleation undercooling, rate of heat extraction, recalescence and solid/liquid interface velocity.

The most powerful technique for the study of the powder microstructure is transmission electron microscopy. The nickel plating route allows the preparation of thin foils, as described in the experimental procedure, and thus complete cross sections of powder particles can be observed.

Complementary to transmission electron microscopy study is X-ray diffraction analysis. X-ray work has been conducted on the as-atomized and heat treated powder samples in order to identify the phases present in the powder microstructure, calculate the lattice parameter of aluminium and study the behaviour of the metastable powder microstructures during exposure at high temperatures. Generally, the X-ray results illustrate a number of significant points relating to phase stability and phase transformations. Study of heat treated powders was deemed necessary because the consolidation of rapidly solidified powders to a fully dense product requires thermomechanical processing, in which the microstructural evolution is difficult to document for the reason that thermal and pressure assisted transformations occur simultaneously. Hence, it was decided to study the thermal and the mechanical working components separately in order to ascertain the relative importance of each and therefore achieve a more in depth understanding. Understanding the changes occurring during thermal processing, provides a scientific base for the comprehension of structures formed during fabrication of metal powders.

Heat treatment of the powder was conducted in a temperature range that is representative of hot working (i.e. 350-550°C). Since the transformation kinetics will vary at each temperature a standard soak time of 1h was chosen initially, in order to ensure that the exposure time typical of extrusion was exceeded.

4.2. General Characteristics

The three powder alloys studied in the present work were produced under similar atomization conditions. Thus, it might be expected to exhibit similar particle size and size distribution.

The size of the powder particles is a very important parameter; it has already been reported, see Section §2.3.2., that it affects both the microstructure and the consolidation behaviour of the powders. The results of the size distribution analysis performed on the as-atomized powder of the three alloy compositions are illustrated in Table 4.1.

Table 4.1. Particle size distribution of the as-atomized powders

Particle Size (μm)	Alloy Composition (wt%)		
	Al-Mg-Cr	Al-Mg-Mn	Al-Mg-Fe
+ 54.9	7.7	0.8	3.1
-54.9 + 33.7	19.5	11.3	21.4
-33.7 + 23.7	15.7	17.8	20.1
-23.7 + 17.7	20.1	17.2	16.2
-17.7 + 13.6	12.7	13.7	11.3
-13.6 + 10.5	11.9	11.7	9.2
-10.5 + 8.2	6.5	9.3	5.2
- 8.2 + 6.4	3.3	8.3	5.0
- 6.4 + 5.0	2.0	5.9	2.9
- 5.0 + 3.9	0.3	3.0	2.6
- 3.9	0.3	1.0	3.0

The simplest form of presenting size distribution results is by plotting the cumulative weight percentage undersize against the particle size on a semi-log scale, see Figure 4.1. The analysis shows that the particle size varies widely from a few microns to 100 μm, with the major percentage (more than 90%) under 50μm. The mean particle size diameter can be defined as the critical diameter corresponding to 50% accumulative weight percentage undersize on the cumulative frequence curve, see Figure 4.1. It was found to be 22.73 μm, 16.50 μm and 20.98 μm for the Al-Mg-Cr, Al-Mg-Mn and Al-Mg-Fe alloys respectively. Figure 4.1 also shows that the powders are very fine with the Al-Mg-Cr being the coarsest, whilst the Al-Mg-Mn is the finest one.

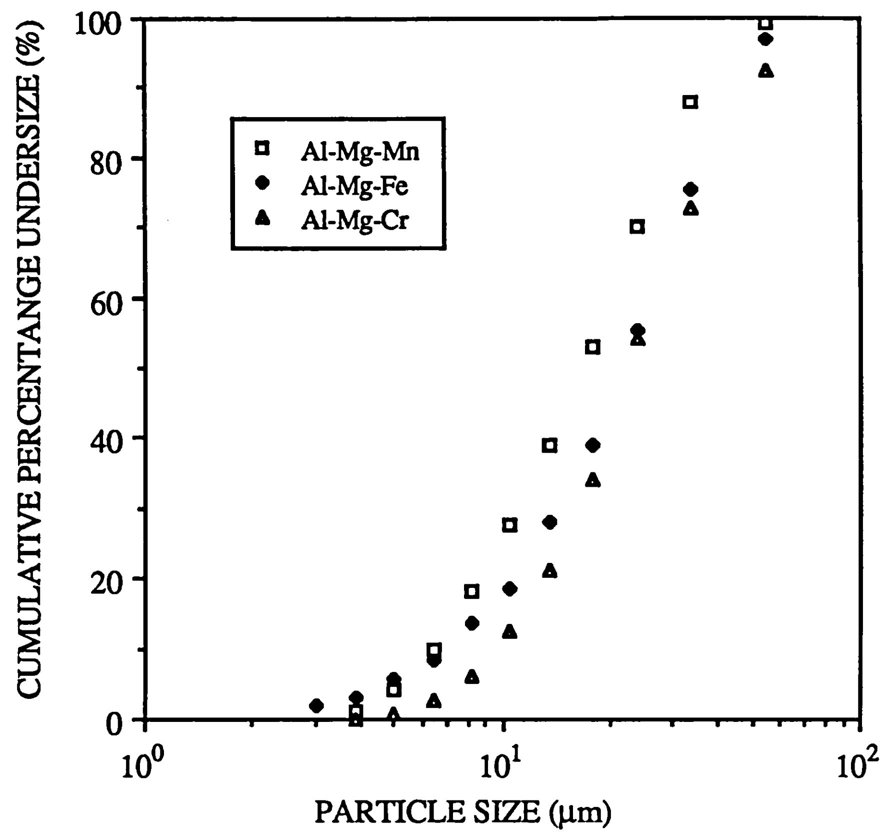

Figure 4.1. Size distribution of the as-atomized powders

The shape of the as-atomized powders has been assessed by using a scanning electron microscope. Figure 4.2 (a)-(c) illustrates typical samples from the three alloy compositions Al-Mg-Cr, Al-Mg-Mn and Al-Mg-Fe respectively. In all cases the powders exhibit smooth surfaces and tend to be spherical, particularly with decreasing size, indicating that the spheroidization rate is greater than the solidification rate of the liquid droplets. The consistent spherical shape of the smaller particles does not imply that they have solidified under lower solidification rates, thus allowing time for spheroidization; on the contrary the finer the droplets the higher the cooling rate experienced.

A number of accicular shaped particles can also be seen, especially in the Al-Mg-Cr alloy, in contrast to the Al-Mg-Mn one in which accicular shaped particles are sparse. The very large particles of all three alloy compositions exhibit mainly an ovoidal shape, suggesting that the magnitude of surface tension forces, acting on the liquid droplet, is not sufficient to spheroidize the larger particles. The effect of surface tension is greater for smaller droplets, because the ratio of 'surface area over droplet volume' increases with decreasing droplet size, thus contributing to spherical shape. Spheroidization is also prevented by the formation of an oxide skin around the liquid droplet, which is typical of the air atomized powders, {Jones (1982); Kim et al (1985)}. The oxide layer reduces the surface tension of the liquid droplets, which produces a greater proportion of irregularly shaped particles. Such particles are more preferable, as will be explained later because their shape affects considerably the compactability of the powder alloy, see Section §5.1.

Finally, the powder microstructure was shown to be very fine. Specimens for optical microscopy study were prepared, but, since the light microscope suffers from the problem of relatively low magnifications and poor resolution, little information could be gained by studying the powder sections. The assessment of the microstructural features of the powder particles has been carried out by using the HVEM and/or the Jeol 120CX conventional transmission electron microscope.

The microstructure of the three alloys and their behaviour during heating varies appreciably with the chemical composition. For this reason an individual study of the microstructural features of each alloy is essential. The micrographs presented in this chapter are representative of a large number of powder particles inspected.

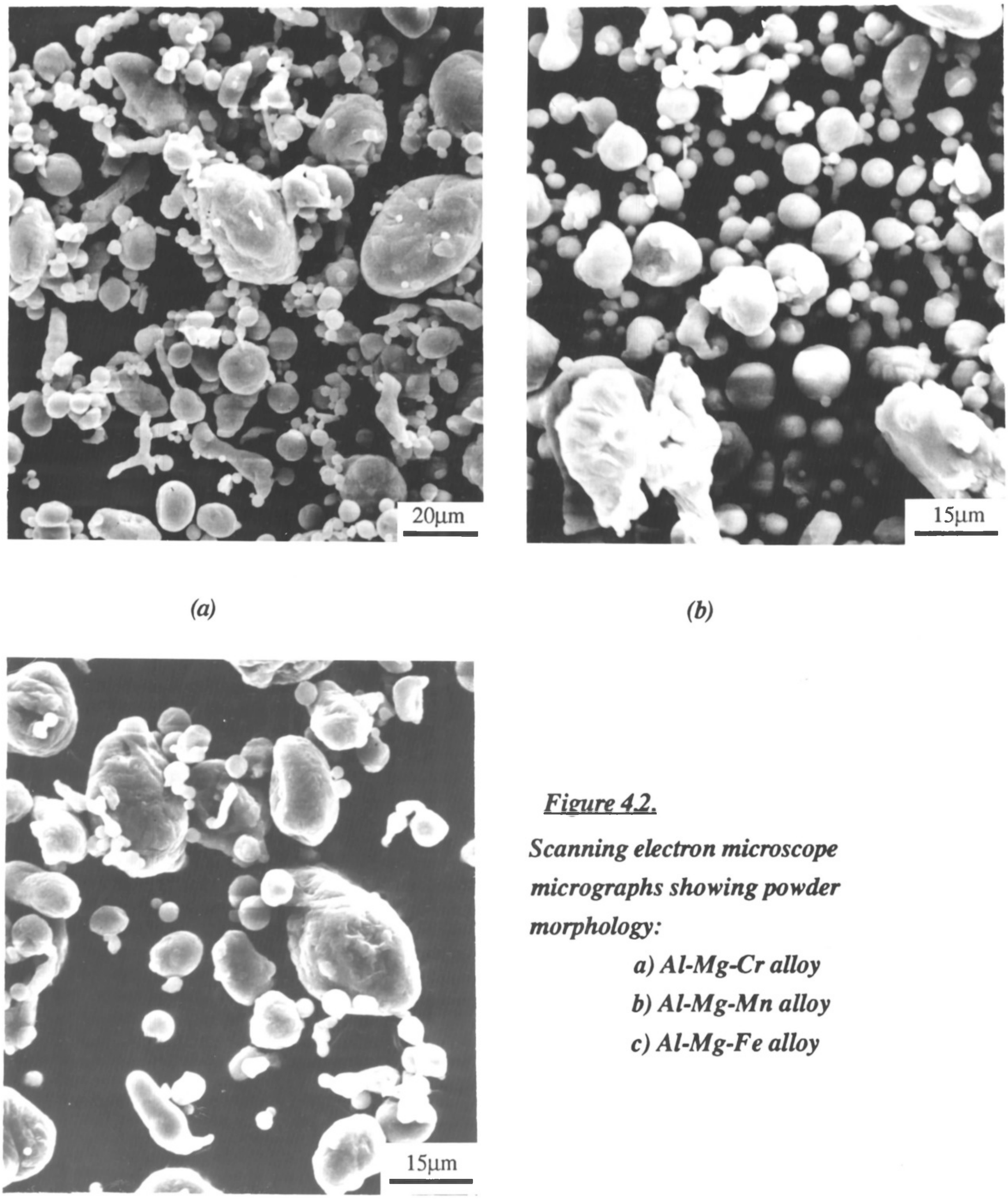

(a)

(b)

(c)

Figure 4.2.

Scanning electron microscope micrographs showing powder morphology:

a) Al-Mg-Cr alloy
b) Al-Mg-Mn alloy
c) Al-Mg-Fe alloy

4.3. Al-Mg-Cr alloy.

The characteristic features of the powder microstructure of this alloy will be described initially, followed by X-ray analysis on the as-atomized and heat treated powders.

4.3.1. Powder Microstructure

A typical example of the microstructure of the Al-Mg-Cr alloy is illustrated in micrographs of Figure 4.3 (a)-(c). Figures 4.3 (a) and (b) display complete cross sections of different sized spherical powder particles, whilst Figure 4.3 (c) typifies an elongated one. The microstructure can be considered uniform, irrespective of the size and shape of the powder particles, composed of dispersoids evenly distributed within the aluminium matrix. The variation of the size of the dispersoids with the powder particle size is very clear in these micrographs, larger dispersoids can be seen in larger powders. Closer inspection reveals that each "dark" particle is not a single phase but an ***aggregate*** of several randomly orientated segregates, as evidenced by a higher magnification micrograph presented in Figure 4.3 (d). The relationship between the size of the aggregate and the size of the powder particles indicates that the aggregates were formed during solidification of the liquid droplets, and their size depends on the solidification rate the liquid droplets experience. The larger powder particles, having solidified more slowly, allow time for the formation of coarser aggregates.

4.3.2. X-Ray Diffraction Analysis

The results of the X-ray investigation, conducted on the as-received and heat treated powder in order to aid the phase identification and understand the aggregate formation, are summarised in Table 4.2. It can be seen that appart from α-Al, three equilibrium phases were detected, the ternary compound $Al_{18}Mg_3Cr_2$ (T) {Samson (1958)}, the Al_3Mg_2 (β) {Samson (1965)} and the Cr_2Al_{13} (θ) {Cooper (1960)} phases. In addition, a number of unidentified reflections were recorded, which could not be assigned to known phases, and therefore were attributed to one or more metastable phases. The unidentified phases may well be the result of metastability brought about by rapid solidification.

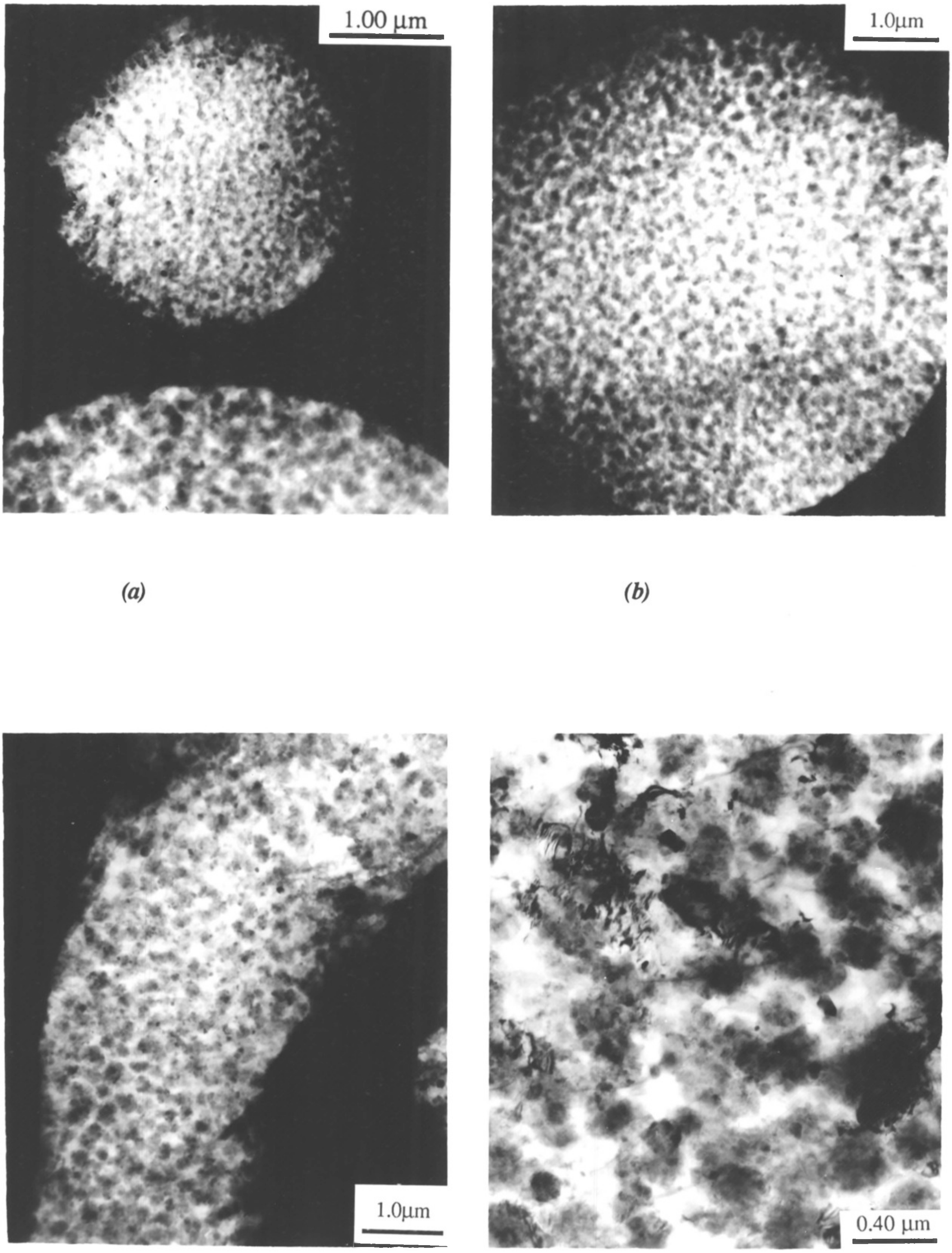

(a) *(b)*

(c) *(d)*

Figure 4.3. Powder microstructure of the Al-Mg-Cr alloy:
(a), (b) different size spherical powder particles
(c) elongated powder particle
(d) Higher magnification of (b)

Table 4.2. Summary of the X-Ray analysis for the Al-Mg-Cr alloy

Powder	Unidentified peaks	$Al_{18}Mg_3Cr_2$ (ASTM 29-18)	Al_3Mg_2 (29-48)	$Al_{13}Cr_2$ (29-14)
as-atomized	strong	strong	weak	weak
100°C 95h	strong	strong	weak	weak
200°C 2h	strong	strong	weak	weak
250°C 1h	strong	strong	weak	weak
300°C 1h	strong	strong	weak	weak
350°C 1h	strong	strong	weak	weak
400°C 1h	strong	strong	weak	weak
450°C 1h	strong	strong	very weak	weak
500°C 1h	strong	strong	very weak	weak
550°C 4h	strong	strong	very weak	weak

Hence, the aggregates, whose size depends explicitly on the size of the powder particles are composed of the unidentified phase(s) and the $Al_{18}Mg_3Cr_2$, Cr_2Al_{13} and Al_3Mg_2 phases, which were formed during solidification of the liquid droplets. At the beginning of solidification Al-Cr-rich primary phases should form in the liquid droplet before other phases, because their liquidus temperature is significantly higher. Subsequently reaction with the remaining liquid occurs (peritectic reaction) and other phases form or transform. The magnesium bearing phases are then probably nucleated at the primary Cr-phases. These conclusions are in line with the reactions reported to occur in the Al-Mg-Cr system, {Mondolpho (1976)}:

$$\text{liq.} + Cr_2Al_{13} \rightarrow Al_{ss} + Al_{18}Mg_3Cr_2 \;\ldots\ldots\ldots\ldots\; 906\ {}^\circ K$$

$$\text{liq.} \rightarrow Al_{ss} + Al_3Mg_2 + Al_{18}Mg_3Cr_2 \;\ldots\ldots\; 710.4\ {}^\circ K$$

The X-ray study results, presented in Table 4.2, indicate the stability of the second phase particles dispersed within the aluminium matrix when powder was heated in the temperature range from 100°C to 550°C. Identical reflections to those arising from the phases observed in the as-atomized powder have also been recorded when the powders were exposed at high temperatures (even after heating for 4h at 550°C), except from the reflections of the Al_3Mg_2 phase. The intensity of the peaks of the Al_3Mg_2 phase decreases gradually at temperatures greater than 400°C, indicating that this phase dissolves at higher temperatures. Moreover, the reflections arising from the ternary compound $Al_{18}Mg_3Cr_2$ are equally strong in both the as-received and heat treated powders suggesting that the greater proportion of this phase has been formed during the solidification process. The conclusion therefore can be drawn that within the time available, solid state reactions do not lead to significant microstructural alterations.

Microstructural stability can also be confirmed by studying the variation of the aluminium matrix lattice parameter ($\mathbf{a}_0$) with temperature. It is well established, that distortion of the aluminium lattice owing to alloying elements in solution results in fluctuations of the lattice parameter with solute concentration. Hence, any precipitation reactions occurring can be detected from the variation of the lattice parameter. In particular, phase transformations occurring during heating may be accompanied by removal of the alloying elements from the solid solution, or thermally assisted diffusion can lead to atoms from the solute rich areas going back into solution. It must be mentioned that a change in solute concentration produces only a small change in lattice parameter, for that reason rather precise parameter measurements have to be made in order to observe variations in solute concentration with any accuracy. In the present work aluminium lattice parameter measurements from the higher order matrix reflections were plotted against the Nelson-Riley function and an $\mathbf{a}_0$ value was obtained by extrapolation (see Section §3.3.4). Despite the procedure giving a very indirect measurement high precision is fairly easily obtainable.

In the as-atomized condition the reflections of α–Al appeared at lower diffraction angles, consequently an increased $\mathbf{a}_0$ was calculated. The increased value of the aluminium lattice parameter of the as-atomized powder, 406.24 pm instead of 404.94 pm for pure α-Al, is attributed to Mg in solid solution because Mg expands the lattice. Actually, the influences of the two alloying elements, Mg and Cr, are contradictory, since Mg expands the lattice while Cr contracts it. In particular, a lattice parameter of 407.9 pm has been reported by Mondolpho (1976) for a binary Al-6.13wt%Mg alloy and a parameter of 402.6 pm for an Al-5.7%Cr alloy. In effect every 1wt% Mg increases the lattice parameter by 0.4489 pm, while every 1wt% Cr decreases it by 0.4105 pm. Clearly, the influence of Mg is more potent.

The different values of $\mathbf{a}_0$ obtained from all the as-received and isochronal heat treatment conditions have been plotted against temperature as illustrated in Figure 4.4. With increasing temperature the aluminium lattice parameter increases slightly, which could be attributed either to the removal of the Cr atoms by precipitation of chromium-rich phases, or to Mg being taken back into solution. The latter explanation is more probable because chromium bearing phases were not observed to precipitate (Table 4.2), while the decreased intensity of the Al_3Mg_2 phase reflections with temperature suggests that dissolution of the Al_3Mg_2 phase allows Mg back into solution.

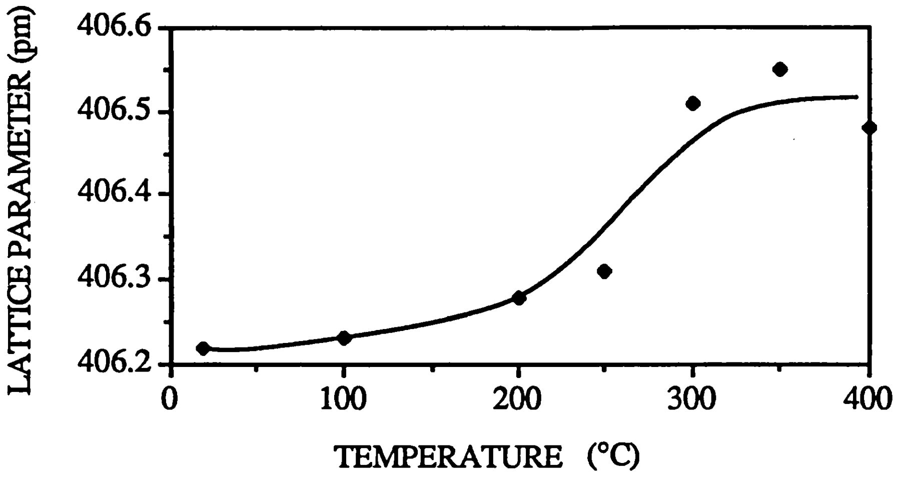

Figure 4.4. Variation of lattice parameter of aluminium with heat treatment temperature (1h duration), for the Al-Mg-Cr alloy.

4.4. Al-Mg-Mn alloy

Amongst the three alloys studied in the present investigation, the manganese bearing one merits more attention because very interesting results have been encountered as far as (i) microstructural formation, (ii) phase identification and (iii) phase transformations during exposure at high temperatures are concerned

4.4.1. Powder Microstructure

The microstructure of this alloy is markedly different from the microstructure of the Al-Mg-Cr one. Typical micrographs of powder particles, varying from small to large, are illustrated in Figure 4.5 (a). The majority of them contain a cellular or dendritic solidification morphology {Figure 4.5 (b), regardless of their size or shape. It can be clearly seen, Figure 4.5 (c), that the cells are precipitation free and the intercellular regions are composed of second phase particles, up to 0.5 μm diameter, formed probably due to solid state decomposition during cooling to room temperature. As the microsegregation distance is small enough in these regions, the boundary area will be rich in solute and therefore ideal sites for nucleation of second phase particles. Efficient extraction of heat from the solidifying droplet could prevent the release of latent heat increasing the temperature and therefore causing solid state decomposition within the droplet. The size of the cells as well as of the second phase particles depends clearly on the size of the powder particles.

A particular characteristic of this alloy is that in the small to medium size powder particles there are areas free of microstructure, as illustrated in Figure 4.6 (a). These segregation free areas can occupy a large volume of the whole particle, see particle A of Figure 4.6 (a), while in other particles the featureless area resembles a rim less than 1μm thick surrounding the bulk of the powder particle, e.g. particle B of Figure 4.6(a). The hypothesis of partitionless solidification in these areas has been confirmed by using high resolution imaging and tilting experiments during transmission electron microscopy study, since these regions were determined to be devoid of substructure or contrast resulting from chemical segregation. The segregation free rim can also be seen in Figure 4.6 (b), from a large powder particle which contains coarse agglomerates up to 1.3 μm diameter. These agglomerates are a quasi-crystalline metastable phase exhibiting icosahedral point symmetry (proof is presented in the following Section §4.4.2).

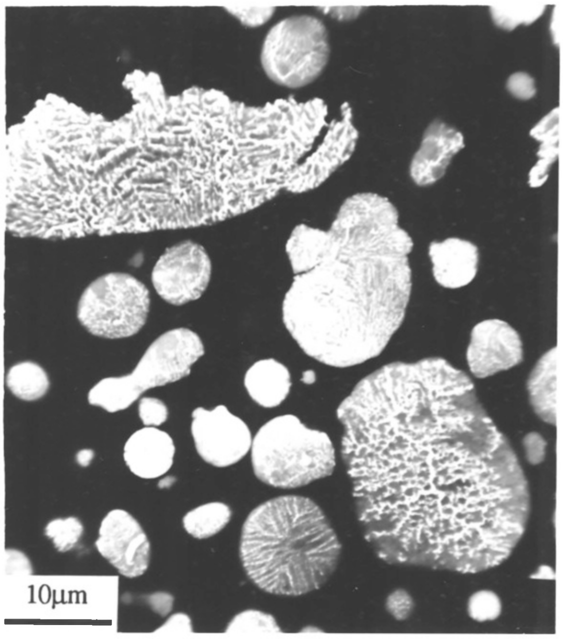

(a)

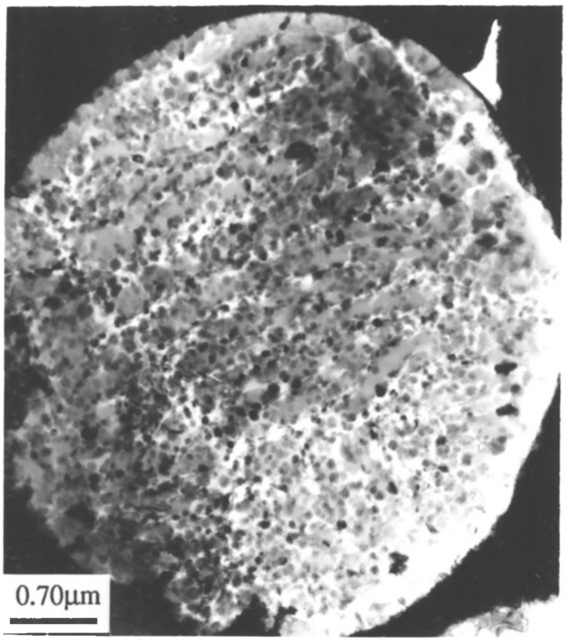

(b)

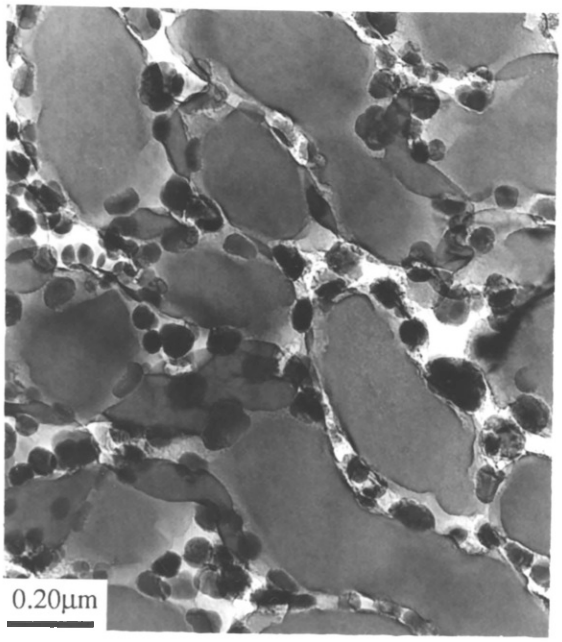

(c)

<u>*Figure 4.5.*</u>

Powder microstructure of the Al-Mg-Mn alloy:
(a) Range of powder sizes
(b) Cellular solidification morphology
(c) Higher magnification of (b)

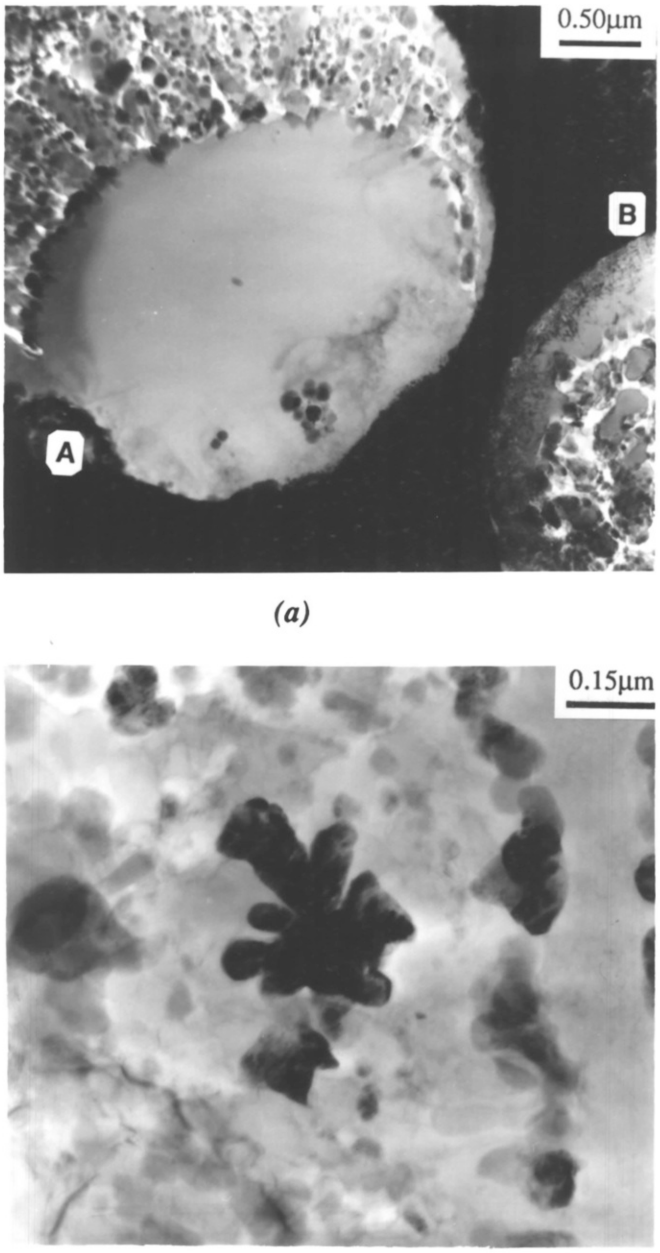

(a)

(b)

Figure 4.6. Powder microstructures of the Al-Mg-Mn alloy
(a) Dual microstructural morphology, partitionless-cellular
(b) Segregation free rim at powder surface

Generally, the larger powder particles contain the coarser "icosahedral phase", while the bulk of the powder particles (15-35μm) exhibit a cellular structure with segregation of solute to the boundaries and in some instances precipitation of Al_3Mg_2, see Section §4.4.2. Finally, the finest powder particles (less than 15 μm) contain a significant proportion of partitionless solidification due to retention in solid solution of the major alloying elements Mg and Mn.

In order to gain an understanding of the formation of the as-atomized powder microstructure, it is instructive to attempt to relate the structure to the solidification behaviour. It has already been reported that the improvements in microstructure and the various structural manifestations afforded by rapid solidification are attributed to large nucleation undercoolings, high solidification interface velocities and high rate of heat extraction during and after solidification. Moreover, the microstructure is largely affected by both the form and the velocity of solidification front. The theory of morphological stability {Mullins and Sekerka (1964)} predicts that if the solid-liquid interface does not remain planar or smoothly curved, the introduction of perturbations leads to a cellular or dendritic front giving rise to microsegregation in the resulting solid. The dual microstructure observed in some powder particles of the present investigation can be attributed to just such a breakdown of the initially smoothly curved solidification front to one of cellular morphology. The area devoid of substructure, clearly seen in Figure 4.6 (a), particle A, is formed at the beginning of solidification. Once nucleation has occurred, apparently near the surface of the liquid droplet, a smooth solidification front proceeds into the droplet with high velocity, as a consequence of the high undercooling achieved prior to nucleation. The resultant solid is the featureless region of the particle. Subsequently, the release of latent heat of the solidified volume causes deceleration of the solidification front, thus allowing time for the introduction of perturbations, decomposition of the smooth front and finally solid segregation resulting in a cellular microstructure. Within the constraints of the powder production equipment utilised for this alloy, the size of the partitionless solidification regions depends on the powder particle size and the nucleation behaviour.

Pertinent to the attainment of homogeneous powder microstructure Hirth (1978) has noted that cooling rates of 10^{12} °K/s are required. However, it is emphasized that this value was claimed to be an upper limit and until data on the actual achievable undercoolings and rates of nucleation become available it would remain an over-estimate. Moreover, it is now accepted that although cooling rates are often specified in descriptions of rapid solidification processes, the unique microstructural and constitutional effects of rapid solidification are a result of high rates of heat extraction or from large undercoolings. High growth rates can be achieved under a wide range of heat flow conditions and therefore cooling rates.

The second example of partitionless solidification observed is the featureless rim clearly seen in Figure 4.6 (b). In this case, it is more difficult to comprehend the solidification mechanism that led to such a microstructure, however, it is highly likely that a behaviour similar to that observed in splat quenched or melt spun materials has also prevailed. Partitionless solidification of a very narrow zone at the chill surface may appear, as a result of high cooling rates being encountered by the liquid droplet in contact with the chill surface (usually copper wheel). In the case of atomization the rapid removal of heat is achieved by the high velocity atomizing gas.

4.4.2. Phase identification

The results of X-ray analysis are displayed in Table 4.3 with representative charts that highlight the characteristics of the diffraction peaks are shown in Figure 4.7. It can be seen that in addition to the α-Al matrix, very weak reflections from the equilibrium Al_3Mg_2 phase [ASTM 29-48, Samson (1965)] were detected as well as a number of unidentified peaks attributed to a metastable phase, see Figure 4.7.

The above mentioned metastable phase has recently been identified by work of Shechtman et al (1984,a), Shechtman and Bletch (1985) and Bancel et al (1985), in Al-Mn binary rapidly solidified alloys. This metastable phase is particularly interesting for crystallographic purposes because it diffracts electron like a single crystal but displays six five-fold, ten three-fold and fifteen two-fold axes characteristic of icosahedral group symmetry, {Shechtman and Bletch (1985)}. For that reason this metastable phase is termed the icosahedral phase. However, such symmetry is inconsistent with crystal translations and therefore the metastable phase could be considered as quasi-crystalline.

In the present work the corresponding d-spacings, listed in Table 4.3, are in excellent agreement with the results published in the literature, {Shechtman and Bletch (1985) and Bancel et al (1985)}. Moreover, the electron diffraction pattern, presented in Figure 4.8 (d), is characteristic of the icosahedral phase, {Shechtman and Bletch (1985)}. Finally, EDX analysis indicated a chemical composition of 70 wt% Al, 26.31 wt% Mn, 2.38 wt%Mg and 0.27 wt%Cr, which is quite close to that of $MnAl_6$ into which the metastable phase transforms, as will be described below. A relatively recent publication on a rapidly solidified alloy Al-5Fe-7Mn by Zaidi et al (1985) gives X-ray diffraction patterns virtually identical to those shown in the present investigation that correspond to the icosahedral phase. Consequently, the unidentified phase reported by Zaidi to have an Al_3Fe_2 composition is indeed the icosahedral phase, in which it is highly likely that some Mn atoms were replaced by Fe ones. Clearly, the formation of these quasi-crystalline phases can be attributed to rapid solidification.

Table 4.3. Experimentally determined d-spacings of the observed phases of the Al-Mg-Mn alloy and summary of the X-ray analysis

	Al_3Mg_2		$Al_{18}Mg_3Mn_2$		Icosahedral		$MnAl_6$	
	(ASTM 29-48)		*(ASTM 29-18)*				*ASTM 6-0665)*	
	reported	observed	reported	observed	reported	observed	reported	observed
1.	2.395	2.4000	8.387	8.426	1.086		2.081	2.0738
2.	2.496	2.4949	2.190	2.1865	1.1	1.1007	2.269	2.2681
3.	2.458	2.4550	2.215	2.2109	1.276	1.2769	1.478	1.4796
4.			2.297	2.2896	1.497		1.892	1.8913
5.			1.2839	1.2819	2.056		1.532	1.5316
6.			4.380	4.3751	2.0624	2.0636	4.925	4.9215
7.			1.3978	1.3985	2.1681	2.1715	2.621	2.6203
8.			1.7119	1.7101	3.33	3.3448	2.535	2.5325
9.					3.83	3.8463	2.187	2.165

Powder	Al_3Mg_2	$Al_{18}Mg_3Mn_2$	Icosahedral	$MnAl_6$
as-received	v.v.weak	ND[1]	strong	ND
100°C-300°C, 1h	weak	ND	strong	ND
350°C, 1h	medium	ND	strong	ND
400°C, 1h	ND	medium	strong	ND
450°C, 1h	ND	medium	ND	medium
500°C, 1h	ND	ND	ND	strong

ND[1] : not detected

With the aid of electron diffraction techniques to compliment the X-ray study, it was possible to determine the different morphologies of the icosahedral phase within individual powder particles, see Figures 4.8 (a), (b) and (c). Figure 4.8 (a) shows one of these morphologies that was observed in abundance in the coarser powder particles, termed as nodular or spherulitic form. A second morphology, of which a three dimensional distinctive star shape can be clearly discerned from the dark field image in Figure 4.8 (b), has been observed in a few powder particles. Such morphology, which actually resembles a flower type arrangement appearing in the form of petals stemming from a central core, could be considered as a growth extension of the first one. A selective growth which has encouraged the arms to expand from the petal regions of

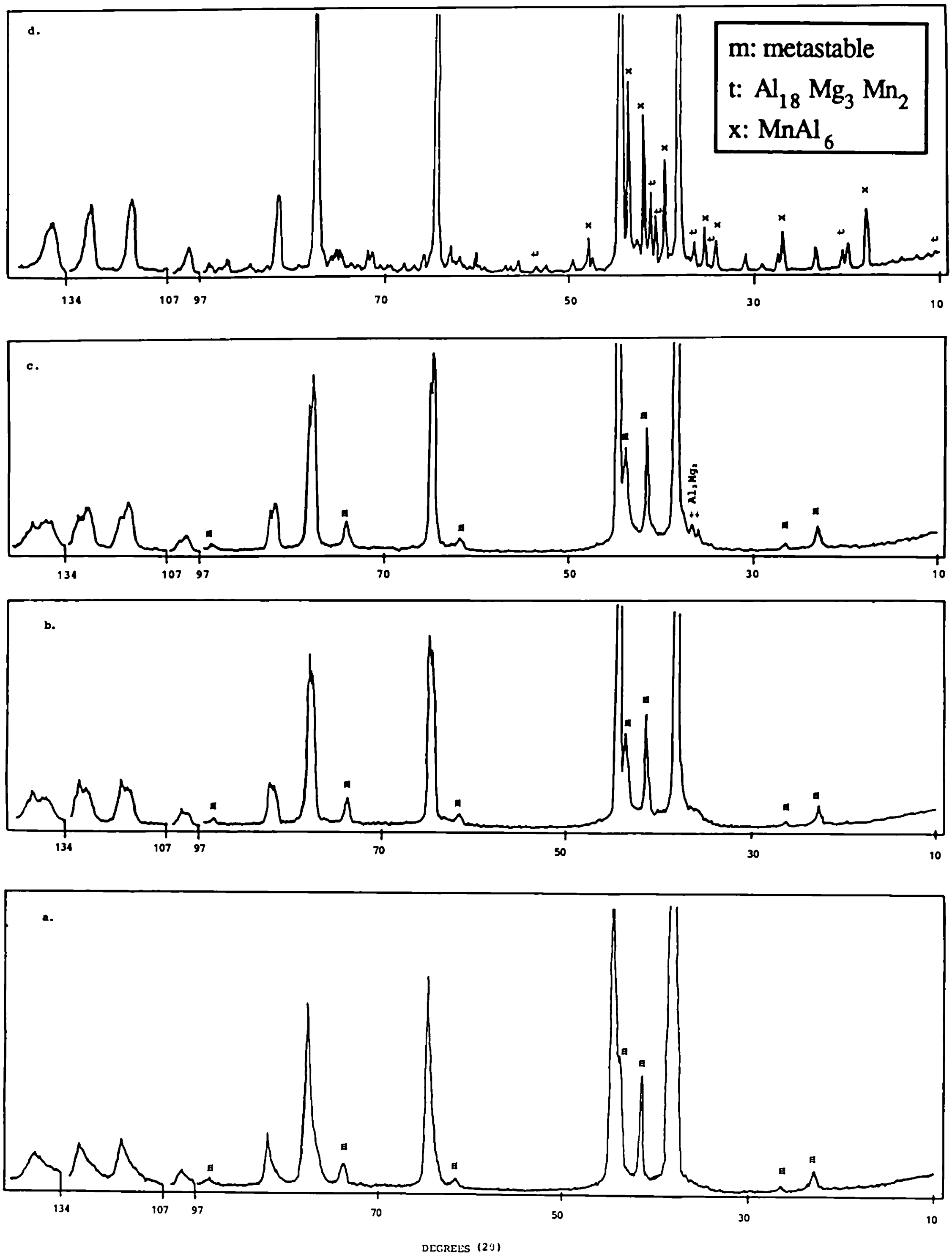

Figure 4.7. Results from X-ray analysis of powder:

(a) as-atomized,

(b) 1h at 300°C,

(c) 1h at 350°C,

(d) 1h at 450°C

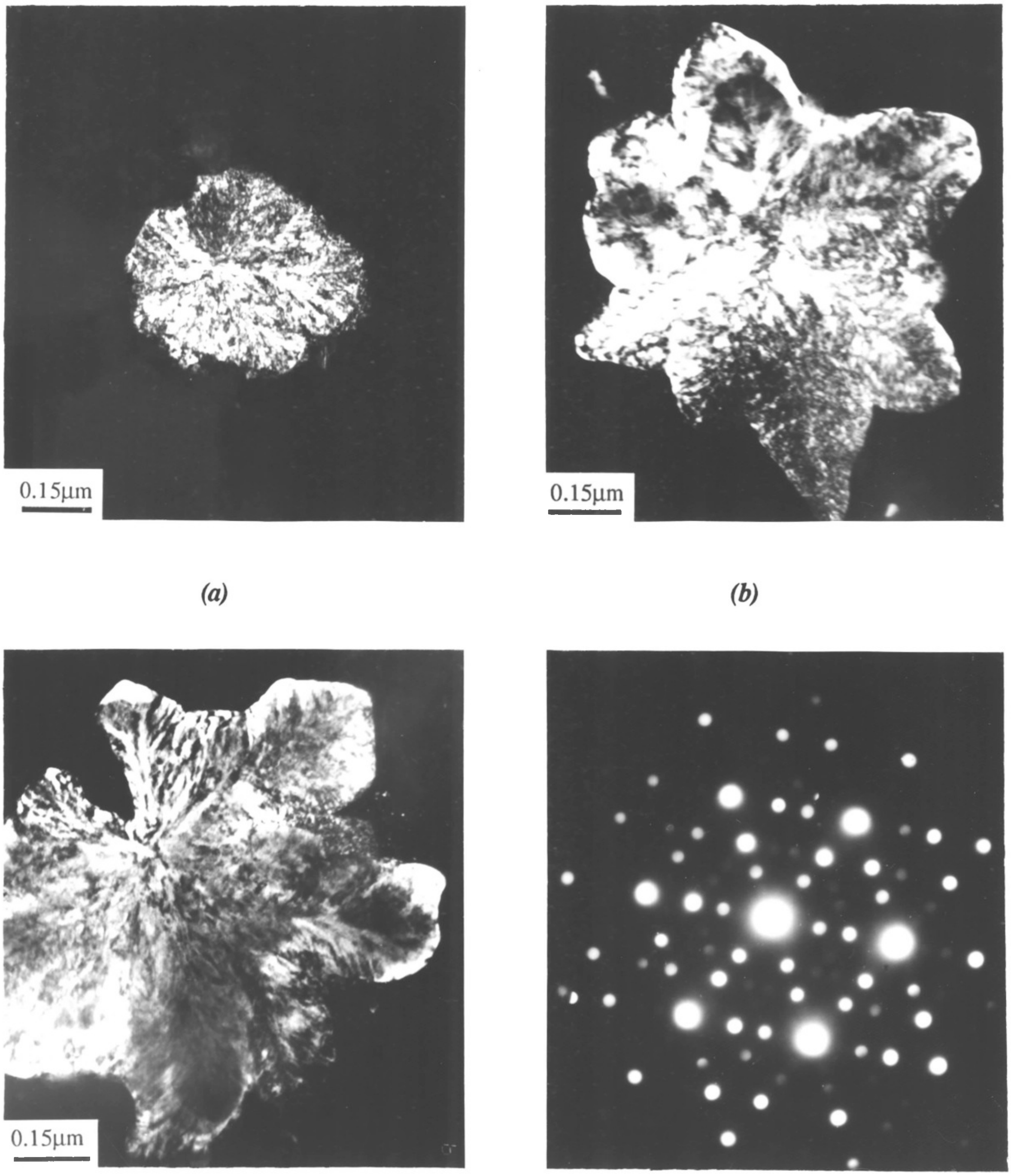

(a) (b)

(c) (d)

Figure 4.8. Metastable Al-Mn phase morphologies:

(a) nodular, dark field image

(b) star shape, dark field image

(c) flower type, dark field image

(d) characteristic SADP

smaller nodules can be better identified in Figure 4.8 (c). Shechtman and Blech (1985) have reported similar morphologies in the study of melt-spun ribbons of binary Al-Mn alloys containing at least 18 wt%Mn thus producing a high volume fraction of the quasi-crystalline phase. In an Al-18%Mn alloy small spherulites, up to 0.3 µm, with petal like edges were observed whereas in a 22-26%Mn alloy a morphology of elongated dendrites stemming from a central core was noted. The conclusion therefore can be drawn that the icosahedral phase's morphology is that of a type of star, which originates from the extension of the petal like edges of the small spherulites.

4.4.3. Heat treatment

By assessing the results of the X-ray analysis, quite important information can be gained, as far as phase transformations are concerned. To aid the understanding of the solid state reactions occurring during heat treatment, a schematic diagram has been drawn, see Figure 4.9.

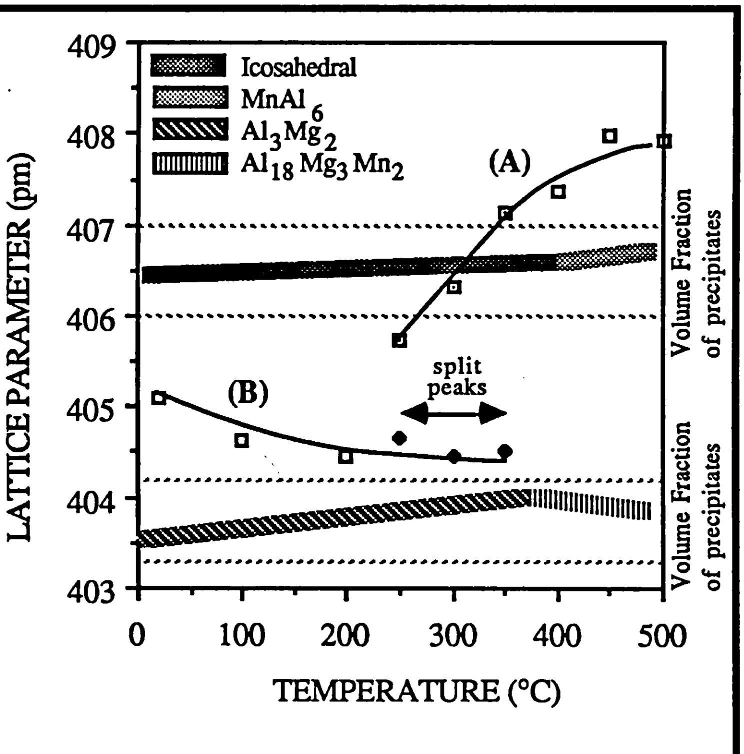

Figure 4.9. Variation of Lattice Parameter with powder heat treatment temperature, for the Al-Mg-Mn alloy.

It can be seen that although the icosahedral phase is a metastable one it was present after heat treatment at 400°C for 1 h, the maximum time investigated. At higher temperatures it was not detected while the reflections of the orthorombic $MnAl_6$ [ASTM 6-0665, Nicol (1953)] phase appeared. It looks highly probable that the icosahedral phase has directly transformed into $MnAl_6$, a transformation also reported by Schechtman and Blech (1985) and Zaidi et al (1985). At even higher temperatures, the reflections of the $MnAl_6$ are stronger, see Table 4.3, and sharper, indicating either an increased volume fraction or coarser $MnAl_6$ precipitates.

Meanwhile, the reflections of the Al_3Mg_2, which were just discernible in the as-atomized powder, become stronger after heat treatment at 300°C and 350°C. Nevertheless, at 400°C the Al_3Mg_2 was not detected, while the reflections of the fcc $Al_{18}Mg_3Mn_2$ [ASTM 29-18, Samson (1958)] phase appear. It is highly likely that the Al_3Mg_2 transforms to the $Al_{18}Mg_3Mn_2$ phase rather than nucleation of $Al_{18}Mg_3Mn_2$ occurring at separate sites. Although microstructural evidence is lacking, this transformation has also been reported by Marshall and Sheppard (1986) for another R/S alloy (Al-12Mg-0.8Mn) during thermomechanical processing. At higher temperatures, the solubility of Mg in aluminium increases and there is no driving force for precipitation and indeed, the $Al_{18}Mg_3Mn_2$ phase dissolves between 450°C and 500°C, (it was not detected by X-ray analysis at 500°C).

An interesting part of the present investigation is the study of the characteristics of the high diffraction angle reflections of aluminium, as well as the variation of the aluminium matrix lattice parameter with temperature. At low temperatures (<200°C) the aluminium peaks are very broad and cannot be resolve into their $k\alpha_1$ and $k\alpha_2$ doublets at high diffraction angles, see Figure 4.7. The possible sources of broadening are related to crystal imperfections, crystal size and mainly to reflections arising from a range of matrix lattice parameters. It has already been shown that the microstructure is not homogeneous and therefore the aluminium matrix contains different amounts of solute in different regions within individual or various particles. It has been reported in the present investigation and in the literature {Mondolpho (1976)} that alloying elements distort the lattice of aluminium, especially Mg which expands the lattice while Mn contracts it. With increasing Mn content the lattice parameter of aluminium decreases approximately linearly to reach a value of 399.6 pm at 15wt%Mn {Mondolpho (1976)}. Hence, in the larger powder particles which contain the Mn-rich icosahedral phase the matrix is depleted of Mn and has an increased lattice parameter, while in the particles which exhibit a cellular structure with precipitates of Al_3Mg_2 within the intercellular regions the matrix is Mn-rich and therefore the lattice parameter is smaller.

Furthermore, in the finest powder particles which contain a significant proportion of partitionless solidification and both Mg and Mn are in solid solution, the lattice parameter reflects the influence of both alloying elements having a higher value than that of pure aluminium.

With increasing temperature the broadening effect becomes more definite. At 250°C the high angle reflections of aluminium split in two, while it appears that within the temperature range 250°C to 350°C there are two distinct lattice parameters of the matrix, see Figures 4.7 and 4.9. A cursory interpretation would attribute this to the separation of the $k\alpha$ doublet into its components, $k\alpha_1$ and $k\alpha_2$, however, at 350°C the peaks related to $k\alpha_2$ have higher intensities. The latter observation nullifies the previously mentioned assumption. It suggests that the two separate sets of aluminium reflections correspond to aluminium containing two different concentrations of alloying elements. Similar observations have been also reported by Shechtman et al (1984,b) in an Al-15%Mn as-spun ribbon. The splitting of the X-ray peaks into two distinct parts within the temperature range of 250°C to 350°C confirms also the explanation given for the peak broadening. At high temperatures (greater than 400°C) no peak splitting has been noted and only one distinctive lattice parameter has been measured, Figure 4.9.

The variation of aluminium lattice parameter can again be interpreted in terms of the precipitation behaviour of the alloying elements. The fine powder particles contain Al_3Mg_2 at cell boundaries which then easily grows during the 1 hour heat treatment. Hence, at temperatures up to 350°C the apparent decrease of the lattice parameter, Figure 4.9, is attributed to the removal of Mg from the solid solution by precipitation and/or coarsening of Al_3Mg_2. This is also confirmed by the increased intensity of the reflections arising from Al_3Mg_2, see Figure 4.7. Precipitation or coarsening of Al_3Mg_2 is driven initially by supersaturation when kinetic restrictions allow until an intermediate temperature between 350°C and 400°C, at which it transforms into $Al_{18}Mg_3Mn_2$, see Figure 4.9 and Table 4.3. It must be noted that the transformation of the Al_3Mg_2 phase into $Al_{18}Mg_3Mn_2$ allows Mg back into solid solution, thus increasing the lattice parameter. On the other hand, in the coarser powder particles which contain the icosahedral phase (Mn-rich), precipitation of Al_3Mg_2 was not encountered in the time available, because during thermomechanical processing the coarse particles contain nodules of the icosahedral phase with little evidence of Al_3Mg_2 precipitation (proof will be presented below). Hence, at temperatures up to 350°C both Mg-lean and Mg-rich matrix are present. Curve A of Figure 4.9 represents the Mg-rich matrix of the coarser powders while curve B the Mg-lean matrix of the finer ones.

At temperatures greater than 400°C the icosahedral phase has transformed into the equilibrium $MnAl_6$ one, which coarsens progressively, creating thus a Mn-depleted matrix. Moreover, Al_3Mg_2 has transformed into $Al_{18}Mg_3Mn_2$ which in turn dissolves resulting in a Mg-rich matrix. Hence, Mg-rich matrix becomes prominent and only one lattice parameter has been recorded, which increases considerably with increasing time and/or temperature.

4.5. Al-Mg-Fe alloy

The third alloy studied in the present work is Al-Mg-Fe. Initially, a detailed account of formation of the powder microstructure and the phases present in the rapidly solidified alloy will be described. Emphasis will be also placed on the decomposition behaviour of the "metastable" powder microstructures when heated at elevated temperatures.

4.5.1. Powder Microstructure

The microstructure of this alloy will also be shown to be very heterogeneous. Striking microstructural differences have been noted among different powder particles and even within the same particle. The latter is a feature commonly reported by other researchers studying rapidly solidified powder aluminium alloys, {Levi and Mehrabian (1982,a); Jones (1969/70); Jacobs et al (1974); Boettinger et al (1986)}. In this section, the characteristic features of the widely varying powder microstructures, that can be directly related to the powder size, will be revealed and an explanation in terms of the solidification mechanisms will be provided.

A typical microstructure of this alloy is illustrated in Figure 4.10 (a)-(c). Figure 4.10 (a) displays a complete cross section of a powder particle, in which regions of differing microstructure can be detected as well as multiple solidification nucleation points. Figure 4.10 (b) highlights a structural discontinuity with two distinctly discernible microstructural regions, region A, where the structure has an extremely fine form, designated *microcellular*, and region B, in which the microstructure exhibits a *coarser cellular morphology*. The microcellular structure comprises of a uniform cellular network of α-Al solid solution with fine intermetallic crystallites at the cell interfaces. Although the transition from a fine microcellular structure to a coarser cellular one could be characterised as relatively abrupt, there is a small transition zone over which the cell size increases.

Another of the microstructural characteristics of the larger powder particles is illustrated in Figure 4.10 (c). Coarse primary intermetallic 'spheroids', up to 0.2 μm, can be seen. These appear to have been formed at the beginning of solidification and have then served as nucleation sites for a fine cellular aluminium matrix extending along radial directions from them.

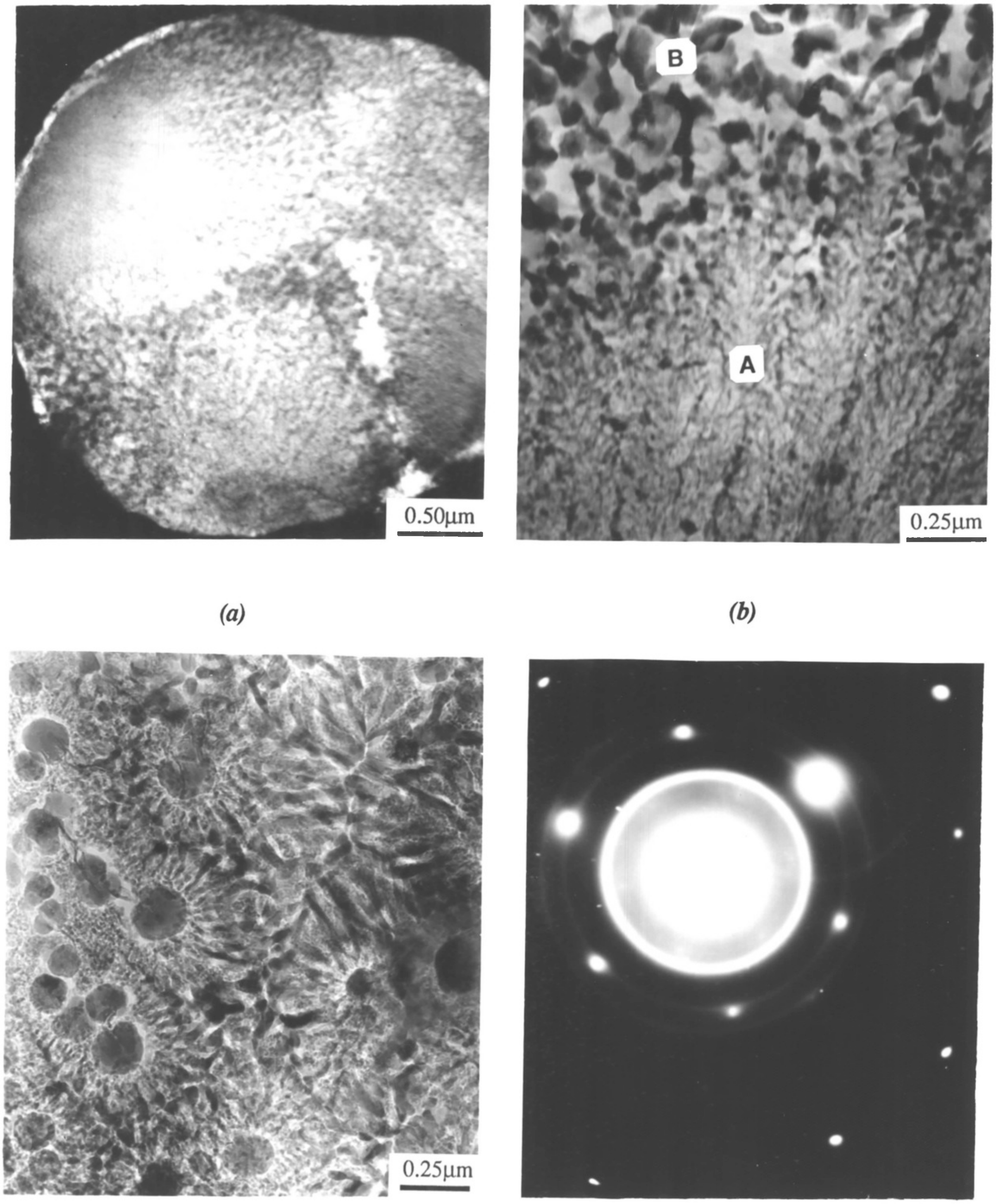

(a) *(b)*

(c) *(d)*

Figure 4.10. Powder microstructures of the Al-Mg-Fe alloy:
(a) Typical cross-section of medium size powder particles,
(b) Dual microstructure morphology, microcellular-coarse cellular,
(c) Coarse primary intermetallic globulars acting as nucleation sites,
(d) Characteristic electron diffraction pattern from the microcellular type of structure

The formation of the as-atomized powder microstructures can be interpreted by considering the theories, {Levi and Mehrabian (1982,b); Jones (1984); Flemings (1974)} that predict the rapid solidification behaviour of the liquid droplets. According to the solidification model proposed by Levi and Mehrabian (1982,b) there are two solidification regimes; adiabatic and isothermal. It useful to recall briefly that in the adiabatic regime a solid liquid interface advances within an undercooled liquid droplet with the release of latent heat and the external heat extraction is a minor consideration. The amount of solid formed in this regime depends on the size of the droplet and the degree of undercooling. In the isothermal regime, "rapid solidification" is terminated and the remaining liquid solidifies at a rate determined by heat transfer to the surroundings.

It is now possible to relate the powder microstructures observed to the solidification regimes and ultimately to powder particle size. Obviously, a decrease in liquid droplet size encourages a large nucleation undercooling and the likelihood of adiabatic solidification. The small to medium size powder particles nucleated herogeneously at the droplet surface, as evidenced by the growth direction of the solid [Figure 4.10 (a)], and the solidification front proceeded into the bulk of the liquid. Once nucleation occurred, the large undercooling created the driving force for a very high velocity solid/liquid interface front whose velocity depended also on the heat transfer coefficient at the droplet environment interface and the growth kinetics of the interface. The resultant microstructure was the microcellular one at a plane front. Thus, the system followed a metastable solidus line as it moves into the two phase region of the phase diagram. Whilst solidification continued the droplet recalesced due to the release of heat of fusion, and at a rate depending on the volume solidified. Recalescence reduced the solidification front velocity until below a critical value a cellular front was formed.

The microcellular structure is typical of the finest powder particles, while the medium sized powders exhibit a variety of microstructures. Quite frequently particles with microcellular and cellular dual solidification morphologies appear. These conclusions have been drawn without the powder being separated in size fractions, followed by individual study; however, the possibility of these being deceptive due to any random sectioning effect can be discounted because of the large number of powder particle observations. In larger powder particles, the nucleation undercooling was probably reduced and solidification events could be predicted by the isothermal regime. Indeed, slower heat extraction rates allowed the formation of coarse intermetallic particles [Figure 4.10 (c)], randomly throughout the droplet which then served as nucleation sites for the remaining liquid to solidify. Similar coarse morphologies have been reported by Sheppard and Zaidi (1986) in an Al-Fe-Mn alloy and this suggests that the addition of iron produces the coarse intermetallics. Certainly it is unlikely that magnesium will create these particles since rapidly solidified powder with higher Mg levels, studied by Tan (1984), contain only cellular morphologies.

The microcellular type of structure has been observed in other Al-Fe alloys subjected to high solidification rates, in which different terminologies have been used to describe the fine microstructure. Jones (1969/1970) has termed it as Zone A, Boettinger et al (1986) as microcellular, and Adam (1982) as microeutectic. Apparently, the iron addition plays a dominant role during the solidification of the Al-Mg-Fe alloy of the present work, and unfortunately promotes an extremely heterogeneous microstructure.

4.5.2. Phase Identification

The X-Ray diffraction study results on powder before and after heat treatment have been analysed and are summarised in Table 4.4. The results indicated that three intermetallic phases are present in the as-atomized powder together with the aluminium matrix; monoclinic equilibrium Fe_4Al_{13} [ASTM 29-42, Black (1955)], which is also described as $FeAl_3$ {Black (1955)}, orthorombic metastable $(Fe,Mn)Al_6$ {Walford (1965)} and an unidentified phase, designated "F". The experimentally determined d-spacings for the unidentified phase and all other phases observed in this alloy are listed in Table 4.4 To aid the identification of the "F" phase a number of equilibrium and metastable phases reported in the literature, involving metastable formation in the Al-Fe alloys, have been considered, such as Fe_2Al_9 {Simensen (1977); $FeAl_x$ {Young and Clyne (1981)}; FeAl {Jones (1969/700; Jacobs et al (1974)}, "S" {Shechtman and Horowitz (1984)}; Al_8Mg_5 {Mondolpho (1976)} and Al_3Mg_2 (ASTM 29-48). Unfortunately, there was not enough information to identify the "F" phase. The majority of these phases have been detected in alloys cooled under lower cooling rates, except for those detected in splats, where the cooling rate and solidification conditions were considerably different to powder atomization.

Figure 4.10 (d) shows an electron diffraction pattern obtained from the microcellular type of structure. The ring pattern superimposed on a spot α-Al pattern is consistent with an intercellular network consisting of fine randomly orientated second phase crystallites. The reflections of these crystallites correspond to the unidentified phase "F" in the X-ray charts listed in Table 4.4. Jacobs et al (1974) have observed, in an Al-8%Fe splat-quenched alloy, similar fine structures comprising of an intercellular network of fine iron-rich crystallites. However, Adam (1982) studying an Al-8Fe-2Mo alloy claimed that the intercellular network was amorphous of approximate composition Al(Fe,Mo). Finally, it is worth mentioning that the "F" phase in the Al-Mg-Fe alloy must be an Fe-rich one because a study by Tan (1984) on Al-Mg binaries indicated no new Al-Mg phases.

Electron diffraction patterns from the intermetallics observed in the coarser structure [Figure 4.10 (c)] could not be obtained because of the foil thickness. However, it is highly likely that these are either Fe_4Al_{13} or $(Fe,Mn)Al_6$, because the larger powder particles have experienced lower solidification rates allowing time for the formation of a coarser structure, unlike the microcellular regions which were formed at higher solidification rates. Identical spheroids have been also reported in both coarse and fine structures of Al-8%Fe splats by Jacobs et al (1974).

The reflections arising from α-Al were broader and shifted towards lower diffraction angles compared with other rapidly solidified Al-Fe alloys indicating an increase in the lattice parameter of aluminium. It is well known {Mondolpho (1976)} that the lattice parameter of aluminium is practically unchanged by Fe content up to the equilibrium solute solubility (0.05%Fe) limit, but shrinks to 401.2 pm when 8.4 %Fe is retained in solution by rapid quenching from the melt. The conclusion therefore can be drawn that the increase of the lattice parameter to 407.1 pm, is solely due to Mg which expands the lattice of Al, as has already been explained for the other two alloys of the present investigation.

4.5.3. Heat treated powder

The results of the X-ray analysis on heat treated powder are also summarised in Table 4.4. It can be seen that up to 350°C the phases present in the as-atomized powder remain practically unchanged and the "F" phase untransformed. Increasing the temperature of batch heating revealed that the metastable phase transformed and only Fe_4Al_{13} and $FeAl_6$ were present in heat treated powder at temperatures greater than 400°C.

Table 4.4. Experimetally determined d-spacings of the observed phases of the Al-Mg-Fe alloy and summary of X-Ray analysis

Metastable "F"			$Fe_{13} Al_4$		$(Fe,Mn)Al_6$	
			(ASTM 29-42)		(ASTM 6-0665)	
Refl. No.	Elect DP	X-Ray DP	reported	observed	reported	observed
1		3.645	2.095	2.097	2.081	2.086
2a		2.475	2.049 ♦		2.269	2.2681
2b						2.249
3		2.455	2.041 ♦		2.153	2.141
4		2.227	2.101	2.104	2.027 ♦	
5	2.120	2.122	2.031 ♦		1.892	1.890
6	1.510	1.513	2.021 ♦		1.478	1.470
7	1.291	1.291	3.545	3.527	4.925	4.901
8	1.071		2.015 ♦		2.621	2.614
9			3.962	3.970	2.535	2.522
10			4.040	4.040	2.217	2.206
11			3.674	3.674	2.187	2.176
12			3.268	3.272		
13			2.062 ♦			
14			4.064	4.058		

Reflections recorded

Powder	Metastable "F"	$Fe_{13} Al_4$	$(Fe,Mn)Al_6$
as-atomized - 350°C 1h	1,2a,3,4,5,6,7	1,4	1,2a,3
450°C 1h	no	1,4,7,9,10,11,12,14	1,2b,3,5,7,8,9,10,11
550°C 1 h	no	1,4,7,9,10,11,12,14	1,2b,3,5,7,8,9,10,11

♦: Reflections superimposed on an aluminum pattern

It will be shown in Section §6.4 that the microstructure of the extrudates exhibited a completely different morphology from that of the original powder. Because of this, a microstructural study on heat treated powder was essential, in order to comprehend and delineate the influence of heating on the powder microstructure. Figure 4.11 (a)-(c) shows representative microstructures from three annealing temperatures covering the working range. At 350°C there were no apparent changes in microstructure from that observed in the as-atomized conditions, indicating the stability of the alloy at this temperature. This is in agreement with the X-ray results confirming that the phases remained unchanged and the the metastable phase "F" untransformed. Heating at higher temperatures resulted in considerable changes in microstructure, typically creating a uniform distribution of needles and plates [Figure 4.11 (b)-(c)] of Fe_4Al_{13} and $FeAl_6$. The examples given are representative of the powder particles studied and accordingly suggest that structural inhomogeneities in the powder can be alleviated by heating, although it should be noted that this may not lead to the most desirable structure.

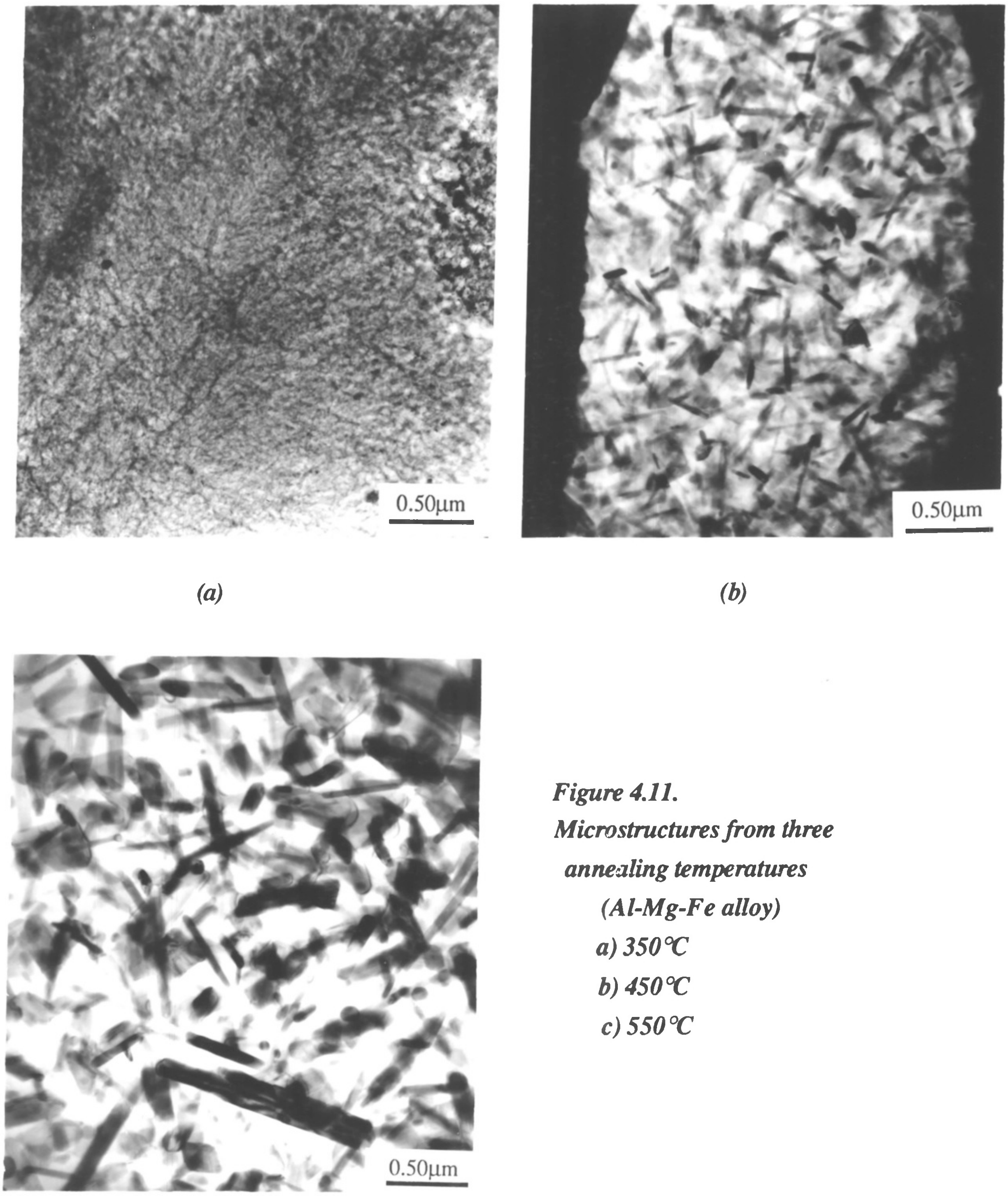

(a)

(b)

(c)

Figure 4.11.
Microstructures from three
annealing temperatures
(Al-Mg-Fe alloy)
a) 350℃
b) 450℃
c) 550℃

In order to investigate the transformations occurring during heating of the powder , in-situ experiments were also performed on the HVEM. This enabled the transformation kinetics of the different microstructural features to be examined more readily. For these experiments the powder was firstly compacted to approximately 100% dense at a temperature at which the microstructure was stable. The short heat treatment and deformation prior to examination had little or no effect on the powder microstructure and hence did not affect the experimental results see Figure 4.12 (a).

In the example presented, a complete powder cross-section can be seen [Figure 4.12 (a)] which exhibits the dual morphology discussed previously. Region M contains the very fine microcellular solidification structure while the coarser, post-recalescence morphology is present in region C. This specimen was heated slowly to 400°C (15 mins) and then held for 90 mins while the structural changes were recorded. Minor changes in structure occurred during the heat-up [Figure 4.12 (b)], when small discrete precipitates appeared in region M, while the coarser region remained relatively unaffected. After 8 mins at 400°C needles and spheroids formed in both the fine and the coarse areas. The number of needle shaped precipitates was higher in the microcellular structure whereas in the coarser region needles could hardly be detected. Such precipitation behaviour would be expected as the fine crystallites of the intercellular network constitute nucleation sites for precipitation. After 20 min the number of precipitates increased in each zone [Figure 4.12 (c)] and needle type precipitates could be observed in the coarse regions. After 45 min the transformations had progressed further, so that coarse needle and spherical shaped precipitates were discernible throughout the specimen. The two differing zones still existed but were not as prominent. After 90 min at 400°C the precipitates were observed to coarsen and the structure became almost homogeneous [Figure 4.12 (d)], with the differing zones barely distinguishable. It must be also mentioned that the oxide film surrounding the particles remained unaffected during heating whilst during extrusion processing it is clear that the oxide film will be sheared. This may be important and is discussed below.

Figure 4.13 shows the variation of lattice parameter of aluminium with temperature. In the as-atomized powder the reflections of α-Al appear at lower diffraction angles than pure aluminium indicating the extension of solute solubility of the alloying elements in the aluminium lattice. The effect of Mg is also apparent being the only one among the three alloying elements Mg, Mn and Fe, that increases the lattice parameter of aluminium. The gradual increase of the aluminium lattice parameter with temperature up to 300°C, in association with the coarsening of the second phase

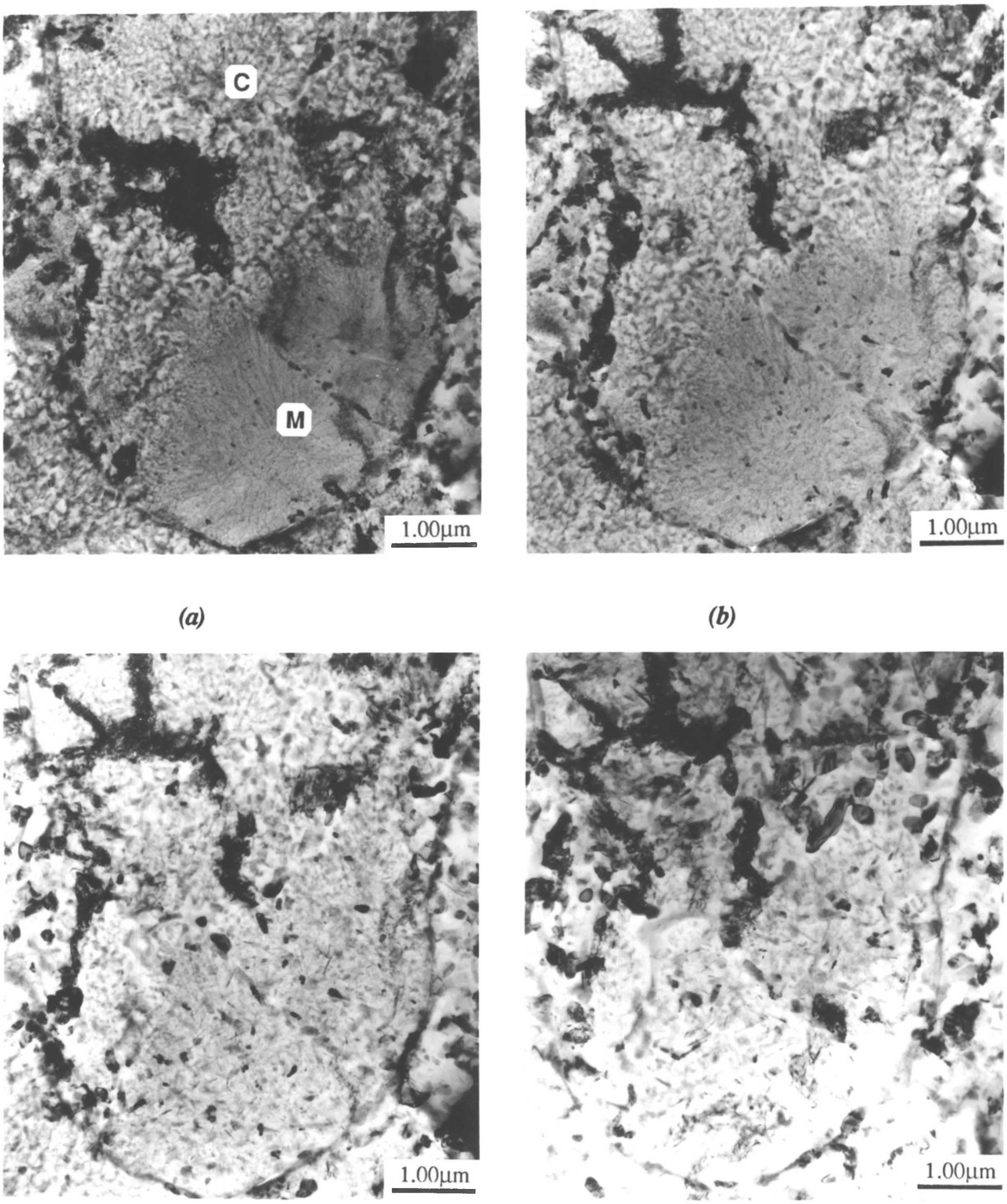

(a) *(b)*

(c) *(d)*

Figure 4.12.

Structural changes during in-situ heating of hot compacted powder specimens (375 ℃):

a) starting microstructure
b) 400℃, just after the heating up period
c) 20 min at 400℃
d) 90 min at 400℃

particles indicate that the two alloying elements, Mn and Fe, precipitate leaving the Mg in solid solution. At 350°C there is a more significant increase in the Al lattice parameter which results from the decomposition of the intercellular region. This can only be explained either by Mg taken back into solution from rich cell boundaries or possibly by the diffusion of Fe and Mn atoms to second phase particles. The latter explanation is improbable since Table 4.4 does not indicate any phase changes occurring at this temperature.

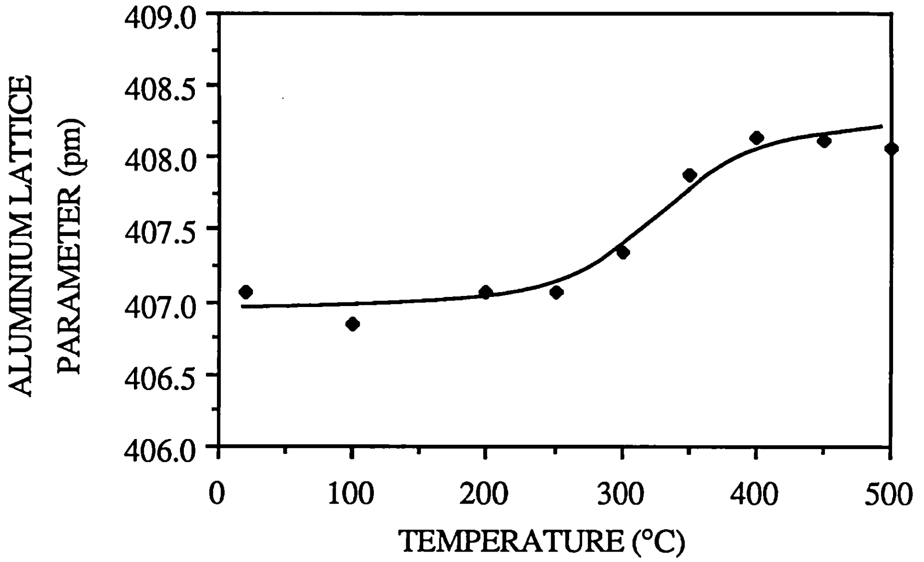

Figure 4.13. Variation of the aluminium lattice parameter with heat treatment temperature for the Al-Mg-Fe alloy.

4.6. Comparison of the three alloys - Summary

It has already been shown that the powder microstructure of the three alloys studied in the present work is heterogeneous, especially of the manganese and iron bearing alloys in which striking variations have been recorded within individual powder particles and as a function of particle size. The Al-Mg-Cr alloy exhibited a much more uniform microstructure irrespective of the size of the powder particles.

The thermal history of the powder is dictated by the solidification characteristics, namely nucleation undercooling, rate of heat extraction to the surroundings and growth kinetics of the moving solid/liquid interface. In small to medium size powder particles (e.g. <1μm to 15-20μm) of the Al-Mg-Mn and Al-Mg-Fe alloys, nucleation at the surface of an undercooled liquid droplet encouraged a smooth solidification front to proceed into the bulk of the liquid droplet at high velocity, thus resulting in featureless and microcellular structures respectively. Recalescence of the fraction of solid within the droplet caused decomposition of the solidification front and finally a coarser cellular microstructure. In the larger powders, which experienced lower solidification rates, the formation of coarse intermetallic phases was promoted. These can be either metastable i.e. the icosahedral phase of the Al-Mg-Mn alloy, and the (Fe,Mn)Al_6 of the Al-Mg-Fe one, or equilibrium i.e. Fe_4Al_{13} also formed in the Al-Mg-Fe alloy. Conversely, in the Al-Mg-Cr alloy the formation of primary high temperature dispersoids within the liquid droplets, which then served as nucleation sites for other phases, led to a uniform microstructure composed of aggregates evenly distributed within the matrix. The size of the aggregates is closely related to the size of the powder particles.

There is an increased tendency for decomposition of the partitionless and microcellular solidified regions of the Mn and Fe containing alloys respectively, when heated at high temperatures. The metastable phases observed in these two alloys, Al-Mg-Mn and Al-Mg-Fe, decomposed at temperatures greater than 400°C and the resultant microstructures at high temperatures (>500°C) contained only $MnAl_6$, and Fe_4Al_{13} and (Fe,Mn)Al_6 precipitates respectively. By comparison, the microstructure of the Al-Mg-Cr alloy remained practically unchanged, which can be attributed to chromium addition, because chromium forms intermetallic phases at comparatively higher temperatures that remain stable during post solidification treatment.

The phase transformation can also be observed by studying the variation of the aluminium matrix lattice parameter (a_0) with temperature, because any distortion of the lattice by the presence of the alloying elements can be recorded. Note that for comparison, the curves, illustrating the influence of heating on the aluminium lattice parameter of all three alloy variants, have been plotted in the same figure (Figure 4.14). Generally, a common characteristic is the increase of the aluminium lattice parameter with temperature; this variation can be interpreted by considering the behaviour of the major alloying elements Mg, Cr, Mn and Fe. An increase in a_0 could be explained either by Mg being taken back into solution or by removal of the transition elements. In Figure 4.14, it can be seen that the aluminium matrix lattice parameter of the Al-Mg-Cr alloy increases moderately with increasing temperature, indicating the microstructural stability of this alloy at high temperatures. By comparison, in the other two alloys the lattice parameter is greatly affected by the heating temperature.

In the Al-Mg-Fe alloy the decomposition of the microcellular structure allows Mg back into solution from solute rich areas (intercellular network), while the formation and coarsening of Fe_4Al_{13} and $(Fe,Mn)Al_6$ dispersoids at temperatures greater than 400°C depletes the matrix of Fe and Mn; these result in an increase in the Al-matrix lattice parameter.

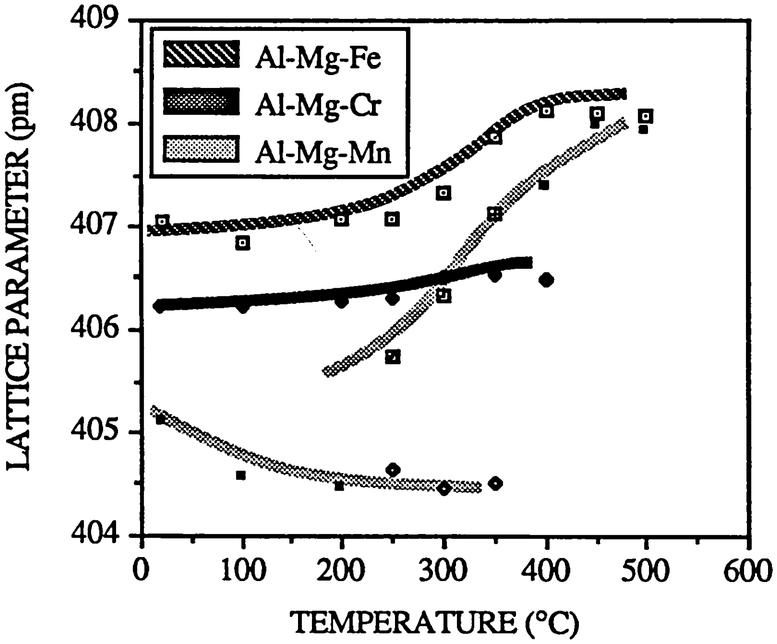

Figure 4.14. Variation of the aluminium lattice parameter with heat treatment temperature

In the Al-Mg-Mn alloy there are Mg-rich and Mg-lean areas giving rise to two different sets of aluminium lattice parameter (especially within the temperature range of 250°C and 350°C). At relatively low temperatures (<350°C) formation and coarsening of the Al_3Mg_2 requires Mg being taken out of the solid solution and therefore the lattice contracts. With increasing temperature the icosahedral phase transforms into $MnAl_6$ which also coarsens, while the fine Al_3Mg_2 precipitates transform into $Al_{18}Mg_3Mn_2$. The latter one dissolves at temperatures greater than 350°C. Hence, the transformations occurring at high temperature allow Mg being taken back into solution and precipitation of Mn-rich phases, thus resulting in a considerable increase in $\mathbf{a}_0$.

Hence, among the three alloys, the Al-Mg-Cr appears to exhibit microstructural stability and thus it is more promising for use at elevated temperatures, when consolidated. On the other hand the Al-Mg-Mn is the most sensitive to temperature variations, while the iron bearing one forms stable dispersoids at temperatures greater than 400°C, thus being also promising for use at elevated temperatures.

4.7. Conclusions

1. A powder characterisation study of three air-atomized powders has been conducted. The study involves size, shape and microstructural analysis of the powder particles, as well as an investigation of their behaviour during heating to high temperatures.

2. The Al-Mg-Mn alloy has relatively the finest median powder particle size among the three alloys, while the chromium containing one has the coarsest.

3. The shape of the powder particles is in general spherical, especially with decreasing size. The chromium bearing alloy contains a larger proportion of ovoidal shaped particles, in comparison with the other two alloys.

4. The addition of a transition element to a base Al-6%Mg results in significantly different microstructures. Complete cross sections of a range of powders have been examined using TEM. Structural variations have been recorded between different size powder particles and even within individual ones in both the Al-Mg-Mn and Al-Mg-Fe alloys.

5. Inhomogeneity of the manganese and iron containing alloys is promoted by the formation of fine structures (microcellular, featureless areas) and/or intermetallic metastable phases formed at the beginning of solidification.

6. The microstructure of the Al-Mg-Cr alloy consists of aggregates of $Al_{18}Mg_3Cr_2$, Cr_2Al_{13}, Al_3Mg_2 and unidentified phase(s) uniformly distributed within the powder particle. The size of individual aggregates is directly related to powder particle size.

7. Three typical powder microstructures were observed in the Al-Mg-Mn alloy attributed to different solidification mechanisms. (i) cellular morphology with solute enriched intercellular regions in the majority of the powder particles, (ii) featureless regions within the medium to fine sized powders and (iii) second phase particles surrounded by areas free of precipitates in coarser powders. Quite often particles with dual , partitionless-cellular, microstructural morphology were observed.

8. The inhomogeneity observed in the microstructure of the Al-Mg-Fe powder particles can be attributed to the solidification behaviour. The small particles exhibit a microcellular structure, the medium sized particles a dual morphology of microcellular and cellular structure, while in the large particles coarse intermetallics, formed during solidification, act as nucleation sites for a cellular aluminium structure.

9. Structural variations within the same powder particles observed in the Mn and Fe bearing alloys have been related to differing interface velocities caused by the degree of nucleation undercooling and recalescence. The latter retards the velocity of the solidification front resulting in a cellular front.

10. The second phase particles in the coarser powders of the Al-Mg-Mn alloy were a quasi-crystalline metastable phase exhibiting icosahedral point symmetry. The icosahedral phase transforms into $MnAl_6$ at temperatures greater than 400°C. The intercellular regions of the finer powders contain Al_3Mg_2 which is encouraged to grow during heating of the powder up to 350°C and then it probably transforms into $Al_{18}Mg_3Mn_2$ which dissolves at higher temperatures (>450°C-500°C).

11. It is postulated that because of varying solute contents of the aluminium matrix in various powder particles of the Al-Mg-Mn alloy, a range of matrix lattice parameters, calculated from the broad peaks in X-ray diffraction, existed. In the temperature range between 250°C and 350°C a splitting of the peaks occurred giving two distinct lattice parameters which originate from Mg-rich and Mg-lean regions of the matrix. At higher temperatures (>400°C) the splitting was not observed since Mg containing phases dissolve and the entire matrix becomes Mg-rich.

12. In the Al-Mg-Fe as-atomized powders, two intermetallic compounds were identified by X-ray analysis, $(Fe,Mn)Al_6$ and Fe_4Al_{13}. An unidentified phase was also observed in the microcellular solidification structure and the d-spacings obtained from both electron and X-ray analysis were in agreement.

13. During heating of Al-Mg-Fe powders at temperatures greater than 400°C, the unidentified phase transforms and the microcellular structure decomposes. The $(Fe,Mn)Al_6$ and Fe_4Al_{13} phases grow and coarsen as needles and spheres. The initial microstructural heterogeneity is only removed after heating for 1h at 550°C.

Consolidation

of

Powders

Chapter 5. Consolidation of Powders

The rapidly solidified particulate produced by atomization must be consolidated into a fully dense material. In the present work the consolidation process was carried out in two stages a) pre-extrusion forming (cold compaction) and b) hot extrusion.

5.1. Pre-extrusion forming

The aim of this first step of the powder consolidation is to give a suitable form to the loose powder and therefore facilitate induction heating and handling at the extrusion press. *Cold compaction* has been utilized because firstly it is simple and secondly decomposition of metastable R/S microstructures, sintering and grain growth that might occur during hot pressing can be avoided. It is well understood that the cold compaction process is a complementary and insignificant one, as far as the thermomechanical process is concerned. This is because metallurgical reactions, such as phase transformations, bonding of the loose powders, building of the substructure and thus attainment of full strength can only be achieved by the shear inherent in the thermomechanical extrusion process. Nevertheless, cold compaction constitutes an indispensable step for the production of powder alloys. Towards this end, a summary of the techniques attempted for the production of sound and coherent billets are briefly presented, in addition to the factors affecting the process.

In the present work the powders have been found to compact with difficulty. Using the single action technique (Experimental Procedure, Section §3.4.1.1) sound and coherent compacts were not produced because they disintegrated into a number of slices or disks during ejection from the die. This is because little or no bonding occurred during the compaction process. In the same way, compacts wrapped with aluminium foil did not have adequate strength and circumferential lines on the surface of the billets, see Figure 5.1 (a), indicate that the compact would be easily broken apart if the foil was removed. It was then considered that the maximum available pressure of the compaction press was not sufficient to produce billets with the necessary coherency to withstand the rigour of ejection; for this reason attempts were made to compact the billets in the extrusion chamber, in which higher pressures could be transmitted to the powder. Nevertheless the experiments were unsuccessful. The reason for this could be that powder particles do not behave as fluids in the transmission of the applied pressure. Hence, pressure applied about one axis produces a lower component about an othogonal axis. Moreover, the friction between the powder particles and the die walls results in a reduction of pressure with increasing distance from the moving ram. Hence, the unequal pressure transmission to the orthogonal axis causes varying densification along the same axis resulting in poor quality compacts, Figure 5.2 (a) shows an optical micrograph from a broken compact. Obviously, the local density of the compact varies widely and lack of interparticulate contact is quite evident.

Among the three alloy compositions the greatest difficulty was encountered in attempts to compact the Al-Mg-Mn bearing alloy. Less difficulty was experienced for the Al-Mg-Fe, while the Al-Mg-Cr was compacted relatively easily. A study of the compaction behaviour of the three alloys, Al-Mg-Cr, Al-Mg-Fe, Al-Mg-Mn revealed the relationship between the compactability and the characteristic features of the powder particles, such as particle size and shape, alloy chemical composition, and hardness. It is clear that the almost spherical shape of the powder particles (Section §4.2) and the narrow range of size distribution result in poor compactability. It has been reported that the green density of the compact increases with increasing powder particle size for a constant pressure, {Paramanand (1984)}. This implies that the coarser fractions transmit more efficiently the applied pressure resulting in better packing of particles and therefore increased density. Furthermore, since the coarser powder particles are not spherical, the interparticle surface area available for mechanical interlocking of particles increases with increasing particle size. Finally, the volume fraction of voids increases with decreasing particle size. It has been shown that the Al-Mg-Cr alloy, apart from having a higher volume fraction of irregularly shaped particles, is the coarsest powder, while the Al-Mg-Mn alloy is the finest one. Thus, it was to be expected that the Al-Mg-Cr alloy would compact more easily than the other two alloys.

Two other parameters that affect the compaction qualities of the powder alloy are the hardness and the chemical composition. The more highly alloyed the powder the harder it is, exhibiting less plasticity and therefore any weld necks are less extensive and break more easily {Paramanand (1984)}.Thus, the Al-Mg-Mn alloy, which exhibits considerably higher hardness {Marshall et al (1986)}, has the finest particle size and is the most heavily alloyed, compacts poorly. Finally, during the ejection from the die elastic recovery takes place resulting in considerable stress inequalities at the triple interface, die wall - billet - air. If the elastic stresses are greater in magnitude than the strength of the weld necks, the billet will break in disks perpendicular to the compaction axis.

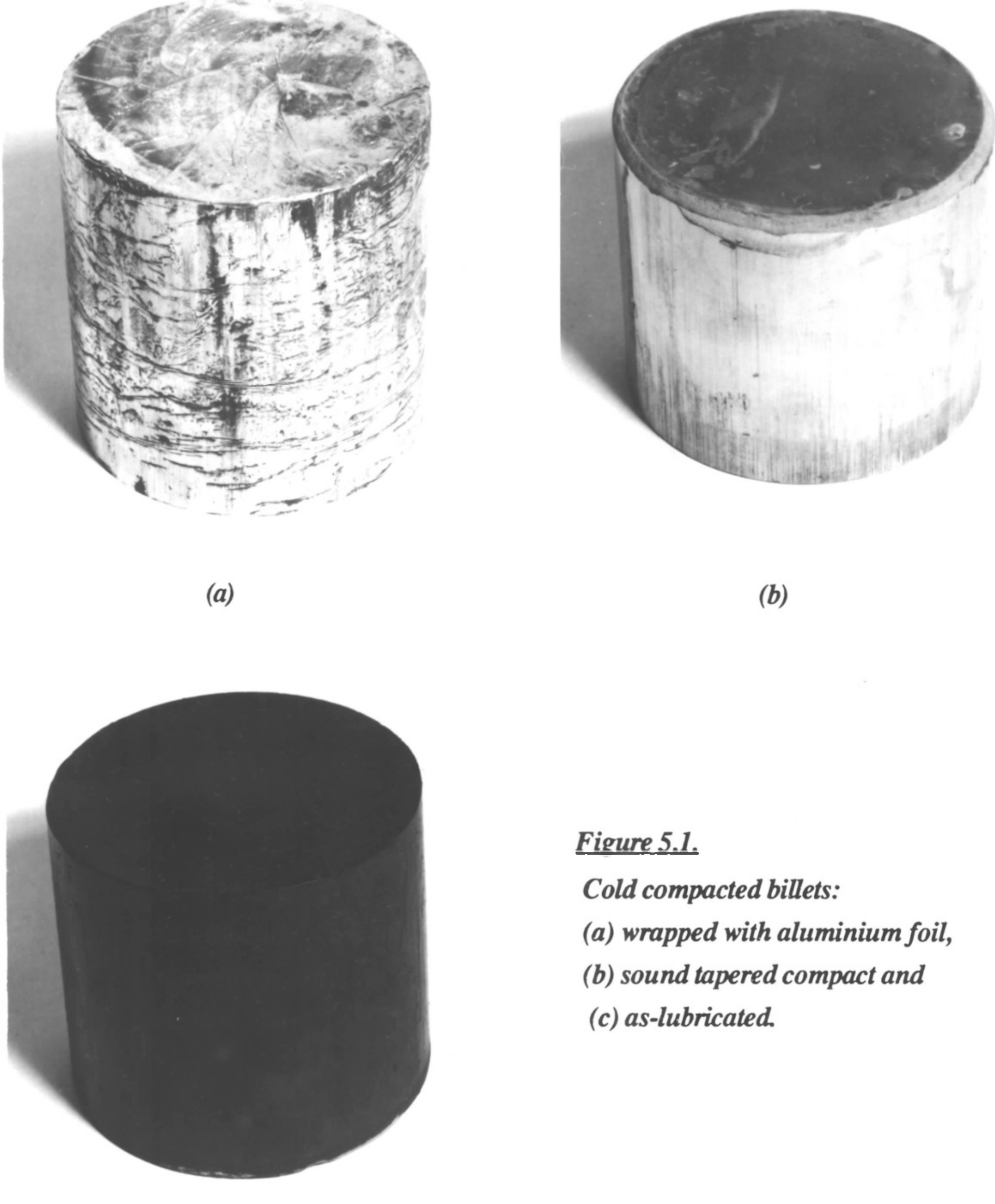

(a)

(b)

(c)

Figure 5.1.

Cold compacted billets:
(a) wrapped with aluminium foil,
(b) sound tapered compact and
(c) as-lubricated.

Sound and coherent billets were only produced by using a tapered die and a double action technique. The tapered die facilitates the ejection of the billets reducing the friction between the die surface and the aluminium particles and causing the elastic recovery to occur more gradually. The double action compaction also causes more uniform distribution of the compaction pressure within the mass of the powder. A typical photograph of a billet produced by this method is shown in Figure 5.1 (b). The billets were then lubricated, see Figure 5.1 (c), as described in Section §3.4.1.2. An optical micrograph representative of an approximately 81% dense billet, from the chromium bearing alloy, is shown in Figure 5.2 (b). It can be seen that the smaller particles are squeezed in between larger particles (arrows marked A) while elongated particles fill the irregularly shaped voids (arrow marked B) increasing the green density of the compact. Clearly the particles have in general undergone little plastic deformation. The amount of plastic deformation depends on the size distribution, the shape of the particles, their hardness and the compaction pressure. The contrast between cold pressed billets and hot pressed is illustrated in Figure 5.2 (b) and (c). The hot pressed powder particles exhibit greater plasticity resulting in an approximately 100% dense billet.

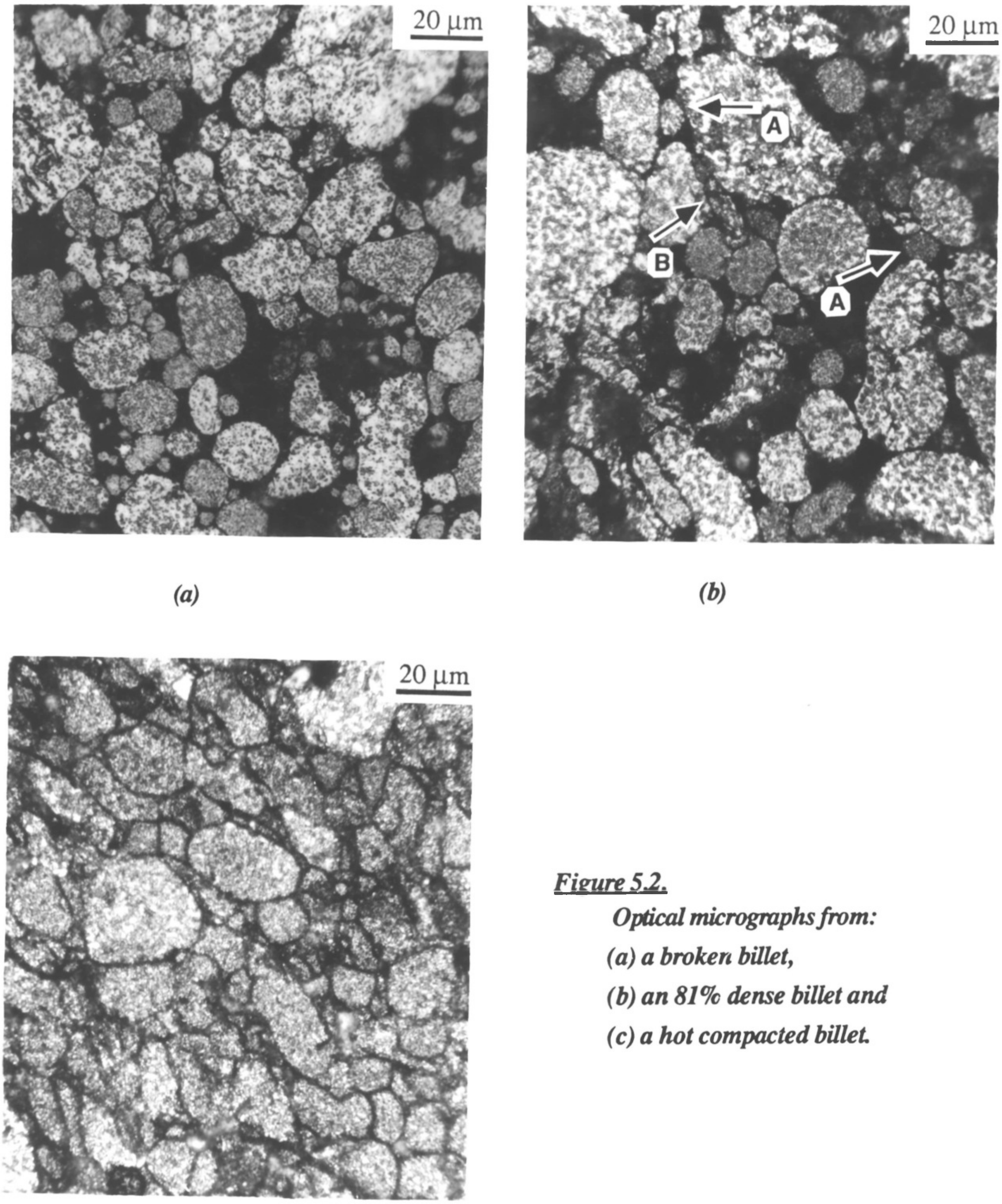

(a)

(b)

(c)

__*Figure 5.2.*__

Optical micrographs from:
(a) a broken billet,
(b) an 81% dense billet and
(c) a hot compacted billet.

5.2. Extrusion Behaviour

Fabrication of the loose powder into an engineering product occurs during the extrusion process. In general, the structure of the final product, that controls the material properties, relies not only on the as-atomized powder microstructure but is also dependent on the changes in the structure during processing. Particularly, the processing parameters are as influential in determining the product structure as the atomization parameters. It is therefore essential to study the extrusion behaviour of each alloy and the development of the microstructure.

Extrusion is a complex hot working process involving interactions between the controlling variables and the high temperature properties of the material. Thus, the deformation process and the building of a coherent structure are metallurgical events, which are controlled by a suitable consideration of the temperature and the applied strain rate. These two factors give conflicting effects. At high temperatures the stress to deform a material for a given strain decreases as the ease of dislocation migration increases, therefore the rate of work hardening decreases due to the enhanced restoration processes. An increase of the strain rate will increase the rate of dislocation generation resulting in higher flow stress, {Jonas et al (1969)}. These two conflicting parameters can be combined into a single one, the temperature compensated strain rate or Zener-Hollomon parameter, written as:

$$Z = \dot{\varepsilon} \exp\left(\frac{\Delta H}{\Re T}\right) = A\left[\mathrm{Sinh}(\alpha\bar{\sigma})\right]^{\eta} \quad \ldots\ldots\ldots\ldots\ldots\ldots\ldots\ldots\ldots\ldots \quad (5.1)$$

where $\dot{\varepsilon}$: mean strain rate

ΔH: activation energy,

α, η: constants,

$\bar{\sigma}$: mean flow stress and

$\Re$=8.314 kJ/mol °K, the universal gas constant.

Thus, the temperature compensated strain rate is proportional to the strain rate and dependent exponentially on the reciprocal temperature (1/T). However, since the strain rate varies throughout the deformation zone, it is necessary to define a mean strain rate, given satisfactorily by the modified Feltham's equation '5.2' shown below. Clearly, the strain rate at which the material deforms depends on the extrusion ratio (lnR), ram speed (v) and billet diameter (D_B). In this equation, the variable, within the present investigation, was the extrusion ratio. Hence, it was possible to accommodate the variation in strain rate through changes in extrusion ratio.

$$\dot{\bar{\varepsilon}} = \frac{6\,v\,(a + b\ln R)\tan\omega\, D_B^2}{D_B^3 - D_E^3} \qquad (5.2)$$

where v: ram speed
R: extrusion ratio
a,b: constants
D_B: billet diameter
D_E: extrudate diameter

Clearly, the extrusion process controlling parameters were the following: billet temperature, ram speed, extrusion ratio, container temperature and lubrication. During the extrusion run the recorded data were: pressure and ram displacement. Compiling these data, a load-displacement curve can be drawn from which the maximum and minimum pressure, the ram speed and the displacement to peak load can be calculated. In the following section, a study concerning the extrusion characteristics and the relationship between the extrusion pressure and the processing parameters such as billet temperature, extrusion ratio and temperature compensated strain rate will be presented.

5.2.1. Characteristics of the Load-Displacement Curves

The shapes of three load-displacement curves are illustrated in Figure 5.3. These curves, obtained from the Al-Mg-Cr alloy, are typical of the extrusion behaviour at three different temperatures, 400°C, 450°C and 550°C, irrespective of the alloy composition. In the beginning they display a non-linear increase in load corresponding to billet compaction to fill the container and the attainment of the theoretical density. In a low temperature extrusion, see Figure 5.3 curve A, the load increases rapidly to a maximum value followed by a steady fall. As the billet temperature is raised (curves B and C) the magnitude of the peak decreases until it becomes scarcely detectable, suggesting that there is a threshold load value below which these pressure peaks do not occur.

The existence of pressure peak in extrusions is a fairy common feature and several possible causes have been suggested to explain its manifestation, such as frictional effects {Johnson and Kudo (1962)} or the formation of the dead metal zone, {Avitzur (1968)}. Evidence against the former hypothesis was provided by Ziegler (1973) who has shown that the peak occurs in indirect extrusion where the friction is almost zero. Temperature differential between the die and tooling has been suggested by

Ascroft and Lawson (1960/61), but no conclusive evidence is available. The most likely explanation is that suggested by Castle and Sheppard (1976) and supported by McShane (1978) and Tan (1984) that the peak is controlled by thermally activated events involving the production, interaction and annihilation of dislocations. Experimental evidence, provided by Sheppard at al (1979) for an Al-5%Mg alloy and by Tan (1984) for Al - 7%Mg, 10%Mg, 12%Mg, and 15%Mg powder extrusions, conclusively showed that during the first stage of extrusion, dislocation generation and migration commences as the pressure is applied, accompanied by deformation of the billet. The dislocations then interact with each other and with any precipitate or oxide particle present. Such interactions inhibit their migration. Hence, to continue the process an increase in pressure is required up to a "breakthrough" value. The density of dislocations increases gradually approaching the density required to establish a quasi-static deformation zone. At peak pressure the steady state deformation zone has not been fully established but this condition is achieved by the time the pressure has diminished. At high temperatures, the dislocation dynamics are aided by thermal energy. The flow stress decreases and an excess of dislocations is generated immediately after the compaction region and before dynamic softening processes commence, thus resulting in a lower peak magnitude or even elimination of the peak, see curve C Figure 5.3.

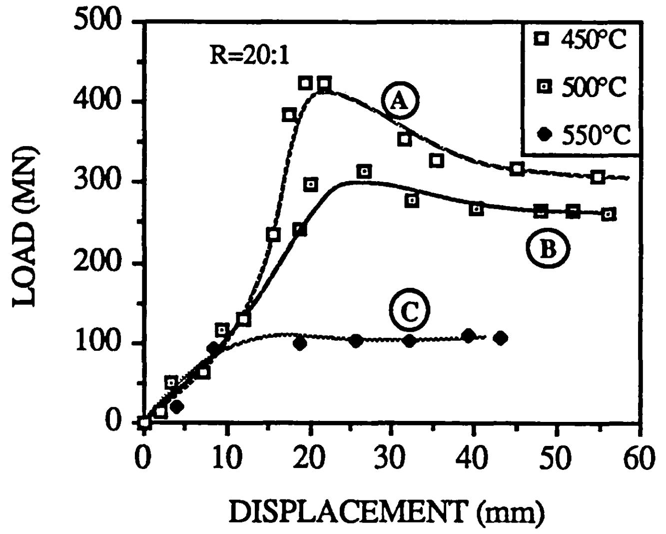

Figure 5.3. Typical variation of Load-Displacement curve with extrusion temperature for the Al-Mg-Cr alloy

It must be pointed out that the peak pressure is a very important factor for industry because it determines the highest pressure required to initiate extrusion and therefore the capacity of the press. In the present investigation, this additional increment of extrusion pressure was shown to be quite significant; with the three alloys examined it resulted, under certain conditions, in a 50% increase over the steady state pressure requirements. Obviously, this could markedly reduce the extrusion range for a specific press capacity. On the other hand there is an upper temperature limit defined by the solidus temperature either of the alloy or of the second phase particles. Hence, extrusion limits are imposed by the properties of each alloy composition. It is therefore essential to study the extrusion limits.

5.2.2. Extrusion Limits

The concept of limit diagrams has already been discussed in Section 2.3.3 and it now seems appropriate to apply this analysis to the results of the three powder alloys. Figure 5.4. illustrates limit diagrams which show the extrusion range for each alloy.

The limit diagrams are determined either by the capacity of the press (lower temperature limit or pressure limit) or the extrudate surface degeneration (high temperature limit). Using the same extrusion ratio there is a low temperature value, below which extrusion was impossible due to insufficient press capacity and a high temperature limit, above which extrudates of poor surface quality were produced. In the present investigation the lower limits were drawn for a press capacity of 5 MN, for direct extrusion using approximately 8 mm/s ram speed and 75 mm diameter container. The surface quality of the extrudates, which dictates, the higher temperature limit, has been assessed qualitatively by visual means only. It must be mentioned that bad surface finish is not necessarily associated with incipient melting, as described in Section 2.3.3, indeed the surface defects have been classified in four categories, Bryant (1971): i) cracks and tears, ii) pick up and die lines, iii) blisters and iv) streaking.

The more dilute alloy, the Al-Mg-Cr, exhibits the widest extrusion limits, see Figure 5.4, in contrast to the Al-Mg-Fe alloy whose extrusion range is severely restricted. Jacobs et al (1974) have reported that Al-Fe binary alloys show high hardness values in the as-atomized condition, and therefore difficulties during consolidation would be expected. Iron additions in Al-Mg alloys reduce the hot workability considerably and hence the extrusion limits of the alloys. This phenomenon can also be attributed to the inhomogeneities observed in the as-atomized microstructure, reported for Al-Fe powder alloys. Inhomogeneous structures lead to a non-uniform distribution of the stress resulting in preferential deformation and therefore high local strains and crack initiation. In contrast with Al-Mg-Fe alloy the Mn bearing alloy displays somewhat contradictory extrusion behaviour. At lower temperatures the pressure requirements approach those of the Al-Mg-Cr alloy, but the surface finish at higher temperatures is similar to that of Al-Mg-Fe alloy, suggesting that the Fe and Mn bearing alloys have lower high temperature flow stresses than the Al-Mg-Cr. This is because, in the present investigation, the cause of bad surface finish at high temperatures can be described as peripheral cracking attributed to hot tearing (sometimes called speed cracking). Hot tearing occurs when the tensile stresses, that are set up at the extrudate surface by excessive friction, exceed the hot yield stress of the material. Hence, hot tearing is a function of the high temperature yield stress, the temperature of the extrudate at the die land area and the frictional forces. Incipient melting of intermetallic phases has also been considered, but discarded for the reason that the phases detected in the heat treated powders do not have low melting points; consequently the incipient melting does not serve as an explanation for the poor surface quality.

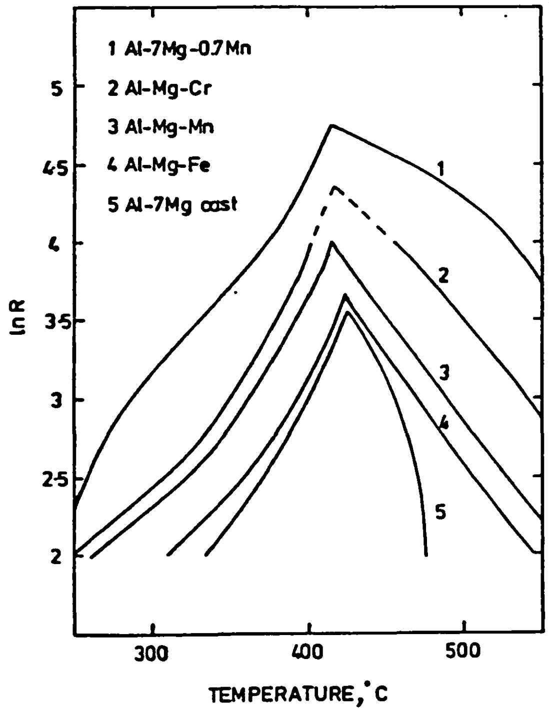

Figure 5.4. Extrusion Limit Diagrams for various aluminium alloys

Since the Al-Mg-Fe alloy requires higher extrusion pressures than the other two alloys (see the next section), the temperature rise during extrusion of this alloy is higher than for the other two, extruded under similar conditions. Consequently, this alloy suffers from hot tearing more severely. On the other hand, the Al-Mg-Mn alloy will be shown to have poorer elevated temperature strength than the Al-Mg-Cr and Al-Mg-Fe alloys; hence localised yielding in the die land area is also likely to account for a deterioration in surface quality.

It is interesting to see how the extrusion ranges of the three powder Al-Mg alloys compare with that of a binary powder Al-7%Mg and a cast alloy. In Figure 5.4 the limit diagrams of an Al-7Mg-0.7Mn alloy {Tan (1984)} and an Al-7%Mg cast alloy {Tan et al (1984)} are also included. Clearly the addition of any of the three alloying elements, Cr, Mn and Fe, to Al-7%Mg restricts the extrusion range. Nevertheless, the powder metallurgy materials exhibit considerable improvement over the conventional cast materials. The cast Al-7%Mg alloy has the narrowest extrusion limits, however it is worth noting that Al-7%Mg alloys are essentially not extrudable and the extrusion limits of this alloy have only been drawn in Figure 5.4 in order to highlight the differences behaviour between cast and rapidly solidified alloys. Note that the specific processing conditions that lead to the optimum microstructure and therefore the best mechanical properties lie within the extrusion range of each alloy. Thus, a more extensive extrusion range will allow better control of structure and properties.

5.2.3. Extrusion Temperature

a) General Characteristics

In order to investigate exclusively the influence of the extrusion temperature on the extrusion process, the other processing parameters, such as extrusion ratio and ram speed must remain constant. In the present work the maximum extrusion pressure requirements for a number of conditions have been assessed for the Al-Mg-Cr alloy, which has the largest extrusion range. It should be noted, however, that similar behaviour occurred in all three alloy compositions.

Figure 5.5 illustrates the effect of the billet temperature on the maximum extrusion pressure, at three different extrusion ratios 10:1, 20:1 and 50:1, for the Al-Mg-Cr alloy. The results show the expected decrease in pressure with increasing billet temperature, for all the extrusion ratios. This is because the energy consumed in redundant work as well as the work of homogeneous deformation decrease with increasing temperature. The work of homogeneous deformation is lower at higher temperatures because, for most of the passage through the deformation zone, the high temperature strength of the material is low. Regression analysis has been conducted in order to reveal the law governing the relationship between extrusion pressure and temperature. The constants as well as the correlation coefficients of the statistical analysis, for both a linear and a power fit, are listed in Table 5.1. Obviously, the correlation for a pressure-temperature exponential relationship is more satisfactory than for a linear fit. It is worthwhile adding that the general temperature-plasticity relationship reported by Pearson and Parkins (1960), $P = A \exp(-\lambda T)$, for cast aluminium alloys has been also verified in the present investigation for rapidly solidified alloys.

Table 5.1. Regression data for the pressure-temperature relationship for the Al-Mg-Cr alloy

R	$P = aT + b$			$P = c \exp(-kT)$		
	a	$b\ 10^{-3}$	R^2	$c\ 10^{-3}$	*k*	R^2
10:1	-2.535	1.65	0.987	4.77	5.11	0.996
20:1	-2.656	1.81	0.977	5.02	4.80	0.998
50:1	-2.710	1.97	0.969	3.67	3.55	0.980
Rect.	-3.736	2.17	0.927	5.04	1.05	0.932

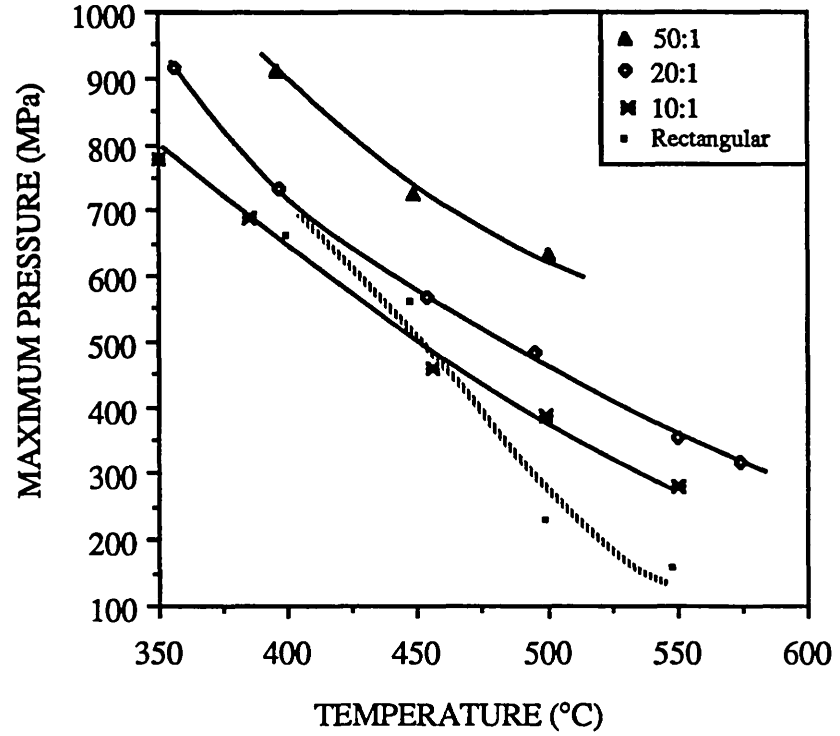

Figure 5.5. Variation of maximum extrusion pressure with temperature for the Al-Mg-Cr alloy

The results presented in Figure 5.5 show that the peak pressure values increase consistently with increasing extrusion ratio. At higher extrusion ratios the work hardening increases, thus requiring higher pressures to initiate extrusion. Furthermore, a detailed study reveals that the rate of the peak pressure reduction increases slightly with higher extrusion ratio (k decreases with increasing R, Table 5.1). This indicates that the amount of heat generated at the beginning of the extrusion is significant enough, at the higher extrusion ratio extrusions, to increase the temperature and therefore decrease the flow stress.

b) Rectangular-bar Extrusions

In Figure 5.5 a curve obtained from the data of rectangular-bar extrusions has also been drawn. Rectangular-bar extrusions were only performed in order to obtain specimens for the study of the properties of the final product along the transverse direction. Note that the ram speed was approximately the same as for the roundbar extrusions and the rectangular die (8x37 mm) gives an approximate reduction ratio of 15:1, see Section §3.4.2. The curve obtained from the rectangular extrusions apparently does not exhibit the same trend as the curves from the roundbar extrusions. The pressure decreases considerably with increasing temperature. In addition, the pressure-temperature relationship in this case is neither a linear nor an exponential one, as evidenced by the poor correlation coefficients, see Table 5.1. This heterogeneous behaviour can be attributed to the mode of deformation. In particular, the deformation zone has been shown by Wood (1978) to vary with the shape of the die and the billet temperature. Moreover, both the strain rate and the temperature have been shown to vary appreciably within the shear zone. Avitzur (1968) has shown that the strain rate of an element near the die entry for rod extrusion can be 90 times as great as the mean strain rate. Hence, the differences of the deformation characteristics of the rectangular-bar extrusions result in different pressure-temperature relationship from the roundbar. However, it must be mentioned that it is not within the scope of this work to investigate the influence of various die shapes on the extrusion pressure and thus offer a comprehensive interpretation.

c) Comparative Study of the three alloys

In the beginning of this section it was reported that the three alloys exhibit similar extrusion behaviour. In spite of this, the pressure requirements vary markedly for each alloy; for this reason a comparative study is essential. Figure 5.6 shows a conventional plot of extrusion pressure versus initial billet temperature for the three powder alloys at a constant extrusion ratio of 20:1. Clearly, the general trend is that the pressure falls consistently with increasing temperature for all the powder alloys. At low temperatures the peak pressure values for the Al-Mg-Cr alloy are considerably lower than for the other two alloys, while the Fe bearing alloy maintains significantly higher peak pressures even at relatively high temperatures (450°C to 500°C). On the other hand the rate at which the peak pressure decreases with temperature, for the Al-Mg-Mn alloy, is considerably higher than for the other two. At temperatures below 450°C the pressure for the Al-Mg-Mn alloy is higher than for the Al-Mg-Cr alloy, but falls substantially when temperature increases.

Obviously, the maximum pressure is a function of the alloy characteristics. The Al-Mg-Cr alloy, consisting of coarser powder particles and being more dilute, exhibits lower pressures at relatively low temperatures. It has already been reported (Section §2.3.2) that the extrusion pressure requirements decrease with increasing powder particle size. Such behaviour would be expected because the energy requirements are reduced for consolidation of a coarser alloy, since with decreasing powder particle size the total surface area of powder is greater and inevitably a greater number of weld necks must be formed during the compaction stage of extrusion, broken in shear and rewelded. Moreover, the oxide film present around each powder particle acts as a barrier to dislocation motion. Thus the larger the particles the fewer barriers exist.

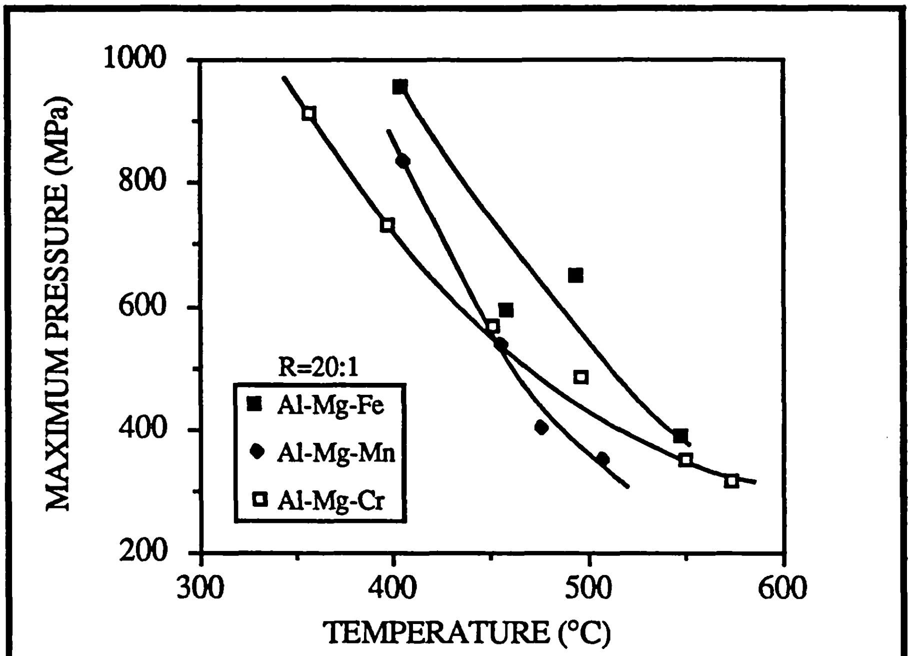

Figure 5.6. Variation of the extrusion pressure with temperature for the three alloy compositions

The Al-Mg-Fe alloy requires, as expected, higher peak pressures than the other two alloys. This can also be explained in terms of its microstructural characteristics. The decomposition of the powder microstructure during heating of the Al-Mg-Fe alloy has been investigated (Section §4.5.3) and it is has been shown that rapid formation of needle and spherical shaped precipitates is promoted with increasing temperature. It will also be shown (Section §5.3.3) that the dead metal zone microstructure, which actually represents the billet microstructure prior to extrusion, consists of a high volume fraction of fine second phase particles. Hence, the fine distribution of a high volume fraction of precipitates provides a barrier to the dislocation motion, so that higher pressures are required to overcome the barrier and to establish a quasi-static deformation zone. At higher temperatures (i.e. 550°C) the thermal energy facilitates dislocation climb and cross slip and thus the hardening effect due to pile-ups is reduced. Hence, the extrusion load decreases approaching that of the Al-Mg-Cr alloy.

Finally, the Al-Mg-Mn alloy, which is the finest of the three alloys, apparently requires more energy for consolidation. The actual particle size can also limit the grain or subgrain development formed by dislocation interactions, thus increasing the flow stress and the extrusion load. At low temperatures the volume fraction of the various precipitates observed is high enough to increase the pressure requirements. However, with increasing temperature it has been shown (Section §4.4.3) that the phase transformations occurring result finally in a microstructure composed of an aluminium matrix and $MnAl_6$ precipitates, see Table 4.3. Hence, since the considerable decrease in volume fraction of fine precipitates is accompanied by structure coarsening, the maximum pressure requirements are reduced.

d) Peak Increment Characteristics

The peak increment can be calculated from the pressure displacement curves using a tangential construction as suggested by Castle and Sheppard (1976). It has already been explained that the "breathrough" pressure of the extrusion is connected with the energy required to set up a deformation zone. Since the peak pressure can be related to the billet temperature, strain rate, and the alloy content, the peak increment should also be related to these parameters. To permit the comparison of the behaviour of the three alloys and to illustrate the expected dependence of the peak increment on the billet temperature, the ratio of peak increment to maximum pressure has been plotted against the initial billet temperature at constant reduction ratio (20:1) for the three alloy compositions, see Figure 5.7. All the alloys show a monotonic decrease in the peak increment with temperature. Clearly, the Al-Mg-Fe alloy retains a considerably higher peak in the pressure up to relatively high temperatures, suggesting that the energy requirements to establish a quasi-static deformation zone are apparently higher for this alloy than for the other two, which is also attributed to dislocation pinning by fine precipitates that are formed during rapid induction heating. However, but due to short processing times (the extrusion process lasts less than 8 mins) homogeneization and coarsening have not been achieved. The number of second phase particles, which are formed during induction heating, depends on the billet temperature and the heating time. Note that the Al-Mg-Fe alloy was heated up with difficulty, thus requiring higher heating times than the other two alloys.

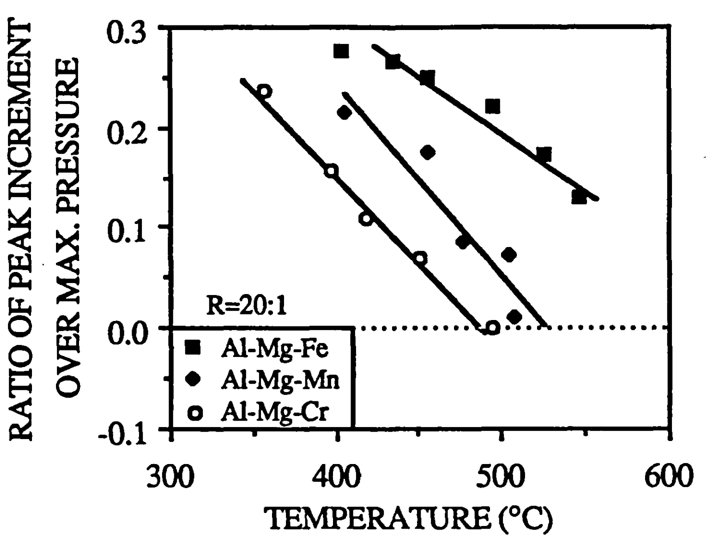

Figure 5.7. Influence of billet temperature on peak pressure increment

5.2.4. Extrusion Ratio

The effect of extrusion ratio variation will be presented for the Al-Mg-Cr alloy. Typical pressure-extrusion ratio curves are illustrated in Figure 5.8, for a temperature range varying between 350°C and 550°C. It can be seen that an approximately linear relationship exists, in each case, between the extrusion ratio and the peak pressure, for constant initial billet temperature and billet length. The statistical analysis for these lines is contained in Table 5.2, in which it can be seen that the results show very good correlation for each temperature.

Table 5.2. Constants of regression analysis of the Pressure-Extrusion Ratio (P-R) relationship for Al-Mg-Cr alloy.

$P = A + B \ln R$

Temperature (°C)	A	B	A/B	R^2
400	289.6	161.1	1.77	0.995
450	125.8	152.5	0.83	0.988
500	48.5	148.3	0.33	0.959
550	32.3	98.0	0.33	0.986

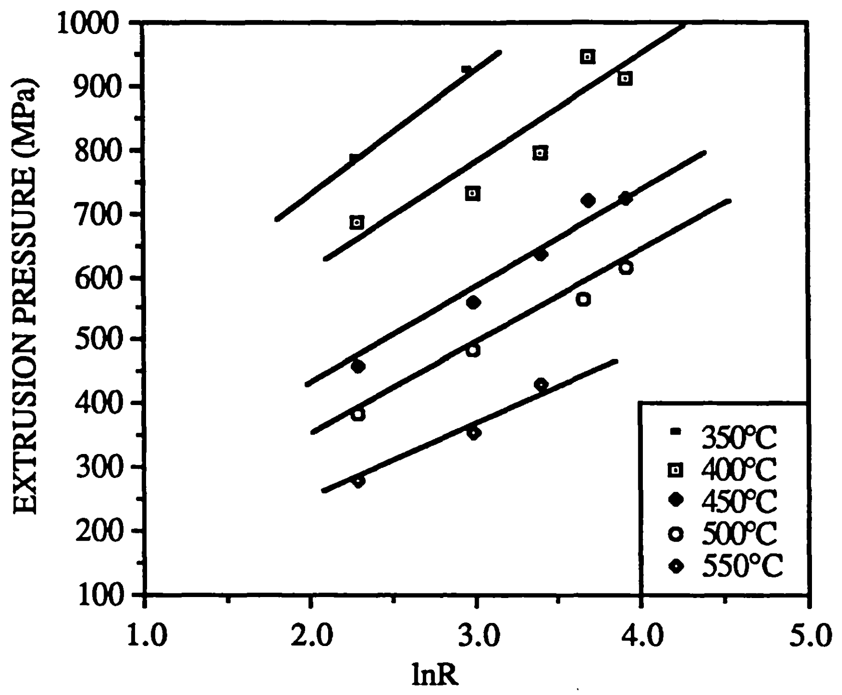

Figure 5.8. Variation of the extrusion pressure with extrusion ratio, at different temperatures, for the Al-Mg-Cr alloy

Generally, an increase in peak pressure with increasing extrusion ratio has been noted. This is in accordance with the trends found by Tan (1984) in powder binary Al-Mg alloys and Parkinson (1983). A significant feature revealed in Table 5.2. is the relative magnitude of the constants A and B. These show a consistent decrease with increasing extrusion temperature. It has been suggested by Johnson (1956) that for cast material the first constant (A) represents the energy consumed in the internal shearing process but not contributing to a shape change, for that reason it is termed *redundant work*. The second constant (B) is an indication of the *homogeneous work of deformation*. In the case of powder metallurgy, McShane (1978) and Sheppard et al (1983,b) have reported that the redundant work was significantly higher for the powder than for the cast extrusions, though Parkinson (1983) also working on the extrusion of some alloyed powders failed to observe any such trends, indicating again the complexity of the process. Clearly, the term A cannot be regarded simply as a measure of the redundant work during the extrusion of powder compacts. A fraction of the total energy required for deformation contributes to the consolidation of the material by interparticle shearing and "pressure sintering". The variation of the ratio A/B (typically 0.33 for cast materials) supports this interpretation. The ratio decreases as the energy required for pressure sintering decreases with increasing temperature. At the highest temperatures the ratio reduces to a level virtually the same as that observed for cast materials. This type of dependency indicates that deformation by extrusion is more efficient at high temperatures.

5.2.5. Temperature Compensated Strain Rate

The results in the previous sections have shown that the extrusion pressure depends on the billet temperature and the extrusion ratio. A more complex analysis, taking into consideration the fact that the extrusion process is thermally activated, involves the study of the influence of the temperature compensated strain rate on the peak pressure.

The concept of temperature compensated strain rate allows the extrusion temperature and the strain rate to be combined into a single parameter. Mathematically, this can be expressed as shown in the following equation:

$$Z = \dot{\varepsilon} \exp\left(\frac{\Delta H}{\Re T}\right) = A\left[\mathrm{Sinh}(\alpha\bar{\sigma})\right]^{\eta} \quad \ldots\ldots\ldots\ldots\ldots\ldots\ldots\ldots \quad (5.1)$$

The temperature compensated strain rate has been calculated at peak pressure, assuming that 90% of the energy provided has been transformed to heat, thus increasing the temperature of the billet. The temperature rise model, developed by Sheppard and Wood (1976), has been used in the present work.

Figures 5.9 to 5.11 illustrate the linear relationships between the extrusion pressure and the natural logarithm of the temperature compensated strain rate for the three alloys. The statistical analysis shows very satisfactory results, see Table 5.3. The graphs show the as-expected trend of increasing peak pressure with increasing extrusion ratio and temperature compensated strain rate.

It has been shown that the extrusion pressure depends linearly on the natural logarithm of the temperature compensated strain rate for a constant extrusion ratio. This relationship emphasizes the strong dependence of the pressure on the extrusion ratio. Hence, since the peak pressure depends linearly on both the natural logarithm of the extrusion ratio and the temperature compensated strain rate, a linear equation combining these parameters could be also derived:

$$P = A^* + B^* \ln R + C^* \ln Z \quad \ldots\ldots\ldots\ldots\ldots\ldots (5.4)$$

This hypothesis is in line with the results reported by Sheppard et al (1982) for direct and indirect extrusions of cast alloys and by Parkinson (1983) and Tan (1984) for aluminium powder alloys.

In the present work excellent corelation coefficients, see Table 5.3, have been derived by a multiple linear regression fit over the whole range of the results. Hence, it may be concluded that the inclusion of the two factors to allow for the variation of peak pressure with temperature compensated strain rate and extrusion ratio, result in an equation applicable over a wide range of processing conditions. Graphical representation of equations with two variables is better illustrated in three dimensional plots. The locus of this equation is a plane typically seen in Figures 5.12 and 5.13, for the Al-Mg-Cr and Al-Mg-Fe alloys respectively.

Table 5.3. Constants of regression analysis of the pressure-lnZ and pressure-lnZ-lnR relationships

$P = A + B\ln Z$					$P = A^* + B^* \ln Z + C^* \ln R$			
Alloy	Extrusion Ratio	A	B	r^2	A*	B*	C*	r^2
Al-Mg-Cr	10:1	-1514.46	77.13	1.00	-2245	931	125	0.986
	20:1	-1369.89	69.01	1.00				
	50:1	-1391.59	75.75	0.99				
Al-Mg-Fe	10:1	-2578.53	111.88	1.00	-3508	112	400	0.992
	20:1	-2317.25	112.48	0.99				
Al-Mg-Mn	20:1	-3499.77	149.65	0.99				

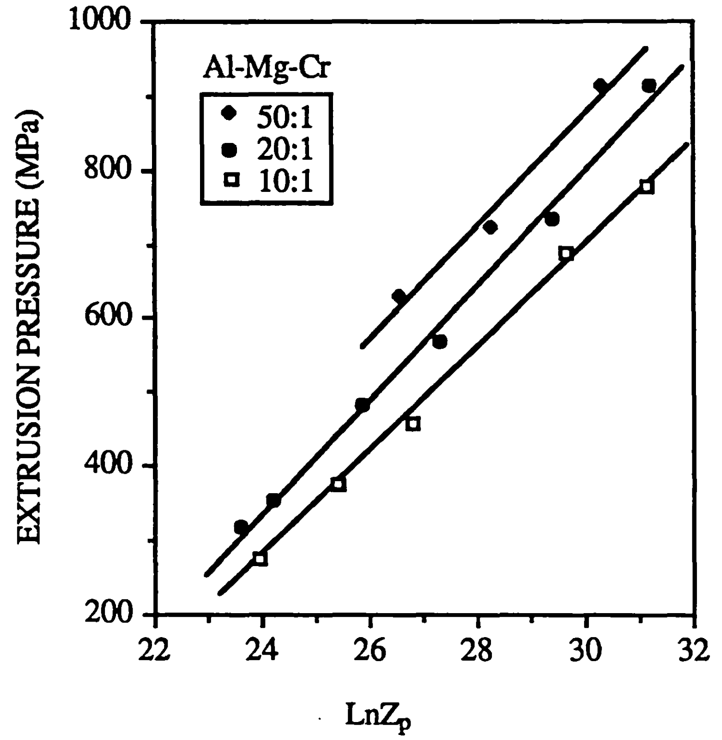

Figure 5.9. Variation of maximum extrusion pressure with temperature-compensated strain-rate.

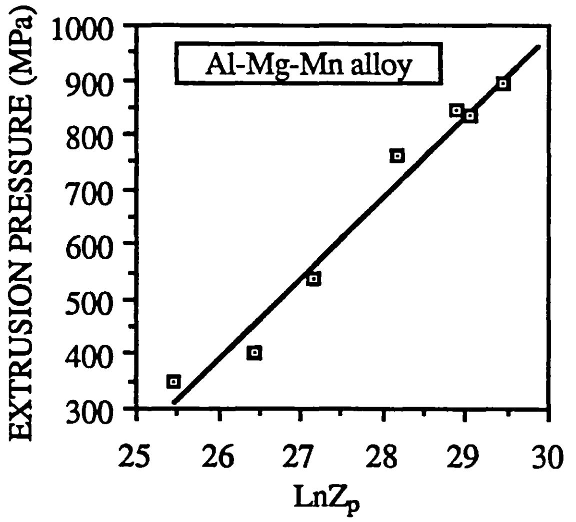

Figure 5.10. Variation of the extrusion pressure with lnZ$_p$

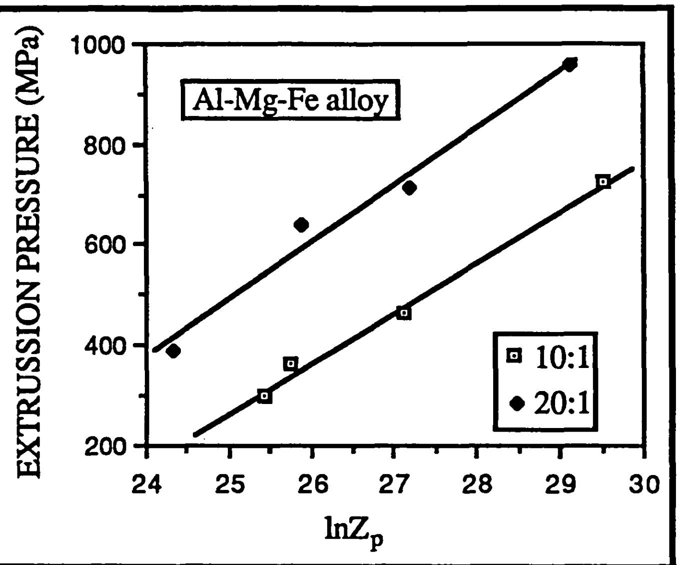

Figure 5.11. Variation of the extrusion pressure with $\ln Z_p$

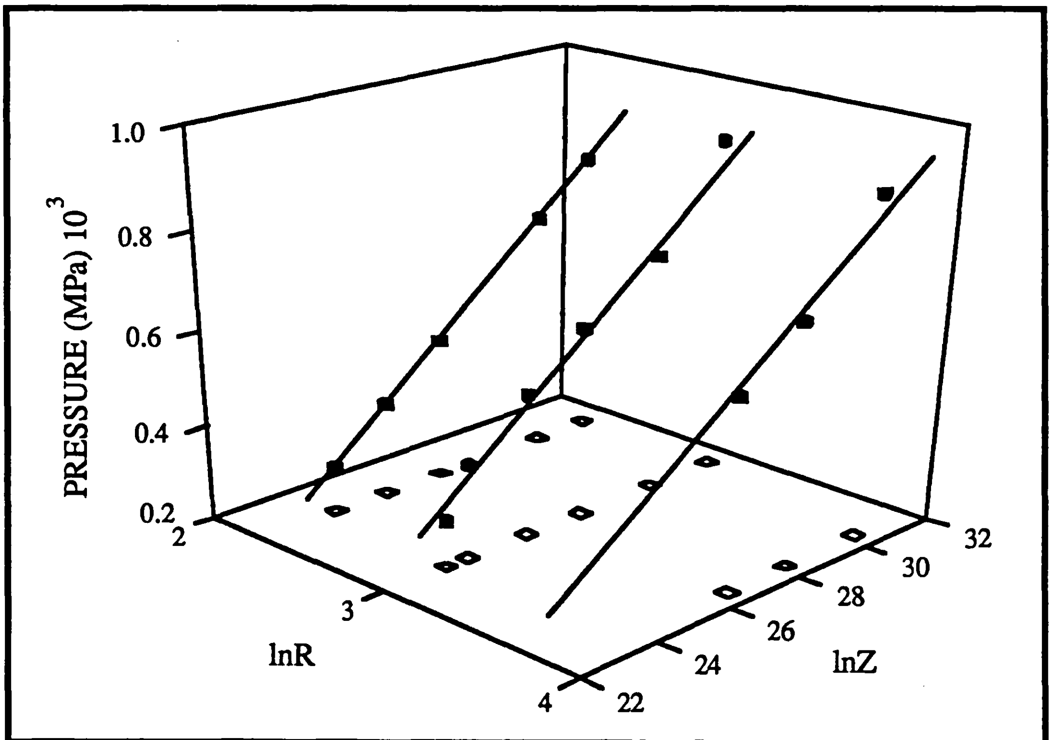

Figure 5.12. Three dimensional plot of the pressure-lnR-lnZ linear relationship fot the Al-Mg-Cr alloy.

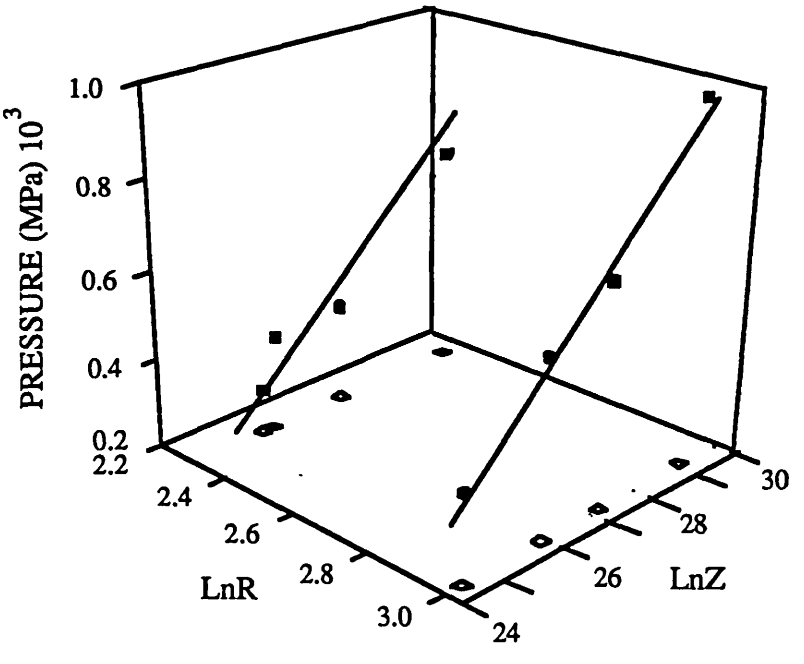

Figure 5.13. Three dimensional plot of the pressure-lnR-lnZ linear relationship for the Al-Mg-Fe alloy.

5.3. Microstructure Evolution

It has already been mentioned that the extrusion process is the most convenient route by which metal powder compacts are converted into 100% dense product. Sheppard and his co-workers (1983, a, b) have proven conclusively that the actual consolidation of the loose powder occurs during deformation.

In order to study the microstructural evolution and to observe the flow pattern of the billets, partial extrusions have been terminated at three different positions on the load displacement curve: before the peak pressure, at the peak and during the steady state, Figure 5.14 (a)-(c) illustrates typical partially extruded billets from the Al-Mg-Cr at 450°C. At the beginning of the extrusion the compact breaks due to the applied pressure and fills the container. This is the stage where the load increases non-linearly with ram displacement, see Figure 5.3. During this stage the air trapped among the powder particles escapes through the interconnecting porosity and the newly formed cracks until the billet attains 100% density, see Figure 5.14 (a). At this stage the powder particles are closely packed but have experienced minimal deformation. However, the attainment of full density does not necessarily mean attainment of maximum strength. Actually the back end of the billet is very brittle and quite often breaks during ejection from the container, as interparticle bonding has not occurred throughout the bulk of the billet. Subsequently, the pressure increases linearly up to the maximum value. Within this stage the extrusion starts without the deformation zone being established, see Figure 5.14 (b).

The deformation zone is generally initiated at maximum pressure and reaches a steady state region after the peak, see Figure 5.14 (c). The deformation zone, also termed the shear zone, has an elliptical shape extending from the interface between billet and container, at the rear of the billet, to the die mouth, see Figure 5.14 (d). The flow of the powder particles occurs from the sides to the centre of the billet where it is extruded through the die. The centre part of the billet moves forward more rapidly than the sides. As the side units enter the deformation zone the powder particles are first of all compressed and then pass diagonally with heavy shearing into the die. Hence, the central elements undergo minimum deformation purely by extensional flow of the powder particles corresponding to the extrusion ratio; while the layers near the surface undergo considerable shear deformation and are stretched out along the sides of the bar. When the powder particles first enter the deformation zone, they have little resistance to shear and therefore the intermetallic bonds formed during compaction, break easily.

These bonds, continuously, break and reweld until the material can shear along preferentially oriented planes, as in the extrusion of cast billets, and full strength is attained. During this stage, the oxide layer surrounding the powder particles ruptures, as will be shown below, forming oxide particles finely dispersed within the as-extruded microstructure. Fragmentation of the oxide layer permits metal/metal contact and thus improved interparticle bonding. The majority of the deformation energy input during extrusion is used up by the shearing of the powder particles and pressure sintering, thus building a coherent material.

Figure 5.15 (a)-(e) illustrates the steady state flow characteristics obtained from partially extruded billets after the peak pressure for the Al-Mg-Mn alloy, at different extrusion ratios from 10:1 to 50:1. It can be seen that the angle of deformation increases with increasing extrusion ratio while the shape of the shear zone remains elliptical independent of the extrusion ratio. The previously mentioned theory that the deformation zone is stable during steady state extrusion is supported by the Figure 5.15 (b_1) and (b_2), in which two partial extrusions were terminated during the steady state at different times.

It has already been noted that the microstructure of the final engineering product depends on the original microstructure and the thermomechanical process during which it is being developed. During the thermomechanical process the effects of both heating and pressure are complementary. In order to understand the microstructural evolution during extrusion, specimens for TEM study were extracted from various locations in partially extruded billets during the steady state, for all three different alloys. The consolidation characteristics are in principle similar for all three powder alloys. However, due to enormous differences in the as-atomized powder structure, an individual study of each alloy was deemed necessary.

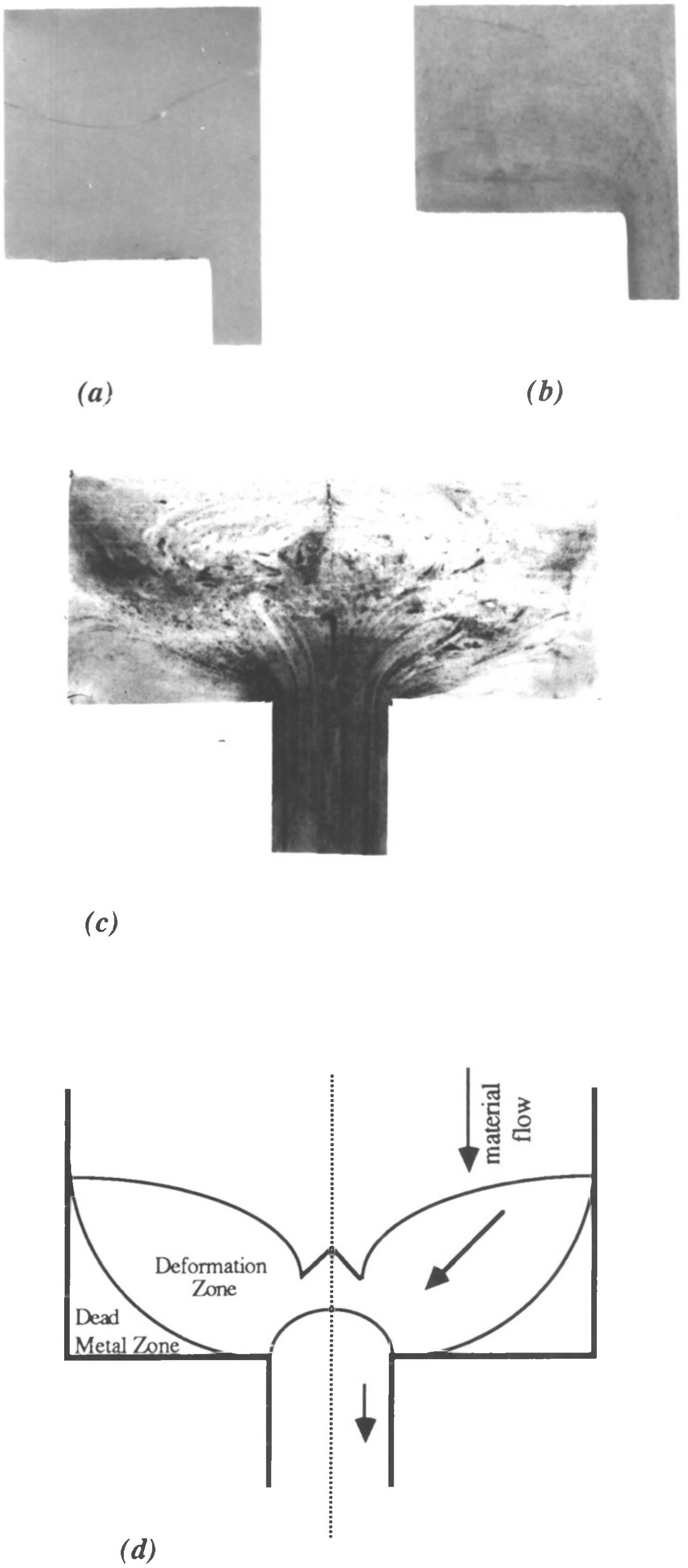

Figure 5.14. Partially extruded billets
(a) before the peak,
(b) on the peak,
(c) during the steady -state and
(d) schematic diagram

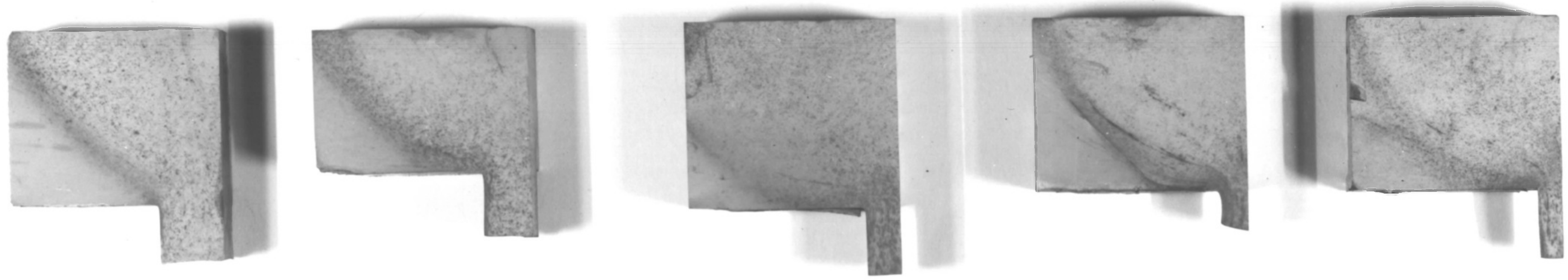

(a) 10:1

(b_1) 20:1

(c) 30:1

(d) 40:1

(e) 50:1

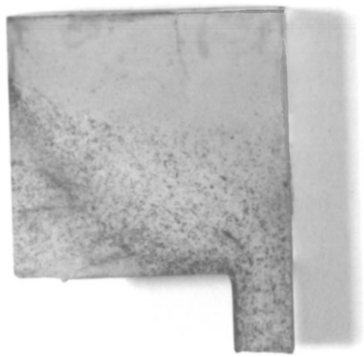

(b_2) 20:1

Figure 5.15. Steady flow pattern of partially extruded billets after the peak pressure of the Al-Mg-Mn alloy

5.3.1. Al-Mg-Cr alloy

The examination of the partial extrusions has allowed the building of a wrought structure from the powder to be evaluated. It is obvious that the microstructure of the dead metal zone is, indeed, the initial microstructure of the compact prior to deformation.

Figure 5.16 displays a partially extruded billet at 400°C and the microstructures corresponding to the indicated locations. The microstructure of the dead metal zone does not differ significantly from the back end of the billet, which is also similar to the as-atomized powder microstructure. This is to be expected, since the microstructure, at both the back end and dead metal zone of the partially extruded billet, reflects exclusively the influence that the induction heating exerts on the powder microstructure, because, at these positions, the powder particles have not been substantially deformed. A typical microstructure of the back end of the billet can be seen in Figure 5.16 (a). It is composed of tightly packed powder particles outlined by the oxide film surrounding them. In some instances the oxide layer has been ruptured (arrowed example), during the first stage of hot extrusion (compaction) in which the billet fills the container and attains approximately 100% density. Clearly, breaking up of the oxide films facilitates metal/metal contact and therefore interparticle bonding. The ease of identification of individual powder particles suggests that the final structure has not been built up yet, since, in the as-extruded microstructure, signs of individual particles are scarcely detectable and a substructure has been developed. Individual powder particles are composed of "dispersoids" evenly distributed within the matrix. The morphology of these dispersoids is also similar to that observed in the as-atomized powder. These dispersoids, see Figure 5.16 (b), are aggregates whose size can be directly related to the size of the powder particles. Larger aggregates were observed in larger powder particles and a size variation between 0.08 μm and 0.95 μm diameter was noted in different size particles.

The powder particles lose their identity when they enter the intense shear zone, in which consolidation occurs and the material attains its full strength. A typical microstructure of the shear zone is illustrated in Figure 5.16 (c) in which a substructure has developed and fine intermetallics or aggregates can be seen mainly at subgrain boundaries. Within the deformation zone the oxide film surrounding the powder particles has been frangmented due to heavy shearing. The broken fragments are redistributed during subsequent working. In the same way the largest aggregates appear to be sheared and redistributed as finer second phase particles within the softer aluminium matrix. Figure 5.16 (d) shows the fibrous microstructure upon exit from the die. Clearly the microstructure is heterogeneous [Figure 5.16 (e)], composed of coarse and fine bands being in intimate contact with each other, originating from coarse and fine powder particles respectively.

X-ray analysis was conducted on specimens extracted from the dead metal zone and shear zone near the die exit. It was found that the X-ray diffraction pattern of the dead metal zone was almost identical to pattern of the as-atomized powder. The detected reflections were attributed, apart from α-Al, to the $Al_{18}Mg_3Cr_2$, Al_3Mg_2, $Al_{13}Cr_2$ and the unidentified phase(s), suggesting that during induction heating (4 to 5 mins to reach 400°C from room temperature) phase transformations did not occur. On the other hand, in specimens extracted from the shear zone near the die exit, X-ray study showed that the unidentified reflections were weakened as well as the reflections arising from the $Al_{13}Cr_2$ and Al_3Mg_2 phase. This latter observation suggests that high temperature deformation aids the diffusion of the atoms in the solid solution, since the number of vacancies increases, and hence dissolution or transformation of the non-equilibrium, $Al_{13}Cr_2$ and Al_3Mg_2 phases occurs.

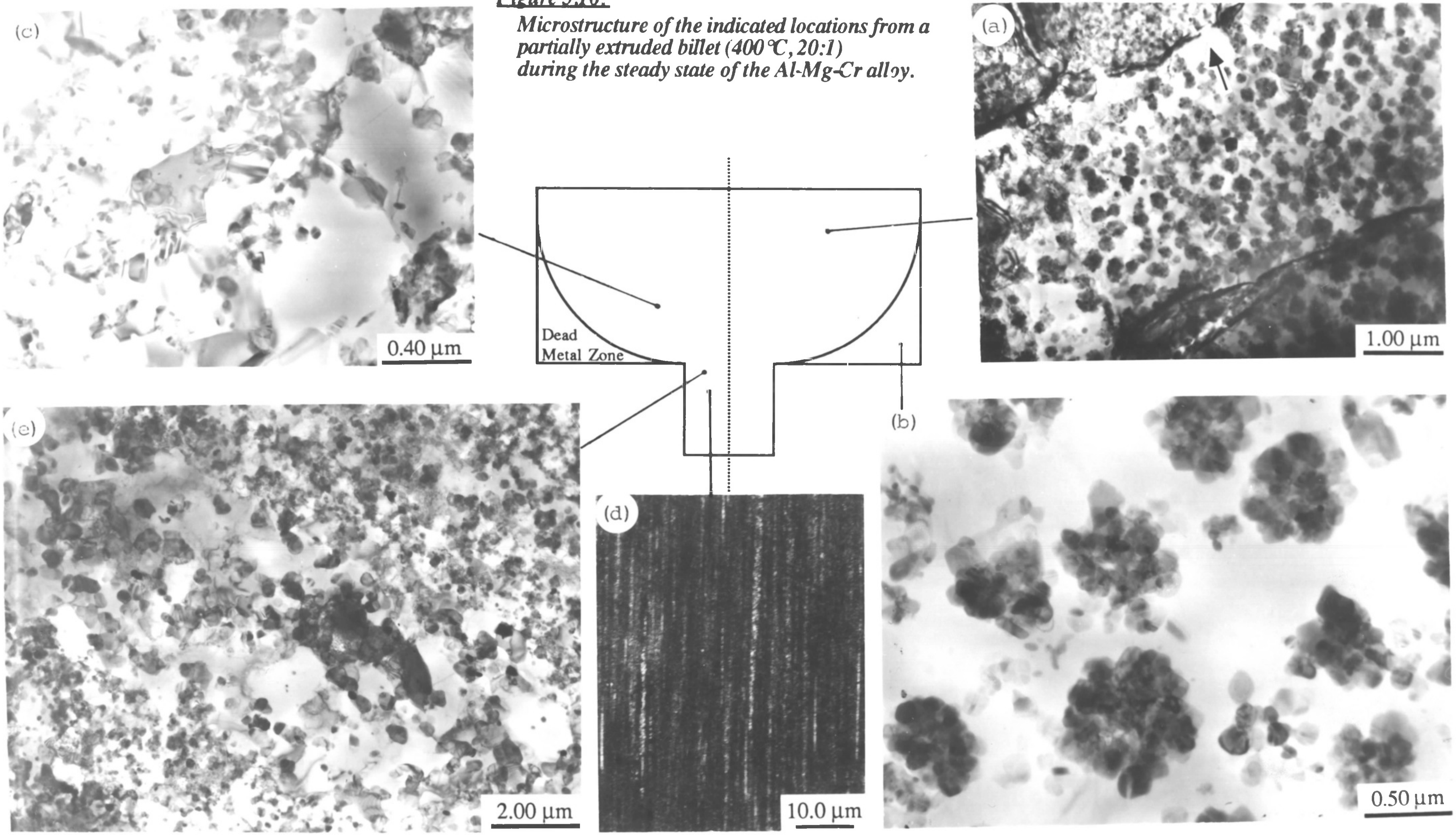

Figure 5.16.

Microstructure of the indicated locations from a partially extruded billet (400 °C, 20:1) during the steady state of the Al-Mg-Cr alloy.

5.3.2. Al-Mg-Mn alloy

The partially extruded billets from this alloy exhibit similar consolidation and flow behaviour to the other aluminium alloy powders, see Figure 5.15. The results, presented in this section, detailing the changes in structure during consolidation have been obtained from a partially extruded billet during the steady state at 400°C for an extrusion ratio of 20:1.

The shear zone outlines a dead metal zone in which the individual powder particles are relatively undeformed and interparticle boundaries unbroken. Typical microstructures of the dead metal zone are illustrated in Figure 5.17 (a)-(c). It is worthwhile to recall that three typical microstructures were observed in the as-atomized powder particles: 1) second phase particles surrounded by areas free of precipitates in coarse powders, 2) featureless regions within the medium to fine size powders and finally 3) cellular morphology decorated with fine intermetallic particles at the interfaces, in the majority of the powders. Figure 5.17 (a) shows that the structure of the coarser powder particles remains relatively unaffected by the rapid heat up to 400°C and the compression stresses during compaction. The icosahedral phase has retained its star shape while the matrix is free of precipitation. The original cellular structure has been transformed into regions of fine needle and plate precipitates while the fine intermetallics at the former intercellular regions have been coarsened, see Figure 5.17 (b). Finally, the partitionless solidification areas have been transformed into a matrix with a high volume fraction of fine needle precipitates as illustrated in Figure 5.17 (c). In this figure a boundary can clearly be seen between two powder particles, in which the particle (A) exhibits very fine plate precipitates at a region along the particle rim, corresponding to the featureless rim mentioned in Section §4.4.1; this also confirms that the featureless rim is solute rich. It is worth noting that at various positions within the back end of the billet no significant differences in microstructure were observed, as-expected, when compared to the dead metal zone; except from positions close to the deformation zone in which the oxide film has fractured, see arrowed example in Figure 5.17 (d).

X-ray analysis conducted on specimens extracted from the dead metal zone indicated that two phase could be detected: the icosahedral phase and $Al_{18}Mg_3Mn_2$, see Figure 5.18 (a). The X-ray results, summarised in Table 5.4 are in good agreement with the results of the heat treated powder indicating that in the dead metal zone the thermal history is the single most important factor.

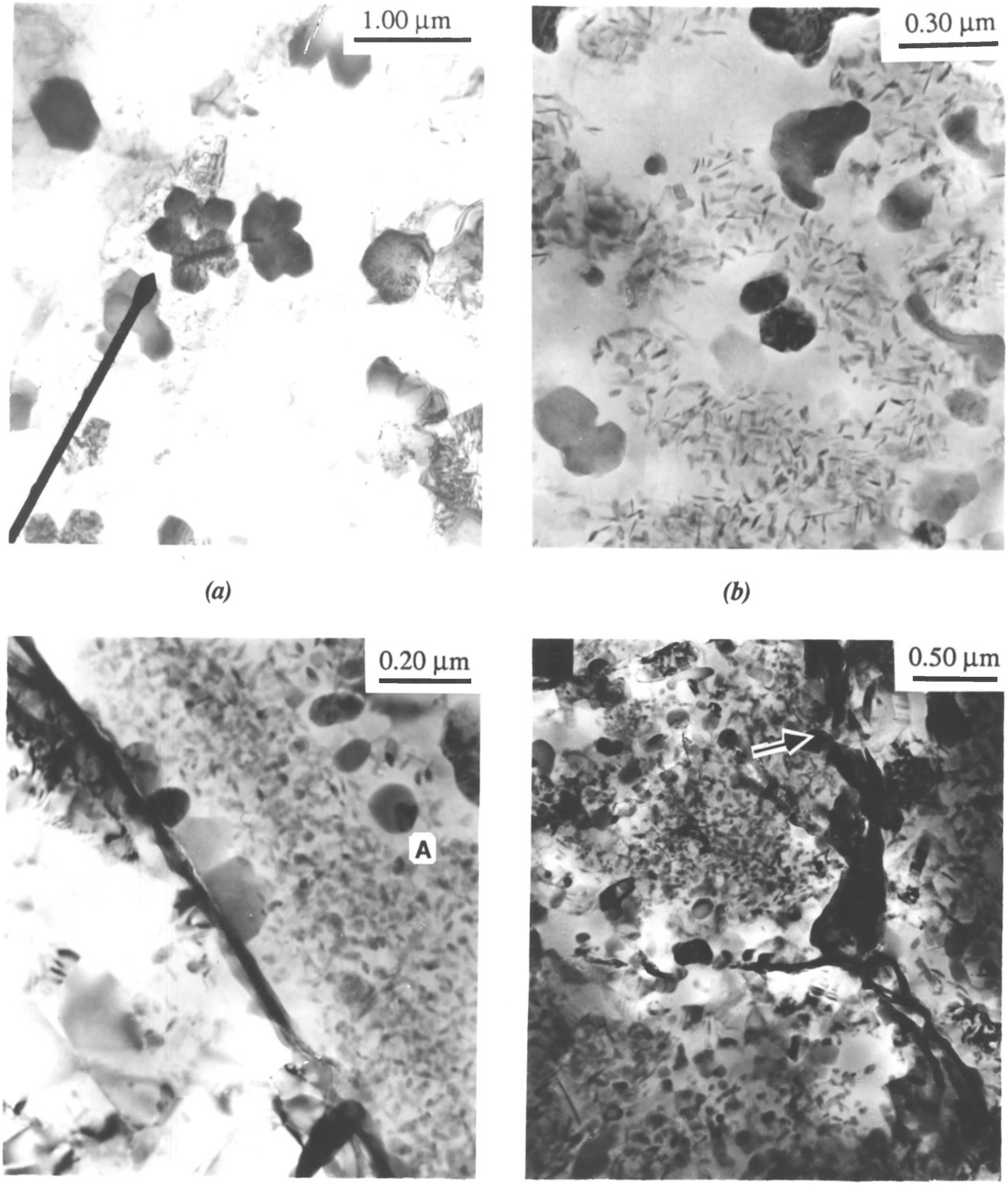

(a) (b)

(c) (d)

Figure 5.17. Structure from DMZ (a)-(c), and back end of the billet (d) of a partially extruded billet during the steady state of the Al-Mg-Mn alloy:

(a) coarser powder particle containing the icosahedral phase;

(b) finer powder particle with dual precipitate morphology;

(c) interparticle boundary and

(d) fractured oxide film at interparticle boundary.

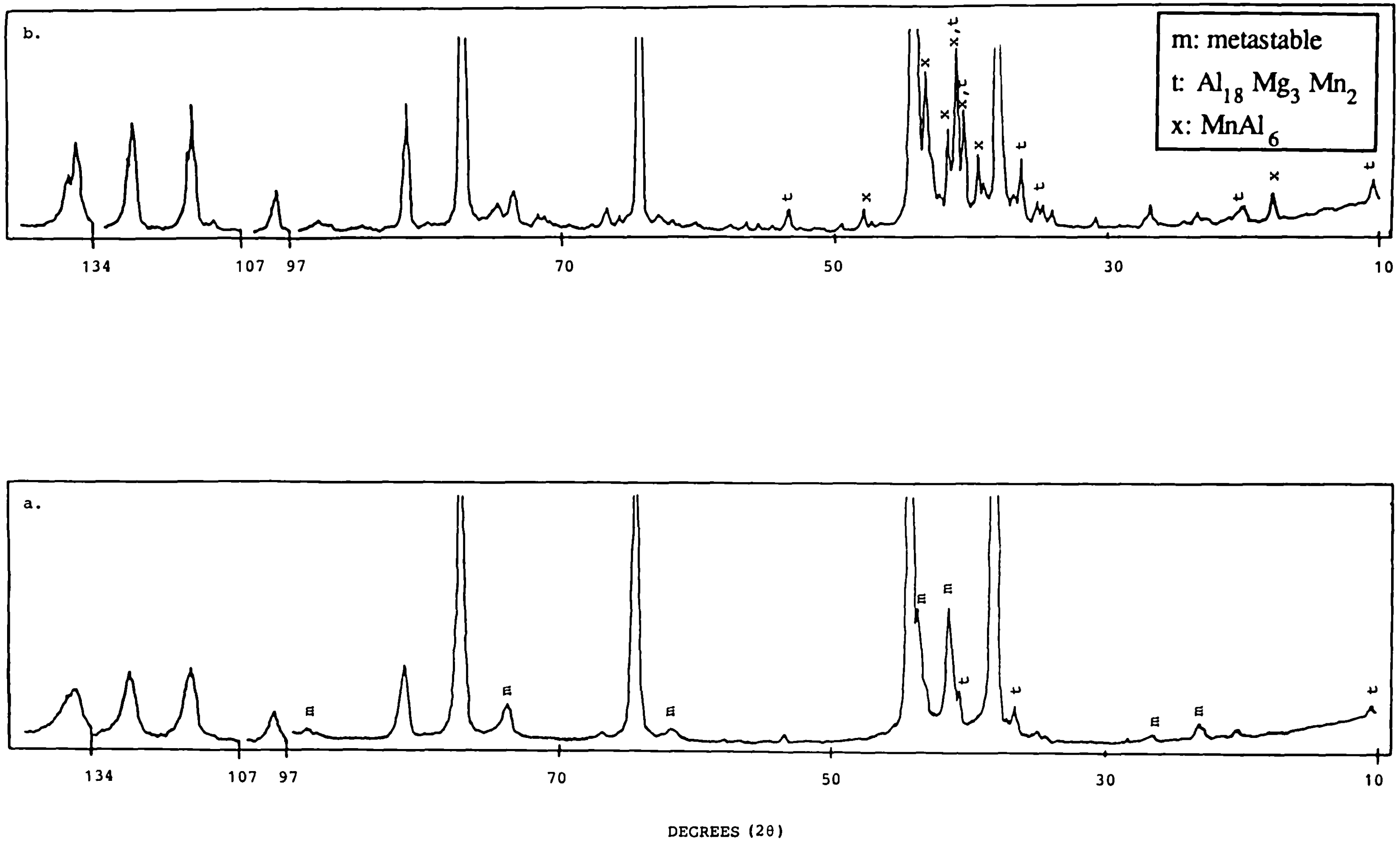

Figure 5.18. X-Ray diffraction patterns from:
(a) the dead metal zone and
(b) near the die exit
of a partially extruded billet of the Al-Mg-Mn alloy

Table 5.4. Summary of the X-Ray results for the Al-Mg-Mn alloy

Consolidated material	Al_3Mg_2	$Al_{18}Mg_3Mn_2$	Icosahedral	$MnAl_6$
400°C-450°C, DMZ[2]	ND[1]	medium	medium	ND
400°C-450°C, ext. [3]	ND	medium	ND	medium
500°C, ext.	ND	ND	ND	strong

ND[1]: not detected, DMZ[2]: dead metal zone, ext[3]: extrudate

Within the shear zone individual powder particles are not identifiable. The structure is composed of fine subgrains with globular and plate precipitates, see Figure 5.19 (a). The very fine precipitates, $Al_{18}Mg_3Mn_2$, affect the dislocation dynamics thus playing an important role in the subgrain formation, see Figure 5.19 (b). In some instances there is evidence of heterogeneity, within the deformation zone, with bands of differing structure. Figure 5.19 (c) shows a band containing second phase particles, identified by using electron diffraction patterns as the icosahedral phase {Figure 5.19 (d), originating from the original coarser powder. However, X-ray analysis on specimens extracted near the die exit of the partially extruded billet at 400°C, showed only $MnAl_6$ and $Al_{18}Mg_3Mn_2$, see Figure 5.18 (b), indicating that the icosahedral phase has been transformed into $MnAl_6$, which is in line with the results of heat treated powder. The isolated bands with nodules of the icosahedral phase would have been too few to be detected by the X-ray technique. Finally at higher processing temperatures (500°C) X-Ray analysis indicated only $MnAl_6$ precipitates in specimens extracted from the extrudate at the die exit.

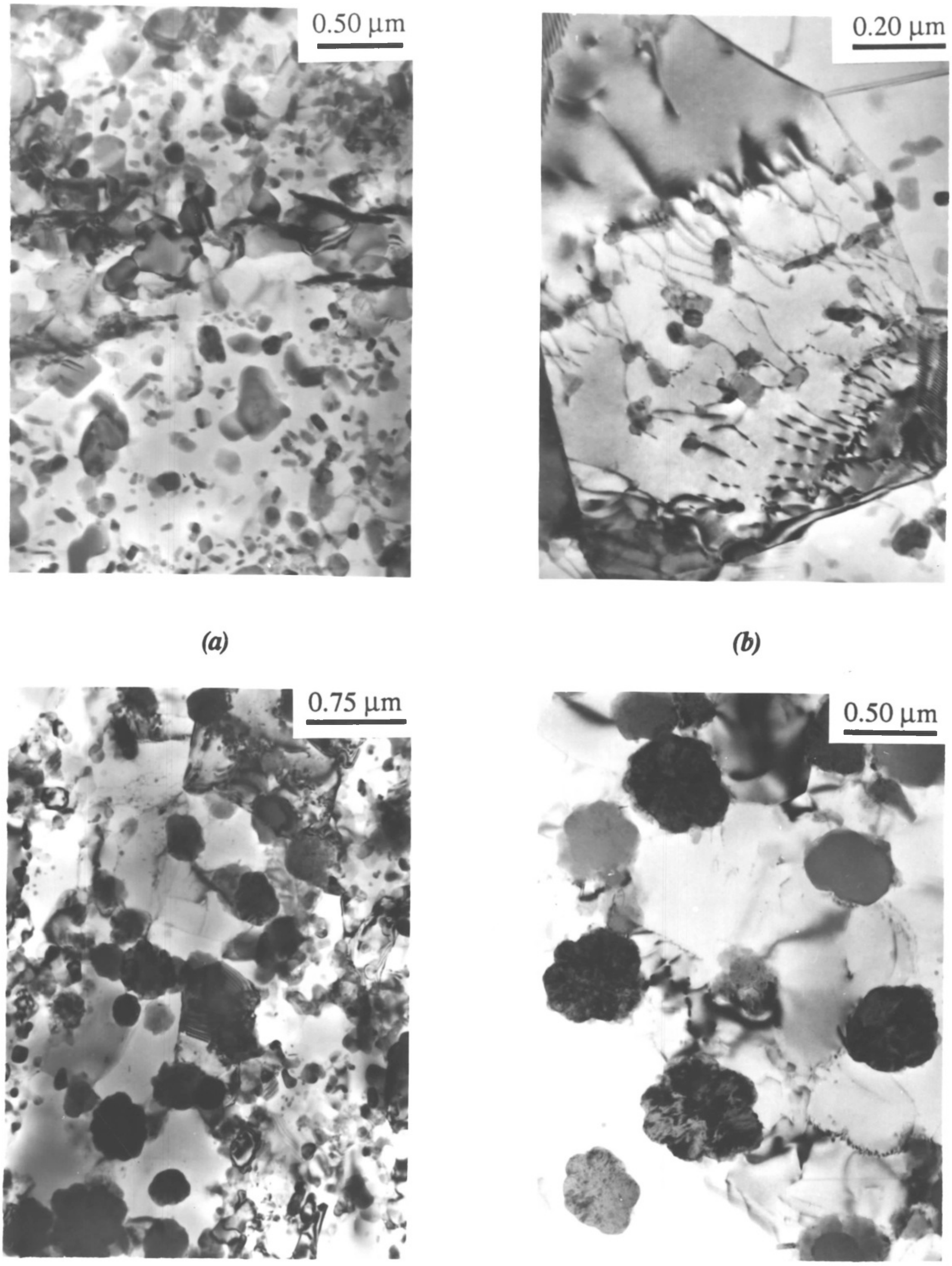

(a) (b)

(c) (d)

Figure 5.19. Microstructure within the deformation zone of the billet:

(a) typical fine grain precipitate microstructure,

(b) influence of small precipitates on dislocation structure,

(c) structural heterogeneity and

(d) precipitates with nodular morphology (icosahedral phase).

5.3.3. Al-Mg-Fe alloy

Figure 5.20 shows a schematic diagram of a partially extruded billet during the steady state at 400°C for an extrusion ratio of 20:1 together with micrographs from specimens extracted from the billet at the locations indicated. Rapid structural changes were observed during extrusion which can be attributed to combined heating and the applied stress.

The morphology of the microstructure of the dead metal zone of this alloy is similar to the other two alloys previously presented, being composed of tightly packed powder particles, that are clearly defined by the characteristic oxide film typical of all air atomized aluminium powders, see Figure 5.20 (a). The particles have undergone only sufficient plastic deformation to ensure that rearrangement produces a fully dense structure. The dead metal zone microstructure gives an indication of powder that has experienced rapid heating and a small amount of deformation. Nevertheless, transformations have occurred when compared to the batch heated powder suggesting that small degrees of deformation influence the rate of change because of enhanced atomic mobility and increases in billet temperature. However, the rapid billet heating (5-8 mins) have not allowed time for homogeneisation of the microstructure and the dead metal zone still exhibits the major inhomogeneities of the powder, (see Section §4.5.1). Adjacent particles with completely different structure were often observed, as shown in Figure 5.20 (a): particle A, has coarse dispersoids; particle B, a high volume fraction of needle shaped precipitates; and particle C a coarse structure and a low volume fraction of precipitates. Moreover, microstructural variations were also observed on a smaller scale, even within the same powder particle. For example coarse and fine dispersoids can be discerned in two different zones, D1 and D2, which do not exhibit a clearly defined interface.

At positions midway from the rear end of the billet to the shear band, the powder particles are elongated, see Figure 5.20 (b). The individual powder particles are still identifiable but the oxide film at the particle interface has ruptured close to the shear zone {indicated in Figure 5.20 (b)}. The majority of needle shaped precipitates can be seen to have been aligned in the flow direction. A substructure of subgrains of low misorientation is being developed, Figure 5.20 (c), suggesting that the alloy deforms by dynamic recovery. However, despite the increasing strain towards the shear band it has not been sufficient to align all the second phase particles along the extrusion direction. Within the deformation zone the oxide layer has been fractured forming individual oxide particles, which are not always easily distinguishable from the precipitates, as in Figure

5.20 (d). The subgrains appear as a banded structure. Obviously, inhomogeneity has not been alleviated, as can also be seen in Figure 5.20 (d), where a band containing coarse dispersoids is adjacent to one containing a high volume fraction of the needle shape precipitates. X-Ray analysis has revealed three phases within the main bulk of the billet, α-Al, Fe_4Al_{13} and $(Fe,Mn)Al_6$. However, in specimens taken from the shear band, the reflections arising from these phases are sharper indicating that during the plastic deformation, heat has encouraged coarsening of the existing precipitates and complete transformation to these phases.

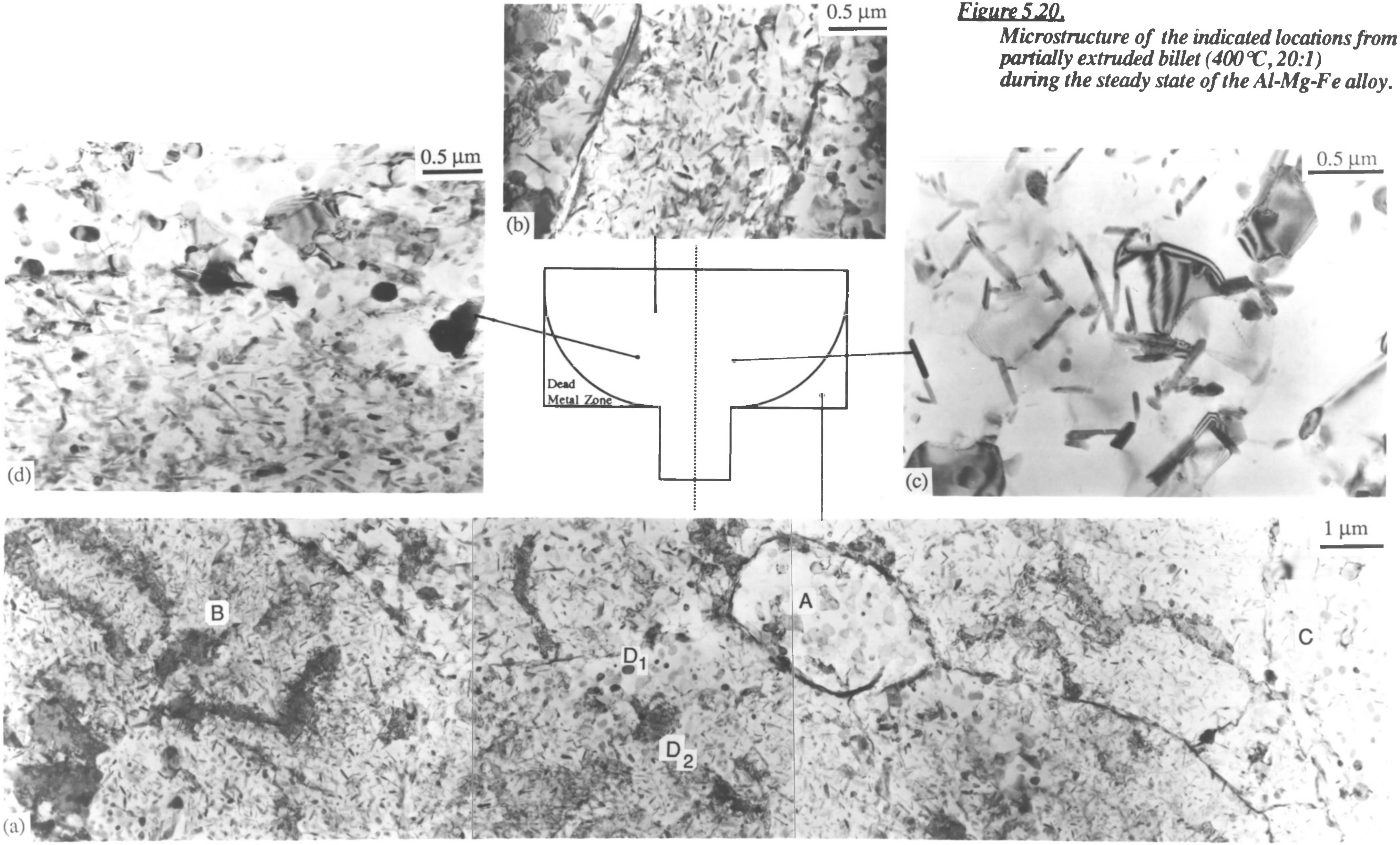

<u>Figure 5.20.</u>
Microstructure of the indicated locations from a partially extruded billet (400 °C, 20:1) during the steady state of the Al-Mg-Fe alloy.

5.4. Summary

Fabrication of the metal powders has been achieved through the extrusion process which combines both consolidation and hot working in a single operation. Cold compaction has been achieved in a tapered die, using a double action technique, resulting in billets having sufficient strength and density to facilitate handling and induction heating. The developed green strength is attributed to mechanical interlocking and cold welding of powder particles.

The Al-Mg-Cr alloy was found to compact relatively easier than the other two alloys, because it is coarser and contains a greater proportion of irregularly shaped powder particles. In contrast the Al-Mg-Mn alloy is the most heavily alloyed, the finest, containing the greatest proportion of spherical powder particles and the hardest, exhibiting less plasticity and poor compaction qualities.

The extrusion process characteristics are similar for all three powder alloys. The peak pressure requirements decrease with increasing temperature. The extrusion limits of these alloys lie between the range of the Al-7Mg powder and cast alloy, with the Al-Mg-Cr displaying the widest range and the Al-Mg-Fe the narrowest. In general the chromium bearing alloy exhibited the best hot working characteristics followed by the manganese one and, lastly, the Al-Mg-Fe alloy.

The extrusion data available indicated that the powder compacts conform to the extrusion behaviour of cast alloys and relationships between pressure, extrusion ratio and temperature compensated strain rate have been established.

The extrusion pressure - temperature relationship has the form: $P = c \exp(-kT)$, indicating that the pressure requirements decrease considerably with increasing temperature. Moreover the rate of the peak pressure reduction increases with increasing extrusion ratio (constant k of the above equation decreases with increasing extrusion ratio, Table 5.1). At lower extrusion temperatures, a peak in the load displacement curve for all three materials accounted for a significant proportion of the total pressure requirements.

Among the three alloys the Fe bearing one requires higher extrusion pressures due to the higher volume fraction of needle and spherical shaped precipitates distributed within the aluminium matrix. The pressure requirements for the Al-Mg-Mn alloy decrease considerably with increasing temperature, suggesting that the coarsening of the structure at temperatures greater than 450°C leads to a substantial decrease in the maximum extrusion pressure. Similar behaviour has been noted for the peak increment of the maximum extrusion pressure for the three alloys.

The extrusion ratio is also related to the peak pressure by a relationship of the form: $P=A+B\ln R$. The first term of this equation represents the redundant work incorporating the work for pressure sintering, whilst the second term represents the work of homogeneous deformation. With increasing temperature the ratio A/B decreases indicating that the deformation is more efficient at higher temperatures.

The best representation of the influence of the extrusion parameters on the peak pressure is described by the equation:

$$P = A^* + B^* \ln R + C^* \ln Z$$

The final microstructure is developed during the extrusion process. Consolidation occurs when the material passes through the intense shear zone. The oxide film breaks forming oxide particles, whilst the individual powder particles lose their identity the substructure is being built up and the material attains its full strength. Deformation encourages phase transformations to occur. The resultant microstructure is fibrous composed of a mixture of bands originating from different powder particles.

Extrudate Structure

and

Properties

Chapter 6. Extrudate structure and properties

6.1. Introduction

The overall objective of the present project was the production of new engineering materials with enhanced mechanical properties in order to comply with the requirements imposed by various industrial applications. Initially, an assessment of the starting material characteristics has been performed followed by a detailed investigation in the parameters that affect the fabrication process. The final step of the present work is to study the mechanical properties of the materials as well as the optimisation of the fabrication route that will give a high performance product. Various mechanical properties of the produced alloys have been evaluated by means of hardness and tensile testing (both regular and notched specimens). Assessment of the results has been performed through the knowledge gained previously from the study of the powder characteristics and the thermomechanical extrusion process.

Since the mechanical properties of metals and alloys depend upon the quality of their microstructure, they can be quite rigorously related to size, shape and dispersion of the second phase particles, as well as to the size of grains/subgrains of the aluminium matrix. These qualities are also dependent on the alloy chemical composition and the parameters of the production route. A quantitative study has been carried out by Hall (1951), Petch, and Armstrong (1969) and the relationship between relating the *yield stress* and the *grain diameter* has been derived.

$$\sigma = \sigma_0 + k D^{-1/2} \quad \text{..} \quad (6.1)$$

where σ: yield stress, D: grain diameter and σ_0, k: constants

Cottrell (1958) has also developed a theory explaining that the *tensile strength* of polycrystalline materials usually exhibits the same form of dependence on grain size as the yield stress. More recently Hockett and McQueen (1970) have shown that for aluminium alloys in the presence of a *hot-worked substructure* the room temperature yield strength is given by a relationship of the form:

$$\sigma = \sigma_0 + k\,d^{-1} \quad \text{...} \quad (6.2)$$

where σ: yield stress, d: sub-grain diameter

The value of σ_0 represents the friction stress on a single dislocation and depends on the various hardening mechanisms. A large value of σ_0, such as for *precipitation and dispersion strengthened alloys*, means that the strengthening efffect of grain/subgrain boundaries plays a much less significant role. The next constant, k, is related to the stress concentration at the grain boundary resulting from a dislocation pile-up, since the propagation of slip from one grain to an undeformed neighbor is associated with it. The value of k is somewhat smaller for grains than for subgrains {Tompson (1977)}.

Hence, in polycrystalline materials, grain refinement is well established as a method of improving mechanical properties, even if this strengthening is rather weak in aluminum alloys, and there are valid criticisms of the particular model. Nevertheless, the general validity of equations '6.1' and '6.2' has been verified experimentally for many alloys. Consequently, the refinement in grain structure that can be achieved through the powder metallurgy route should offer improvements in strength in comparison with conventional ingot metallurgy products.

One method of relating the influence of the processing parameters to the developed microstructure is illuminated by the relationship between subgrain size and temperature compensated strain rate. The mean subgrain size diameter, d, has been established {McQueen and Jonas (1975)} to be a function of the natural logarithm of the temperature compensated strain rate, and a linear relationship is applicable.

$$d^{-1} = A + B \ln Z \quad \text{.....................................} \quad (6.3)$$

Accordingly, the higher the temperature of deformation and the lower the strain rate the larger are the subgrains formed.

Hence, a relationship between the strength and processing parameters can easily be derived by combining the equations '6.2' and '6.3'.

$$\sigma = C + K \ln Z \quad \text{....................................} \quad (6.4)$$

The alloys of the present work are dispersion strengthened ones and the strengthening mechanisms are attributed to effective pinning of dislocations by a fine dispersion of intermetallic particles. If the second phase particles are sheared, the associated strengthening effect depends on the intrinsic properties of the particles. If they are looped or bypassed, the associated strengthening effect is only dependent on the particle size and spacing, and is independent of intrinsic particle properties. Thus, effective strengthening is achieved when a considerable volume fraction of fine and hard intermetallics are distributed uniformly within the matrix and are relatively stable at moderate temperatures.

It is therefore obvious that the mechanical properties depend on the processing parameters and especially on the temperature. Towards this end, a presentation of the structure of each alloy composition is deemed necessary followed by a detailed account of its mechanical properties. Finally the varying microstructural features among the three alloys will be highlighted and emphasis will be placed on the parameters that influence the final properties. The micrographs presented below are representative of the major proportion of the structures observed from specimens extracted from longitudinal sections.

6.2. Structure and properties of the Al-Mg-Cr alloy

The micrographs obtained from the as-extruded material revealed a fibrous structure over the complete cross section of the extrudates and this type of microstructure was observed for all extrusion temperatures and ratios. An example, representative of the as-extruded microstructure, has already been given in Section §5.3.1. [Figure 5.16 (e)], in which coarse and fine bands can be discerned.

As has already been mentioned the structure varies according to the control exercised during processing, because the processing parameters, such as extrusion ratio, heating time and temperature affect the precipitation and coarsening kinetics of the material. A typical microstructure of an extrudate processed at low temperature (400°C, 20:1, $\ln Z=29.38$) is illustrated in Figure 6.1 (a), in which either discrete precipitates or aggregates (formed during atomization) can be readily distinguished at the subgrain boundaries. Evidence of the original powder particles has not been observed indicating that during plastic deformation interparticle bonding has occurred, the oxide layer has been fragmented due to the heavy shear, and the loose powder particles have been transformed into a fully dense and coherent product. The deformation is controlled by dynamic recovery, leading to a substructure of subgrains of low misorientation. The second phase particles have been very effective as obstacles to dislocation movement assisting in the formation and stabilization of the substructure. The structure coarsens progressively as the temperature of the extrusion increases (decreasing Z). Figure 6.1 (b) is from an extrudate processed at high temperature (575°C, 20:1, Z=23.58). In this figure the precipitates are coarser, situated within the aluminium matrix and on subgrain boundaries, while aggregates cannot be discerned, indicating that these have been transformed to individual particles under the combined effect of elevated temperature and deformation. Hence, it is obvious that the substructure depends on the process and the subgrain size can be described in terms of the variation of the temperature or the temperature compensated strain rate. The higher the temperature of deformation, the lower the temperature compensated strain rate, the larger are the subgrains formed.

However, due to the short processing times (the extrusion process including induction heating takes less than 8 min) the final size of the subgrains and the precipitates depends largely on the as-atomized powder microstructure. A good example is illustrated in Figure 6.2 (a) and 6.2 (b) in which two types of bands can be distinguished, one fine and one coarse within the same extrudate processed at 450°C, 10:1 (Z=26.80). In the fine band the size of the aggregates is less than 0.2μm diameter while in the coarse band they vary from 0.25μm to 0.50μm. Furthermore, the variation in powder particle size, results in bands with different size subgrains and precipitates. Fine bands with fine dispersoids and small subgrains originate from finer powder particles, for example smaller powder particles less than 6μm diameter are composed of aggregates less than 0.18 μm diameter, which is in agreement with the size of the aggregates (0.20μm) measured in the fine band of Figure 6.2 (a). Figure 6.2 (c) shows a very fine band with aggregates less than 0.08 μm, presumably originating from the finest powder particles.

Clearly, the as-extruded microstructure is heterogeneous and for that reason any attempt to derive a relationship between the subgrain size and the processing parameters has been unsuccessful. Moreover, the subgrain size is restricted by the spacing of the dispersoids and oxide particles. The continuous oxide layer surrounding the powders has been disrupted within the shear zone and is distributed as isolated particles. The oxide particles were not visible under all the processing conditions indicating that the oxide forms very fine particles which are not easily distinguishable from the dispersoids. The volume fraction of the oxides depends on the thickness of the oxide film and surface area of the powder particles; the finer the powder the higher the total oxide content, and the higher the volume fraction of oxide particles. Tan (1984)

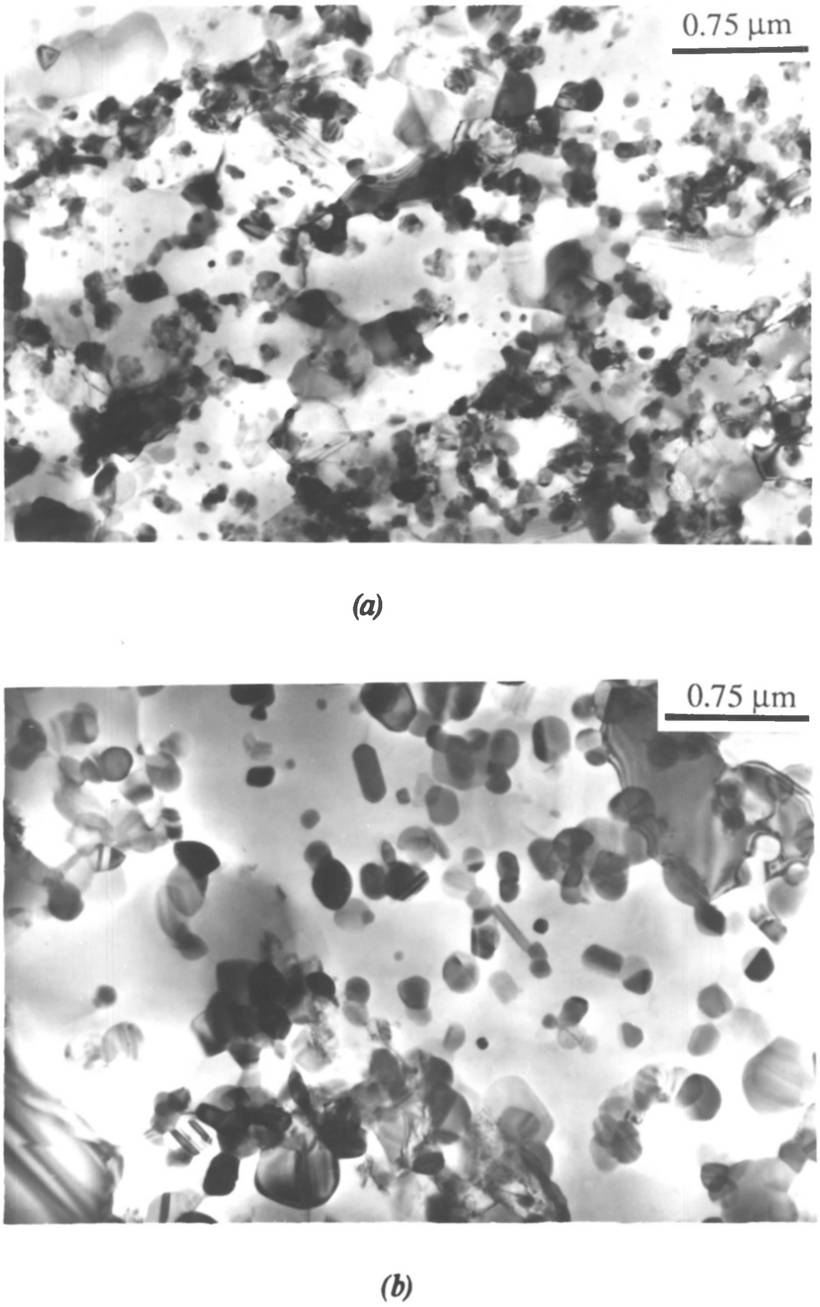

Figure 6.1. Extrudate microstructures of the Al-Mg-Cr alloy:
(a) 400 ℃, 20:1, lnZ=29.13 and
(b) 575 ℃, 20:1, lnZ=23.58.

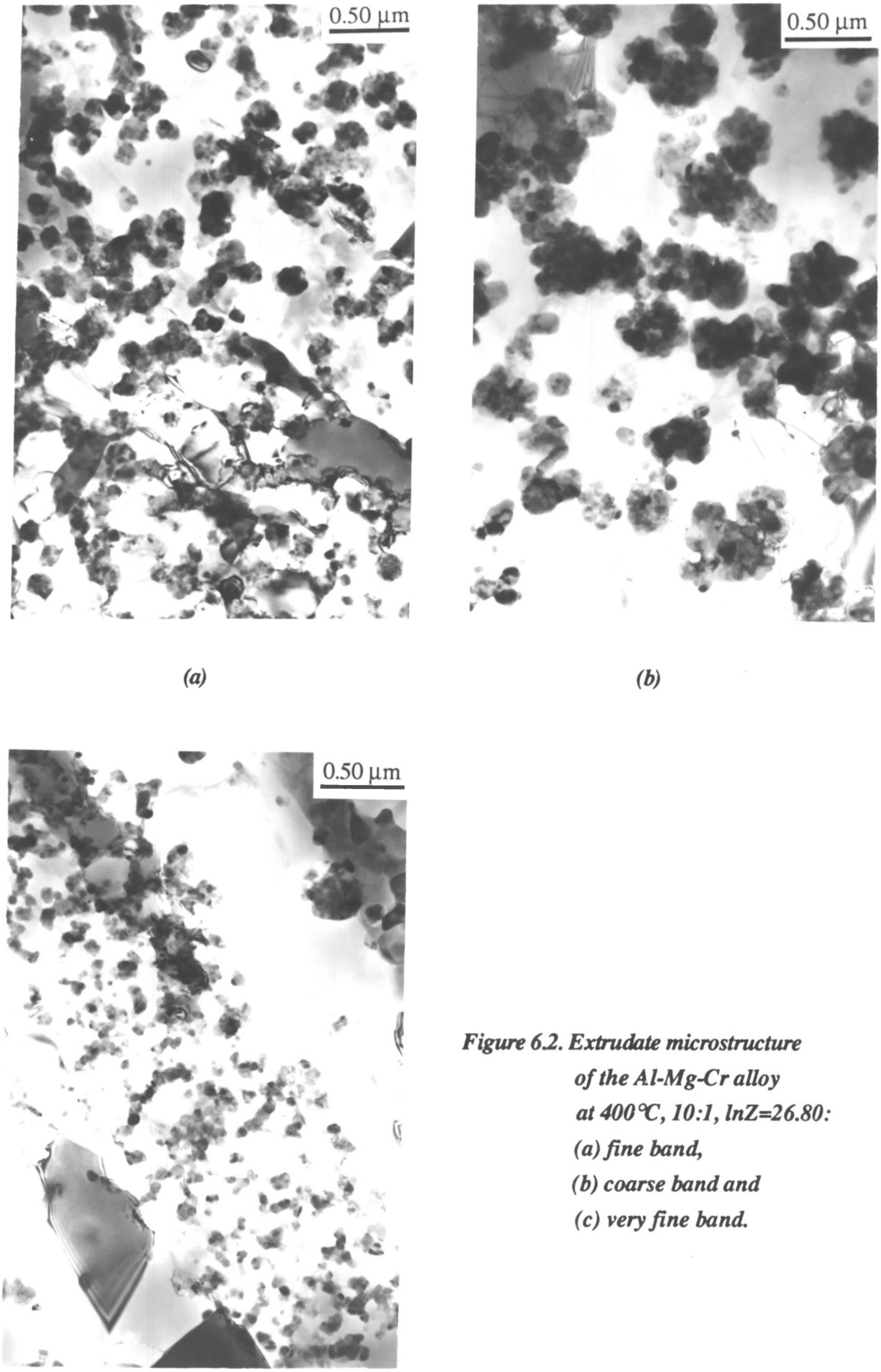

(a)

(b)

(c)

Figure 6.2. Extrudate microstructure of the Al-Mg-Cr alloy at 400°C, 10:1, lnZ=26.80:
(a) fine band,
(b) coarse band and
(c) very fine band.

has reported that in an Al-10%Mg powder alloy with a similar size distribution the oxide particles form stringers aligned in the extrusion direction. This is because the oxide concentration in the Al-%10Mg was more than twice the concentration in the Al-Mg-Cr alloy of the present work, thus the oxide film is thicker forming larger particles and therefore the oxide stringers are discernible. Several effects have been attributed to the oxide particles due to the fragmentation of the oxide film. Easterling and Thölen (1973) showed that they can reduce the theoretical strength of the 100% dense material. This reduction is attributed to stress concentrations at the interparticle boundaries, as Strömgen et al (1973) have also suggested. However, Sheppard and his co-workers {Sheppard and Chare (1972); Chare and Sheppard (1973)} have shown that when hot working follows cold compaction and the mean strain exceeds about 2, the second phase particles, being insoluble in the matrix, increase the strength of the final engineering product.

In order to identify the dispersoids, X-Ray studies were performed and the results, presented in Table 6.1, indicate that apart from α-Al matrix the phases detected in the extrudates are the unidentified phase/phases, and the equilibrium $Al_{18}Mg_3Cr_2$, Al_3Mg_2 and Cr_2Al_{13}. The main difference between the X-ray diffraction patterns of the as-atomized powder and the as-extruded material is in the intensity of the peaks of the latter two compounds, which is considerably lower in the as-extruded material. The conclusion can therefore be drawn that during the thermomechanical process a considerable volume fraction of the Al_3Mg_2 and Cr_2Al_{13} phases either transform or dissolve. Transformation of Al_3Mg_2 into $Al_{18}Mg_3(Cr, Mn)_2$ has already been reported previously to occur in the Al-Mg-Mn alloy of the present work at temperatures greater than 400°C. Such a transformation increases the volume fraction of the $Al_{18}Mg_3Cr_2$ phase, and therefore the intensity of the reflections. However, the volume fraction of the Al_3Mg_2 phase in the as-atomized powder does not appear to be significant enough (the intensity of its reflections is very weak) in comparison with the $Al_{18}Mg_3Cr_2$ phase and it is highly likely that such transformation would not considerably increase the intensity of the $Al_{18}Mg_3Cr_2$ phase reflections.

The main characteristics that determine the microstructure and thus the properties of the dispersion strengthened aluminium alloys prepared by rapid solidification arise from the size distribution of the powder particles and the quality of the 'interparticle bonding' (efficiency of the consolidation process). The size distribution of the metal powders and the resultant microstructure has been extensively discussed and it is well established that the size of the intermetallic particles that affect the strength of the material varies with the size of the powder particles. Large second phase particles are considered detrimental to ductility and toughness. The next dominating characteristic, the 'interparticle bonding', depends exclusively upon the thermomechanical process.

Table 6.1. Summary of the X-Ray results for the Al-Mg-Cr alloy

Extrudates	Unidentified peaks	$Al_{18}Mg_3Cr_2$ (ASTM 29-18)	Al_3Mg_2 (ASTM29-48)	$Al_{13}Cr_2$ (ASTM 29-14)
300°C 10:1	weak	strong	very weak	very weak
450°C 10:1	weak	strong	very weak	very weak
450°C 20:1	weak	strong	very weak	very weak
575°C 20:1	weak	strong	very weak	very weak

The dependence of mechanical properties of the as-extruded material has been assessed over the whole range of processing conditions. Since the temperature exerts the greatest influence on the as-extruded microstructure, the relationship between extrusion temperature and mechanical properties, i.e. hardness and room temperature tensile properties, will be presented initially.

In general, hardness is a measure of the resistance of the material to plastic deformation. The hardness test is very useful because it is simple, quick and gives an indication of the room temperature mechanical properties of the material. Figure 6.3 illustrates the variation of hardness with billet temperature for three different extrusion ratios low, medium and high, 10:1, 30:1 and 50:1 respectively, which are representative within the range of acceptable extrudates. The results show an unequivocal decrease in hardness with increasing temperature, which is consistent with the increase in the subgrain size, and coarsening of the dispersoids observed at higher temperatures.

The tensile properties exhibit similar behaviour to hardness. A gradual deterioration in 0.2% proof stress and ultimate tensile strength (UTS) with increasing temperature, as shown in Figure 6.4, has been observed over the three different extrusion ratios studied. This behaviour is also attributed to coarsening of the sub-structure and thus the ease of dislocation motion. The ductility of this alloy, expressed by the elongation (%) to fracture, does not exhibit any consistent behaviour (see Figure 6.4) and consequently apart from a general tendency to increase with temperature, any other firm conclusions are difficult to establish. Clearly, the ductility is very poor, although better results were expected, since binary R/S Al-7%Mg, 10% and

15% Mg alloys, studied by Tan (1984) exhibit ductility values higher than 10%. The main factors that affect ductility are firstly the consolidation efficiency, i.e. how well the powder particles are bonded and secondly the distribution of second phase particles. The Al-Mg-Cr alloy of the present work is heavily alloyed and the volume fraction of the dispersoids maybe too high for satisfactory ductility. It has also been shown that the structure is heterogeneous being composed of coarse and fine bands, which contain coarse and fine dispersoids respectively, aligned in the extrusion direction. The coarse particles nucleate voids more easily, in comparison with smaller dispersoids. Moreover, the particles that compose the aggregates nucleate voids that coalesce more rapidly.

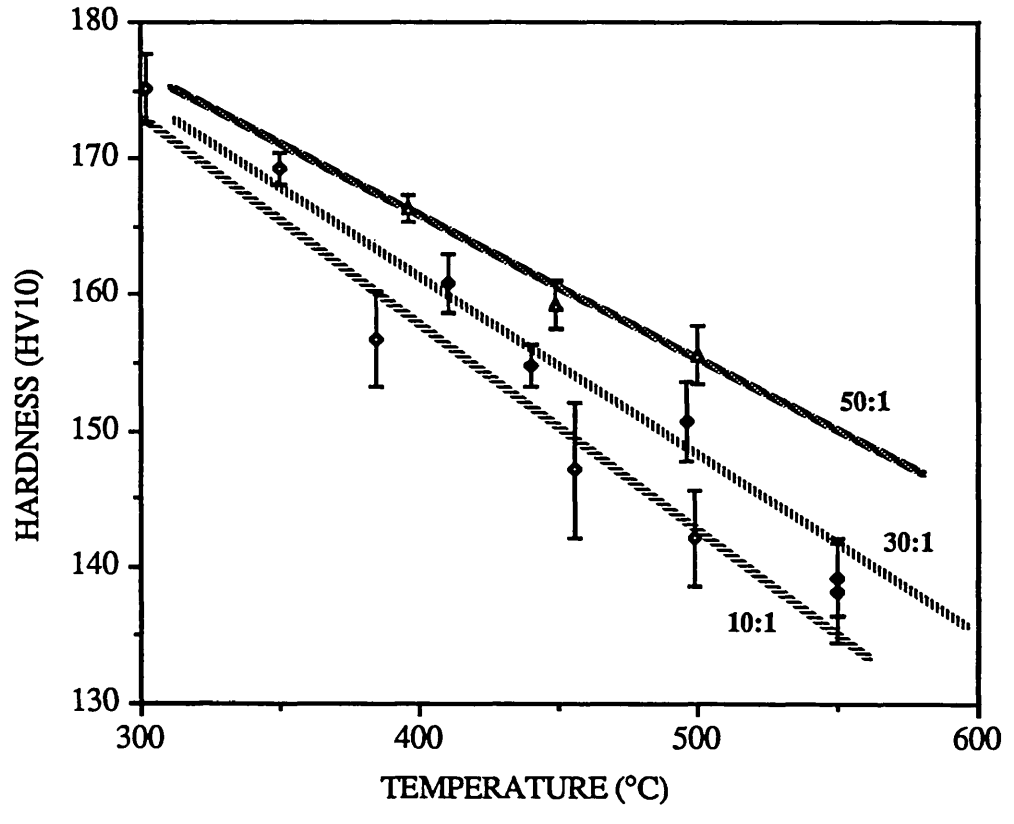

Figure 6.3. Effect of billet temperature on the hardness of the Al-Mg-Cr alloy, for three extrusion ratios

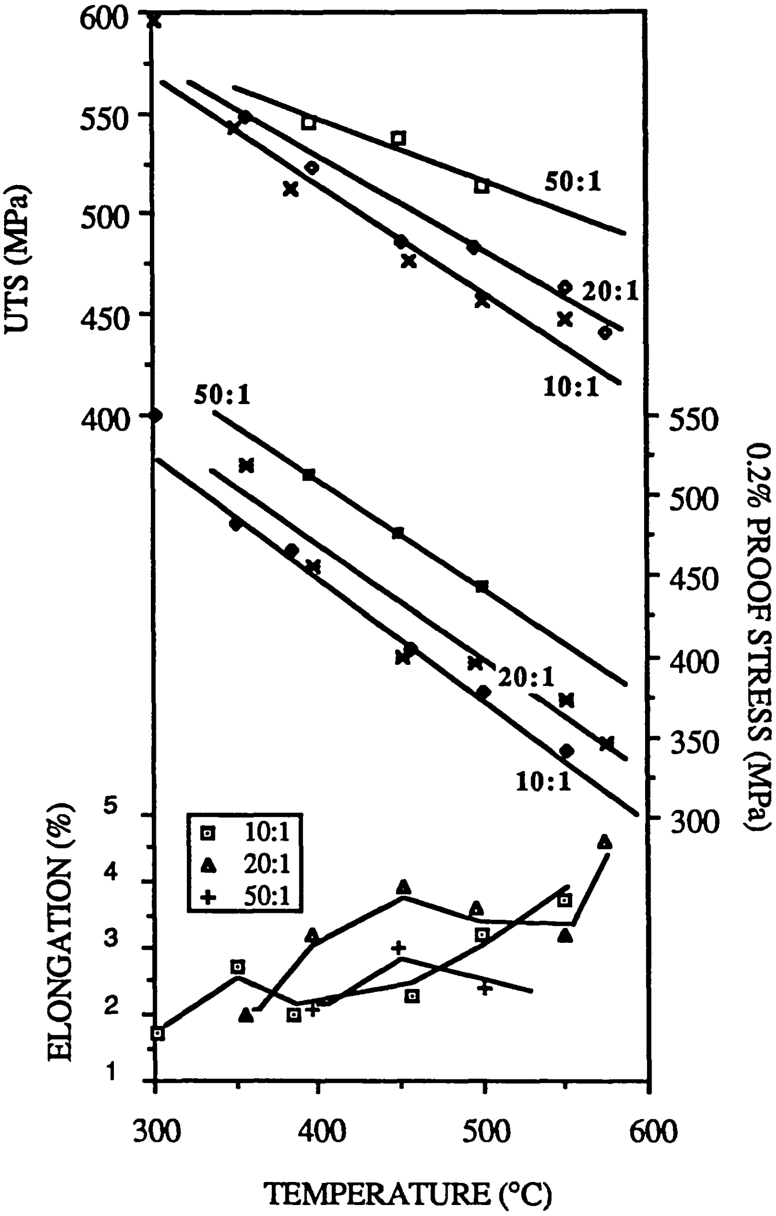

Figure 6.4. Variation of Tensile Properties with billet temperature for the Al-Mg-Cr alloy

The other processing parameter is the reduction ratio, which in contrast to temperature, does not seem to be very significant. The hardness results obtained at two different temperatures, 400°C and 500°C, have been plotted against the natural logarithm of the extrusion ratio, see Figure 6.5. Obviously, the hardness exhibits a moderate increase with increasing extrusion ratio and can be attributed to better dispersion of the second phase particles as well as to a smaller subgrain size. However, since the variation of the hardness appears to be very little, an average value has been calculated at each temperature. The results, 161.0±3.5 and 149.1±4.8 at 400°C and 500°C respectively, confirm the small deviation from the mean value, which can be clearly seen in Figure 6.5, where the white line in the middle of each shaded area represents the average hardness for that temperature and the shaded area represents the standard deviation. It can be seen that the majority of the experimental data lie within the shaded area. Hence, it is obvious that the influence of extrusion ratio is less significant on hardness than that of the temperature.

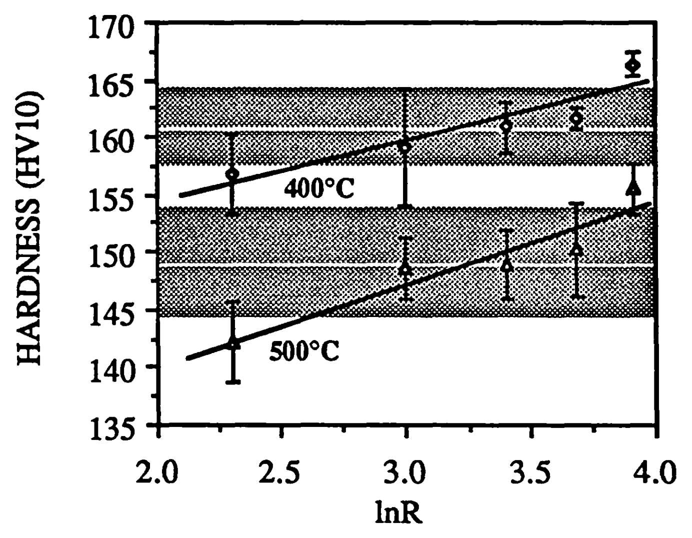

Figure 6.5. Effect of extrusion ratio on the hardness of the Al-Mg-Cr alloy

The tensile results obtained at billet temperature 450°C with varying extrusion ratio display identical behaviour to the hardness results. The temperature of 450°C was chosen because acceptable extrudes were produced over the whole range of extrusion ratios. Figure 6.6 shows that some variation in strength occurs mainly attributed to more efficient dispersion and redistribution of aggregates at higher reduction ratios. Sheppard and Chare have also reported (1972), in an investigation of the extrusion parameters and properties of extrudates, that the reduction ratio had little effect on the hardness, elongation and proof stress, but these powders were relatively low in alloy content with few dispersoids.

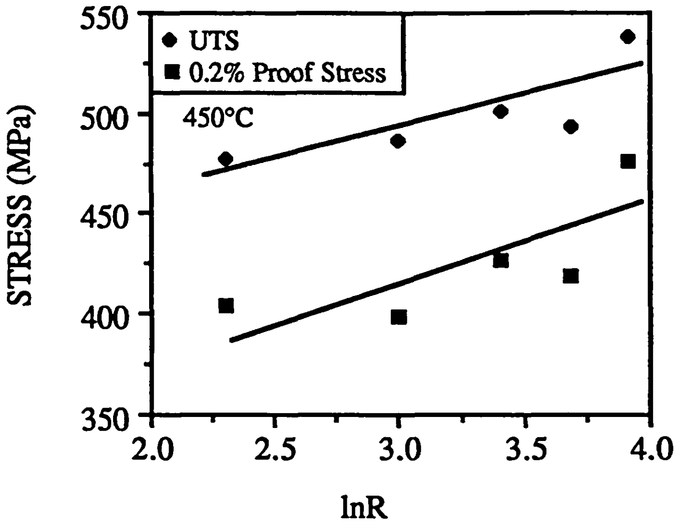

Figure 6.6. Variation of room temperature tensile properties with extrusion ratio for the Al-Mg-Cr alloy.

The results presented previously have shown that the mechanical properties depend on the billet temperature and extrusion ratio. So far the influence of these two parameters has been studied. In order to gain a better understanding of the influence of the processing parameters on the mechanical properties of the material, a more complex analysis has been conducted taking into consideration that these two variables can be combined into the temperature compensated strain rate. For that reason the results of tensile tests have been plotted against the natural logarithm of the temperature compensated strain rate, lnZ [Figure 6.7 (a)] and a linear relationship has been obtained between lnZ and both the 0.2% proof tensile stress and the U.T.S, indicating the dependence of the material strength on the temperature and microstructural features.

$$\sigma_{pr} = -172.42 + 21.28 \ln Z \quad (R^2 = 0.92) \quad \ldots\ldots\ldots\ldots \quad (6.5)$$

$$\sigma_{UTS} = 143.28 + 12.68 \ln Z \quad (R^2 = 0.90) \quad \ldots\ldots\ldots\ldots \quad (6.6)$$

Similar relationships have been derived between tensile properties and the reciprocal of the absolute temperature, highlighting the importance of processing temperature on the proof stress and UTS.

$$\sigma_{UTS} = 218.40 + 199.11 \frac{1}{T} 10^3 \quad \{R^2 = 0.99\} \quad \ldots\ldots\ldots\ldots \quad (6.7)$$

$$\sigma_{Pr} = -102.86 + 380.38 \frac{1}{T} 10^3 \quad \{R^2 = 0.97\} \quad \ldots\ldots\ldots\ldots \quad (6.8)$$

Finally, Figure 6.7 (b) illustrates similar behaviour between hardness values and the natural logarithm of the temperature compensated strain rate yielding the relationship:

$$H_V = 52.50 + 3.67 \ln Z \quad (R^2 = 0.93) \quad .... \quad (6.9)$$

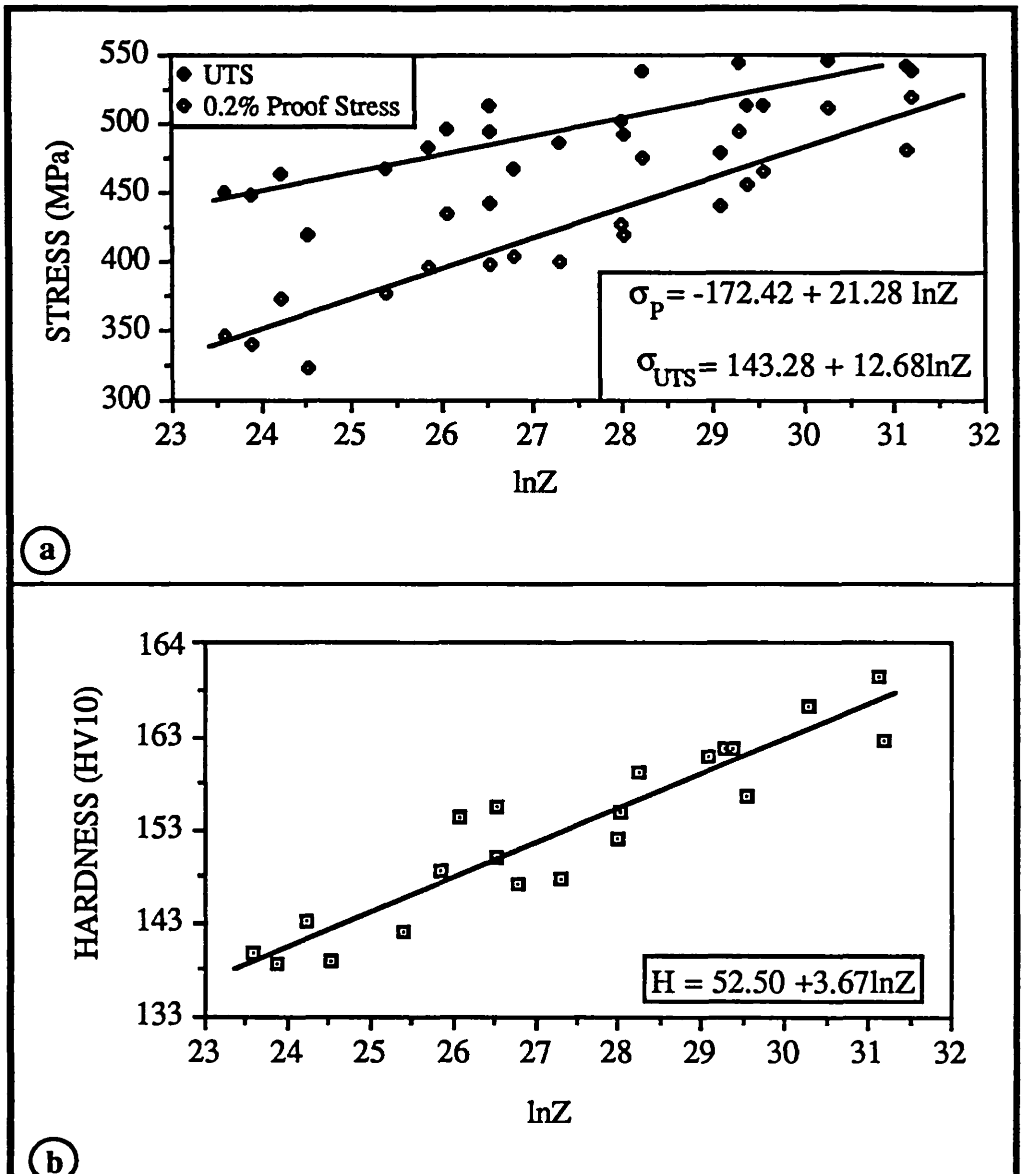

Figure 6.7. Effect of temperature compensated strain rate (lnZ) on
(a) room temperature tensile properties and
(b) hardness, of the Al-Mg-Cr alloy

The scatter evident in Figure 6.7 (a) and (b) can be attributed to the heterogeneity of the substructure, due to zones with different sized subgrains and dispersoids. Nevertheless, the large number of data points together with the good correlation coefficients support the validity of the relationships. The results in Figure 6.7 (a) and (b) show an increase of the yield strength, UTS and hardness with increasing temperature compensated strain rate, which are consistent with those anticipated for the subgrain size, indicating that at lower values of Z (higher temperature) the recovery processes are more rapid resulting in larger subgrains. Thus both the proof stress and the UTS fall with increasing extrusion temperature. The other feature of some importance is that under low Z processing conditions the dispersoids are in general coarser.

The toughness of the alloy is reflected by the ratio of the notched tensile fracture stress over the proof stress, see Figure 6.8. Toughness and ductility are affected by the volume fraction and distribution of the second phase particles. As the amount of coarse particles increases the notch sensitivity of the alloy increases as void nucleation becomes more prevalent. With increasing temperature the subgrain size increases and the dispersoids coarsen, resulting in a drop of the toughness. The apparently poor toughness would be the most limiting factor for the application of this alloy, but the material utilized in this study contains a rather high proportion of the alloying elements. Obviously, more dilute alloys are required.

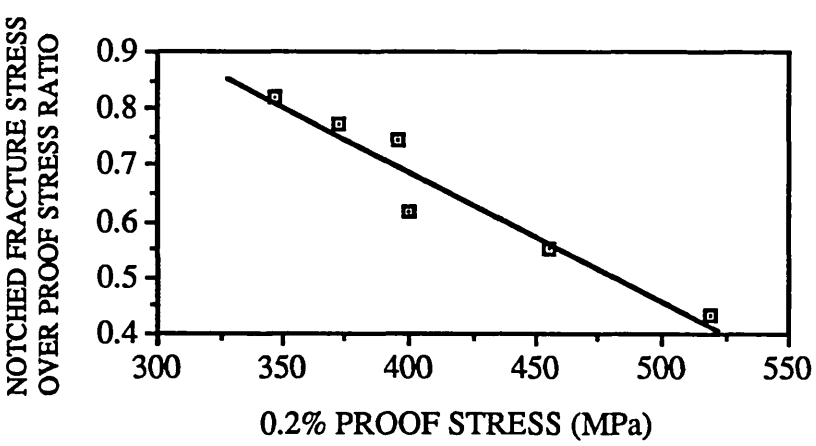

Figure 6.8. Variation of notched tensile stress over proof stress ratio with the 0.2% proof stress, for the Al-Mg-Cr alloy.

In order to reveal the behaviour of the material at elevated temperatures, tensile tests were performed at 150°C, 250°C and 350°C utilizing material extruded at low (400°C) and high (550°C) temperatures at R=20:1. The specimens were held at the elevated temperature for 100h. The variation of proof and tensile strengths are shown in Figure 6.9, in which it can be seen that both the tensile and proof strength decrease considerably with increasing test temperature. This characteristic is not only due to precipitate coarsening, recovery, recrystallization or any other process that could degrade performance of strengthening mechanisms, but it mainly is attributed to the fact that at elevated temperatures ($T>0.5T_m$) deformation is occurring by mechanisms other than dislocation glide, which is the deformation mechanism at low and intermediate temperatures. These alternate mechanisms include dislocation climb, cross-slip, grain boundary diffusion, bulk diffusion and grain boundary sliding. Moreover, deformation at elevated temperature may cause additional slip systems to operate. Finally, it is also worth mentioning that after 100h at 350°C the tensile strength and proof stress of both the low and high temperature extrudates decrease to approximately similar values, see Figure 6.9. This is attributed to the operative deformation mechanisms at elevated temperatures, which proceed more rapidly with increasing temperature and result in a deterioration of the strength which is independent of the as-extruded microstructure.

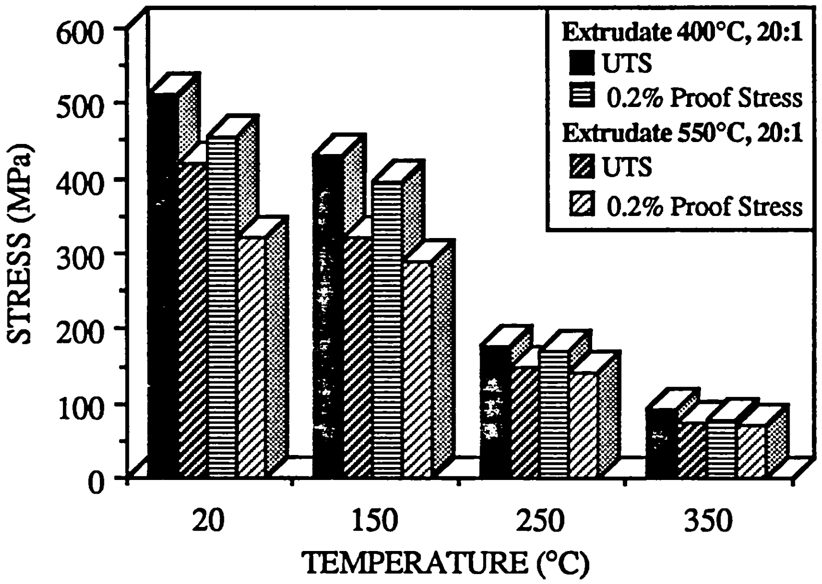

Figure 6.9. Variation of elevated temperature tensile properties with temperature of two extrudates produced at low (400°C) and high (550°) temperatures (after 100h), for the Al-Mg-Cr alloy.

In addition, to roundbar extrusion, rectangular section extrudates have been produced within a temperature range 400°C to 550°C, in order to study the properties of the material along the transverse direction. The results are illustrated in Tables 6.2 and 6.3. It can be seen (Table 6.2), that the proof stress along the transverse direction is smaller than along the longitudinal direction, even at high temperatures at which consolidation is more efficient; while variation has also been observed within longitudinal specimens extracted from different locations. The proof stress is higher in the middle of the extrudate. Such behavior is attributed to the inhomogeneity of plastic deformation. Bonding in the transverse direction is poorer and thus the material is weaker, while within the longitudinal direction the strain rate and the temperature variation result in heterogeneous behaviour. Since the temperature compensated strain rate is higher in the middle of the extrudate the proof stress is also higher. However, it must be noted that the variation in proof stress is not very significant as it can also be seen from the average values calculated for each temperature, and the results are consistent with those obtained from the roundbar extrudates. In fact, ductility is the single most important variable that is largely affected by the location of the specimen. Clearly, the ductility along the transverse direction is almost zero, see Table 6.3, which is attributed to the fibrous as-extruded microstructure.

Temperature (°C)	Proof Stress (MPa)			Mean Value
	Tranverse Direction	Longitudinal direction		
		Middle	Edge	
400	452.1	460.5	465.4 ±19.6	460.9 ±11.5
450	442.1 ±15.6	458.4 ±10.9	469.8 ± 6.4	454.6 ±14.6
500	403.3 ± 3.3	408.7 ± 3.7	411.7 ± 3.4	407.2 ± 4.7
550	359.7 ± 6.4	365.0 ± 0.8	362.5 ± 0.0	362.0 ± 4.4

Table 6.2. Variation of proof stress with temperature and location of the specimen for the Al-Mg-Cr alloy.

Temperature (°C)	Elongation (%)		
	Tranverse Direction	Longitudinal direction	
		Middle	Edge
400		1.8 ±1.1	0.8 ±0.3
450	0.8 ±0.3	3.1 ±0.3	3.6 ±0.4
500	0.7	3.5 ±1.8	2.7 ±0.8
550	1.3 ±0.1	3.4 ±0.1	3.2 ±0.6

Table 6.3. Variation of elongation with temperature and location of the specimen for the Al-Mg-Cr alloy.

Fracture normal to the longitudinal direction occurs predominantly in a transgranular manner forming slanted fracture surfaces; failure occurs via a void nucleation and coalescence mechanism forming fine dimples, see Figure 6.10 (a) and (b), which is characteristic of ductile fracture. A schematic diagram of the fracture mechanism is illustrated in Figure 6.11, in which it can be seen that the powder particles are stretched in the extrusion direction. During tensile testing voids are nucleated, rapidly grow and coalescence. A similar type of fracture has been observed in specimens extracted from the transverse direction, typically seen in Figure 6.12 (a)-(c). The fracture surface is ridged and striplike. However, a higher magnification, see Figure 6.12 (c) reveals that fracture occurs by void nucleation at the dispersoids and coalescence. Clearly, in the fracture surface parallel to the extrusion direction the number of particles which nucleate voids is larger, because although the as-extruded microstructure appears uniform and the dispersoids evenly distributed, during extrusion the second phase particles and the oxides are closer spaced on planes in the extrusion direction, thus resulting in more rapid void coalescence.

Finally, the plane strain fracture toughness (k_{IC}) of this alloy has been assessed from notched tension tests by using the equation '6.10' {Dieter (1981)}, given below. The k_{IC} value is a measure of the material's minimum resistance (with respect to thickness) to catastrophic failure (rapid crack advance). The toughness of the Al-Mg-Cr alloy does not vary significantly with direction, which was expected, for it is dependent upon void nucleation at the dispersoids which are spherical and uniformly distributed. Hence, an average value of 11.3±0.8 MPa√m has been calculated for all the extrusion conditions; this value is very useful in order to compare the three alloys studied in the present work.

$$k_{IC} = \frac{P}{D^{3/2}} \left[1.72 \frac{D}{d} - 1.27 \right] \quad \text{........................} \quad (6.10)$$

where P: fracture load, D:specimen diameter, d: notch diameter.

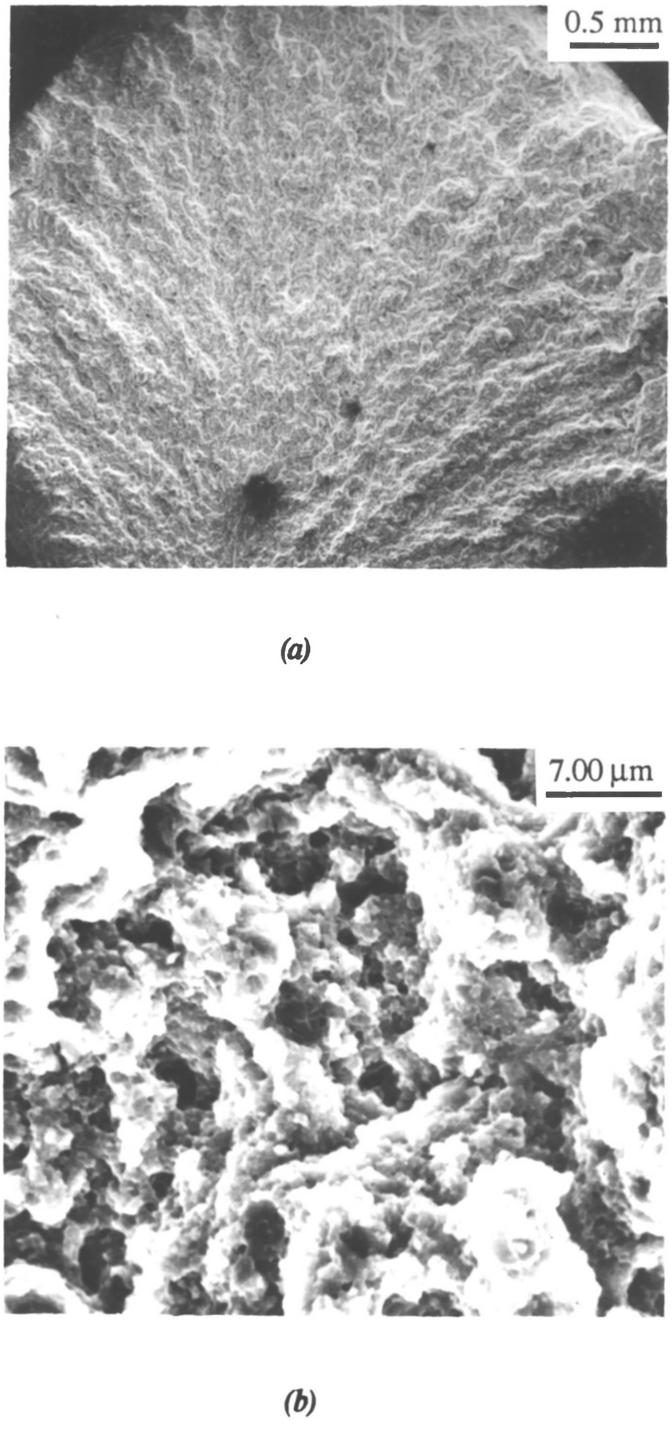

Figure 6.10. Scanning electron micrographs showing fracture surfaces of specimens extracted from the longitudinal direction:
(a) low magnification and
(b) high magnification

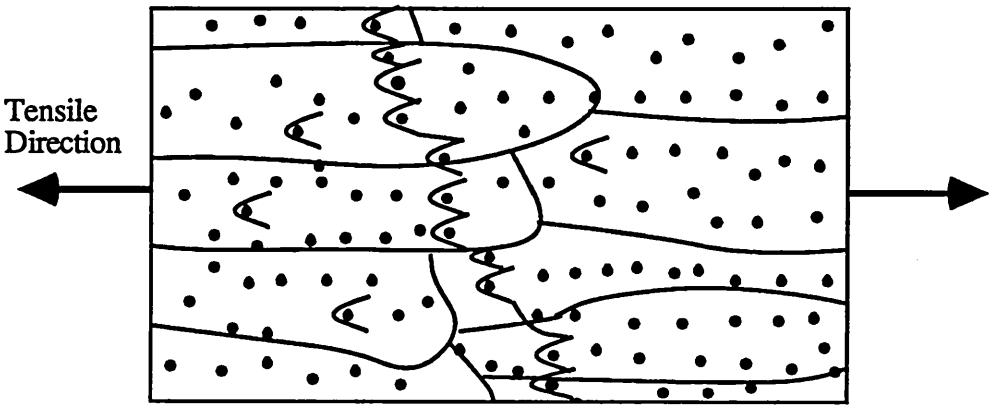

Figure 6.11. Schematic representation of fracture mechanism (void nucleation and coalescence) operating during tensile testing of specimen extracted from the longitudinal direction.

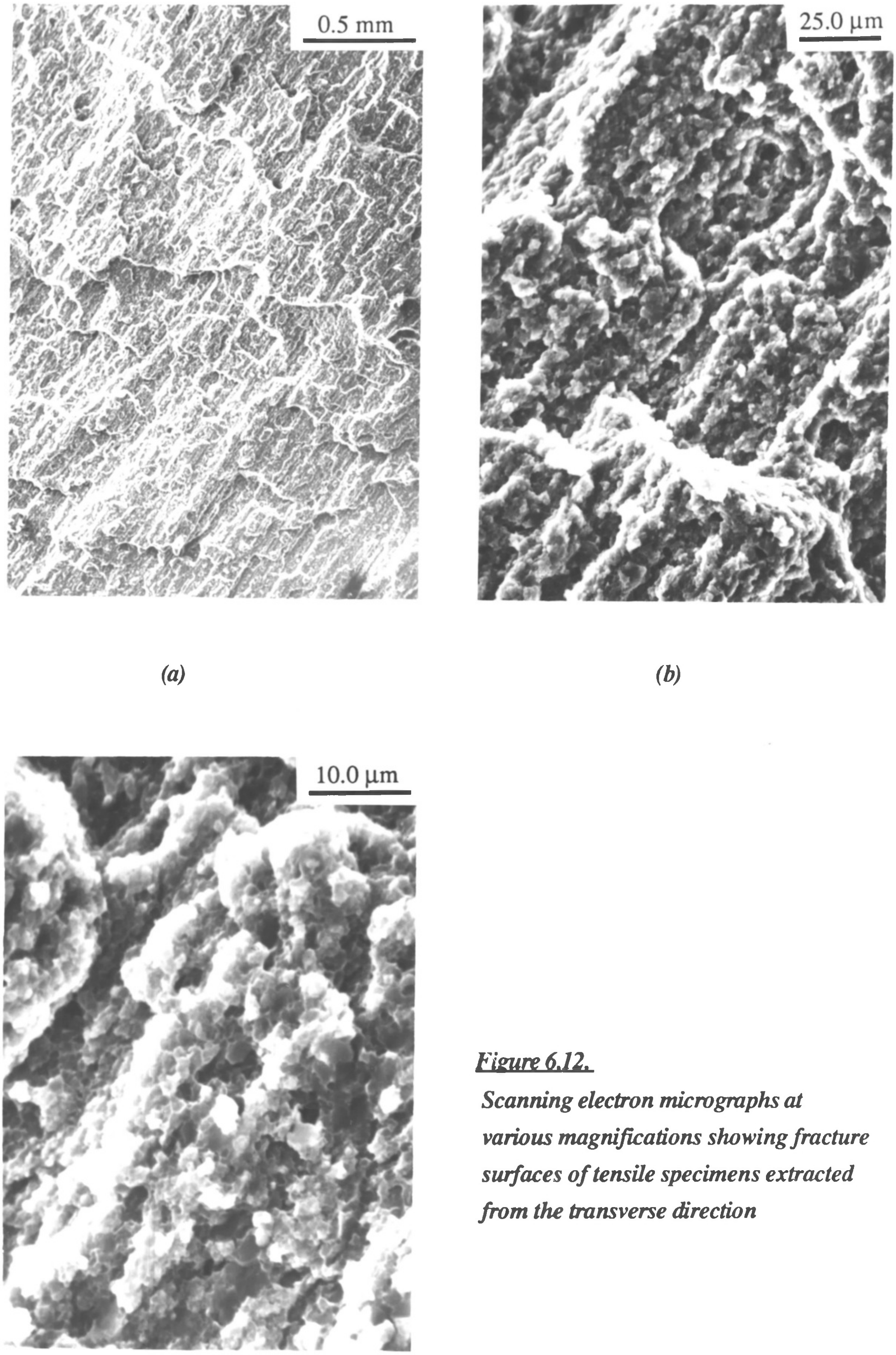

(a)

(b)

(c)

Figure 6.12.
Scanning electron micrographs at various magnifications showing fracture surfaces of tensile specimens extracted from the transverse direction

6.3. Structure and properties of the Al-Mg-Mn alloy

Figure 6.13 (a) (400°C, 20:1) is a typical as-extruded microstructure in which bands are discernible orientated in the extrusion direction. The strains experienced by the powder particles as they pass through the deformation zone and encounter the velocity discontinuity associated with entrance to the die orifice result in a fibrous structure. The main softening mechanism is dynamic recovery as evidenced by the presence of small equiaxed subgrains, see Figure 6.13 (b). There is little evidence of the original powders and oxide particles could not be distinguished from intermetallic particles, as in the previously studied alloy. Oxide stringers were also not observed, which was expected since the oxide concentration of this alloy is quite low, see Table 3.1.

Occasionally, there were examples of second phase particles, whose morphology was identical to the original nodular morphology of the icosahedral phase, see Figure 6.13 (c). However, it has not been established if the icosahedral phase has been retained through extrusion or transformed to nodules of $MnAl_6$. Indeed, the X-ray diffraction patters from the extrudates show only $MnAl_6$ and $Al_{18}Mg_3Mn_2$. It is also likely that the isolated islands of nodules may be too few for detection by X-ray. At higher processing temperatures (e.g. 500°C) a coarser subgrain and precipitate structure was found and electron and X-ray diffraction patterns indicated only $MnAl_6$ precipitates, see Table 5.4. The intensity of $MnAl_6$ increases with temperature and/or heating time, indicating the increase of the volume fraction of the $MnAl_6$ phase.

An important feature illustrated by the micrographs in Figure 6.14 (a)-(c) concerns the coarsening resistance of the substructure and respective precipitates when consolidated at higher temperatures. The microstructures suggest that this alloy is very sensitive to temperature and coarsens considerably during high temperature deformation. The subgrain size is determined by the dynamic recovery process occurring in the deformation zone under the imposition of shear stresses. The mean subgrain size increases with decrease of the temperature compensated strain rate. The subgrain size was determined by using a linear intercept method and a linear relationship has been derived between the reciprocal subgrain size and natural logarithm of the temperature compensated strain rate, as shown in Figure 6.15, of the form:

$$d^{-1} = -9.12 + 0.38 \ln Z \qquad (R^2=1.00) \;\ldots\ldots\ldots\ldots\ldots\ldots\ldots\ldots\ldots\ldots \; (6.11)$$

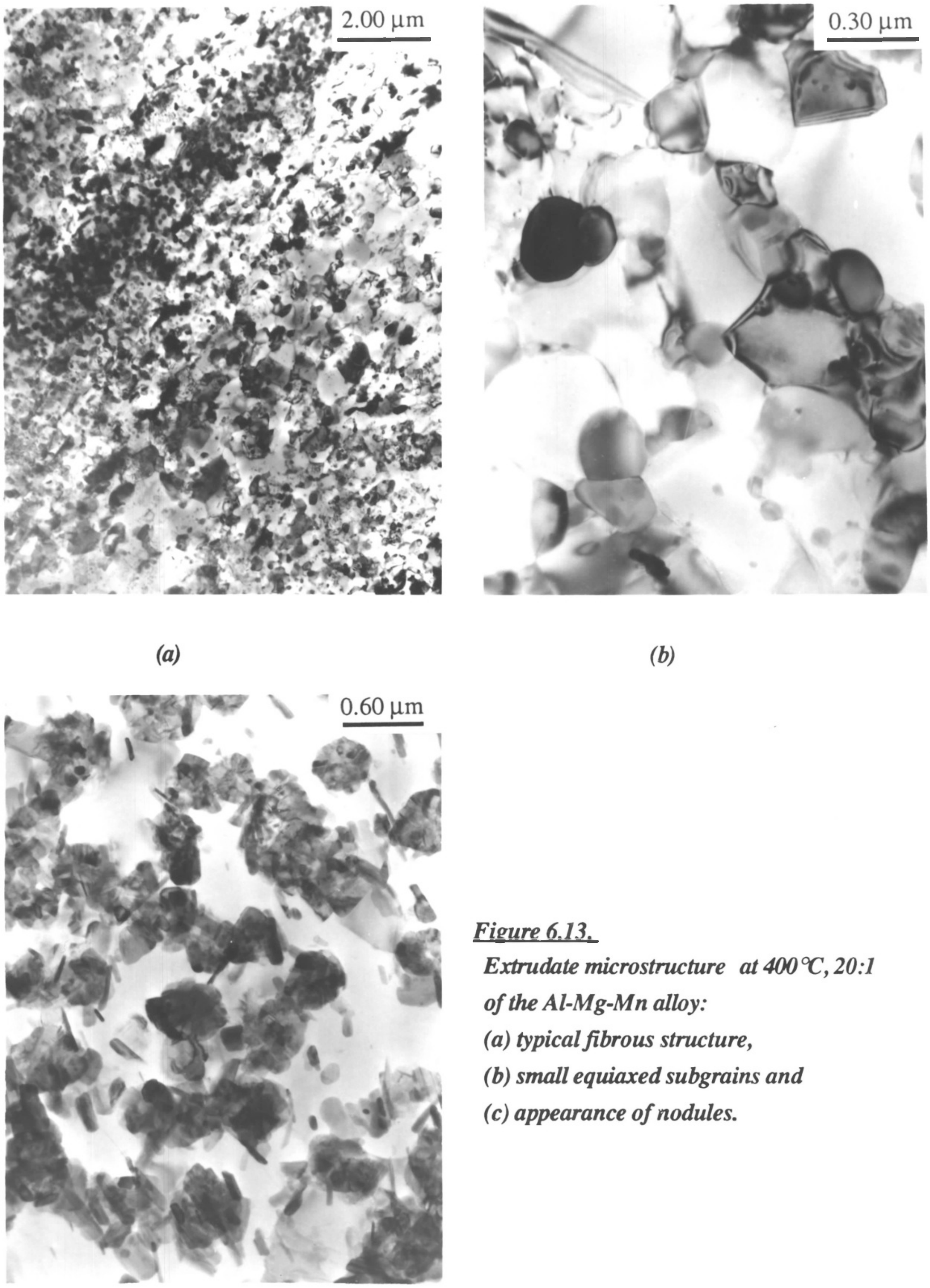

(a)

(b)

(c)

Figure 6.13.
Extrudate microstructure at 400°C, 20:1 of the Al-Mg-Mn alloy:
(a) typical fibrous structure,
(b) small equiaxed subgrains and
(c) appearance of nodules.

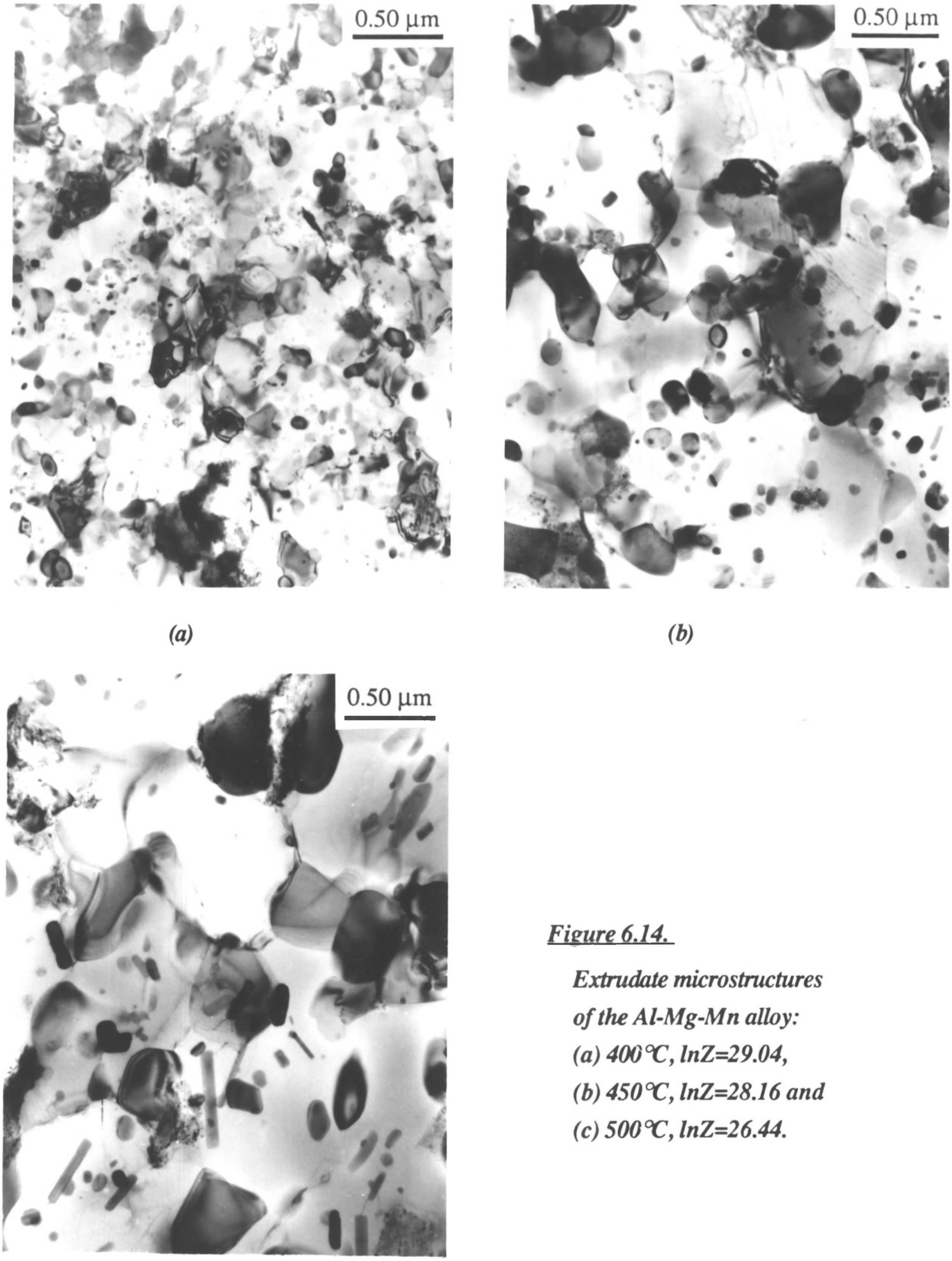

(a)

(b)

(c)

__*Figure 6.14.*__

Extrudate microstructures of the Al-Mg-Mn alloy: (a) 400°C, lnZ=29.04, (b) 450°C, lnZ=28.16 and (c) 500°C, lnZ=26.44.

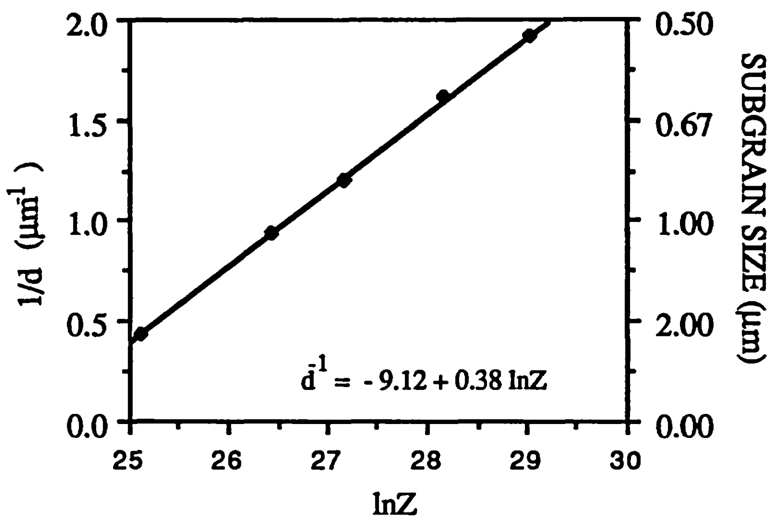

Figure 6.15. Variation of the subgrain size with lnZ for the Al-Mg-Mn alloy

It has been already reported that refinement of the microstructure enhances various strengthening mechanisms and a quantitative relationship between subgrain size and tensile strength has been observed to hold for a variety of materials. In the present work the results are in agreement with the theoretical predictions, see Figure 6.16 (a), in which the yield stress decreases with increasing subgrain diameter and the relationship between subgrain size and yield stress takes the form:

$$\sigma_y = 412.0 + 88.8\ d^{-1} \qquad (R^2 = 0.98) \qquad \ldots\ldots\ldots\ldots\ldots\ldots\ldots\ldots \quad (6.12)$$

Obviously the constant (σ_0=412.0) of the equation '6.12' has a high value in comparison with the slope of the line (k=88.8), indicating that subgrain strengthening is weak in this alloy and the main strengthening mechanism is attributed to the fine dispersion of the intermetallic particles. In the same Figure 6.16 (a), it can be seen that the hardness plotted against the reciprocal subgrain size exhibits similar behaviour to the yield stress. This was expected because subgrain boundaries generally inhibit dislocation glide, which is the deformation mechanism at low temperatures (room temperature).

Since the subgrain size varies with the processing parameters, a similar dependence of the mechanical properties on the temperature compensated strain rate can be derived. Hardness and yield stress decrease with increasing extrusion temperature and decreasing strain rate. The results are illustrated in Figure 6.16 (b) and the linear relationship between yield stress and lnZ is of the form:

$$\sigma_y = -405.4 + 34.1 \ln Z \qquad (R^2 = 0.98) \qquad \dots\dots\dots\dots\dots\dots \quad (6.13)$$

Obviously, coarsening of the microstructure with increasing processing temperature leads to significant strength losses, e.g. when the processing temperature increases 100°C, the yield stress drops approximately 120MPa. Complementary tensile tests were performed at elevated temperatures, in order to study the behaviour of the material during high temperature deformation. Specimens extruded at 400°C and 450°C were subsequently tested at three different temperatures after heating for 100h, at 150°C, 250°C and 350°C which are representative of potential service temperatures for this aluminium alloy. The results are illustrated in Figure 6.17 in which the 0.2% proof stress and tensile strength have been plotted in a bar chart against testing temperature. It can be seen that the strength of the material deteriorates. Clearly, the general character of slip changes with increasing temperature because of the greater ease of cross-slip and the operation of multiple slip systems, so that a metal which deforms at room temperature with the formation of long planar slip lines, may deform at high temperatures with a wavy slip mode. In general, strengthening at elevated temperatures can be considered more difficult because as it has already been reported deformation at high temperatures occurs by dislocation climb, cross-slip, grain boundary diffusion and subgrain boundary sliding, and thus effective strengthening is only achieved by blocking all contributors to plastic deformation.

The properties of this alloy have been also studied along the transverse direction and the results are illustrated in Table 6.4. Apparently, the fracture stress of the material is lower in the transverse direction than in the longitudinal one. This is because the as-extruded microstructure is fibrous and consequently the second phase particles, which have needle like and spheroidal shapes, are aligned in the extrusion direction, hence a greater concentration of potential void nucleation particles are lying on planes extending along the longitudinal direction causing fracture at lower stresses (see schematic diagram in Figure 6.18). The fracture surfaces are similar to those previously observed in the Al-Mg-Cr alloy, i.e. typical dimple ductile surfaces.

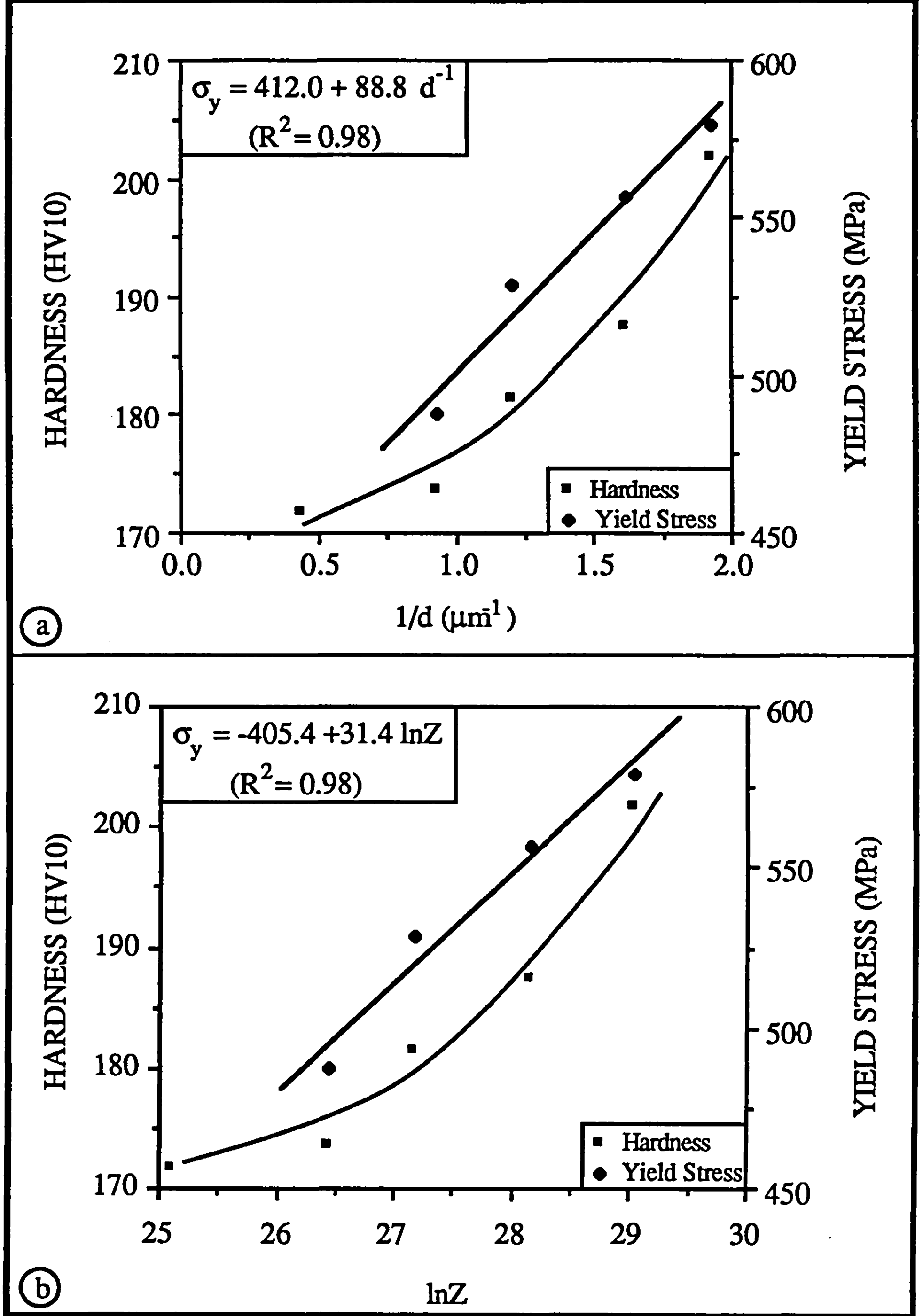

Figure 6.16. Variation of Hardness and Yield Stress with:
(a) reciprocal subgrain size and
(b) temperature compensated strain rate (lnZ),
for the Al-Mg-Mn alloy

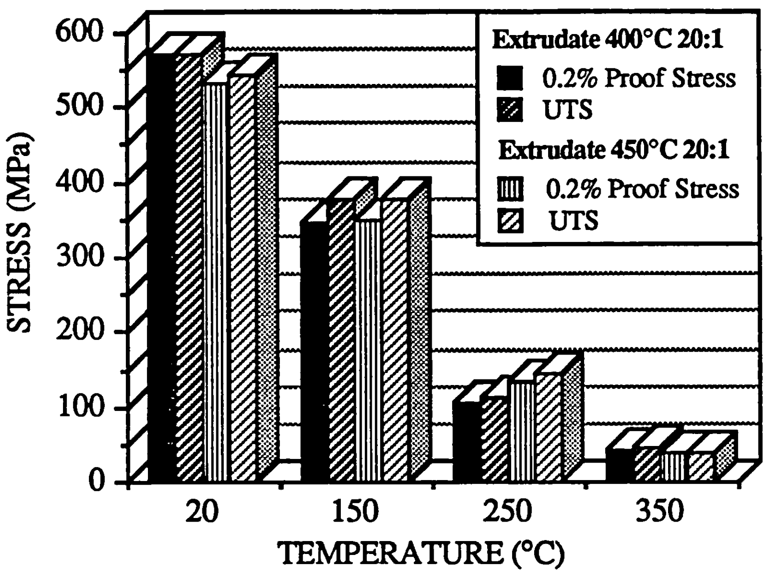

Figure 6.17. Variation of elevated temperatures tensile properties with testing temperature (after 100h) for the Al-Mg-Mn alloy

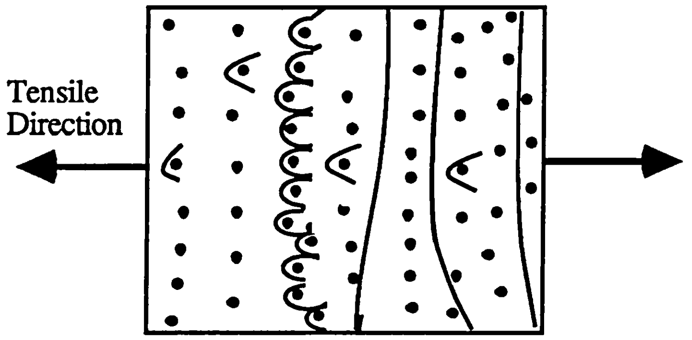

Figure 6.18. Schematic representation of fracture mechanism operating during tensile testing of specimen extracted from the transverse direction.

Temperature (°C)	Fracture Stress (MPa)		
	Tranverse Direction	Longitudinal direction	
		Middle	Edge
400	561.0 ±61.0	601.0 ± 7.3	587.9
450	531.5 ±31.0	559.9 ±15.0	549.2 ±10.0
500	514.4 ±42.0	575.8 ±17.0	549.5 ±31.0

Table 6.4. Variation of fracture stress with temperature and location of the specimen for the Al-Mg-Mn alloy.

The toughness of this alloy is reflected by the stress intensity factor (k_I), which provides a meaningful measure of the ability of a material to deform plastically in the presence of a severe stress concentration. The stress intensity factor is a basic material property and changes with important variables, such as temperature and strain rate. For materials with a strong temperature dependence, as the Al-Mg-Mn alloy of the present work, the stress intensity factor increases as the processing temperature increases. The critical stress intensity factor (k_{IC}) values were calculated by the equation '6.10' and the results are summarised in Table 6.5.

Temperature (°C)	Critical Stress Intensity factor (k_{IC}), MPa$\sqrt{m}$
400	11.48 ± 0.4
450	12.20 ± 0.9
500	12.80 ± 1.0

Table 6.5. Variation of the critical stress intensity factor with temperature, for the Al-Mg-Mn alloy.

6.4. Structure and properties of the Al-Mg-Fe alloy

The structure of the extrudates of this alloy exhibits, as expected, some banding with regions varying in both subgrain size, and size and shape of the dispersoids. This can be seen in Figure 6.19 (a) in which the different microstructure bands are orientated in the extrusion direction. Occasionally, there were examples showing the retention of the original powder particles and associated oxide film [Figure 6.19 (b)]. However, in the majority of the wrought structure the oxide was not distinguishable from the intermetallic dispersoids, similar to the Al-Mg-Cr and Al-Mg-Mn alloys, and stringers were not observed in contrast to other reports, i.e. Sheppard et al (1983,c).

The dominant softening process was dynamic recovery, as in the previously studied alloys. This is not in agreement with the Al-Mg powder alloys studied by Tan (1984), in which the deformation mode was shown to be dynamic recrystallization. This may be attributed to the significant amount of the second phase particles formed with the transition elements, which apparently inhibit dislocation migration and therefore dynamic rectrystallization. The size of the subgrains and the second phase particles depends upon the extrusion parameters with the temperature exerting the greatest influence on microstructure as can be seen in Figure 6.20 (a) and (b). These are fairly typical micrographs of as-extruded microstructure at 400°C and 550°C respectively. Generally, the subgrain size was observed to be heterogeneous due to the inhibition of the subgrain boundary motion by the high volume fraction of precipitates distributed throughout the matrix. The microstructure of the extrudates is also heterogeneous characterised by the formation of long bands that contain two types of structure. Bands with a high volume fraction of dispersoids distributed mainly at the subgrain boundaries can be clearly seen in Figure 6.21 (a) and bands with a high volume fraction of needle type precipitates aligned in the extrusion direction, together with spherical dispersoids within the matrix [Figure 6.21 (b)]. The former bands originate from the powder particles with a coarse cellular structure, while the latter originate from the microcellular structure observed in the finer powder particles where transformation has occurred during thermomechanical treatment. The precipitates were either Fe_4Al_{13} or $(Fe,Mn)Al_6$, as indicated by electron diffraction patterns, see Figure 6.22 (a)-(j), and X-ray study, see Table 6.6. No orientation relationships were detected between the precipitates and the matrix, and it was not possible to classify the precipitate shape of the two second phases detected.

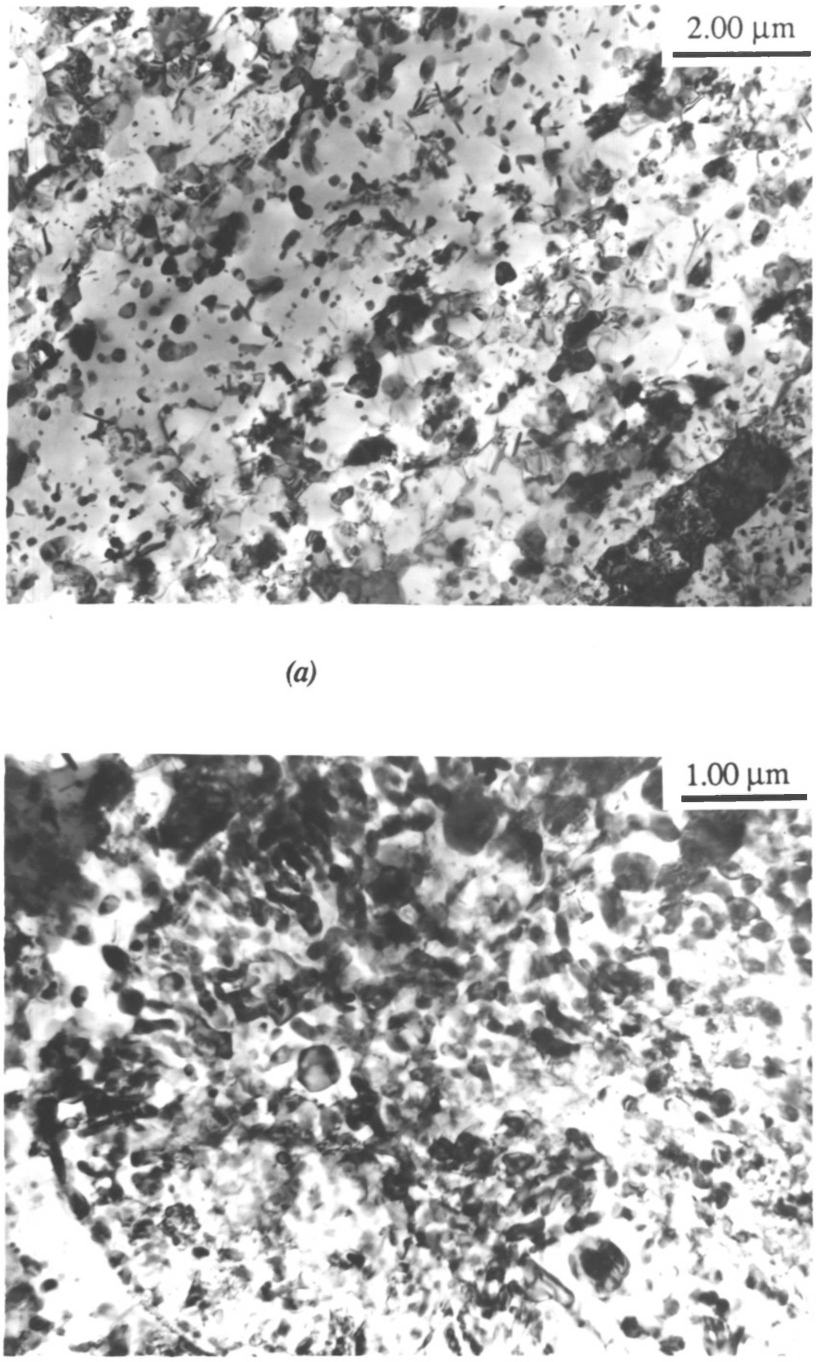

(a)

(b)

Figure 6.19. Extrudate microstructures of the Al-Mg-Fe alloy:
(a) typical banded microstructure and
(b) retention of a powder particle

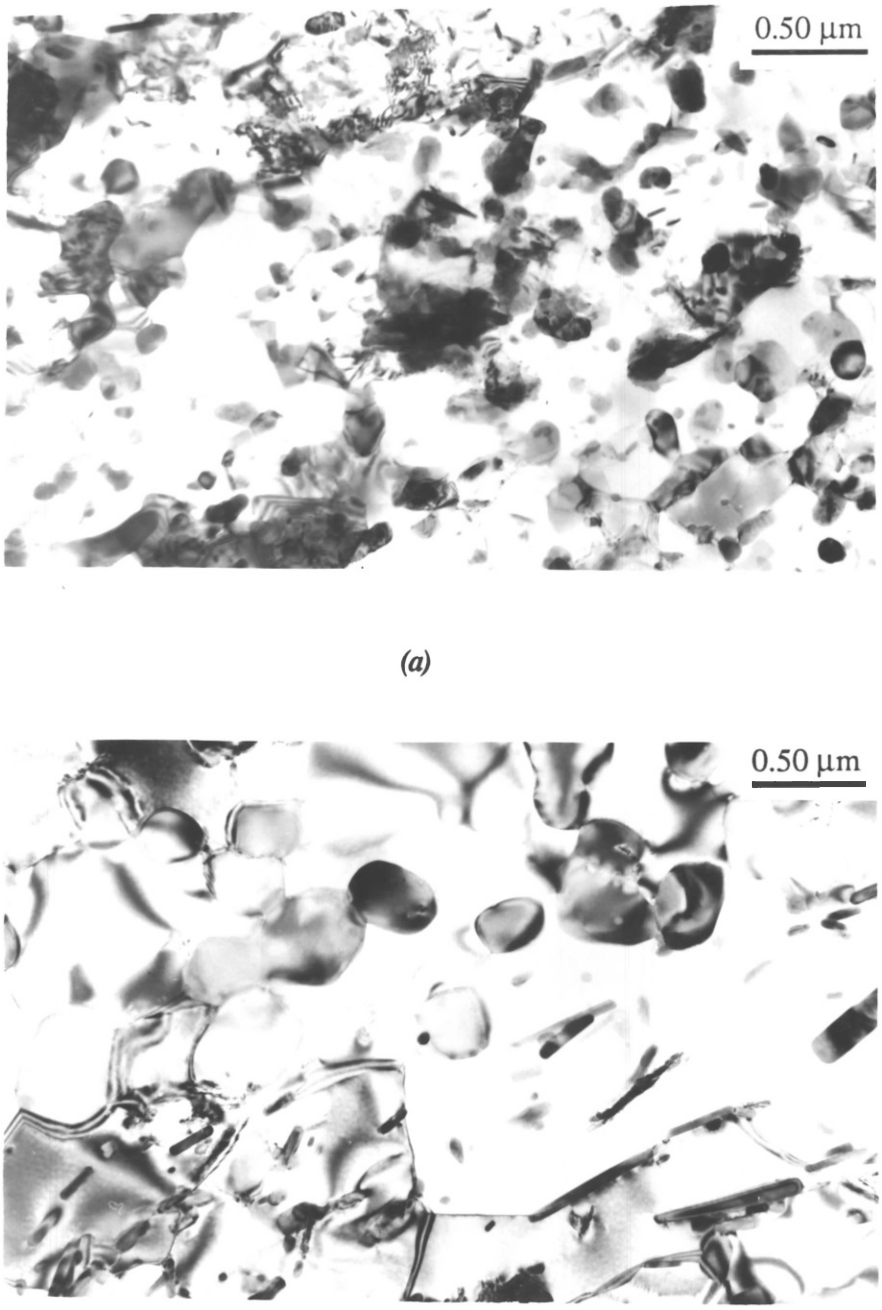

(a)

(b)

Figure 6.20. Influence of the processing temperature on the as-extruded microstructure of the Al-Mg-Fe alloy:
(a) 400°C, 20:1 and
(b) 550°C, 20:1.

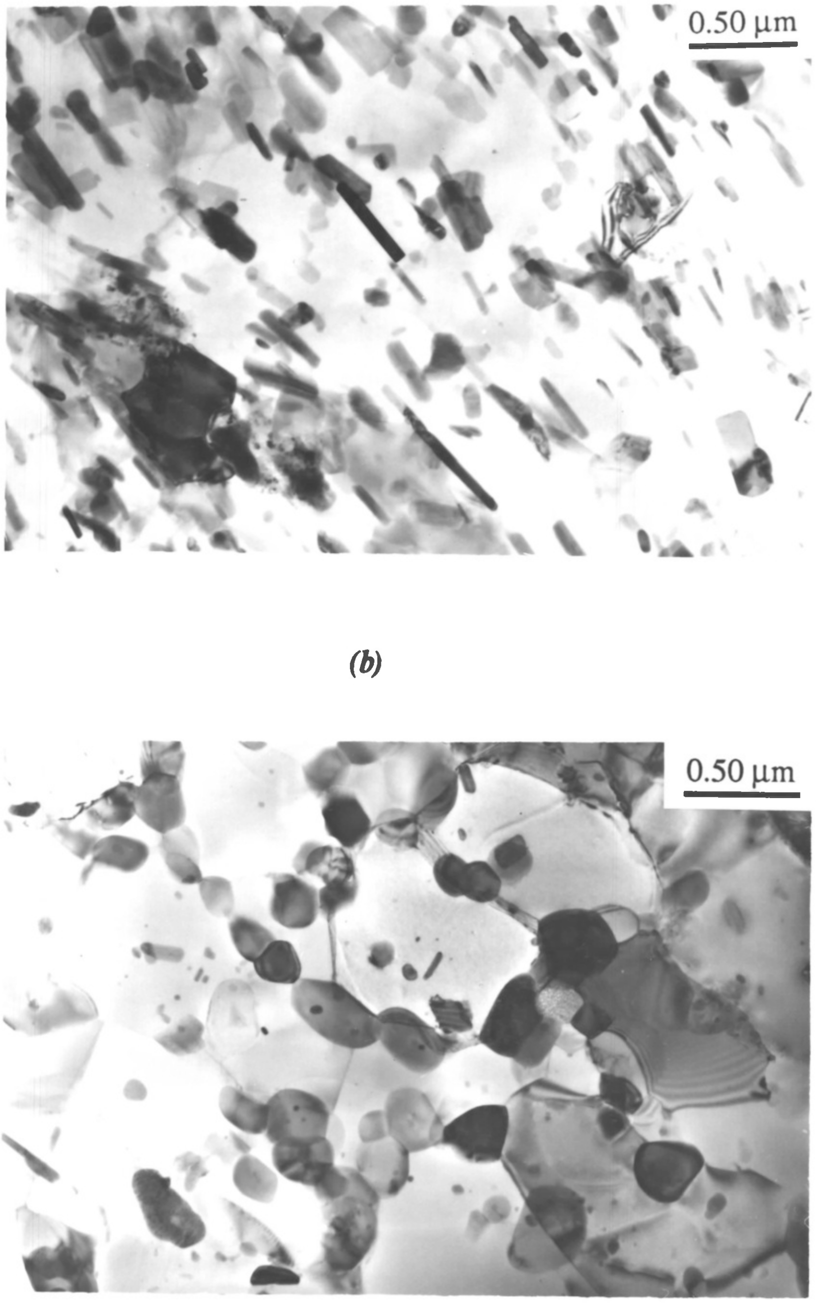

(b)

(a)

<u>*Figure 6.21.*</u>

Heterogeneous as-extruded microstructure of the Al-Mg-Fe alloy:
(a) bands with dispersoids distributed on the subgrain boundaries and
(b) bands with a high volume fraction of needle shaped precipitates.

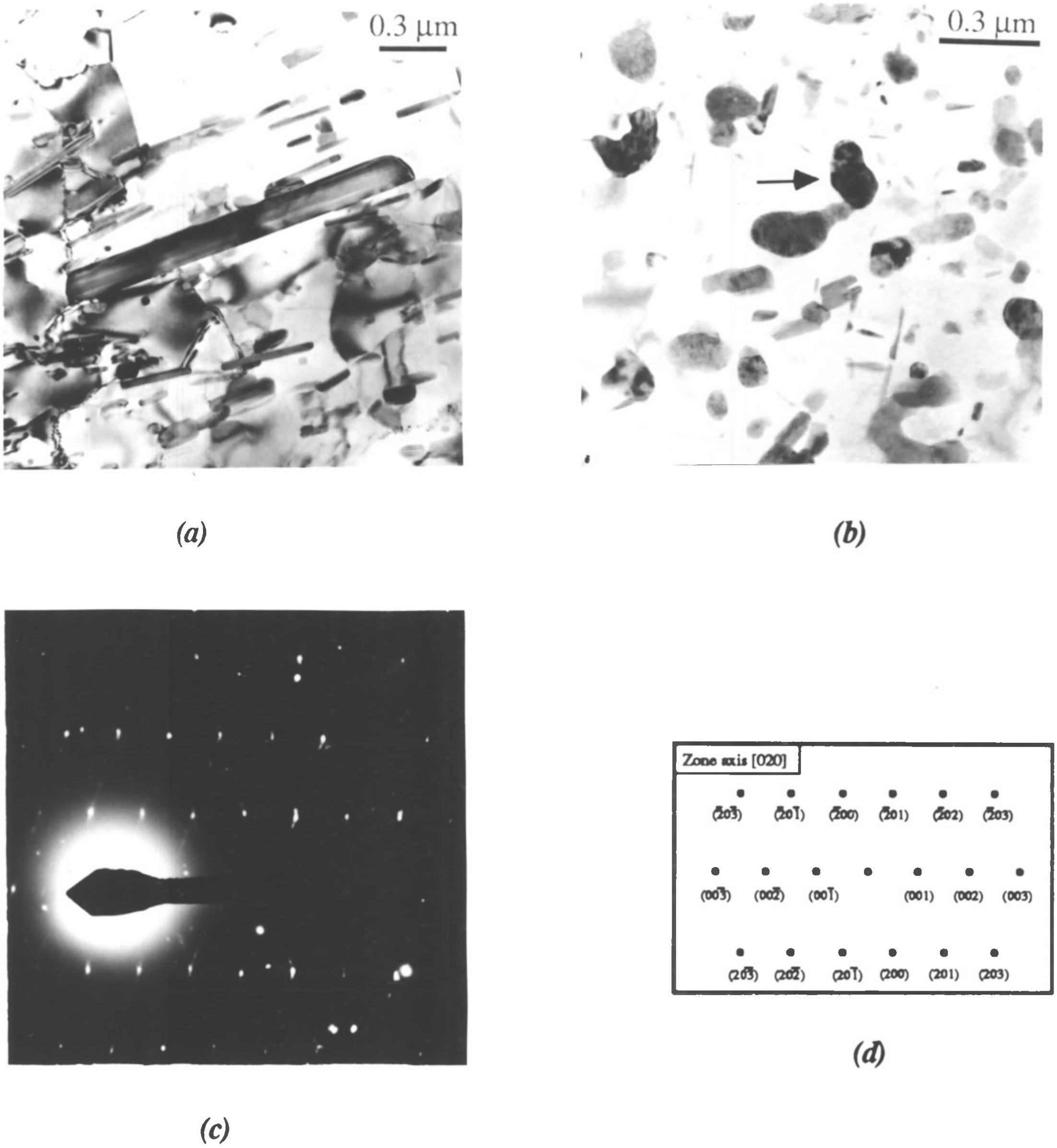

(a) *(b)*

(c) *(d)*

Figure 6.22. ***Fe_4Al_{13} dispersoids (a)-(b) with a characteristic diffraction pattern (c) and the schematic diagram (d)***

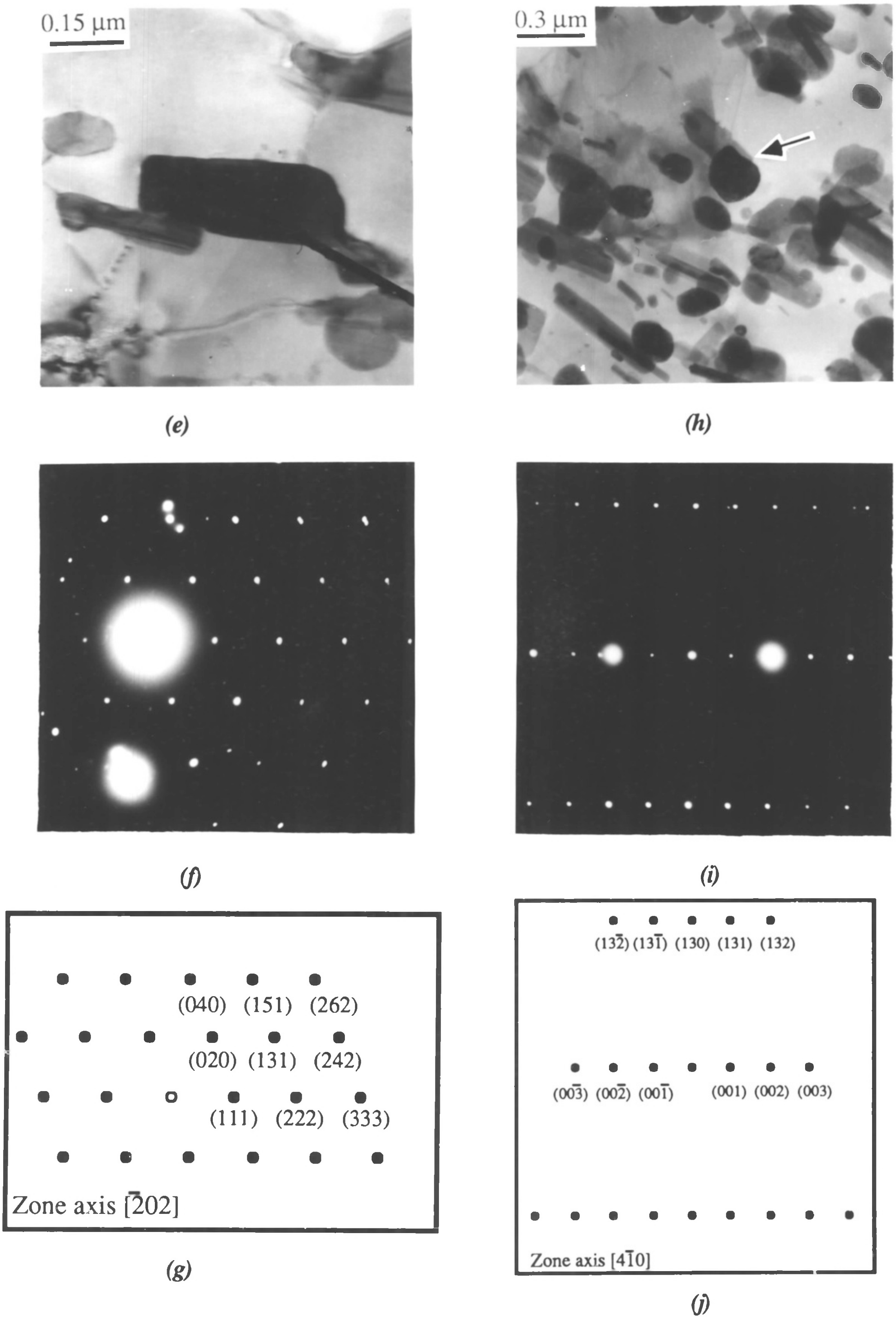

(e) *(h)*

(f) *(i)*

(g) *(j)*

Figure 6.22. $(Fe,Mn)Al_6$ dispersoids (e) and (h), with characteristic diffraction patterns (f) and (i) and schematic diagrams (g) and (j) respectively.

Table 6.6. Summary of the X-Ray Results for the Al-Mg-Fe alloy			
Extrudates	**Metastable "F"**	**$Fe_{13}Al_4$**	**$(Fe,Mn)Al_6$**
450°C 20:1	not detected	strong	strong
500°C 50:1	not detected	strong	strong

The dependence of the mechanical properties on the processing parameters and therefore the developed microstructure has been investigated and the results are presented in Figures 6.23 (a)-(b) and 6.24. It can be that the 0.2% proof stress and tensile strength decrease with increasing temperature or decreasing temperature compensated strain rate [Figure 6.23 (a)] and increasing extrusion ratio [Figure 6.23 (b)]. Similar behaviour is also exhibited by the influence of the processing parameters on hardness, see Figure 6.24. The most important processing parameter is the temperature which dictates the microstructure and therefore controls the mechanical properties. This can be clearly seen in Figure 6.24 in which the rate and the range of hardness decrease with increasing extrusion temperature (curve A) is much greater than the hardness increase with increasing extrusion ratio (curve B).

A cursory review of the literature on rapidly solidified aluminium alloys containing mainly magnesium or iron with or without other alloying elements showed that the Al-7Mg-5Fe alloy has considerably good room temperature properties. The results for this alloy were compared with those determined under equivalent conditions for three Al-Mg powder alloys and with three Al-8%Fe-X alloys processed to give optimum combinations of strength and ductility. The room temperature properties of these alloys are summarised in Table 6.7. The Al-7Mg-5Fe alloy of the present work gave the highest tensile strength but a ductility less than that which can be considered commercially viable. On the other hand it can be seen that increasing the extrusion temperature, produces a coarser but more homogeneous structure and the level of ductility increases considerably. It is therefore essential to manipulate all the parameters affecting the inhomogeneity including those of atomization and of production/consolidation route in order to produce an alloy with improved mechanical properties.

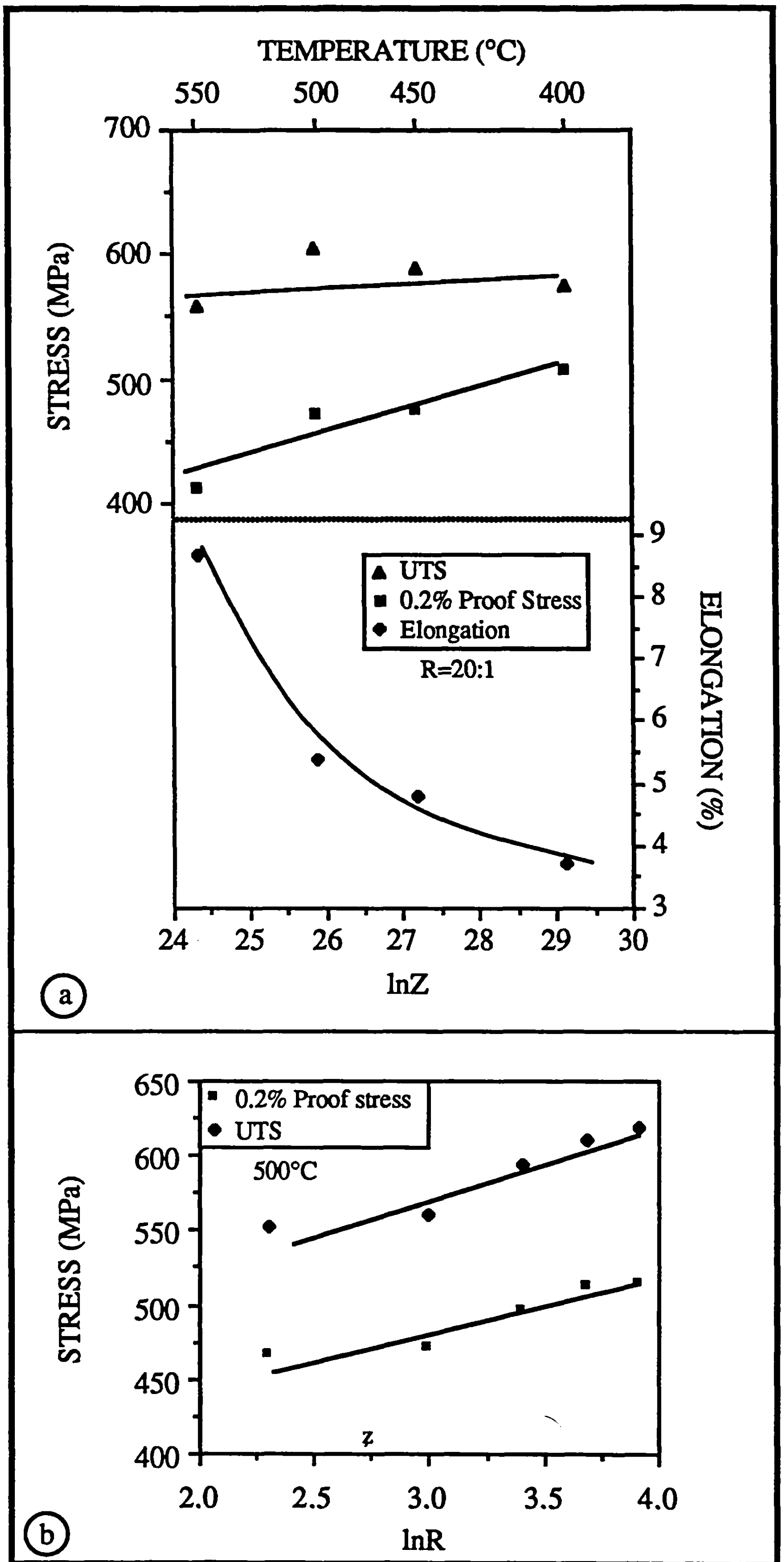

Figure 6.23. Effect of extrusion temperature, temperature compensated strain rate (a), and extrusion ratio (b) on the tensile properties of the Al-Mg-Fe alloy

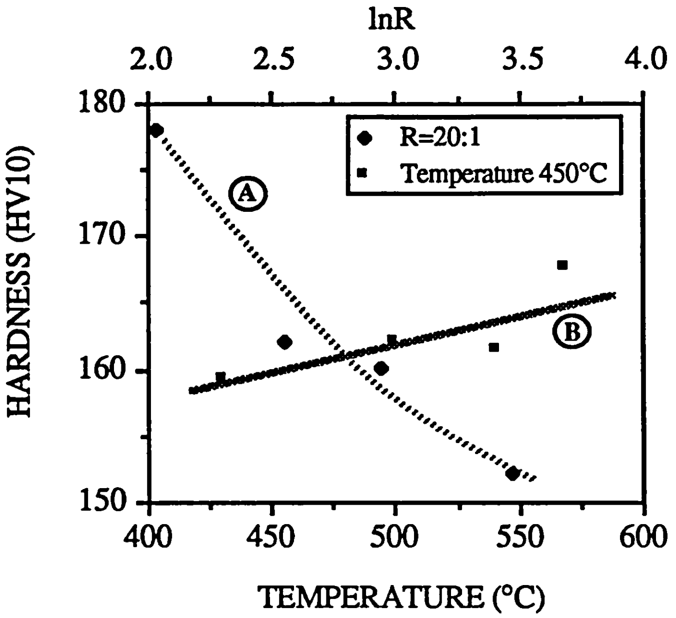

Figure 6.24. Effect of processing parameters:
billet temperature (A), and extrusion ratio (B)
on the hardness of Al-Mg-Fe alloy

Alloy Composition	UTS (MPa)	El. (%)	Reference
Al-7Mg *	473	21.3	Tan (1984)
Al-12Mg *	556	11.2	Tan (1984)
Al-15Mg *	565	11.7	Tan (1984)
Al-6Mg-5Fe *	575	3.7	This work
Al-6Mg-5Fe #	585	11.5	This work
Al-8Fe	572	5.0	Tietz & Palmer (1981)
Al-8Fe-3.4Ce	550	9.0	Tietz & Palmer (1981)
Al-8Fe-2Mo	492	6.7	Tietz & Palmer (1981)

* atomized powder extruded at 400°C, 20:1
# atomised powder extruded at 550°C, 20:1

Table 6.7. Tensile properties of some Al-Fe-X R/S alloys

For completeness the properties of this alloy have been assessed at elevated temperatures. The results are illustrated in Figure 6.25, in which it is obvious that the proof stress and tensile strength of this alloy drop significantly with temperature, exhibiting similar behaviour to the previously reported alloys. It must also be highlighted that after 100h at 350°C the tensile properties of extrudates processed at both 400°C and 500°C have almost the same values, a characteristic identical to the previously studied alloys. This suggests that during high temperature deformation the strengthening mechanisms are equally inefficient, independent of the quality of the developed microstructure during different processing conditions, thus resulting in a small variation in their mechanical properties.

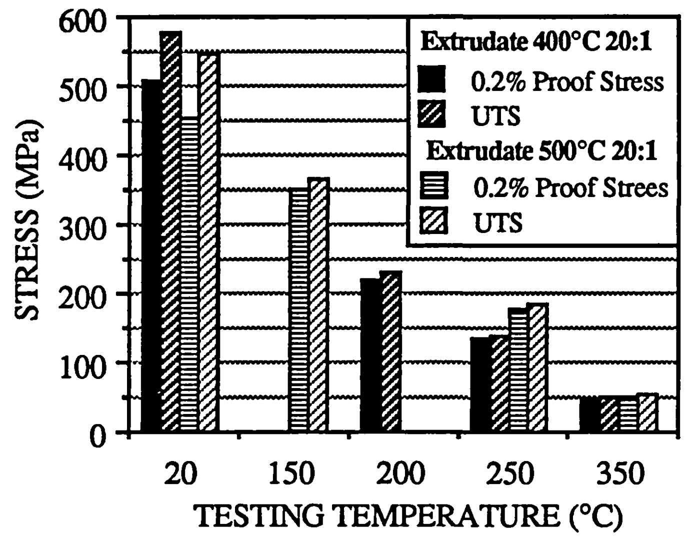

Figure 6.25. Variation of elevated temperature tensile properties with temperature for two extrudates of the Al-Mg-Fe alloy.

Finally, in order to gain a better understanding of the properties of the material it is essential to study the properties of the extrudates along both directions, i.e. the transverse and the longitudinal. Tensile tests and sharp-notch tension tests were performed, as described in the experimental procedure, on specimens extracted from both longitudinal and transverse directions from the rectangular-bar extrudates. The results are presented in Tables 6.8 - 6.11, in which the variation of the tensile properties with the temperature and the location of the extrudate is revealed. Obviously, the properties along the transverse direction are poorer and at temperatures less than 450°C the transverse direction specimens fractured when the tensile stress only just exceeded the proof stress, see Table 6.9. At higher processing temperatures the resultant microstructure was more homogeneous, and the ultimate tensile strength was appreciably higher than the proof stress. The elongation to fracture remains relatively high for this alloy with better values in the extrusion direction and especially at the edge of the extrudate. This is because the deformation is not homogeneous and the circumference of the extrudate has experienced lower Z values (higher temperature due to frictional effects) and higher shear stresses, consequently better bonding has been achieved. The toughness of this alloy also exhibits directionality similar to the other mechanical properties, as illustrated by the critical stress intensity factor values presented in Table 6.11.

Temperature (°C)	0.2% Proof Stress (MPa)		
	Tranverse Direction	Longitudinal direction	
		Middle	Edge
400 450 500	504.8 ± 3.6 473.0 ± 4.4 448.8 ± 6.3	529.4 ± 1.0 474.4 ± 2.0 475.2 ± 5.3	544.6 ± 6.6 500.1 ± 5.0 475.12

Table 6.8. Variation of 0.2% proof stress with temperature and location of the specimen for the Al-Mg-Fe alloy.

Temperature (°C)	Tensile strength (MPa)		
	Tranverse Direction	Longitudinal direction	
		Middle	Edge
400 450 500	537.6 ± 1.0* 531.3 ± 1.8* 539.4 ± 1.0	580.1 ± 4.3 587.6 ± 5.5 559.5 ±38.4	610.1 ± 7.8 607.1 ±17.0 616.8

*: Indicates fracture stress

Table 6.9. Variation of tensile strength with temperature and location of the specimen for the Al-Mg-Fe alloy.

Temperature (°C)	Elongation (%)		
	Tranverse Direction	Longitudinal direction	
		Middle	Edge
400	1.3 ± 0.1	2.5 ± 1.0	4.0 ± 0.5
450	2.3 ± 0.1	5.0 ± 0.4	5.4 ± 1.6
500	3.4 ± 0.7	4.8 ± 1.2	7.6

Table 6.10. Variation of the elongation with temperature and location of the specimen for the Al-Mg-Fe alloy.

Temperature (°C)	Critical Stress Intensity factor, (MPa$\sqrt{m}$)		
	Tranverse Direction	Longitudinal direction	
		Middle	Edge
400	10.327	14.199	14.239
450	10.943	13.130	14.103
500	14.347	16.389	16.416

Table 6.11. Variation of the critical stress intensity factor with temperature and location of the specimen for the Al-Mg-Fe alloy.

6.5. Comparison of the alloys and discussion

The study of the structure and properties of each alloy of the present work has been presented separately. However, in order to design new alloys based upon the knowledge of these three alloys, it is considered essential to compare them.

Figure 6.26 (a) shows that the hardness of all three alloys increases moderately with extrusion ratio when the temperature is constant. Conversely, increasing the extrusion temperature results in a significant hardness reduction, again for all three alloy compositions, see Figure 6.26 (b). The rate of hardness decrease is noticeably higher for the Al-Mg-Mn alloy, indicating a less thermally stable dispersion of hardening precipitates than in the Cr and Fe bearing alloys. However, the specific hardness values under identical conditions vary with alloy content, such that $H_{Mn}>H_{Fe}>H_{Cr}$. This appears to reflect the total addition (in weight percentage) of each element, and hence the potential volume fractions of the respective intermetallic phases.

The three alloys behaved differently during tensile testing. Typical load extension curves are illustrated in Figure 6.27. During most tests, the Al-Mg-Cr alloy exhibited a clearly defined yield point, followed by a smooth increase in load with only a moderate work hardening rate. On the contrary, in the other two alloys sharp yield points were followed by uneven yielding manifested by the appearance of jerks in the plastic region of the load-strain curve. The very low work hardening rate in the region of discontinuous yielding was then replaced by a rapid increase in work hardening. The discontinuous yielding appeared irrespective of the extrusion conditions and therefore the yield stress of the Al-Mg-Mn and Al-Mg-Fe alloys. Discontinuous or serrated yielding (sometimes called the Portevin-Le Chatelier effect or jerky flow) has been reported by Thomas (1966) for Al-Mg cast alloys, and more recently by Tan et al (1984) for Al-Mg powder alloys. In Al-Mg alloys this effect is generally attributed to vacancy enhanced dynamic strain aging, described by Cottrell (1953), in which moving dislocations are repeatedly locked by solute atoms. The magnesium solute atoms continuously diffuse to catch up with the dislocations and then repin them. Thomas (1966) has reported two types of discontinuous yielding, only one of which could be explained in terms of Cottrell atmospheres, and that did not occur at the yield point but rather after a critical amount of strain required to create a certain excess of vacancies necessary to increase the solute diffusion to a critical amount. A more recent study of three commercial Al-Mg alloys, by Lloyd (1980), has highlighted the importance of magnesium content on serrated yielding during room temperature testing. Severe discontinuous yielding occurred in 5083 alloy (4.46%Mg, 0.84%Mn), while the

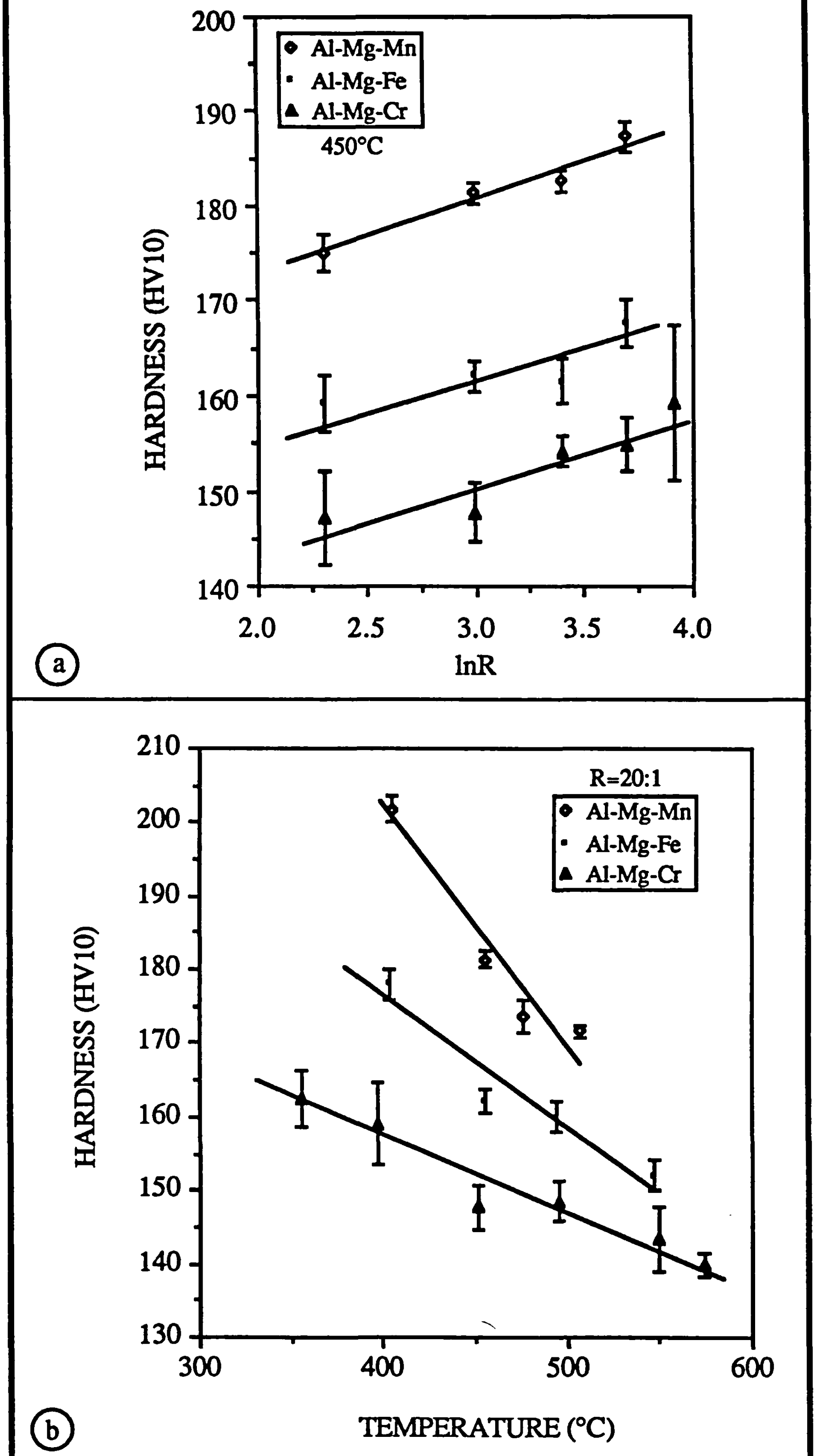

Figure 6.26. Variation of extrudate hardness with
(a) extrusion ratio and
(b) extrusion temperature

serrations were barely perceptible in a 5052 alloy (2.34%Mg, 0.24%Cr). In the present work, the absence of discontinuous yielding in the Al-Mg-Cr alloy is most likely to be a consequence of insufficient magnesium being available to influence dislocation mobility. Note that a large volume fraction of $Al_{18}Mg_3Cr_2$ dispersoids compose the structure of this alloy, thus depleting the matrix of magnesium. In the Al-Mg-Fe alloy magnesium containing phases were not recorded while in the Al-Mg-Mn alloy the $Al_{18}Mg_3Mn_2$ phase was shown to dissolve when the extrusion temperature exceeds 450°C, and therefore the magnesium in solid solution is available for strain aging. Finally, it must be noted that the appearance of this phenomenon is independent of the changing microstructural features such as precipitate and subgrain size.

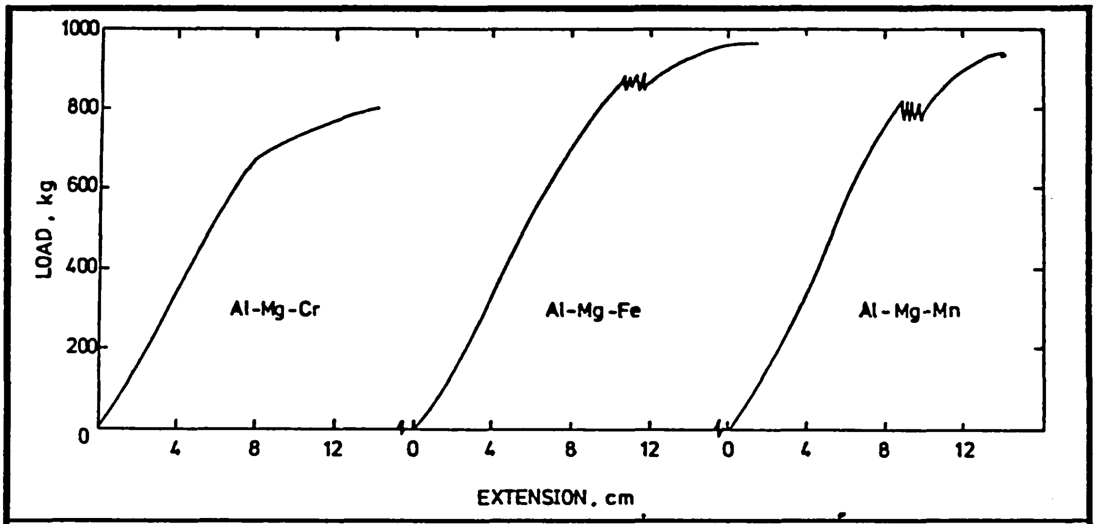

Figure 6.27. Influence of alloy composition on tensile behaviour

The effect of extrusion temperature on the room temperature tensile properties of the three alloys is shown in Figure 6.28. The tensile strength deteriorates with temperature and differs for the alloys investigated, with the Fe bearing one exhibiting the highest values. It can be seen that the Al-Mg-Fe alloy maintains a tensile strength in excess of 550 MPa. On the other hand, the 0.2% proof stress is in complete agreement with the hardness results with the Al-Mg-Mn alloy exhibiting a more pronounced decrease in strength than the other two alloys. This is because at higher extrusion temperatures, this alloy exhibits less resistance to coarsening. The fine $Al_{18}Mg_3Mn_2$ precipitates have been shown to dissolve at temperatures higher than 450°C and the $MnAl_6$ dispersoids coarsen. Fine precipitates perform a dual function, providing dispersion hardening and substructural strengthening by restricting subgrain growth. On this account, at high temperatures the coarse precipitates do not serve any longer as an effective barrier to dislocations and the coarser substructure results in significant strength losses.

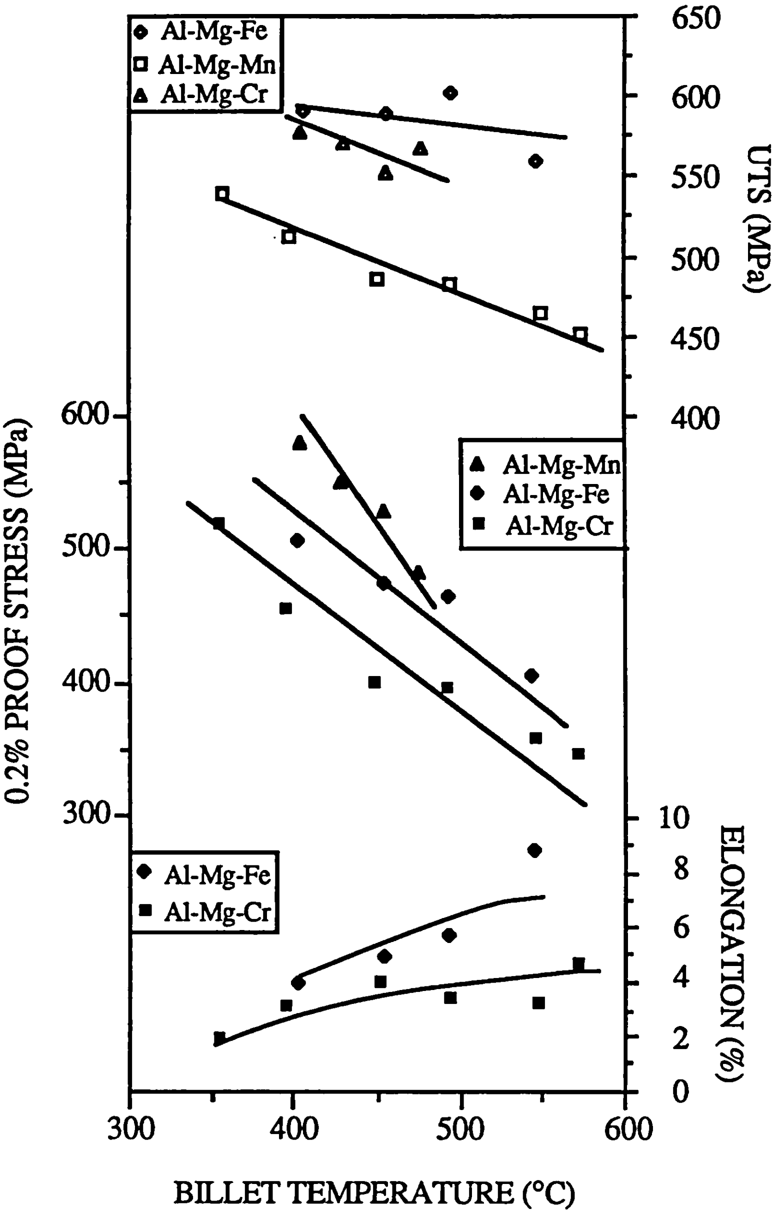

Figure 6.28. Effect of billet temperature and alloy composition on room temperature tensile properties (R=20:1).

Among the three alloy compositions the variation of the mechanical properties with direction was fairly high for the Al-Mg-Fe alloy, while for the Al-Mg-Cr alloy the variation was very little, see Tables 6.2-6.6 and 6.8-6.11. This is attributed to the inhomogeneity of the as-extruded microstructure; the Al-Mg-Cr alloy has a much more uniform microstructure than the other two alloys. The microstructural variety of the Al-Mg-Mn alloy is reduced during the thermomechanical processing and with increasing temperature, while the heterogeneity of the Al-Mg-Fe is only alleviated after heating for a considerable period of time. Moreover, since the Al-Mg-Fe alloy is composed of needle and spheroidal precipitates, the high volume fraction of needles aligned in the extrusion direction causes anisotropy. However, despite the great heterogeneity of the microstructure of the Al-Mg-Fe alloy, it exhibits higher ductility and k_{IC} values suggesting that this alloy is far better than the other two. This alloy also exhibits the best ductility, which is generally greater than 4%. Conversely, the ductility of the Al-Mg-Mn alloy is very poor; values between 0 and 2% were observed in the extrusion direction, but no general trend was observed (results are not included in Figure 6.28).

Another important property of the metallic materials is the modulus of elasticity, which is a measure of the stiffness of the material. The greater the modulus the smaller the elastic strain resulting from the application of a given stress. Since the modulus is determined by the binding forces between atoms, it is the most structure insensitive of the mechanical properties. However it is affected by the alloying elements. The additions of the transition elements to Al-Mg produced important changes in the elastic modulus. A value of 68.7 GPa has been reported for an Al-7Mg powder alloy studied by Tan (1984), while the moduli of the Al-Mg-Cr, Al-Mg-Mn and Al-Mg-Fe alloys of the present work are 76.3, 83.5 and 78.8 GPa respectively. These moduli are also higher than those of high strength 7075 (71.7 GPa) and the current high temperature alloy 2219 (73.1 GPa).

Finally, the elevated temperature properties of the three alloys and also for comparison purposes of Al-7%Mg, are illustrated in Figure 6.29. It is clear that the additions of the transition elements raise the strength levels at all temperatures examined. The Al-Mg-Mn alloy has the highest proof stress at ambient temperatures; at temperatures greater than 150°C its strength levels are only marginally better than the Al-7%Mg. The Al-Mg Cr alloy achieves superior properties at temperatures greater than 200°C, which is a somewhat surprising result in view of the excellent high temperature strength associated with the Al-Fe rapidly solidified alloys, {Thursfield and Stowell (1974)}. Chromium bearing alloys are commonly regarded as having moderate strengths but are usually acknowledged as having good thermal stability, thus a third alloying element is required for additional strengthening, {Jones (1980)}.

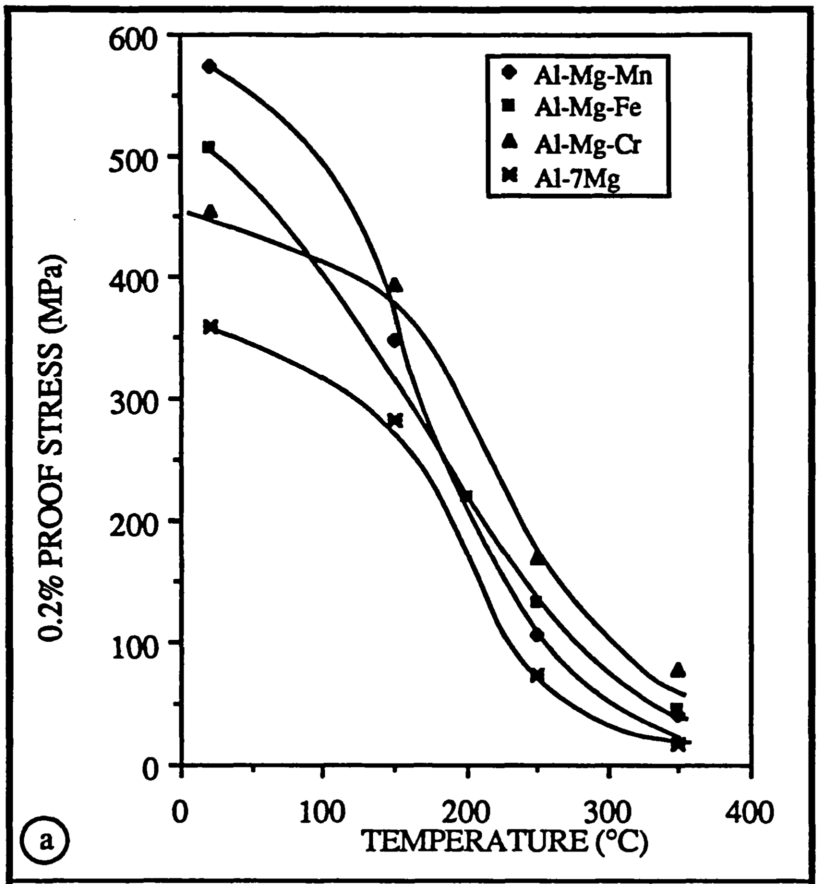

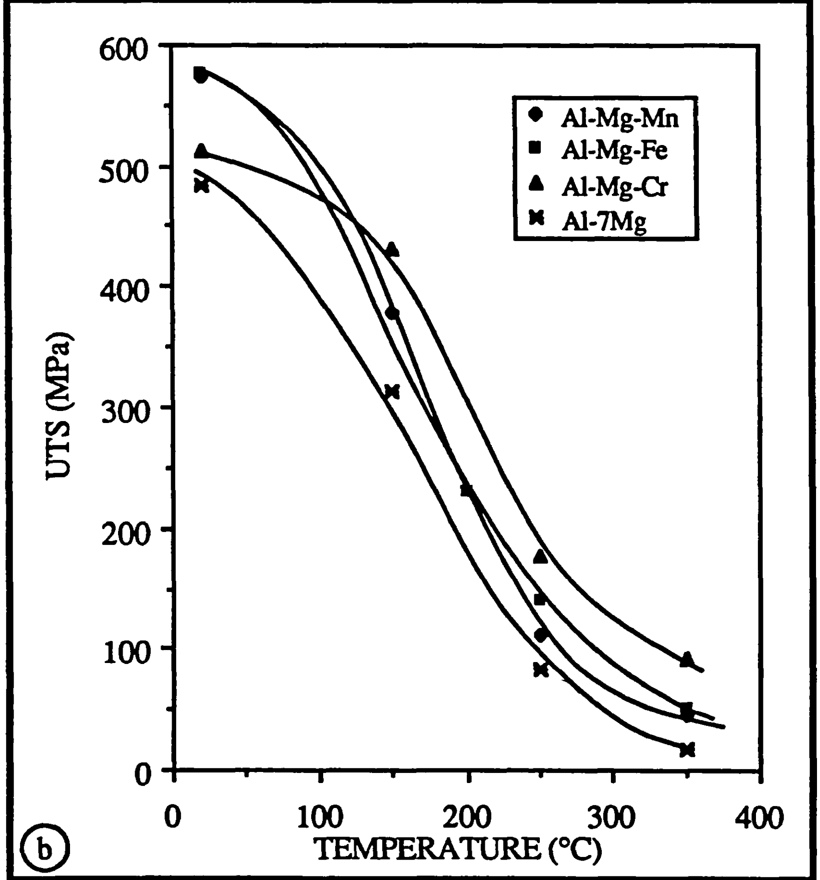

Figure 6.29. Variation of proof stress (a) and UTS (b) at elevated temperatures after 100h, of extrudates produced at 400°C, 20:1.

In addition to adequate strength during elevated temperature service, it is envisaged that some applications for aluminium alloys will require a preference for good retention of room temperature properties after exposure to high temperatures. Experiments with Al-Mg-transition element alloys indicate an excellent retention of properties after 100h at temperatures up to 350°C. Within the limits of experimental error, the hardness of extrudates from each alloy composition did not vary after the exposure indicated. Moreover, no significant change in precipitate size or dispersion was observed in the extrudate heat treated for 100h at 350°C. Thus, the three alloys studied exhibit good structural stability at possible service temperatures up to 350°C.

6.6. Conclusions

The as-extruded microstructure of all three alloys has been shown to be fibrous composed of different structure bands aligned in the extrusion direction. Generally, the final microstructure reflects the inhomogeneity of the original powder. During the thermomechanical processing the substructure has been built up associated with phase transformations resulting in a wrought structure with a non uniform distribution of second phase particles within the matrix. The Al-Mg-Cr alloy generally exhibited a much more uniform microstructure but with bands of coarse and fine dispersoids/aggregates originating from different size powder particles. The dispersoids were the unidentified phase/phases, and the equilibrium $Al_{18}Mg_3Cr_2$, Al_3Mg_2 and Cr_2Al_{13}. The Mn bearing alloy has relatively a more homogeneous microstructure, composed of $MnAl_6$ and $Al_{18}Mg_3Mn_2$ precipitates dispersed within the aluminium matrix; the $Al_{18}Mg_3Mn_2$ phase dissolves when the extrusion temperatures is greater than 450°C. Finally, the Al-Mg-Fe alloy is composed of two types of bands: Bands with a high volume fraction of dispersoids distributed at the subgrain boundaries, originating from the coarser cellular microstructure and bands with a high volume fraction of needle type precipitates aligned in the extrusion direction, originating from the microcellular structure. The precipitates were either Fe_4Al_{13} or $FeAl_6$, regardless of their size or shape. The mode of deformation for all three alloys was dynamic recovery, since dynamically rectrystallized grains were not observed.

The present investigation has shown that the single addition of a transition element Cr, Mn and Fe to a base Al-7%Mg alloy results in improved strength levels over a range of temperatures from ambient to 350°C. However, the use of dispersion strengthening results in a drastic reduction in tensile ductility. The mechanical properties depend on the microstructure and it is clear that heterogeneity has a detrimental effect. Obviously, an heterogeneous microstructure causes to a non-uniform distribution of stress, thus resulting in preferential deformation, high local strains and crack initiation.

It was found that the extrusion temperature has the most profound influence on extrudate properties at room temperature. During tensile testing discontinuous yielding was observed for the iron and manganese containing alloys, but was not apparent for the chromium bearing one, because the high volume fraction of the $Al_{18}Mg_3Cr_2$ phase in the latter alloy does not leave a sufficient amount of magnesium in solid solution for dynamic strain aging. The appearance of discontinuous yielding in both iron and manganese alloys was independent of extrusion conditions and therefore of the microstructural features that determine the tensile properties. The best combination of ambient temperature tensile properties was exhibited by the Al-Mg-Fe alloy. By comparison the tensile properties of the Al-Mg-Mn alloy were more susceptible to variations in extrusion parameters, particularly temperature, which indicates poor resistance of the second phase particles to coarsening during deformation. All three alloys exhibited Young's moduli values superior to conventional aluminium alloys.

After 100h exposure at elevated temperatures the chromium bearing alloy showed superior tensile properties in the temperature range 200°C-350°C. The elevated strength of the Al-Mg-Mn alloy was relatively poor and only marginally better than that of the binary Al-7%Mg used for comparison. Obviously, the manganese containing dispersoids do not aid thermal stability.

The additions of 3%Cr and 5% Fe to Al-7%Mg base alloy have improved strength levels and elastic modulus over a range of temperatures but consideration of dynamic properties is a further requirement. Variations in the chromium or iron concentrations may also lead to improvements in extrusion behaviour and the optimum combination of properties.

Finally, the properties of the as-extruded material are greater in the longitudinal direction than in the transverse one, especially for the iron bearing alloy. In general, alignment of the precipitates in the extrusion direction creates dispersoid stringers and thus lower interparticle spacing and inadequate bonding. The fracture toughness of the three alloys is also poor, which is attributed to the high volume fraction of second phase particles. Clearly, for adequate toughness properties, more dilute alloys are required.

General Discussion
and
Conclusions

Chapter 7. General Discussion and Conclusions

In the previous chapters of this presentation it has been shown that the characteristics, which mainly determine the microstructure and therefore the mechanical properties of the dispersion strengthened aluminium alloys prepared by rapid solidification, arise from both the size distribution of the powder particles and the quality of the 'interparticle' bonding developed during the hot working process. The relation of the powder particle size to the as-atomized powder microstructure has been extensively discussed previously and it is well established that the size and the dispersion of the intermetallic particles which affect the strength of the consolidated material vary with the size of the powder particulates. The heterogeneity of the microstructure is attributed to different solidification mechanisms that have been experienced by the various sized powder particles.

The powder microstructure of the three alloys varies considerably with the chemical composition. Among the three alloys the Al-Mg-Cr exhibits a much more uniform microstructure, while the iron bearing one is the most heterogeneous. This heterogeneity is retained even after the thermomechanical process. Conversely the heterogeneity of the powder microstructure of the Al-Mg-Mn alloy is largely alleviated during heating and deformation. The remarkable variation of the microstructure of the three alloys, which have been solidified under similar conditions, is a result of the solidification behaviour determined by the alloying elements. Aggregates were formed in the chromium alloy during rapid solidification. These aggregates were nucleated within the liquid droplet, because the liquidus temperature of the chromium phases is high, and the cooling rate was not high enough to suppress their formation. Subsequently, the already formed phases have served as nucleation sites for the solidification of other phases or they have reacted with the liquid (peritectic reaction). The size of the aggregates increases consistently with increasing powder particle size. This is because the larger powder particles have experienced lower solidification rates and thus there was more time available time for growth. The rapid solidification regime has only affected the fine dispersion of the second phase particles within the matrix and the formation of metastable phase(s). Formation of non-equilibrium phases is a common characteristic of all three alloy compositions studied in the present work, since in each alloy a metastable phase has been observed. The microstructural features of the other two alloys, Al-Mg-Fe and Al-Mg-Mn, are strictly related to rapid solidification mechanisms. In general, iron containing alloys exhibit a tendency to form the eutectic α-Al/$FeAl_6$, when solidified at higher cooling conditions. Since the alloy in the present work has experienced relatively high solidification rates, the formation of eutectic has been suppressed and a microcellular structure has appeared instead. In the same way, high solidification rates have resulted in the featureless regions of the as-atomized Al-Mg-Mn powder particles. Such behaviour has been recorded at the smallest powder particles or during the first stage of the solidification of medium sized powders. The rapid solidification stage was then followed by moderate solidification rates, due to recalescence, and thus the resultant microstructure was of a cellular type for both the iron and manganese bearing alloys (second stage of medium sized powder particles or larger particles).

Decomposition of the powder microstructure during heating has not been recorded in the chromium alloy, which would be expected. On the contrary, in the Al-Mg-Fe alloy the metastable phase 'F' has been transformed into $(Fe,Mn)Al_6$ and Fe_4Al_{13}, while decomposition of the Al-Mg-Mn alloy, which has been shown to be the most temperature sensitive alloy, has revealed a number of significant points. Heating up to 400°C does not affect the icosahedral phase and little or no precipitation occurs in the powders containing this phase, while in the finer powders the Al_3Mg_2 transforms (>350°C) into $Al_{18}Mg_3Mn_2$, which in turn dissolves at temperatures greater than 450°C. The icosahedral phase transforms into the equilibrium phase $MnAl_6$ at temperatures higher than 400°C.

Major structural changes have occurred during high temperature deformation. In general the powder particles lose their identity and the rapidly solidified metastable microstructures have quickly responded to high local shear stresses and high temperature. The microstructural stability of the Al-Mg-Cr alloy has been retained in the wrought structure, while in the other two alloys the various powder microstructures have behaved differently and it is not surprising that bands of dissimilar microstructure were formed. Alignment of both subgrains and intermetallic particles occurred but most significantly the powder oxide film was disintegrated to a point where it became indistinguishable from other particles. The extrudate microstructure of the Al-Mg-Mn alloy contains a random distribution of both $Al_{18}Mg_3Mn_2$ and $MnAl_6$ precipitates, while at higher processing temperatures (>500°C) a coarser and more uniform and homogeneous structure has been observed, containing only $MnAl_6$. Homogenisation of the microstructure of the iron bearing alloy did not occur during extrusion, within the scope of the processing conditions examined, although improvements were obtained by increasing the billet temperature; formation of both spheres and needle particles was promoted at higher temperatures irrespective of phase (Fe,Mn)Al_6 or Fe_4Al_{13}.

The mechanical properties of the alloys have been shown to vary with the processing conditions. The general trend tends towards decreases in the proof stress, the tensile strength and the hardness with increasing extrusion temperature, and decreasing reduction ratio. Poorer properties were observed along the transverse direction. The fabrication causes highly directional flow and thus alignment of the second phase particles in stringers causing anisotropy of the tensile properties. The chromium alloy exhibits relatively isotropic behaviour, while the greatest anisotropy has been noted in the iron bearing alloy. In general large, second phase particles are extremely detrimental to ductility and toughness. Thus, when they are aligned in stringers they result in considerable strength loses. Moreover, the heterogeneous microstructure influences mechanical properties with the likelihood of poor fracture behaviour due to localised strains and preferential crack initiation. At elevated temperatures the Al-Mg-Cr alloy achieves superior properties, which may be the result of microstructural uniformity and a relatively high resistance to coarsening. Finally, it must be mentioned that the poor toughness of these alloys is attributed mainly to the very high density of second phase particles observed.

The study of these three rapidly solidified alloys, together with another one, Al-6%Mg-5%Fe-3%Cr (unpublished work), which due to the high volume fraction of the precipitates was extremely brittle, indicated that new more dilute alloys must be designed. Magnesium is useful, because it reduces the overall density of the alloy and increases the corrosion resistance {Tan (1984)}. On the other hand the transition elements offer considerable advantages, i.e. Mn increases the modulus, Cr is useful in favouring microstructural stability and thus high temperature properties, and Fe increases the strength at ambient and elevated temperatures. Based on the findings of this project two alloy compositions are suggested:

- Al-4%Mg-2.5%Mn-2.5%Cr, which should have a high modulus and reasonable strength and
- Al-4.5%Mg-3%Cr-2%Fe, which should have high elevated temperature strength.

References

Adam (1981)	C.M. Adam: "Structure/Property Relationships and Applications of R/S Al-alloys", "Rapidly Solidified Amorphous and Crystalline Materials", Proc. of Mat. Res. Soc. Annual Meeting, Nov. 1981, Boston, Massachusetts, Ed. B. H. Kear, B. C. Giessen and M.Cohen, vol. 8, North Holland, 1982, pp. 411-422.
Adam (1985)	C.M. Adam: "Rapid Solidification Technology: The potential for Innovative Alloy Properties", NATO Scientific Affairs Division Workshop, "Rapid Solidification Technologies", March 18-22, 1985, Castle of Theuren, FRG.
Adam and Bourdeau (1980)	C.M. Adam and R.G. Bourdeau: "Transition and refractory element additions to rapidly solidified aluminum alloys", Proc. 2nd Int. Conf. on Rapid Solidification Processing: Principles and Technologies II; Ed. R. Mehrabian, B. Kear and M. Cohen, Claitors Publishing Division, Baton Rouge, LA, 1980, pp. 246-259.
Armstrong (1969)	R. W. Armstrong: "Advances in Materials Research IV", Wiley International Publications, 1969.
Arzt et al (1983)	E. Arzt, M. F. Ashby and K. E. Easterling: "Practical applications of hot isostatic pressing diagrams: Four case studies", Met. Trans. A, vol. 14A, 1983, pp. 211-221.
Ashcroft and Lawson (1960/61)	K. Ashcroft and G. Lawson: Jnl. Int. of Metals, 1960-61, 89, p. 369.
Avitzur (1968)	B. Avitzur: "Metal Forming processes and analysis", McGraw-Hill,1968.
Bancel et al (1985)	P. A. Bancel, P. A. Heiney, P. W. Stephens, A. I. Goldman and P. M. Horn: "Structure of Rapidly Quenched Al-Mn" Phys. Review Let., vol. 54, No.22, June 1985, pp. 2422-2425.
Black (1955)	P. J. Black:"The structure of $FeAl_3$", Acta Cryst., vol.8 (1955), pp. 43-48, and ASTM 29-42.
Boettinger et al (1986)	W. J. Boettinger, L. Bendersky, and J. G. Early: "An Analysis of the Microstructure of Rapidly Solidified Al-8wt% Fe Powder", Met. Trans. A, vol. 17A (1986), pp. 781-790.
Bryant (1971)	A. J. Bryant: Zeitschrift für Metallkunde, vol. 62 (1971), p.701.
Castle and Sheppard (1976)	A. F. Castle and T. Sheppard: "Pressure required to initiate extrusion in some Al-alloys", Metals Technology, Oct. 1976, pp. 465-475.

Chare (1972)	P. J. M. Chare: "The extrusion of atomised powders of some aluminium alloys", Ph.D. Thesis, University of London, 1972.
Chare and Sheppard (1973)	P. J. M. Chare and T. Sheppard: "Powder extrusion as a primary fabrication process for Al-Fe alloys", Powd. Met., 1973, vol. 16, No. 32, pp. 437-458.
Cohen et al (1980)	M. Cohen, B. H. Kear and R. Mehrabian: Proc. 2nd Int. Conf. on Rapid Solidification Processing: Principles and Technologies II; Ed. R.Mehrabian, B.Kear and M.Cohen, Claitors Publishing Division, Baton Rouge, LA, 1980, p. 1.
Conserva and Leoni (1975)	M. Conserva and M. Leoni: "Effect of thermal and thermo-mechanical processing on the properties of Al-Mg alloys", Met. Trans. A, vol. 6A, 1975, pp. 189.
Cooper (1960)	J. Cooper: Acta Ctrystallogr., vol. 13 (1960), p. 257, and ASTM 29-14.
Cottrel (1958)	A. H. Cottrel: "Theory of brittle fracture in steel and similar metals", Trans. Met. Soc. AIME, April 1958, vol. 212, pp. 192-203.
Cottrell (1953)	A. H. Cottrell: Phil. Mag., 1953, 44, p. 829.
Delves (1974)	R.T. Delves: "Crystal Growth", 1, 40; 1974, Oxford, Pergamon Press.
Dieter (1981)	G. Dieter: "Mechanical Metallurgy" , McGraw Hill, 1981.
Drive (1985)	D. Driver: "Development in aero-engine materials", Metals and Materials, vol. 1 (1985), No. 6, pp. 345-354.
Duwez et al (1960)	P. Duwez, R. H. Willens and W. Klement, Jr: "Continiuous Series of Metastable Solid Solutions in Silver-Copper Alloys", J. Appl. Phys., vol. 31 (1960), pp.1136.
Duwez et al (1965)	P. Duwez, R. H. Willens and R. C. Crewdson: "Noncrystalline Structure in Solidified Gold-Silicon Alloys", J. Appl. Phys., vol. 36 (1965), p. 2267.
Easterling and Thölen (1973)	K. E. Easterling and A. R. Thölen: "The role of surface energy and powder geometry in powder compaction", Powder Metallurgy, 1973, vol. 16, No. 31 , pp.112 - 118.
Fischmeister (1978)	H. Fischmeister: Powd. Met. Int., vol. 10 (1978), #3, pp. 119-123.
Flemings (1974)	M. C. Flemings: "Solidification Processing", McGraw-Hill Series in Materials Science and Engineering, 1974.

Froes and Pickens (1984)	F.H. Froes and J.R. Pickens: "Powder Metallurgy of Light Metals Alloys for Demanding Applications", Journal of Metals, 36(1), 1984, pp. 14-28.
Gill et al (1981)	W. N. Gill, J. W. Jang, and J. C. Mollendorf: "Rapid Solidification of subcooled metallic drops", Chem. Eng. Comm., 1981, vol. 12, pp. 3-31.
Grant (1982)	N. J. Grant: "Rapid Solidification of Metallic Particulates", Jnl. of Metals, vol. 35 (1983), No. 1, pp. 20-27., and Proc. of AIME Symp. on High Strength Powd. Met. Aluminium Alloys, Dallas, TX, Feb. 17-18, 1982, pp.3-18.
Hall (1951)	E. O. Hall: Proc. Phys. Soc., 1951, B64, 747.
Hewitt et al (1973)	R.L. Hewitt, W. Wallace and M.G. deMalherbe: "The Effects of Strain - Hardening in Powder Compaction", Powd. Met., 1973, vol.16, No.31, pp. 88 - 105.
Hewitt et al (1974)	R. L. Hewitt, W. Wallace and M.C. deMalherbeg: "Plastic Deformation in Metal Powder Compaction", Powder Metallurgy, 1974, vol. 17, No. 33, pp. 1-12.
Hirst and Ursell (1958)	S. Hirst and D. H. Ursell: "Some limiting factors in extrusion", Metal Treatment 1958, pp. 409-416.
Hirth (1978)	J.P. Hirth: "Nucleation, Undercooling and Homogeneous Structures in Rapidly Solidified Powders", Met. Trans. A, vol. 29, March 1978, pp. 401-414.
Hockett and McQueen (1970)	J. E. Hockett and H. J. McQueen: "Proc. 2nd Int. Conf. Strength of Metals and Alloys, 1970, pp. 991-995.
In-Hyung Moon (1984)	In-Hyung Moon and Kyung-Hyup Kim: "Relationship between compacting pressure green density, and green strength of copper powder compacts ", Powder Metallurgy 1984, Vol. 27, No. 2, pp. 80 - 84.
Jacobs et al (1974)	M. Jacobs, A. Doggert and M. Stowell: "The microstructure of Al-8%Fe-based alloys prepared by rapid quenching from the liquid state", Journal Mat. Sci, vol. 9, p. 1631-1643.
Johnson & Kudo (1962)	W. Johnson and H. Kudo: "The mechanics of Metal extrusion", Manchester University press, 1962.
Johnson (1955)	W. Johnson: Bisra Rep. MW/E/55/64, 1955.
Johnson (1956)	W. Johnson: J. Mech. Phys. Solids, 1956. vol. 4, p.829.
Jonas et al (1969)	J. J. Jonas, C. M. Sellars, and W. J. McG.Tegart: "Strength and structure under hot-working conditions", Metallurgical Reviews, 1969, Review 130, pp. 1-24.

Jones (1969/70)	H. Jones: "Observations on a structural transition in Al alloys hardened by rapid solidification", Mat. Sc. Eng., 1969/70, 5, pp. 297-299.
Jones (1978)	H. Jones: "Developments in Aluminium Alloys by Solidification at higher coling rates", Aluminium, April 1978, vol. 54, No. 4, pp. 274-281.
Jones (1980)	H. Jones: Proc. 2nd Int. Conf. on Rapid Solidification Processing, Reston, 1980, Claitors Publications, p. 306.
Jones (1982)	H. Jones: "Rapid Solidification of Metals and Alloys", Monograph No. 8, The Inst. of Metallurgists, London, 1982.
Kim et al (1985)	Young-Won Kim, W. M. Griffith and F. H. Froes: "Surface Oxides in P/M Aluminium Alloys", Jnl. of Metals, Aug. 1985, vol. 32, No. 8, pp. 27-33.
Kunin and Yurschenco (1963)	N.E. Kunin and B.D. Yurschenco: Porsch Kovaya Met., 1963, vol.18, p. 3.
Langer (1974)	J. S. Langer: Rev. Mod. Phys., 1980, 53, 1.
Lawley (1986)	A. Lawley: "Modern Powder Metallurgy Science and Technology", Jnl. of Metals, vol. 38, No. 8, Aug. 1986, pp. 15-25.
Levi and Mehrabian (1982,a)	C.G. Levi and R. Mehrabian: "Microstructures of Rapidly Solidified Aluminium Submicron Powders", Met. Trans. A, vol. 13A, January 1982, pp.13-23.
Levi and Mehrabian (1982,b)	C.G. Levi and R. Mehrabian: "Heat Flow during Rapid Solidification of Undercooled Metal Droplets", Met. Trans. A, vol.13A, Feb. 1982, pp. 221-234.
Lloyd (1980)	P. J. Lloyd: "The deformation of Commercial Al-Mg alloys", Met. Trans. A, vol. 11A, August 1980, pp. 1287-1294.
MacCormack (1986)	I. B. MacCormack: "Dispersion strengthened P/M aluminium alloys", Metals and Materials, vol. 2, No. 3, March 1986, pp. 131-137.
Marshall (1986)	G.J. Marshall: "Microstructure of rapidly solidified Al-powder alloys", Proc. of Aluminium Technology '86, March 11-13, 1986, London.
Marshall and Sheppard (1986)	G. J. Marshall and T. Sheppard: "Structural development during production of tubes from rapidly solidified aluminium alloy powder", Mat. Sc. and Techn., June 1986, vol. 2, pp. 666-619.
Marshall et al (1986)	G.J. Marshall, E.K.Ioannidis and T. Sheppard: "Extrusion behaviour and mechanical properties of three rapidly solidified Al-Mg-transition element powder

	alloys", Powder Met., vol. 29, Januarry 1986, No.1, pp. 57-64.
McQueen and Jonas (1975)	H. J. McQueen and J. J. Jonas: "Recovery and deformation", "Treatises on Materials Science", vol. 6, Academic Press, 1975, pp. 393-493.
McShane (1978)	H. McShane: "Fibre-reinforced Materials fabricated by powder extrusion", Ph.D. Thesis, University of London, 1978.
Mehrabian (1982)	R. Mehrabian: "Rapid Solidification", Int. Metals Reviews, 1982, vol. 27, No.4, pp.185-208.
Mondolfo (1976)	L. F. Mondolfo: "Aluminium Alloys, Structure and Properties", Butterworth, 1976.
Mullins and Sekerka (1964)	W.W. Mullins and R.F. Sekerka: "Stability of a Planar Interface During Solidification of a Dilute Binary Alloy", J. Appl. Phys., 1964, vol. 35, pp. 444-451.
Nicol (1953)	A. D. I. Nicol: " The structure of $MnAl_6$", Acta Crystallographica, 1953, 6, pp. 285-293, and ASTM 6-0665.
Paramanand (1984)	Paramanand and P. Ramakrishnan: "Effect of powder characteristics on compaction parameters and ejection pressure of compacts"; Powder Metallurgy 1984, Vol. 27, No. 3, pp. 163-168.
Parkinson (1983)	R. D. Parkinson: "Deformation Processing of atomised Al- powders", Ph.D. Thesis, University of London, 1983.
Pearson and Parkins (1960)	Pearson and Parkins: "The Extrusion of Metals", Chapman and Hall, 1960.
Penrice (1958)	T. W. Penrice: "Compaction of powders using moulds made from reversible gels"; Powder Metallurgy, 1958, No. 1- 2, pp. 79 - 84.
Pickens (1981)	J. R. Pickens: "Review Aluminium Powder Metallurgy Technology for High-Strength Applications", Journal of Materials Science, vol.16 (1981), pp. 1437-1457.
Samson (1958)	S. Samson: Acta Cryst., 11, (1958), 851, and ASTM 29-18.
Samson (1965)	S. Samson: Acta Cryst., 1965, 19, p. 401, and ASTM 29-48.
Savage and Froes (1984)	S.J. Savage and F. H. Froes: "Production of Rapidly Solidified Metals and Alloys", Journal of Metals, April 1984, TMS-AIME, pp. 20-33.
Schey (1983)	J. A. Schey: "Tribology in Metal Working; Friction, Lubrication and Wear", ASM, Metals Park, Ohio,

	1983, pp. 403-441.
Sekerka (1965)	R. F. Sekerka: J. Appl. Phys., vol. 36 (1965), p. 264.
Sekerka (1973)	R. F. Sekerka: "Crystal growth: An Introduction", 403; 1973, Amsterdam, North-Holland.
Sellars and Tegart (1966)	C. M. Sellars and W. J. McG. Tegart: Mém. Sci. Rev. Mét., 63 (1966), p. 731.
Shapiro and Kolhhof (1974)	I. Shapiro and I. M. Kolhhof: J. Phys. Colloid Chem., 1974, 51, 483.
Shechtman and Blech (1985)	D. Shechtman and I. A. Blech:"The microstructure of Rapidly Solidified Al_6Mn", Met. Trans. A, vol. 16A, June 1985, pp. 1005-1012.
Shechtman and Horowitz (1984)	D. Shechtman and E. Horowitz: "Metastable phases of rapidly solidified Al-rich Al-Fe alloys", Report DARPA, MDA 903-83-K0400, Jan. 1984.
Shechtman et al (1984,a)	D. Shechtman, I. Blech, D. Gratias and J.W. Cahn: "Metallic Phase with Long - Range Orientational Order and No Translational Symmetry", Phys. Rev. Lett., vol. 53, 1984, p.1951.
Shechtman et al (1984,b)	D. Shechtman, R. J. Schaefer and F. S. Biancaniello: "Precipitation in Rapidly Solidified Al-Mn Alloys", Met. Trans. A, vol. 15A, Nov. 1984, pp.1987-1997.
Sheppard (1981)	T. Sheppard: Metals Technology, 1981, vol. 4, p.130.
Sheppard and Chare (1972)	T.Sheppard and P. J. M. Chare: "The extrusion of atomised Al-powders", Powder Met., 1972, Vol. 15., 29, pp.17-41.
Sheppard and McShane (1980)	T. Sheppard and H. B. McShane: "Strength of cold - pressed compacts", Powder Metallurgy, 1980, No. 3, pp. 120-125.
Sheppard and Raybould (1973)	T. Sheppard and D. Raybould: "A new approach to the contruction of extrusion-limit diagrams, giving structural information with application to superpure Al and Al-Zn-Mg alloys", Jnl. of the Inst. of Metals, vol. 101, 1973, pp. 73-78.
Sheppard and Tutcher (1980)	T. Sheppard and M. G. Tutcher: "Development of duplex deformation substructure during extrusion of a commercial Al-5Mg-0.8Mn alloy", Metal Science, Dec. 1980, pp. 579-589.
Sheppard and Wood (1976)	T. Sheppard and E. P. Wood: "On the pressure required for the extrusion of shaped Al sections", Proc. of 17th MTDR Conf., Birminham, 1976, MacMillan, London.
Sheppard and Zaidi (1986)	T. Sheppard and M.A Zaidi: "Effect of Preheat

time-temperature and properties of extrusions prepared from Al-Fe-Mn Rapidly solidified powders", Materials Sci., and Techn., Jan. 1986, vol.2, pp. 69-77.

Sheppard et al (1979) T. Sheppard, M. G. Tutcher and H. M. Flower: "Development of recovered dislocation substructures during plastic flow", Metals Science, Aug. 1979, pp. 473-481.

Sheppard et al (1982) T. Sheppard, P. J. Tunnicliffe and S. J. Patterson: "Direct and indirect extrusion of a high strength aerospace alloy", Journal of Mechanical Working Company Technology, vol.6 (1982), pp. 313-331.

Sheppard et al (1983, a) T. Sheppard, M. A. Zaidi, and G. H. Tan: "Production of high strength aluminium alloys by extrusion of atomised powders", Powder Metallurgy 1983, vol. 26, No 1, pp. 10-16.

Sheppard et al (1983,b) T. Sheppard, H. B. McShane, M. A. Zaidi and G. H. Tan: "The extrusion of atomised Al-alloy compacts and composites", Journal of Mechanical Working Technology, vol. 8 (1983), pp.43-70.

Sheppard et al (1983, c) T. Sheppard, M.A. Zaidi and G.H. Tan: "Microstructural Aspects of Extrusion of Rapidly Solidified Al-10Mg alloy powder", Metal Science, vol. 17, Dec. 1983, pp. 563-572.

Sheppard et al (1983,d) T. Sheppard, N. C. Parson and M. A. Zaidi: "Dynamic recrystallization in Al-7Mg alloy", Metal Science, vol. 17, Oct. 1983, pp. 481-490.

Simensen (1977) C. J. Simensen and R.Vellasamy: "Determination of Phases present in cast material of an Al-0.5wt%Fe-0.2wt%Si alloy", Zeit. f. Metallkunde, 68(1977), pp. 428-431.

Starke (1982) E. A. Starke, Jr.: "The Application of the Fundamentals of Strengthening to the Design of New Aluminium Alloys", Proc. of the 6th Int Conf on Strength of Metals and Alloys, Mehlbourne, Australia, Aug. 1982, pp. 1025-1044.

Starke and Wert (1985) E. A. Starke, Jr. and J. A. Wert: "The strengthening Mechanisms of Aluminium Powder Alloys", Proc. of a TMS-AIME Symp. on 'Aluminum Powder Metallurgy', Ed. G.J. Hildeman and M.J. Koczak, Fall Meeting, Toronto, Canada, Oct. 13-17 1985, pp. 3-23.

Strömgren et al (1973) M. Strömgren, H. Aström, and K. E. Easterling: "The effect of interparticle contact area on the strength of cold - pressed aluminium powder compacts", Powder Metallurgy, 1973, vol. 16, No. 32, pp. 155-165.

Tan (1984) G.H. Tan: "Extrusion of Rapidly Solidified Al-Mg alloys", Ph.D Thesis, University of London, 1984.

Tan et al (1984) G. H. Tan, M.A. Zaidi and T. Sheppard: "Extrusion and properties of an Al-10Mg alloy prepared from rapidly solidified powder", Powder Met., 1984, vol. 27, No. 1, pp.3-8.

Thomas (1966) A. T. Thomas: "Tensile Deformation behavior of an Al-Mg alloy", Acta Metall., 1966, vol.14, pp.1363-1374.

Thursfield and Stowell (1974) G. Thursfield and J. Stowell: "Mechanical properties of Al-8%Fe-based alloys prepared by rapid quenching from the liquid state", Jnl. of Mat. Sci., vol. 9 (1974), pp. 1644-1660.

Tietz and Palmer (1981) T. E. Tietz and I. G. Palmer: "Advanced P/M Al-alloys", Paper presented at "Advances in Powder technology", (Proc. Conf.), Louisville, KY, USA, Oct. 1981, ASM, Metals Park, Ohio, pp.189-224.

Tiller et al (1953) W. A. Tiller, K. A. Jackson, J. W. Rutter and B. Chalmers: "The redistribution of solute atoms during the solidification of metals", Acta Metall., Jul. 1953, vol. 1, pp. 428-437.

Tompson (1977) A. W. Tompson: "Substructure strengthening mechanisms", Met. Trans. A, vol. 8A, June 1977, p. 833.

Vierod (1983) R. P. Vierod: "Effect of Copper Additions on Deformation Processing of Aluminium Alloys", Ph.D. Thesis, University of London, 1983.

Walford (1965) L.K. Walford: "The structure of the intermetallic phase $FeAl_6$", Acta Cryst., 18(1965), pp. 287-291.

Wollkind (1979) D. J. Wollkind: "Precipitation and properties of solid state materials", 4,111; 1979, New York, Marcel Dekker.

Wood (1978) E. P. Wood: "The extrusion of shaped aluminium alloy sections", Ph.D. thesis, University of London, 1978.

Young and Clyne (1981) R. M. Young and T.W.Clyne: "An Al-Fe intermetallic phase formed during controlled solidification", Sc. Met., vol. 15, 1981, pp. 1211-1216.

Zaidi et al (1985) M. A Zaidi, J. S. Robinson and T. Sheppard: "Extrusion of Al-5Fe-7Mn alloy prepared from rapidly solidified powder", Mat. Sc. and Technology, vol. 1, Sep. 1985, pp. 737-742.

Ziegler (1973) W. Ziegler und K. Siegert: "Indirectes Strangpressen von Leichtmetals", Zeitschrift für Metallkunde, 1973, Bd. 64,44, p.224.